AD-A230 173

(12)

NANOCOMPOSITES FOR ELECTRONIC APPLICATIONS

Period October 1, 1988 to September 30, 1989

DTIC
ELECTE
DEC 18 1990
S D
D
DTIC FILE COPY

Final Report

OFFICE OF NAVAL RESEARCH

Contract No. N00014-86-K-0767

DARPA Order No. 1131

APPROVED FOR PUBLIC RELEASE--DISTRIBUTION UNLIMITED

Reproduction in whole or in part is permitted for any purpose of the Unites States Government

L. Eric Cross

TABLE OF CONTENTS

	Page
ABSTRACT	2
1.0 INTRODUCTION	4
2.0 TOPICS OF STUDY	4
3.0 FERROELECTRIC RELAXORS	5
3.1 Tungsten Bronze Structure Relaxors	5
3.2 Perovskite Type Relaxor Ferroelectrics	6
3.2.1 Dynamic Aspects of Behaviour	6
3.2.2 Optically Transparent Relasor Based Nanocomposites	7
3.3 Nanostructure - Property Relations in Complex Lead Perovskite	8
4.0 SYNTHESIS OF NANO-SCALE POWDERS	9
4.1 Lead Titanate Powders	9
4.2 Lead Magnesium Niobage (PMN) Studies	9
4.3 Use of the RESA Method to Synthesize AlN.	9
4.4 Sol-Gel Processing of Oxide Superconductors	10
5.0 MAGNETOELECTRIC NANOCOMPOSITES.	10
6.0 NANOCOMPOSITE SECOND HARMONIC GENERATING WINDOW MATERIALS	11
7.0 CERAMIC: POLYMER NANOCOMPOSITES FOR MICROELECTRONIC PACKAGING	13
8.0 ELLIPSOMETRIC STUDIES OF NANOCOMPOSITES AND INTERFACES	15
8.1 Future Direction	15
9.0 ADDITIONAL STUDIES	15
10.0 PAPERS PRESENTED IN REFEERED JOURNALS.	16
11.0 PRESENTATIONS AT NATIONAL AND INTERNATIONAL MEETING	17
12.0 INVITED PRESENTATIONS.	19
13.0 LIST OF APPENDICES	19

ABSTRACT

This document reports work carried out over the third year of a University Research Initiative (URI) on "Nanocomposites for Electronic Applications." The program is funded through the Office of Naval Research under contract N-00014-86-K-0767 from DARPA order number 1131. Over the year the work has moved more towards the detailed study of the relaxor ferroelectrics as a model system for self assembling nanocomposites.

In the perovskite structure lead magnesium niobate (PMN) a sequence of studies of the kinetics of the polarization process under both weak and high electric fields points up the close similarity of PMN to the magnetic spin glass systems. Application of the Vogel-Fulcher relation predicts the kinetics of the freezing process which immobilizes the micro-polar structure, and permits calculation of the relaxation at higher temperatures and frequencies. Studies of internal friction relate this behaviour to the dielectric through conventional electrostriction. New evidence has also been obtained through TEM observations of the order-disorder of B site cations in the $A(B_1B_2)O_3$ structure which gives rise to the fossil chemistry and nano-polar response.

In the tungsten bronze structure relaxors a major breakthrough is the clear documentation of spin glass behaviour in an already polar matrix, for properties in directions orthogonal to the polar axis. For the $Ba_xPb_{1-x}Nb_2O_6$ solid solutions at compositions close to the morphotropic phase boundary (MPB) this behaviour is seen in both ferroelectric tetragonal and orthorhombic species.

Work has continued developing transparent relaxor compositions by hot pressing and optical and electro optic properties are under study.

For ultra fine particle the work on lead titanate has been completed and shows that ferroelectric behaviour in this composition persists to particle dimensions of order 100A°. These fine particle ferroelectrics are being used to study ferrofluid phenomena in suspensions in insulating dielectric liquids.

Studies of composites for non critical phase matching are now focused upon Fresnoite (Barium titanium silicate) in a fluoroberyllate glass matrix and these studies have lead to the evolution of non critical phase matching in gadolinium molybolate.

A range of preparative studies have involved sol-gel techniques applied to PMN and PMN:PT solid solution and to the reactive submerged arc (RESA) technique for generating fine particles.

Details of the studies on the contract are given in the 18 technical appendices which are papers published on the contract studies.

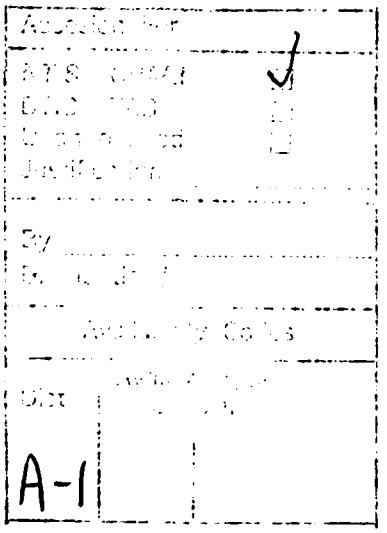

1.0 INTRODUCTION

This report documents work carried out over the third year of a University Research Initiative (URI) on "Nanocomposites for Electronic Applications." The program is funded through the Office of Naval Research under contract N-00014-86-K-0767 from DARPA order number 1131. The area proposed for study relates to functional (electronic) rather than structural composites and stems from earlier work on electronic macro-composites which was supported by DARPA and ONR contracts. In these earlier studies it was demonstrated that the average materials figure of merit for certain piezoelectric and pyroelectric applications could be vastly improved over that of either component of the composite. These enhancements were effected by using the phase interconnection (connectivity) to control the manner in which fluxes and fields thread through the composite and in this way enhancing the tensor components of value and depressing the components which were antagonistic to device performance.

These earlier studies were focused primarily upon large area composites for sonic and ultrasonic tranduction in water, where the wavelength of the waves are very long and effective averaging can be achieved with very course internal structures.

The purpose of the present program is to explore the extension of these composite ideas towards high frequency and optical applications where for effective averaging the internal scale must now be well below the wavelength of visible light i.e. in the nanometer region.

To provide properties which are likely to be of interest, and to make major use of the primary skills of this Laboratory it is natural to select a 'soft' ferroelectric type material as one component of the composite. For such systems however, since the ferroic response depends on a long range cooperative phenomenon it is natural to expect major changes even in the single phase component as the scale is reduced into this nanometer region. Such changes have been a major interest for the program of study.

2.0 TOPICS OF STUDY

Over the first two years of the contract period work was divided almost evenly between the generation of nanoscale particles of simple ferroelectrics, refining the methods to produce particles with more perfect surfaces and simple morphologies for later assembly into nanocomposite

structures, and the exploration of the relaxor ferroelectric families which are self assembling polar nanocomposites. With the realization of the major problems of architecting useful composites from nano-scale constituent phases, the balance of effort has moved strongly toward the self assembling systems.

Work upon the nano particle systems has been largely re-focused to explore the changes in the ferroelectric properties associated with the scaling and the powders are being used in liquid suspension as components of new and interesting dielectric ferrofluids.

A new more detailed study of the kinetics of weak field polarization in the relaxors have revealed a striking similarity to the kinetics of magnetization in spin glass systems. Current work is now exploring both dielectric and elastic responses in the lead magnesium niobate:Lead titanate system.

For the tungsten bronze structure relaxors, a detailed study of the optical and thermal expansion show unequivocal evidence of the existence of a polar nanostructure well above the temperature of the dielectric maximum and a strong connection in these materials to spin glass behaviour. Low temperature studies of the compositions near the morphotropic phase boundary in the Lead barium niobate bronzes has shown a startling relaxation in the poled single crystal when fields are applied normal to the polar axis. Perhaps the first instance of spin glass response in a polar phase.

Work on the magneto-electric and the nonlinear optic composites is being continued, but at a lower level.

The ellipsometric studies of the silicon based systems have now been completed and the more intransigent oxide systems are now the primary topic for study.

3.0 FERROELECTRIC RELAXORS

Self assembling nanocomposites structures.

3.1 TUNGSTEN BRONZE STRUCTURE RELAXORS

A very detailed and careful study of the glassy polarization in barium strontium niobates $Ba_{0.4}Sr_{0.6}Nb_2O_6$ (SBN 40 T_c ~ 75°C) $Ba_{0.25}Sr_{0.75}Nb_2O_6$ (SBN 25 T_c ~ 56°C) and $Ba_{2-x}Sr_xK_{1-y}NayNb_5O_{15}$ (BSKNN) has been carried out in conjunction with Dr. G. Burns and F.H. Dacol at IBM and with R.R. Neurgaonkar at Rockwell. Studies of both refractive index and elastic strain

as a function of temperature confirm the existence of a polarization at temperatures well above that of the dielectric maximum, which is itself above the temperature at which true remanence collapses. A detailed account is given in appendix 1.

Raman studies of the SBN 40 carried out again in cooperation with IBM and Rockwell show clear phonon anomalies associated with the dielectric maximum at T_c, and with the first onset of micro-polarization at (T_d). A more complete discussion is given in appendix 2.

In the lead barium niobate system, single crystals at compositions close to the morphotropic phase boundary which occurs near $Pb_{0.63}Ba_{0.37}Nb_2O_6$ have been examined for their dielectric properties in the temperature range form 10 to 300°K. Both lead rich crystals which are in the orthorhombic ferroelectric symmetry and barium rich crystals in the tetragonal ferroelectric symmetry show strong dielectric relaxation for fields applied normal to the polar axial direction. The dispersion appears remarkable similar to that in the perovskite relaxors, but is unique in that it occurs in a polar phase. Clearly the dielectric response is not due to a phase change, but is a "freezing in" of local polar moments. These moments can be oriented at low temperature to produce a remanence which is very small compared to the major ferroelectric polarization.

We believe that these fascinating behaviours can throw new light onto the whole spin glass behaviour. Details are given in appendix 3 and appendix 4 and appendix 5.

3.2 PEROVSKITE TYPE RELAXOR FERROELECTRICS

3.2.1 Dynamic Aspects of Behaviour

Dielectric and low frequency internal friction measurements have been carried out on PMN and PLZT relaxors. The purpose of these measurements was to study the dynamical nature of the micro-polar regions in these materials and the possibility of short-range interactions between them. These micro-polar regions are believed to be superparaelectric with the direction of spontaneous polarization thermally fluctuating between equivalent directions. The kinetics of the polarization fluctuations were studied by modelling the dielectric relaxation using the Vogel-Fulcher relationship. Activation energies on the order of kT were obtained from the modelling in addition to the prediction of a static freezing temperature. The static freezing temperature has been found to be in close agreement to

the temperature of the collapse in the remanent polarization on heating from a poled state. The implications are that short range interactions control the kinetics of the fluctuations and the freezing process, as in the magnetic spin glasses.

The internal friction measurement method used was a low frequency large amplitude resonance technique. The linear and nonlinear elastic and anelastic constants were calculated from the shape of the resonance curve. Elastic and anelastic softening in the non- linear coefficients were observed. All four coefficients were found to be strongly field dependent. The implication is that the spontaneous deformation may also thermally fluctuate between equivalent directions and that the micro-polar regions may then interact elastically. The existence of a large internal microstrain in some relaxors was confirmed by x-ray line broadening measurements. This brings up the possibility that various freezing mechanisms may exist in different relaxors determined by the nature of the dominant interactions.

Presently the field, compositional, and stress dependence of the kinetics of the polarization fluctuations are being investigated for various relaxor families using the same techniques. The dielectric non-linearities are being calculated to compare with the elastic non-linearities in an attempt at establishing the interactions which dominate the freezing process in each relaxor systems. The frequency dependence of the non-linear elastic and dielectric responses are also being measured. The eventual goal is to try to explain the differences between the various relaxors on the basis of different interactions and freezing mechanisms. Another goal of this investigation is to understand the mechanism of how long range polar order develops from relaxors as the composition is adjusted towards a normal ferroelectric or as an electric field is applied. Much time is also being invested in attempt to more fundamentally understand (model) the kinetical aspects of relaxors and the mechanism by which ordering fields can speed-up and/or slow down the fluctuations.

3.2.2 Optically Transparent Relaxor Based Nanocomposites

One of the primary tasks for studies on this URI was to explore the possible application of nanocomposite systems in the control of visible light. Since the self assembling relaxor ferroelectrics have been shown to contain nanopolar regions with sizes in the range of 5 to 20 n meters, whose orientation can be controlled by electric field they are of major importance to these studies.

Since it is both expensive and time consuming to grow single crystals of the compositions of interest, and the resultant samples are often of small size and inadequate optical properties it was vital to explore other methods of producing transparent samples.

For the lead magnesium niobate (PMN) by using a 1/2 mole% addition of Lanthanum oxide (La_2O_3) it has proven possible to produce good transparent samples using hot isostatic pressing (HIP) processing (appendix 6). The macro symmetry of PMN is cubic, so that the grains are optically isotropic and in a high density pore free ceramic the grain boundaries do not scatter at optical wavelength.

A more detailed account of the dielectric, optical and electro optic properties of hot pressed PMN and of PMN solid solutions with lead titanate is given in Appendix 7. From the behaviour of the refractive index as a function of temperature it is shown that polar micro-regions persist to temperatures well above that of the dielectric maximum, as is expected in relaxor nanocomposites. dispersion of the refractive index is well described by a single term Sellmeier equation. High quadratic electro-optic effects were observed and the quadratic g coefficients shown to be similar to those in other lead containing perovskites.

Results of a preliminary study of hot pressed ceramics in the Lead Scandium tatalate (PST) lead magnesium niobate system are reported in Appendix 8. Hot uniaxial pressing was carried out using the facilities at Plessey Research Caswell and data are given for dielectric behaviour, microstructure and optical transmittance.

3.3 NANOSTRUCTURE-PROPERTY RELATIONS IN COMPLEX LEAD PEROVSKITES

Transmission electron microscope studies on several complex lead perovskite compounds with the general formula $Pb(B'B'')O_3$ and their solid solutions have been used to demonstrate the very strong role which local ordering of the B site cations plays in controlling the dielectric response. It is shown that compositions exhibiting no cation ordering or very high degrees of order behave more like normal ferroelectrics, whilst the strong relaxor spin glass like behaviour is best expressed in compositions which show strictly limited short range ordering. A hypothesis is suggested which relates the 0.3 polar connectivity in these nanocomposites to the 0.3 order disorder connectivity. This work is presented in Appendix 9.

4.0 SYNTHESIS OF NANO-SCALE POWDERS

4.1 Lead Titanate Powders

A detailed study of the preparation of nanometer size lead titanate particles by chemical co-precipitation has now been completed (Appendix 10). Crystallization was carried out by low temperature heat treatment of the as precipitated powders produced by a precipitation reaction from a $Pb(NO_3)_2$:$TiCl_4$ and H_2O_2:$TiCC_4$ solution by slow addition of ammonia solution. TEM techniques were used to explore the symmetry of individual crystallites and to show that ferroelectric tetragonal particles ($c/a \simeq 1.065$) occurred over the size range above 10 nm. Both the particle size and the phase content could be regulated by the heat treatment and powders exhibiting both cubic and tetragonal crystalline phases were produced.

4.2 Lead Magnesium Niobate (PMN) Studies

The sol-gel method is of increasing importance for the fabrication of both bulk and thin film ferroelectric perovskites. In the study discussed in Appendix 11, the structure of a gel used in the production of Lead magnesium niobate containing different mole fractions of the lead magnesium and niobium ions has been explored using TEM methods. The work has revealed that the as prepared gels have a course texture and contain some crystallites often up to a few nanometers in size. Analysis by EDS and SAEDP show that this phase separation is on a very fine scale.

In the preparation of PMN, the appearance of a non stoichometric pyrochlore structure phase at low temperatures often complicates the processing and degrades the resultant electro-mechanical properties. Work described in Appendix 12 reports studies of a range of Diphasic gels which were made up using a small concentration of perovskite type PMN seeds. The unseeded gels calcined at 775°C for 2 hours gave ~ 98% of the perovskite structure phase. The use of 1% of PMN seeds not only gave completely pure perovskite PMN but also lowered the crystallization temperature for the gel by some 75°C.

4.3 Use of the RESA Method to Synthesize AlN

The reactive electrode submerged are (RESA) process has been applied to the synthesis on nanoscale particles of aluminum nitride using liquid nitrogen or liquid ammonia as the dielectric fluid surrounding the arc. For liquid nitrogen a mixture of γ aluminum oxide and hexagonal aluminum

nitride was produced, probably due to oxygen contamination in the nitrogen bath. Powders formed in the liquid ammonia were a mixture of hexagonal aluminum nitride and aluminum metal, consisting of large polyhedra 30-100 nm in size and exceedingly fine particles less than 10 nm in size. A detailed account is given in appendix 13.

4.4 Sol-gel Processing of Oxide Superconductors

Bulk materials and thin films of pure homogeneous $YB_2Cu_3O_{7-x}$ and $Bi_2SR_2CACu_2O_{8-x}$ composition were prepared by a nanocomposite solution-sol-gel (SSG) process. This work is discussed in Appendix 14.

5.0 MAGNETOELECTRIC NANOCOMPOSITES

Magnetoelectric composites consist essentially two phases; a piezomagnetic phase and a piezoelectric phase. When placed in a magnetic field the piezomagnetic phase is strained and this strain is transferred to the piezoelectric phase which is electrically polarized producing an electric field across the composite. We have prepared $BaTiO_3$-$CoFe_2O_4$ composites with 3-0 type connectivity of different compositions by the different methods and measured their properties including the dielectric and magnetoelectric properties at high frequencies. To improve the magnetoelectric output from these samples we also have prepared $BaTiO_3$-$CoFe_2O_4$ and $Pb(Zr,Ti)O_3$-$CoFe_2O_4$ composites with 2-2 type connectivity by tape casting.

Tapes of Ni-Zn ferrite, $CoFe_2O_4$, $BaTiO_3$ and PZT have been prepared. In 2-2 type composites for the series type equivalent circuit of the piezoelectric phase the $CoFe_2O_4$ layers can be shorted so that the piezoelectric properties of the PZT and $BaTiO_3$ remain unaltered (See the Figures 1 and 2 below). The 2-2 type composites (60% PZT - 40% $CoFe_2O_4$) have shown much higher piezoelectric d_{33} constants (~140 pc/N) compared to that of 3-0 type composites (~5pc/N). The 2-2 composites demonstrated good magnetoelectric properties in an experiment designed to test the sample for transducer application. Future work is planned to compare the performance of 2-2 type composites with similar composites of 3-0 type connectivity and to study their properties including the dielectric, piezoelectric and magnetoelectric properties as functions of frequency to evaluate their performance as magnetic field sensors. The dependence of the resonance frequency on the layer thickness will also be studied.

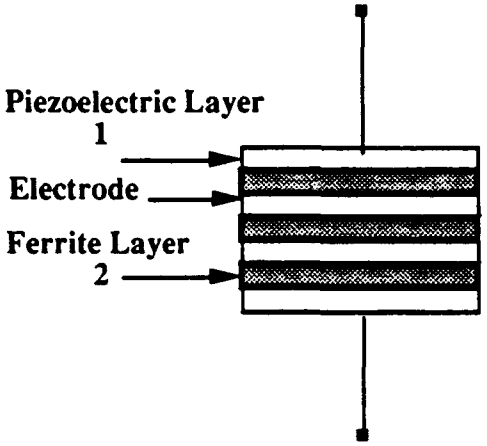

Figure 1 Magnetoelectric Multilayer Composite

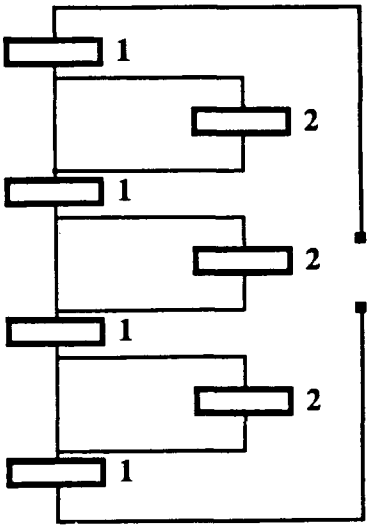

Figure 2 Equivalent Circuit

6.0 NANOCOMPOSITE SECOND HARMONIC GENERATING WINDOW MATERIALS

Efficient second harmonic generation is greatly facilitied by non-critical phase-matching (NCPM). In single crystals NCPM is a fortuitous event, the wavelength of which can be only slightly controlled by temperature tuning or crystal chemical substitutions. We are utilizing form birefringence, which arises from the interaction between a light wave and the shape of a particle, to develop a design scheme for composites where we can tailor the NCPM wavelength by changing the physical configurations of the composite.

Results from common effective media theory, which is valid in the limit of vanishing particle size, indicate that form birefringence is sufficient to achieve NCPM at infrared wavelengths, where chromatic dispersion tends to be small (e.g. fluoroberyllate glasses have dispersions as low as 0.003 between 5.0 μm and 2.5 μm). A more detailed approximation based on the

exact field solutions for a dilute suspension of infinite cylinder predicts that the selection of the proper particle size enhances form birefringence by as much as ten percent compared to that for vanishingly small particles, as is shown in Figure 1. From this data, we predict that a composite composed of 2.5 volume percent of 40 nm diameter fresnoite cylinders ($n \approx 1.7$, $d_{31} = 5.9$ pm/V) in a fluoroberyllate glass matrix ($n \approx 1.3$) can achieve approximately one percent conversion of a fundamental beam of 5.0 μm wavelength and 1.0 gigawatt/cm^2 power density to its second harmonic. We are currently beginning calculations based on an embedded dipole model which will extend our predictions to finite particle axial rations, non-dilute suspensions, and particles with anisotropic optical properties. We expect to submit the first publication on this application in May.

In anticipation of results confirming predicted NCPM for small birefringences in the infra-red, we have written a fortran program which predicts NCPM wavelengths for biaxial materials. In the corse of using this program, we have found that β' - $Gd_2(MoO_4)_3$ is capable of NCPM in the near infrared. We have confirmed our prediction (Figure 2) using an optical parametric oscillator and are currently characterizing the NCPM temperature and angular bandwidths. We expect to submit a letter for publication in March.

Finally, we will couple the form birefringence and NCPM wavelength formulations into a design scheme which we will use to create a real composite.

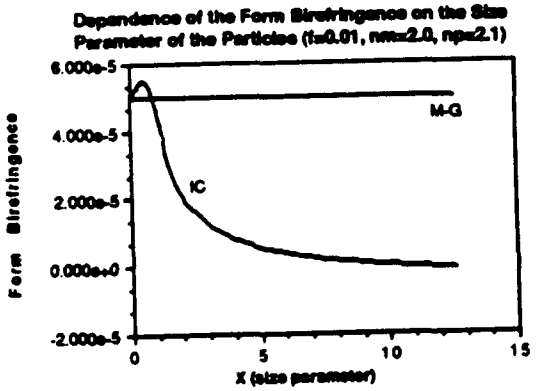

Figure 1

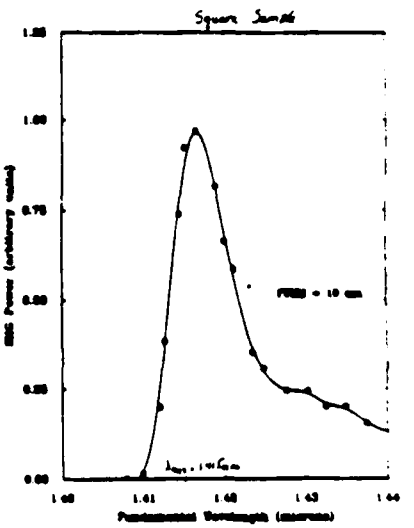

Figure 2

7.0 CERAMIC: POLYMER NANOCOMPOSITES FOR MICROELECTRONIC PACKAGING

This research deals with the potential use of silica/polyimide composites for substrate applications. Some important parameters that will be studied include: dielectric constant, dielectric loss, coefficient of thermal expansion, and mechanical integrity. Low dielectric constant and loss are important material properties to enhance signal speeds and decrease crosstalk between signal lines. The coefficient of thermal expansion (CTE) of the substrate should match closely to the device material, Si or GaAs (3.5-5 ppm/K), to alleviate thermal stresses. The mechanical integrity is also an important parameter so that the substrate can support the IC chips and also withstand handling during processing.

Much research has been done on porous silica substrates to reduce the dielectric constant but mechanical integrity and processability are the limiting factors. Polyimides are commonly using as interlayer dielectrics on Si or GaAs integrated circuits but do not exhibit the desirable CTE. Silica was chosen as a starting material because of its low dielectric constant (K = 3.8) and loss with temperature and frequency. A drawback of silica is the low CTE (~0.6 ppm/K). Polyimides were also chosen because of its low dielectric constant (K = 2.7) and loss but higher CTE (~35 ppm/K). Therefore, a composite of silica and polyimide is one of the paths toward achieving a CTE match while achieving a low dielectric constant. Combining the ceramic and polymer will also improve the mechanical integrity as compared to porous silica.

Silica (Cabosil) and polyimide will be mixed in such a manner to form 0-3 and 3-3 connectivities. Cabosil (20-50 nm) will be used in this study to investigate the effect of a large volume fraction of surfaces that make up the composite. These surfaces have been known to exhibit unique properties not predictable by mixing rules of composite materials. The homogeneity in nanocomposites can, in principle be higher than microcomposites, which have problems of differential settling of the dispersed phase during processing. Thus, the uniqueness and homogeneity are reasons for studying composites with a structure on the nanoscale. Micron particle size silica will also be used to compare the particle size effect. The transition from 0-3 and 3-3 connectivity with various loadings will be investigated by measuring the resistivity and applying percolation theory.

This work is discussed in Appendix 15.

8.0 ELLIPSOMETRIC STUDIES OF NANOCOMPOSITES AND INTERFACES

In nanostructures as well as in nanocomposite materials, as the size of the individual regions (grains) in materials are reduced to nanometer scale, it is evident that the surface to volume ratio of the regions (grains) becomes a very important factor in determining the physical properties of the final materials. In fact, since the bonding of the ions/atoms at the interface between grains is not the same as that inside the grain, the true chemical composition and the physical properites (such as dielectric constant, refractive index, optical absorption) of the surface and interface layers will be different form those of the bulk grain. Spectroscopic ellipsometry was employed in this study (i) to characterize such nanostructures, (ii) to determine the composition and structure of nonstoichiometric compounds, (iii) to follow the evolution of interfaces and recrystallization process on heat treatment, and (iv) to detect extremely thin layer and/or transitional regions between different layers. Before undertaking such studies on various oxides which are important for optoelectronics, preliminary investigations were carried out on nonstoichiometric Si-C and Si-Ge systems.

In the case of c-Si implanted with carbon ions the regression analysis of SE data was shown to be able to distinguish the chemical mixture of silicon and implanted carbon against the physical mixture of silicon and silicon carbide. On annealing such an-implanted specimens at high temperatures, the recrystallization of Si and the formation of crystalline silicon carbide could be followed by SE.

Virgin and germanium implanted crystalline silicon samples oxidized at high temperatures were examined. The interposing layer between the oxide and silicon substrate was found to be composed of a thin layer of crystalline germanium-silicon alloy Ge_xSi_{1-x} with the composition x accurately determined by SE. The effect of the strain due to lattice mismatch and quantum confinement of the interface was also investigated. The interface thickness determined by SE is found to be in excellent agreement with that obtained by comparison to that obtained by high-resolution transmission electron microscopy. It is shown that the composition of the alloy and not the thickness of the interface layer of Ge_xSi_{1-x} alloy is responsible for the enhancement of the oxidation rate of Ge^+-implanted c-Si.

Then single crystal silicon samples implanted with oxygen ions were analyzed by SE. In the as-implanted state, the thickness and the

composition of the understoichiometric oxide compound SiO_x formed in each layer were determined. The oxygen concentration is compared with the theoretically expected value. On high temperature annealing SiO_2 is formed and the damaged silicon is annealed, resulting in epitaxially grown c-Si from the substrate. SiO_2 was seen to redistribute on high temperature annealing. These results were confirmed by the Rutherford backscattering technique carried out on the same samples.

Depth profiling of silicon monoxide film on vitreous silica reveals the inhomogeneity of the oxygen concentration in the film. The composition x in the nonstoichiometric silicon oxide, SiOx, and the thickness of each layer of the film were determine. Such a nonstoichiometric compound was also observed at the interface between c-Si and its thick thermal oxide layer using the anti-S reflection technique. The result shows that this transitional region is 10 ± 0.9Å thick and composed of $SiO_{0.9 \pm 0.1}$.

8.1 Future Direction

Similar SE studies on nonstoichiometric oxides in Ba-), Sr-O, and BaSr-O systems will be undertaken. When once the studies on the alkaline earth oxides werein the oxygen ions are embedded in octahedral environment are completed, we will take up the cases of tetrahedral oxides BeO and ZnO, and the cases of $SrTiO_3$ and cubic phase of $BaTiO_3$ wherein oxygen ions have strong anisotropic charge distribution. It is hoped that these studies will lead to a clearer understanding of the dependence of the electronic polarizability of oxygen ions on its immediate surroundings. This is necessary before we can meaningful characterize (and thus modify the preparation parameters to improve the final product) the wide variety of nanocomposites of ferroelectric and optoelectronic materials.

9.0 ADDITIONAL STUDIES

An interesting rational for the high interest in Nanocomposite structures for Electronic Multifunctional Ferroic Nanocomposites is given in appendix 16. The study looks at the potential application for magnetic nanocomposites in magnetic recording, magnetic ferrofluids for seals and bearings and for their uses in vibration damping and in heat engines. At self assembling magnetic nanocomposites and their applications. For the ferroelectrics, the focus is upon the self assembling relaxor nanocomposites and their very wide range of potential applicability in capacitors,

transducers, agile systems, actuators, electo optic and optical switching systems. Ferroelectric system are also discussed and the possibility of super parelasticity is considered.

An interesting new type of nanostructure has been investigated in the mineral fresnoite $Ba_2TiSi_2O_8$. Single crystals of fresnoite grown in MRL, and polar glass ceramics based on fresnoite are known to have a most unusual anomaly in their pyroelectric response near 160°C, which causes the pyroelectric coefficient to begin to decrease rapidly and in fact pass through zero at 190°C.

In this study (Appendix 17) the appearance of nanodomains of an incommensurate structure is shown to occur on cooling form high temperature. The strain in these incommensurate regions appears to be too small to precipitate a ferroelectric phase as occurs in the germanium analogue ($Ba_2TiGe_2O_8$), but there is evidence of a very weak biaxiality in the canoscopic figure obtained when observing the silicate along the c axis. We believe that this unusual incommensurate transition may be responsible for the pyroelectric anomalies in the silicate.

A brief study of the pyroelectric, piezoelectric and dielectric properties of β BaB_2O_4 is presented in appendix (17). Piezoelectric coefficients and electro mechanical coupling coefficients in the borate are low and uninteresting however the pyroelectric figure of merit p/K, where p is the pyroelectric coefficient and K the relative dielectric permittivity is quite attractive for some device applications.

10.0 PAPERS PRESENTED IN REFEREED JOURNALS

1. N.C. Kim, D.A. McHenry, S.J. Jang and T.R. Shrout. "Fabrication of Optically Transparent Lead Magnesium Niobate Polycrystalline Ceramics Using Hot Isostatic Pressing," J. Am. Ceram. Soc. 73 (1990).

2. D.A. McHenry, J. Giniewicz, S.J. Jang, A. S. Bhalla and T.R. Shrout. "Optical Properties of Hot Pressed Relaxor Ferroelectrics," Ferroelectrics 93, 351-359 (1989).

3. C.A. Randall and A.S. Bhalla. "Nanostructural-Property Relations in Complex Lead Perovskites," Japanese Journal of Applied Physics 29 (2), 327-333 (February 1990).

4. P. Ravindranathan, E. Breval, S. Komarneni and R. Roy. "Studies of Polymeric ($Pb(Mg_{1/3}Nb_{2/3})O_3$ Gels," Materials Letters 8 (5), 161-164 (June 1989).

5. P. Ravindranathan, S. Komarneni and R. Roy. "Solid-State Epitaxial Effects in Structurally Diphasic Xerogel of $(Pb(Mg_{1/3}Nb_{2/3})O_3$," J. Am. Ceram. Soc. Communications.

6. R. Guo and A.S. Bhalla. "Pyroelectric, Piezoelectric, and Dielectric Properties of β-BaB2O4 Single Crystal," J. Appl. Phys. 66 (12), 6186-6188 (December 1989).

11.0 PRESENTATIONS AT NATIONAL AND INTERNATIONAL MEETINGS

1. R. Guo, A.S. Bhalla, C.A. Randall, Z.P. Chang and L. E. Cross. "Low Temperature Ferroelectric Properties of Morphotropic Phase Boundary Lead Barium Niobate ($Pb_{1-x}Ba_xNb_2O_6$) Compositions," 91st Annual American Ceramic Society Meeting, Indianapolis, IN, April 23-26 (1989).

2. R. Guo, A.S. Bhalla C.A. Randall and L. E. Cross. "Low Temperature Dielectric and Pyroelectric Studies of the Morphotropic Phase Boundary Lead Barium Niobate (PBN) Single Crystals," IMF-7, Saarbrucken, West Germany, August 28-September 1 (1989).

3. A.S. Bhalla, R. Guo, L. E. Cross, G. Burns, F.H. Dacol and R.R. Neurgaonkar. "Study of the Glassy Polarization Phase in the Tungsten Bronze Family by Measurements of Strain, Optical Indices, and Polarization," IMF-7, Saarbrucken, West Germany, August 28-September 1 (1989).

4. G. Burns, F.H. Dacol, R.R. Neurgaonkar, A.S. Bhalla and R. Guo. "Raman Measurements of the Ferroelectric $Ba_{0.4}Sr_{0.6}Nb_2O_6$," IMF-7, Saarbrucken, West Germany, August 28-September (1989).

5. D.A. McHenry, J.R. Giniewicz, S.J. Jang, A.S. Bhalla and T.R. Shrout. "Optical and Dielectric Properties of (1-x) $Pb(Mg_{1/3}Nb_{2/3})O_{3-x}PbTiO_3$ Ferroelectric Ceramics," 91st American Ceramic Society Meeting, Indianapolis, IN, April (1989).

6. D.A. McHenry, J.R. Giniewicz, S.J. Jang, T.R. Shrout and A.S. Bhalla. "Optical and Electro-Optical Properties of Lead Magnesium Niobate-Lead Titanate," International Symposium on Application of Ferroelectrics (ISAF'89), Saarbrucken, West Germany.

7. J.R. Giniewicz, D.A. McHenry, S.J. Jang, T.R. Shrout, A.S. Bhalla and F.W. Ainger. "Characterization of (1-x) $Pb(Mg_{1/3}Nb_{2/3})O_{3-x}PbTiO_3$ and $Pb(Sc_{1/2}Ta_{1/2})O_3$ Transparent Ceramics Prepared by Uniaxial Hot-Pressing," International Symposium on Application of Ferroelectrics (ISAF'89), Saarbrucken, West Germany.

8. D.A. McHenry, J.R. Giniewicz, S.J. Jang, T.R. Shrout and A.S. Bhalla. "Electrical and Optical Properties of Relaxor Ferroelectrics," India-Japan Meeting on Dielectrics (1989).

9. J.R. Giniewicz, D.A. McHenry, S.J. Jang and T.R. Shrout. "Hot Uniaxial Pressing of Relaxor Ferroelectrics in the PMN-PT System" Ferroelectrics 93, 395 (1989).

10. J.K. Yamamoto, C.A. Randall, S.A. Markgraf, A.S. Bhalla and M.A. Saifi. "Characterization of Single Crystal Fibers from Ceramics," 91st American Ceramic Society Meeting, Indianapolis, IN (1989).

11. R. Brodeur, C.A. Randall, A.S. Bhalla and R.E. Newnham. "Relationship Between Processing Properties and Ferroelastic Domain Density of $YBa_2Cu_3O_{7-\delta}$," 91st American Ceramic Society Meeting, Indianapolis, IN (1989).

12. S.A. Markgraf, C.A. Randall and A.S. Bhalla. "Incommensurate Phases in the System $Ba_2TiSi_2O_8$-$Ba_2TiGe_2O_8$," submitted to the Seventh International Meeting on Ferroelectrics, Saarbrucken, West Germany, August (1989).

13. J.K. Yamamoto, S.A. Markgraf, C.A. Randall and A.S. Bhalla. "Growth and Characterization of Ferroelectric/Polar Single Crystal Fibers," Seventh International Meeting on Ferroelectrics, Saarbrucken, West Germany, August (1989).

14. C.A. Randall, A.S. Bhalla, T.R. Shrout and L.E. Cross. "A Discussion of the Classification of Complex Lead Perovskites," Seventh International Meeting on Ferroelectrics, Saarbrucken, West Germany, August (1989).

15. D.D. Vieland, et al. "Elastic Non-Linearities in Relaxor Ferroelectrics," American Physical Society, St. Louis, MO, March.

16. D.D. Vieland, et al. "Field Dependence of the Internal Friction in PLZT," American Ceramic Society Meeting, Indianapolis, IN, April (1989).

17. P. Ravindranathan, U. Kumar, A.S. Bhalla and R. Roy. "Processing Studies and Dielectric Properties of $Pb(Mg_{1/3}Nb_{2/3})O_3$-$PbTiO_3$ System," 91st Annual Meeting, American Ceramic Society Meeting, Indianapolis, IN, April 23-27 (1989).

18. P. Ravindranathan, S. Komarneni and R. Roy. "Sol-Gel Processing of P Solid Solutions: Stabilization of the Perovskite Phase," 91st Annual Meeting, American Ceramic Society Meeting, Indianapolis, IN, April 23-27 (1989).

19. S. Komarneni, P. Ravindranathan, A.S. Bhalla and R. Roy. "Solution Sol-Gel Processing of Superconductors," International Conf. on Superconductivity, Bangalore, India, January 10-14 (1990).

20. P. Ravindranathan, S. Komarneni, A.S. Bhalla and R. Roy. "Preparation of Lead Magnesium Niobate-Lead Titanate, (1-x) $Pb(Mg_{1/3}Nb_{2/3})O_{3-x}PbTiO_3$ Thin Films by Solution-Sol-Gel Method (SSG)," International Symp. on Applications of Ferroelectrics, Urbana-Champaign, IL, June 6-8 (1990).

21. D.V. Miller, et al. "Electrical Properties of $BaTiO_3$ Suspensions," 91st Annual Meeting, American Ceramic Society Meeting, Indianapolis, IN (1989).

22. G. Harshe, J.H. Adair, T.T. Srinivasan and R.E. Newnham. "Preparation of Magnetoelectric Composites by Heterocoagulation Technique," 90th Annual Convention, American Ceramic Society Meeting, Cincinnati, OH, May 2-5 (1988).

12.0 INVITED PRESENTATIONS

1. A. Das, T.T. Srinivasan and R.E. Newnham. "Ceramic/Polymer Nanocomposite Properties of Microelectronic Packages," MRS (1989).

2. R.E. Newnham, S.E. McKinstry and H. Ikawa. "Multifunctional Ferroic Nanocomposites," MRS (1989).

13.0 LIST OF APPENDICES

1. A.S. Bhalla, R. Guo, L.E. Cross, G. Burns, F.H. Dacol and R.R. Neurgaonkar. "Study of the Glassy Polarization Phase in the Tungsten Bronze Family by Measurements of Strain, Optical Indices, and Polarization."

2. G. Burns, F.H. Dacol, R.R. Neurgaonkar, A.S. Bhalla and R. Guo. "Raman Measurements of the Ferroelectric $Ba_{0.4}Sr_{0.6}Nb_2O_6$.

3. R. Guo, A.S. Bhalla, C.A. Randall and L. E. Cross. "Low Temperature Dielectric and Pyroelectric Studies of the Morphotropic Phase Boundary Lead Barium Niobate (PBN) Single Crystals."

4. R. Guo, A.S. Bhalla, C.A. Randall and L. E. Cross. "Dielectric and Pyroelectric Properties of the Morphotropic Phase Boundary Lead Barium Niobate (PBN) Single Crystals at Low Temperature (10 - 300K)."

5. R. Guo, A.S. Bhalla, C.A. Randall, Z.P. Chang and L.E. Cross. "Polarization Mechanisms of Morphotropic Phase Boundary Lead Barium Niobate (PBN) Compositions."

6. N.C. Kim, D.A. McHenry, S.J. Jang and T.R. Shrout. "Fabrication of Optically Transparent Lead Magnesium Niobate Polycrystalline Ceramics Using Hot Isostatic Pressing," J. Am. Ceram. Soc. 73 (1990)

7. D.A. McHenry, J. Giniewicz, S.J. Jang, A. S. Bhalla and T.R. Shrout. "Optical Properties of Hot Pressed Relaxor Ferroelectrics," Ferroelectrics 93, 351-359 (1989).

8. J.R. Giniewicz, D.A. McHenry, T.R. Shrout, S.J. Jang, A.S. Bhalla and F.W. Ainger. "Characterization of (1-x) $Pb(Mg_{1/3}Nb_{2/3})O_{3-x}PbTiO_3$ and $Pb(Sc_{1/2}Ta_{1/2})O_3$ Transparent Ceramics Prepared by Uniaxial Hot-Pressing.

9. C.A. Randall and A.S. Bhalla. "Nanostructural-Property Relations in Complex Lead Perovskites," Japanese Journal of Applied Physics 29 (2), 327-333 (February 1990).

10. G.R. Fox, E. Breval and R.E. Newnham. "Crystallization of Nanometer Size Coprecipitated $PbTiO_3$ Powders."

11. P. Ravindranathan, E. Breval, S. Komarneni and R. Roy. "Studies of Polymeric $(Pb(Mg_{1/3}Nb_{2/3})O_3$ Gels," Materials Letters 8 (5), 161-164 (June 1989).

12. P. Ravindranathan, S. Komarneni and R. Roy. "Solid-State Epitaxial Effects in Structurally Diphasic Xerogel of $(Pb(Mg_{1/3}Nb_{2/3})O_3$," J. Am. Ceram. Soc. Communications.

13. T. Ono, P.W. Brown, J.H. Adair and P. Ravindranathan. "Synthesis of Ultra-Fine AlN Powders by the Reactive-Electrode Submerged-Arc Method (RESA)."

14. S. Komarneni, P. Ravindranathan, A.S. Bhalla and R. Roy. "Solution-Sol-Gel Processing of Superconductors."

15. A. Das, T.T. Srinivasan and R.E. Newnham. "Ceramic/Polymer Nanocomposite Properties for Microelectronic Packages."

16. R.E. Newnham, S.E. McKinstry and H. Ikawa. "Multifunctional Ferroic Nanocomposites."

17. S.A. Markgraf, C.A. Randall, A.S. Bhalla and R.J. Reeder. "Incommensurate Phase in $Ba_2TiSi_2O_8$."

18. R. Guo and A.S. Bhalla. "Pyroelectric, Piezoelectric, and Dielectric Properties of β-BaB2O4 Single Crystal," J. Appl. Phys. 66 (12), 6186-6188 (December 1989).

APPENDIX 1

STUDY OF THE GLASSY POLARIZATION PHASE IN THE TUNGSTEN BRONZE FAMILY BY MEASUREMENTS OF STRAIN, OPTICAL INDICES, AND POLARIZATION

A. S. Bhalla
R. Guo
L.E. Cross
G. Burns
F. H. Dacol
R.R. Neurgaonkar

STUDY OF THE GLASSY POLARIZATION PHASE IN THE TUNGSTEN BRONZE FAMILY BY MEASUREMENTS OF STRAIN, OPTICAL INDICES, AND POLARIZATION

A.S. BHALLA, R. GUO and L.E. CROSS
Materials Research Laboratory, The Pennsylvania State University
University Park, PA 16802

G. BURNS and F.H. DACOL
IBM T.J. Watson Research Center, P.O.Box 218
Yorktown Heights, NY 10598

R.R. NEURGAONKAR
Rockwell International Science Center, Thousand Oaks, CA 91360

Abstract There has been considerable discussion of crystalline ferroelectrics with a glassy polarization phase. There are materials in which there is evidence for regions of local, randomly oriented polarization far above the transition temperature T_c, up to a temperature T_d.

We report accurate temperature dependent measurements of optic indices of refraction, the birefringence and the strain in the ferroelectric tungsten bronze crystals $Ba_{0.4}Sr_{0.6}Nb_2O_6$ (BSN40, T_c ~75°C), $Ba_{0.25}Sr_{0.75}Nb_2O_6$ (BSN25, T_c ~56°C) and $Ba_{2-x}Sr_xK_{1-y}Na_yNb_5O_{15}$ (BSKNN). From the experimental data, it appears that far above the ferroelectric T_c, up to a temperature T_d, the crystals appear to possess a local, randomly oriented polarization, P_d, with the same T_d value irrespective of their chemical composition and T_c. Various aspects of our understanding of the polarization behavior and other effects in this ferroelectric system are discussed.

INTRODUCTION

Composition fluctuation plays the key role for relaxor behavior which was proposed by Smolenskii (1970)[1] and has been demonstrated by Setter and Cross (1980)[2] using the composition fluctuation in the Sc:Ta arrangement on the B site of $Pb(Sc_{1/2}Ta_{1/2})O_3$ perovskite structure. For any arbitrary direction in the relaxor ferroelectric there is a very broad distribution of Curie temperatures. For this type of system at any temperature within the Curie range, there is a volume fraction of small polar microregions in a matrix of nonpolar but high permittivity paraelectric phase. The behavior of such a system will depend critically upon the size of the polar regions. For every small volume, the energy

barrier E to reorientation of the polar vector would have the same order as KT, and the polar vector of the micro-volumes is no longer stable to thermal fluctuation. For large micro-volume where E is much larger than KT, a time stable domain configuration may develop. In both instances, we may expect the polar vectors of separated regions not to be strongly correlated, so that in the absence of an orientating external field, P the mean polarization of a representative macro-volume will be zero both above and below T_c the temperature of the dielectric maximum. That, however, will lead to a wide regimen above T_c for which although $P=0$, the mean square polarization is not equal to zero. Therefore, any property tensor coupled quadratically to the polarization, such as thermal expansion or optical refractive index, might be expected to change above T_c as $\overline{P^2}$ changes. Evidences to validate such argument have been reported previously for lead magnesium niobate (Jang et.al., 1980)[3] of the perovskite-type structure, strontium barium niobate (Bhalla et. al., 1987)[4] of the tungsten bronze type structure. A review reporting related efforts has been given by Cross (1987)[5].

Measurements of the electric polarization, P_s, thermal strains, x_1 and x_3, optical indices of refraction, n_1 and n_3 and birefringence, Δn_{ij}, on single crystals of tungsten bronze family, e.g. $Ba_{0.4}Sr_{0.6}Nb_2O_6$ (BSN40, T_c~75°C), $Ba_{0.25}Sr_{0.75}Nb_2O_6$ (BSN25, T_c~55°C), $Ba_{2-x}Sr_xK_{1-y}Na_yNb_5O_{15}$ (BSKNN) and $Pb_{0.33}Ba_{0.67}Nb_2O_6$ (PBN33, T_c~360°C), showed the temperature dependence of these properties above the transition temperature, confirming the nonzero values of $\sqrt{\overline{P_3^2}}$. The magnitudes of $\sqrt{\overline{P_3^2}}$ deduced from sets of data gathered from several independent methods, x_i vs. T, n_i vs. T, and Δn_{ij} vs. T, are in good agreement with each other, as are the values of T_d, and also indicate the substantial polarization fluctuations to temperatures well above the dielectric maximum at T_c.

THEORETICAL CONSIDERATIONS

Thermal Expansion

In the tungsten bronze type crystals, the prototype symmetry is 4/mmm so that the thermal expansion is anisotropic with components x_3 along the 4-fold axis and x_1 in the perpendicular plane. The ferroelectric symmetry is 4mm and the very high dielectric anisotropy at T_c shows that fluctuations are confined to the 4-fold axis, i.e. the ferroelectricity is uniaxial. For these cases, the polarization fluctuation induced strains will be given by

$$x_3 = \Delta c/c_0 = Q_{33}\overline{P_3^2} \quad (1)$$

$$x_1 = \Delta a/a_0 = Q_{13}\overline{P_3^2} \quad (2)$$

where Q, electrostrictive coefficient, is a fourth rank tensor written in contracted notation.

Optical Refractive Index

In the bronze family, there is a standing birefringence in the uniaxial tetragonal prototype, i.e. $n_3 \neq n_1$ and a birefringence Δn_{31}. Since that all polarization must occur along the ferroelectric (c-, or 3-) axis, then in contracted notation, we have for the indices of refraction

$$\Delta n_3 = - g_{33} (n_3^0)^3 \overline{P_3^2}/2 \quad (3)$$

$$\Delta n_1 = - g_{13} (n_1^0)^3 \overline{P_3^2}/2 \quad (4)$$

where n^0 is the index of refraction if there were no polarization of any sort present, whether along the c-axis (n_3^0) or perpendicular to it (n_1^0) and g_{ij} is the quadratic electro-optic constant. The change of optical birefringence $\delta(\Delta n_{31})$ will be given by (for $n_3^0 = n_1^0 = n_0$):

$$\delta(\Delta n_{31}) = \frac{1}{2} n_0^3 (g_{33} - g_{31}) \overline{P_3^2} \quad (5)$$

EXPERIMENTAL TECHNIQUE

The reversible polarization, P_r, was obtained by the integration of the pyroelectric current versus temperature measured by a method developed by Byer and Roundy (1972)[6]. The poled single crystal sample was heated in an air oven with automatic heating rate control. The pyroelectric current was measured by a picoammeter.

Thermal expansion measurements were carried out from room temperature to about 500°C by using a high sensitivity linear variable differential transformer (LVDT) dilatometer. Heating/cooling rate of 0.5°C/min was chosen and regulated by a microprocessor based temperature controller. Single crystal rods cut with length parallel to both c- and a-axis were mounted inside a fused silica holder which is set upright in a

vertical furnace, and the thermal expansion or contraction was recorded on an X-Y recorder.

The index of refraction parallel to P_r (n_3) and perpendicular (n_1) were measured by the minimum deviation technique (Burns et al., 1983, 1986)[7]. Oriented single crystal prisms were used in an oven in conjunction with various lasers as light sources.

The birefringence, Δn_{31}, was also directly measured. An a-cut plate was polished into a wedge shape with a known wedge angle (5-7°). Δn_{31} was measured using a polarizing microscope with a hot stage and the sodium D-lines as a light source (λ = 589.3nm). The birefringence was determined by

$$\Delta n_{31} = \lambda/d \sin \theta \qquad (6)$$

where θ is the wedge angle, and d is the separation between the interference fringes resulting from the varying thickness of the wedge.

RESULTS AND DISCUSSION

Room temperature values of several physical constants derived experimentally and used for the calculations of $\sqrt{\overline{P_3^2}}$ are summarized in Table I.

Figure 1 shows the indices of refraction both parallel and perpendicular to the tetragonal c-axis of single crystal BSN25 (at λ=632.8nm). As can be seen, the changes in n_3 are considerably larger than those perpendicular to the tetragonal axis (n_1). Continuous change in values of both n_1 and n_3 can be seen rather than a classical soft mode behavior for which a discontinuous in index of refractions is expected.

Figure 2 shows birefringence, Δn_{31}, as a function of temperature for single crystal BSN25. As is evident from Figure 2, Δn_{31} decreases with temperature and goes through zero (at a temperature well above T_c) and the crystal changes from optically positive to negative.

Figure 3 shows the thermal strain data, $x_1=\Delta a/a$, measured by LVDT for BSN25 single crystal. Using an extrapolation of the high temperature curve, it is possible to calculate the arrest of the change which is due to the onset of $\sqrt{\overline{P_3^2}}$. As can be seen from Figure 3, the deviation from the linear high temperature behavior occurs at a temperature (~360°C) approximately.

Temperature dependence of the pyroelectric coefficient p and the integrated reversible spontaneous polarization P_r of single crystal BSN25 are plotted in Figure 4. BSN25 is a typical relaxor-type ferroelectrics in which a ferroelectric-paraelectric phase transition is reported strongly temperature and frequency dependent[8]. In contrast to the polarization fluctuation behavior revealed by other techniques (as the results presented in Figures 1,2 and 3), P_r measured by Byer and Roundy method quickly goes to zero at a temperature immediately higher than T_c (~56°C at 1KHz by dielectric measurements).

Figure 5 summarizes the value of $\sqrt{\overline{P_3^2}}$, obtained from independent measurements, i.e. n_3, n_1, Δn_{31}, and $\Delta a/a$, calculated by using the corresponding equations (1) through (5). Also plotted is the reversible polarization data P_r from Figure 4. It is evident that the polarization calculated from the $\overline{P^2}$ is larger than the saturation polarization deduced from a simple Byer-Roundy thermal depolarization method and showing quantitatively the slow decay of $\sqrt{\overline{P_3^2}}$. Data derived from thermal expansion, using measured electrostrictive constants[9,10] of BSN40, and from optical index of refraction (as well as from birefringence), using known quadratic electro-optic constants (again from BSN40) agree well. Considering the difference between the physical quantities that are measured, each independent measurement yields an excellent account for the polarization characteristics in a glassy phase transition. The Q and g coefficients in the case of BSN25 are not available and hence these values of BSN40 are used in the calculation of $\sqrt{\overline{P_3^2}}$.

It has been known through previous investigation conducted by Glass(1969)[8] that the ferroelectric-paraelectric phase transition becomes more diffuse when Sr:Ba ratio increases. Figure 6 shows the results[4] of similar measurements done on BSN40. BSN25 shows more pronounced relaxor behavior for which the $\sqrt{\overline{P_3^2}}$ decays slower compared with BSN40. Nevertheless, both BSN40 and BSN25 show almost same T_d, even though there are differences in their compositions. It has been reported that T_d of PLZT is approximately equal to T_c of PZT (Burns et.al.,1983,1986)[7] and T_d of $Pb(Ti_{1-x}Sn_x)O_3$ is found[11] to be equal to T_c of $PbTiO_3$. In BSN crystals, there is no end member for which an estimate of T_d can be made. However, a compositional insensitive T_d do seems to exist in this system.

Similar studies have also been carried out for 'stuffed' tungsten bronze BSN crystals in which all six A-sites in a unit cell are occupied by cations (e.g., $Ba_{2-x}Sr_xK_{1-y}Na_yNb_5O_{15}$ or BSKNN in short) and rare-earth element doped BSKNN. Figure 7(a)

shows the indices of refraction both parallel and perpendicular to the tetragonal c-axis of single crystal BSKNN(1)II ($Ba_{0.8}Sr_{1.2}K_{0.5}Na_{0.5}Nb_5O_{15}$, T_c~175°C) for λ=632.8nm; Figure 7(b) shows the thermal strain $\Delta a/a$ measured by LVDT for BSKNN(1)II single crystal; the temperature dependence of the pyroelectric coefficient p and the reversible spontaneous polarization P_r of single crystal BSKNN(1)II are plotted in Figure 7(c). P_d values determined by the independent measurements again are shown in Figure 7(d) (the values of $\sqrt{\overline{P_3^2}}$ obtained from n_3, Δn_{31}, and $\Delta a/a$ have been given).

Figure 8 shows the plots of $\sqrt{\overline{P_3^2}}$ (determined from the birefringence data) vs the temperature for the compositions BSKNN(2)I, BSKNN(1)II, and Nd doped BSKNN single crystals. As shown in Figure 8, BSKNN(2)I ($Ba_{1.5}Sr_{0.5}K_{0.75}Na_{0.25}Nb_5O_{15}$, T_c~220°C) showed much sharper drop of the P_d at the T_c while BSKNN(1)II shows a slow decay of it. Although there is a larger difference in the T_c for BSKNN(1)II and BSKNN:Nd, their T_d's yield again almost the same values.

Besides BSN, lead barium niobate $Pb_{1-x}Ba_xNb_2O_6$ (PBN) composition is another example of bronze-type relaxor ferroelectrics (of either tetragonal or orthorhombic ferroelectric phase). Since the T_c of PBN is in the range of 270°C and above (e.g. Subarao et. al., 1960)[12], it has been difficult to measure the polarization by the Byer-Roundy method due to the high temperature conductivity. Figure 9 shows the value of P_d for $Pb_{0.33}Ba_{0.67}Nb_2O_6$ single crystal (which is of the tetragonal symmetry and far from the morphotropic phase boundary) obtained by the optical birefringence measurement. A T_d~500°C could be possible from the plot. T_c~350°C was obtained from dielectric vs temperature measurement. The particular composition has reasonably sharp T_c and very small diffuse phase transition characteristics. Thus the magnitudes of the P_d and P_s are very close for most of the temperature region. Also the T_c of dielectric measurement is in the same range as can be deduced from $\sqrt{\overline{P_3^2}}$ vs T in Figure 9.

SUMMARY

Measurements of thermal expansion and of the temperature dependence of index of refraction (or birefringence) can be used as independent ways to qualitatively define the characteristics of relaxor-type ferroelectric phase transitions.

From the experimental data, it appears that far above the ferroelectric T_c up to a temperature T_d, there exists a local , randomly oriented polarization P_d, with a T_d value insensitive to their compositions.

TABLE I. Values of the Q and g Coefficients Used for Calculation of $\sqrt{\overline{P_3^2}}$ for Most Crystals of Tungsten Bronze Family

Electrostrictive Constant (m^4/C^2)	$Q_{31} = -0.71 \times 10^{-2}$
	$Q_{33} = 3 \times 10^{-2}$
Quadratic Electro-optic Coefficient (m^4/C^2)	$(g_{33}-g_{13}) = 0.068$

REFERENCES

1 G.H. Smolenski, Proc. 2nd IMF Kyoto 1969, Phys. Soc. Jpn. 26 (1970).
2 N. Setter and L.E. Cross, J. Appl. Phys., 51, 4356 (1980).
3 S.J. Jang, L.E. Cross, and R.E. Newnham, Ferroelectrics, 23, 187 (1980).
4 A.S. Bhalla, R. Guo, L.E. Cross,G. Burns, F.H. Dacol and R.R. Neurgaonkar, Phys. Rev. B36(4), 2030 (1987).
5 L.E. Cross, Ferroelectrics, 76, 241 (1987).
6 R.L. Byer and C.B. Roundy, Ferroelectrics, 3, 333 (1972).
7 G. Burns and F.H. Dacol, Phys.Rev. B28, 2527 (1983). Ibid Jpn. J. Appl. Phys. 24, Suppl. 24-2, 85 (1986).
8 A.M. Glass, J. Appl. Phys., 40, 4699 (1969).
9 T. Shrout, A Phenomenological Theory for Predicting the Temperature Dependence of Elastic Constants in Simple Proper Ferroelectric Tungsten Bronzes, Ph.D Thesis, Penn. State Univ. (1981).
10 P. Asadipour, Polarization Mechanisms in Relaxor Ferroelectrics, MS Thesis, Penn State Univ., (1986).
11 G. Burns and F.H. Dacol, Sol. State Commun. 58, 567 (1986).
12 E.C. Subarao, G. Shirane and F. Jona, Acta Cryst. 13, 226 (1960).

FIGURE CAPTIONS

FIGURE 1. The measured n_1 and n_3 for BSN25 single crystal at 632.8nm.

FIGURE 2. Optical birefringence Δn_{31} for BSN25 measured with the sodium D-lines. The results for heating and cooling overlap each other.

FIGURE 3. Thermal strain measured by LVDT dilatometer for BSN25 along the a-axis.

FIGURE 4. Temperature dependence of the pyroelectric coefficient p and reversible spontaneous polarization P_r for BSN25 single crystal measured by Byer and Roundy method.

FIGURE 5. $\sqrt{\overline{P^2}}$ vs. T for BSN25, as calculated from n_3 vs. T (in solid circles), n_1 vs. T (in open circles), Δn_{31} vs. T (in solid triangles), and $\Delta a/a$ vs. T (in open rectangles). P_r vs. T from p vs. T measurements is also shown.

FIGURE 6. $\sqrt{\overline{P^2}}$ vs. T for BSN40, as calculated from n_3 vs. T (in solid circles), n_1 vs. T (in open circles), Δn_{31} vs. T (in solid triangles), and $\Delta c/c$ vs. T (in solid rectangles). P_r vs. T from p vs. T measurements is also shown as the solid line.

FIGURE 7. (a) the indices of refraction both parallel and perpendicular to the tetragonal c-axis at λ=632.8nm; (b) the thermal strain $\Delta a/a$ measured by LVDT dilatometry method; (c) the temperature dependence of the pyroelectric coefficient p and the integrated reversible spontaneous polarization P_r; and (d) a summary of the values of $\sqrt{\overline{P_3^2}}$ obtained from n_3 (in solid circles), Δn_{31} (in solid triangles), and $\Delta a/a$ (in open rectangles) of single crystal BSKNN(1), type II (the P_r value is also shown).

FIGURE 8. $\sqrt{\overline{P^2}}$ data derived from optical birefringence measurements for BSKNN(1), type II; BSKNN(1), type I; and Nd doped BSKNN.

FIGURE 9. $\sqrt{P^2}$ data derived from optical birefringence measurements for PBN33.

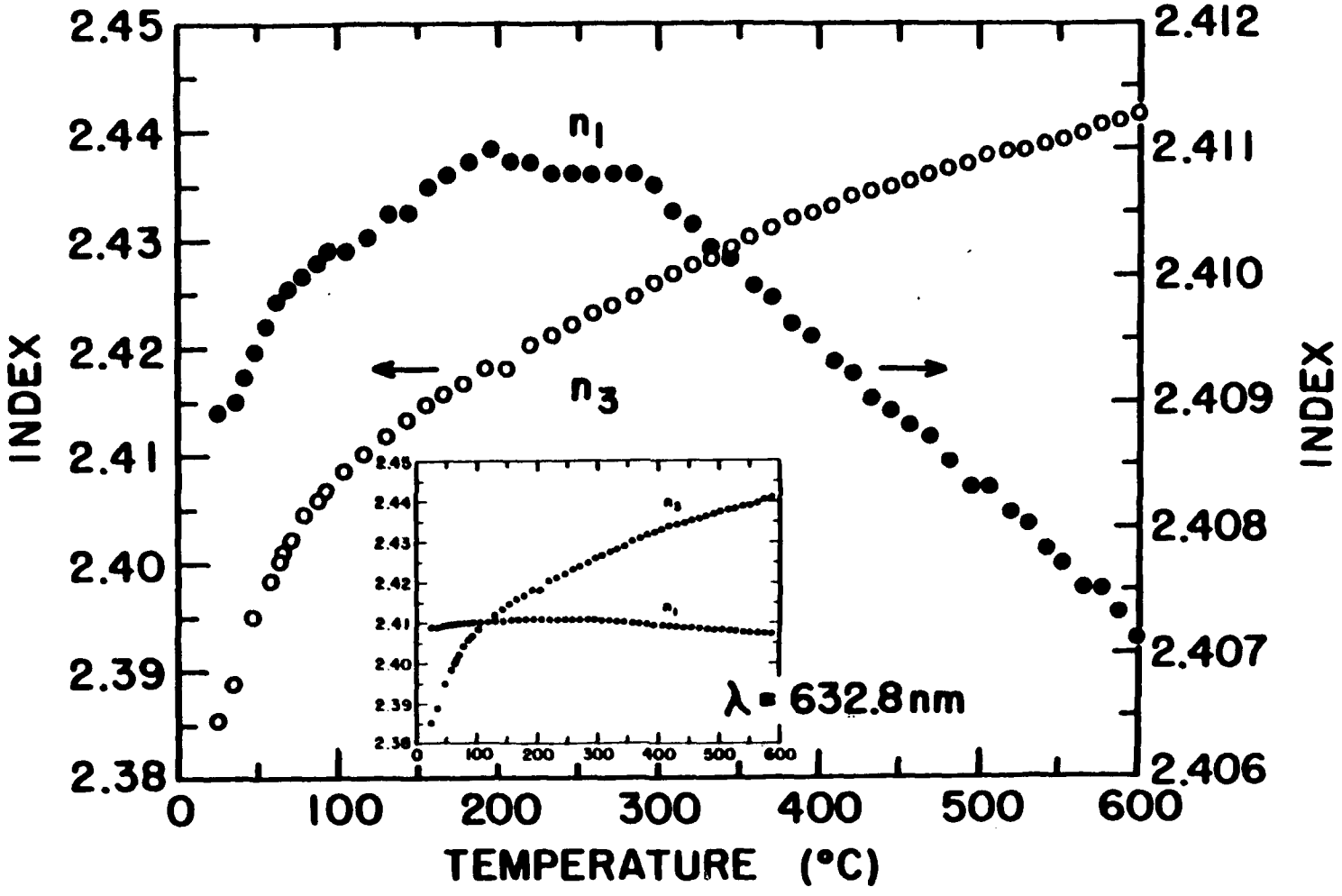
2.45
2.44
2.43
2.42
2.41
2.40
2.39
2.38
INDEX
2.412
2.411
2.410
2.409
2.408
2.407
2.406
INDEX
n_1
n_3
λ = 632.8nm
0
100
200
300
400
500
600
TEMPERATURE (°C)

Fig. 1.

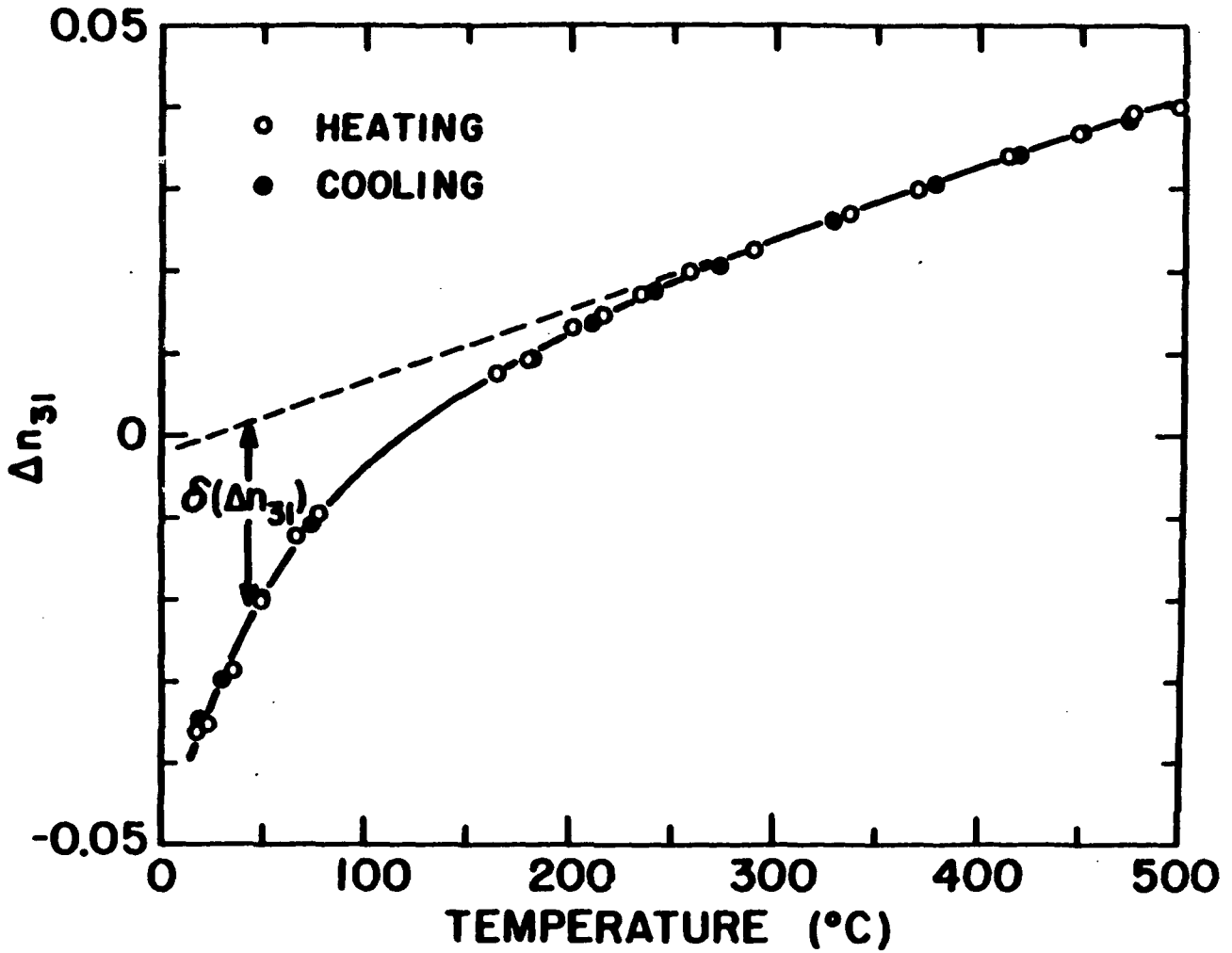
0.05
0
-0.05
Δn_{31}
HEATING
COOLING
$\delta(\Delta n_{31})$
0
100
200
300
400
500
TEMPERATURE (°C)

Fig. 2

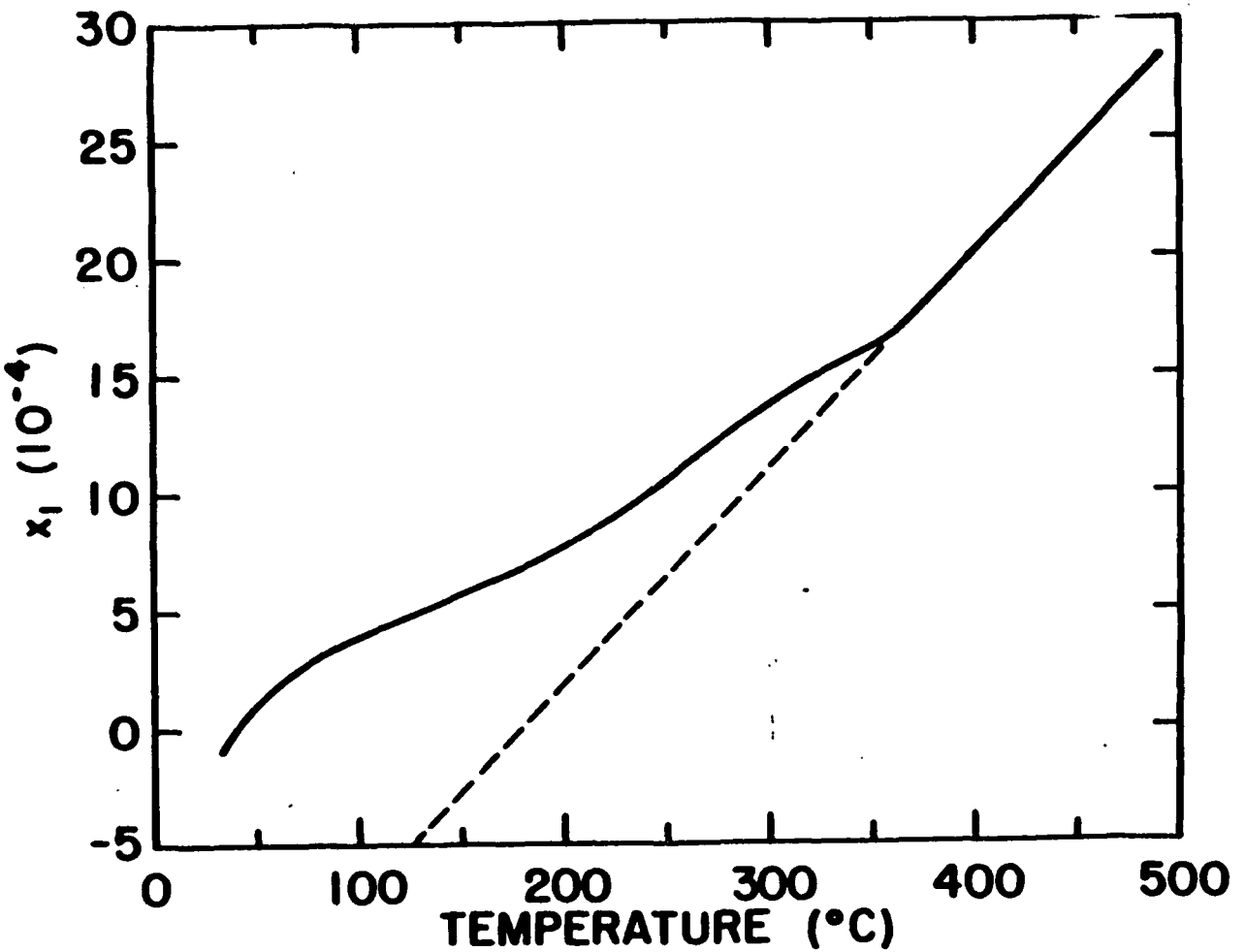
30
25
20
15
10
5
0
-5
x_1 (10^{-4})
0
100
200
300
400
500
TEMPERATURE (°C)

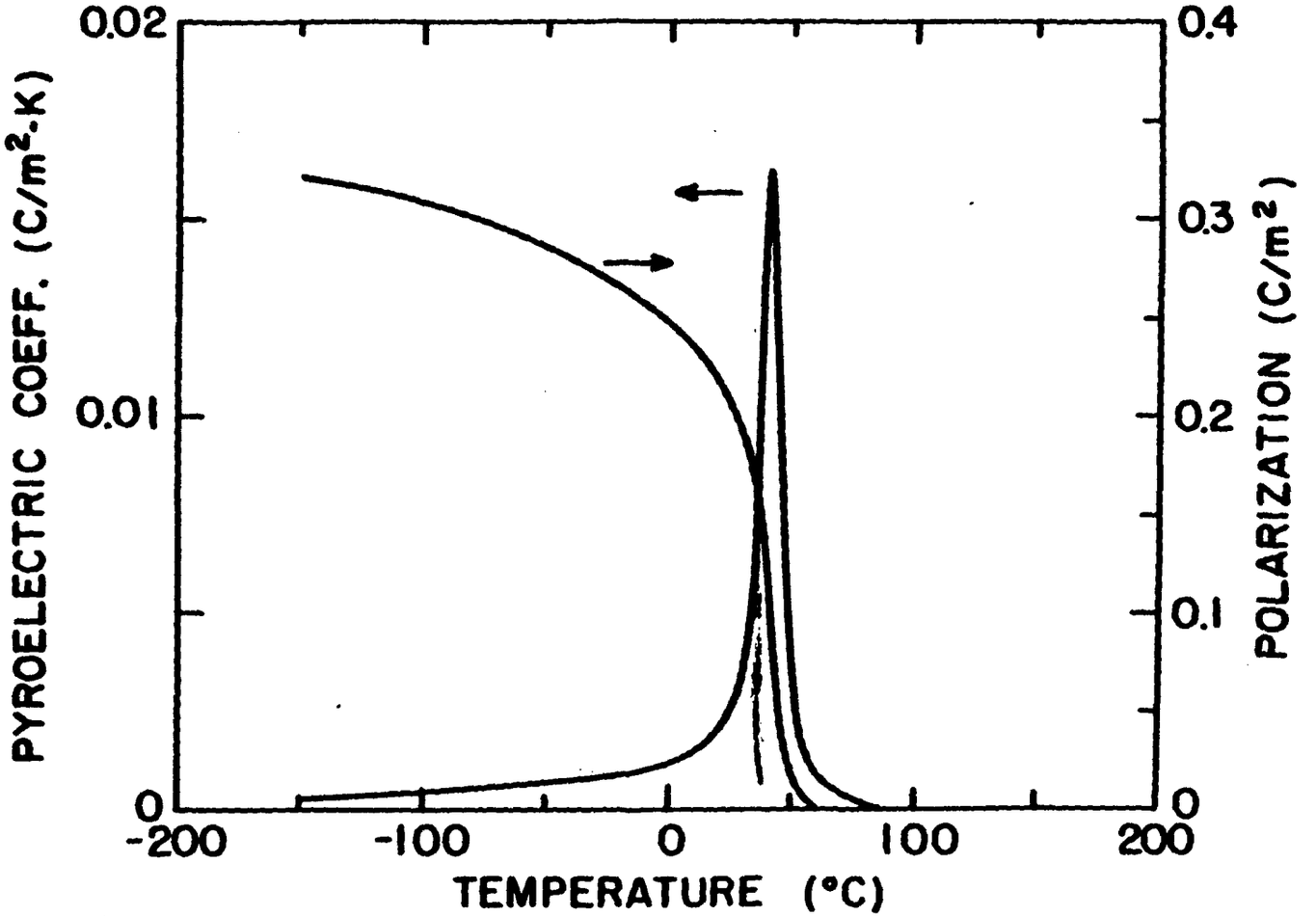
0.02
0.01
0
0.4
0.3
0.2
0.1
0
-200
-100
0
100
200
PYROELECTRIC COEFF. (C/m²-K)
POLARIZATION (C/m²)
TEMPERATURE (°C)

Fig. 4.

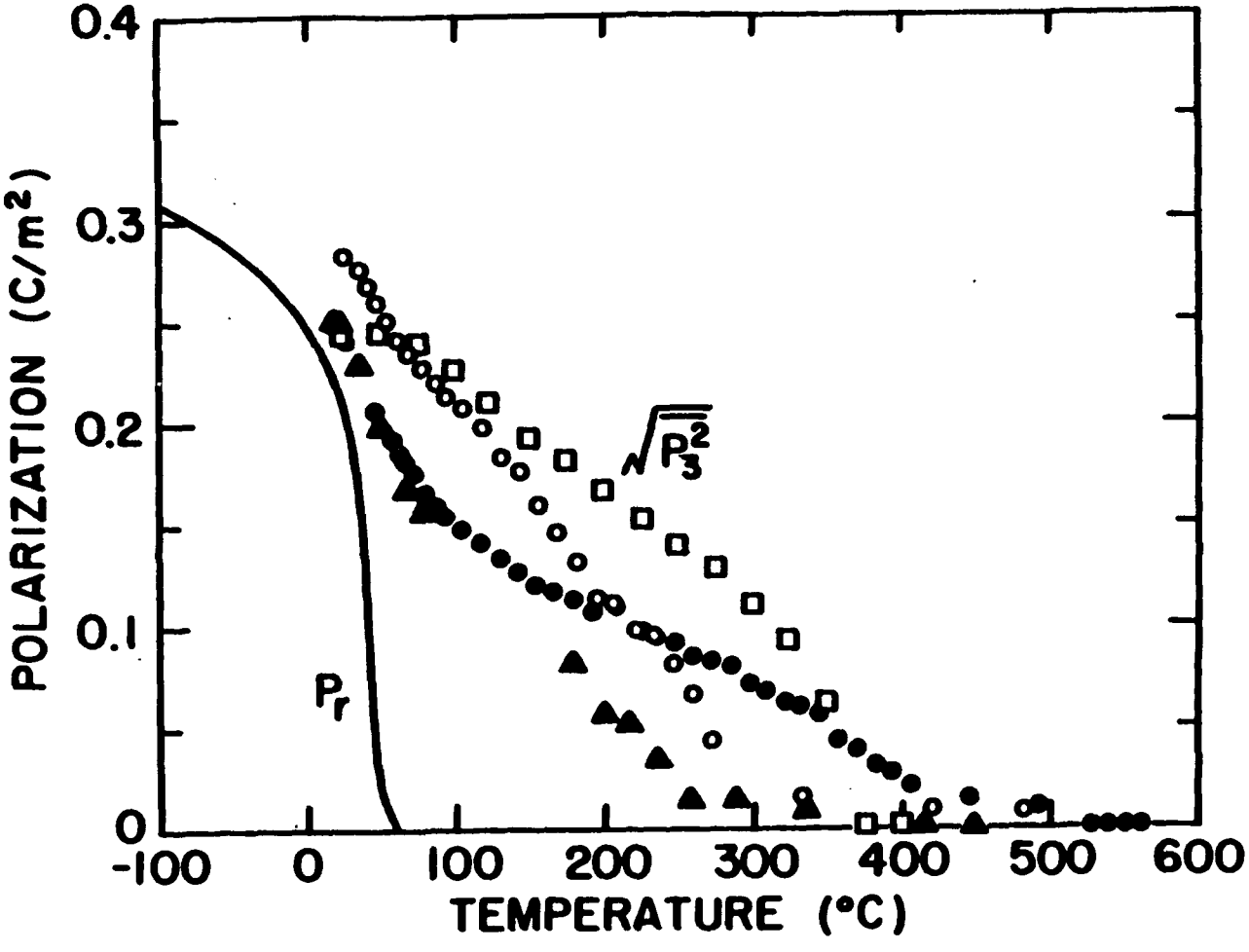
0.4
0.3
0.2
0.1
0
POLARIZATION (C/m²)
P_r
$\sqrt{\overline{P_3^2}}$
-100
0
100
200
300
400
500
600
TEMPERATURE (°C)

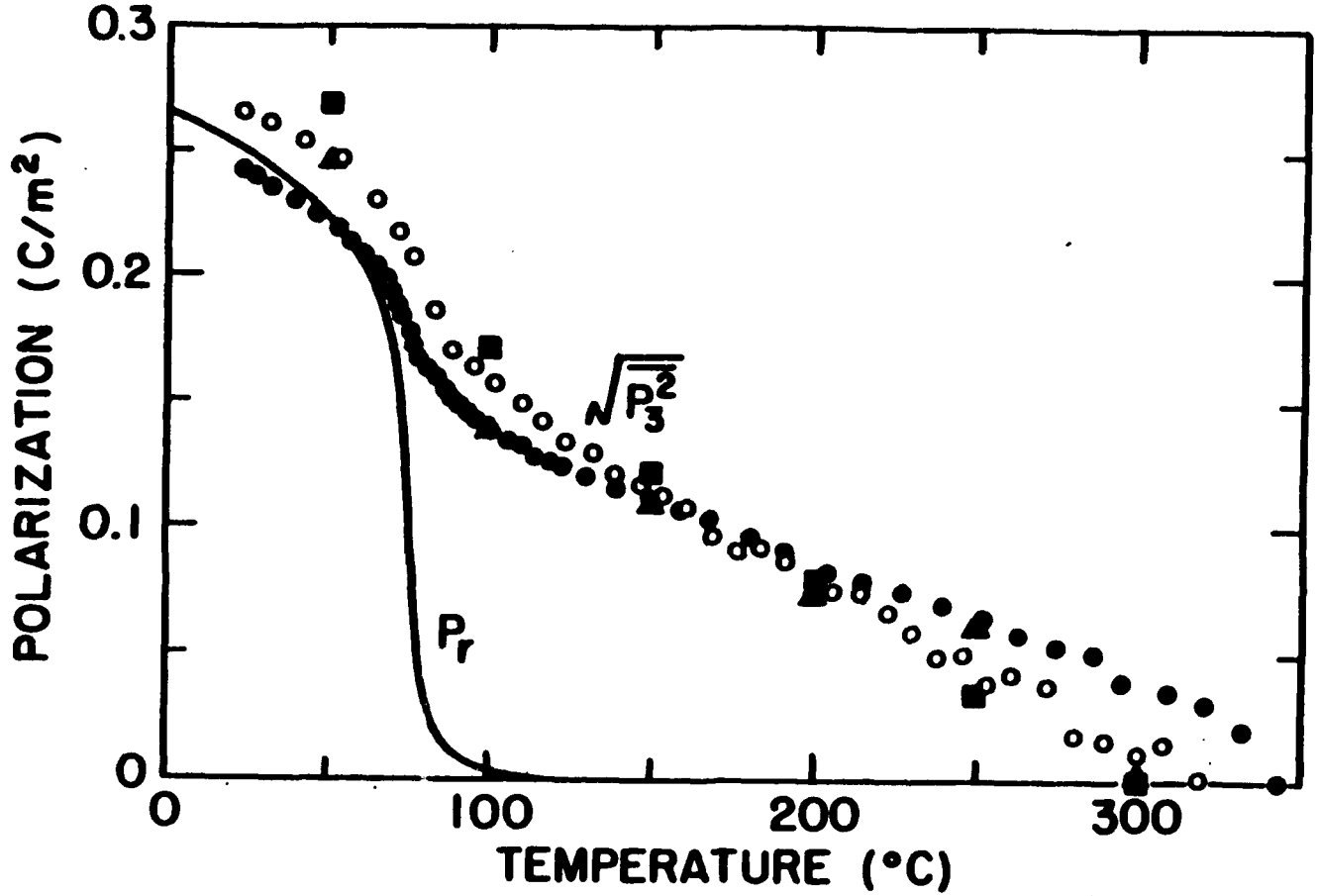
0.3
0.2
0.1
0
POLARIZATION (C/m²)
$\sqrt{\overline{P_3^2}}$
P_r
0
100
200
300
TEMPERATURE (°C)

Fig. 6

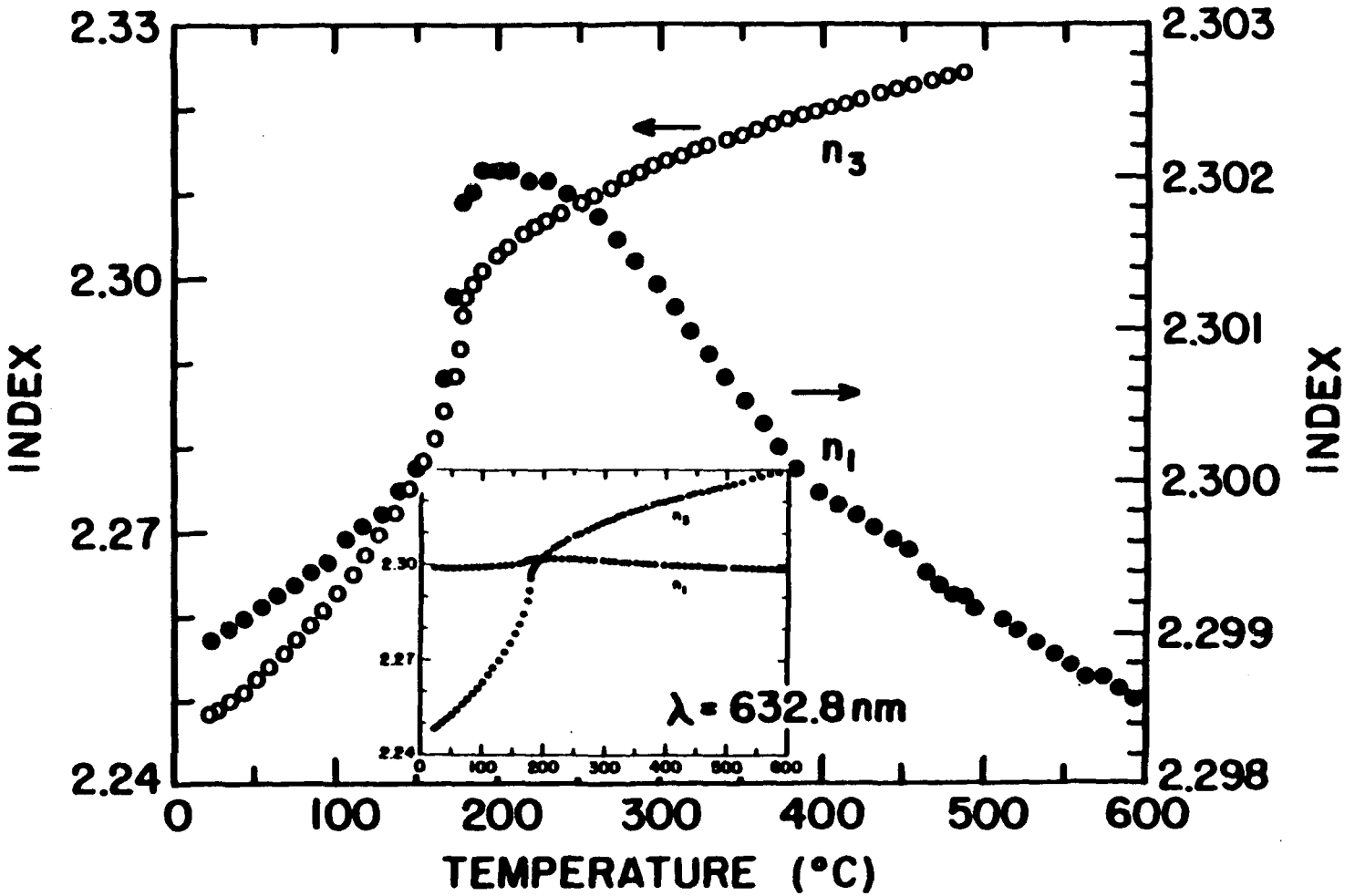
2.33
2.30
2.27
2.24
INDEX
2.303
2.302
2.301
2.300
2.299
2.298
INDEX
n_3
n_1
λ = 632.8nm
0
100
200
300
400
500
600
TEMPERATURE (°C)

Fig 7(a)

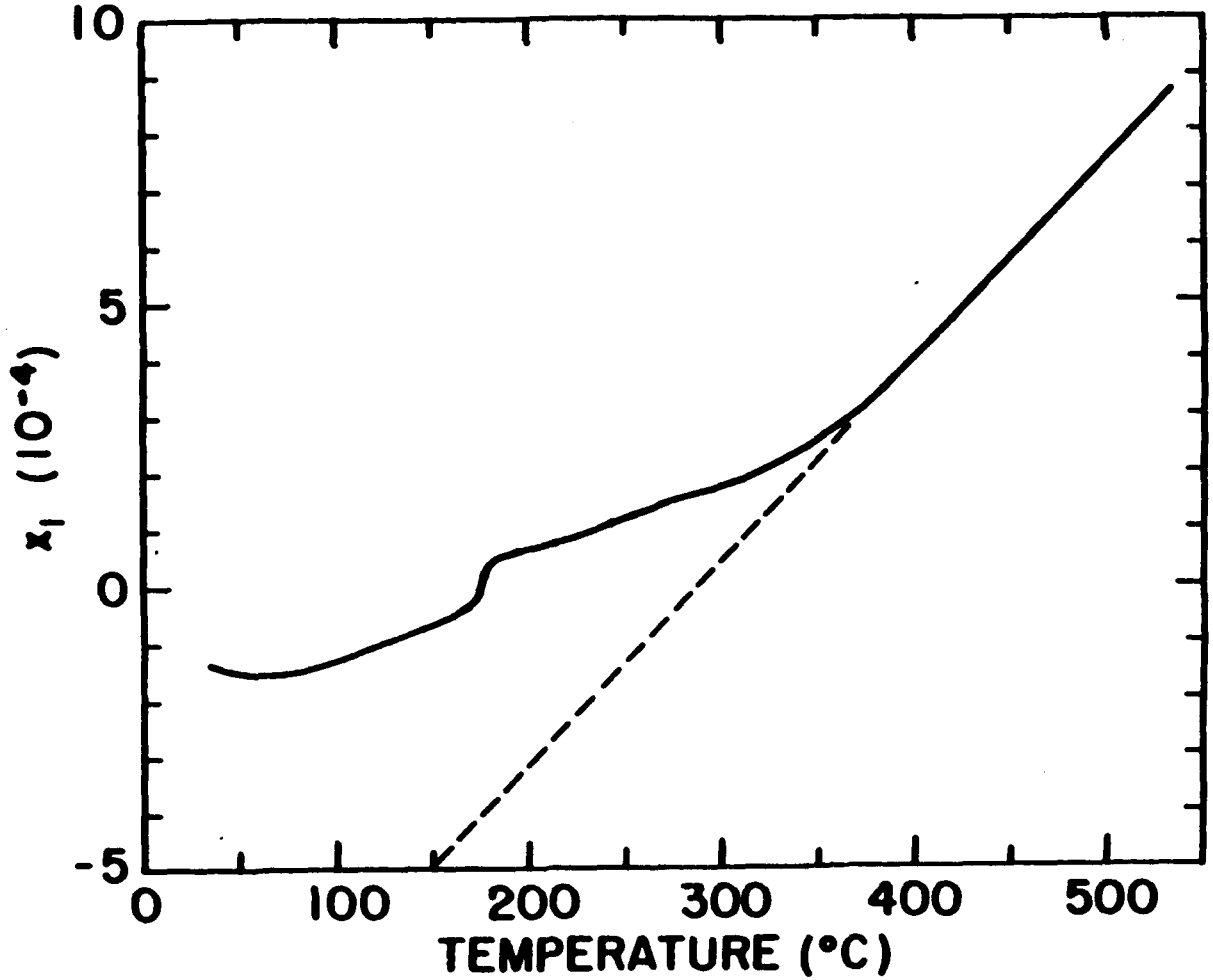

Fig 7(b)

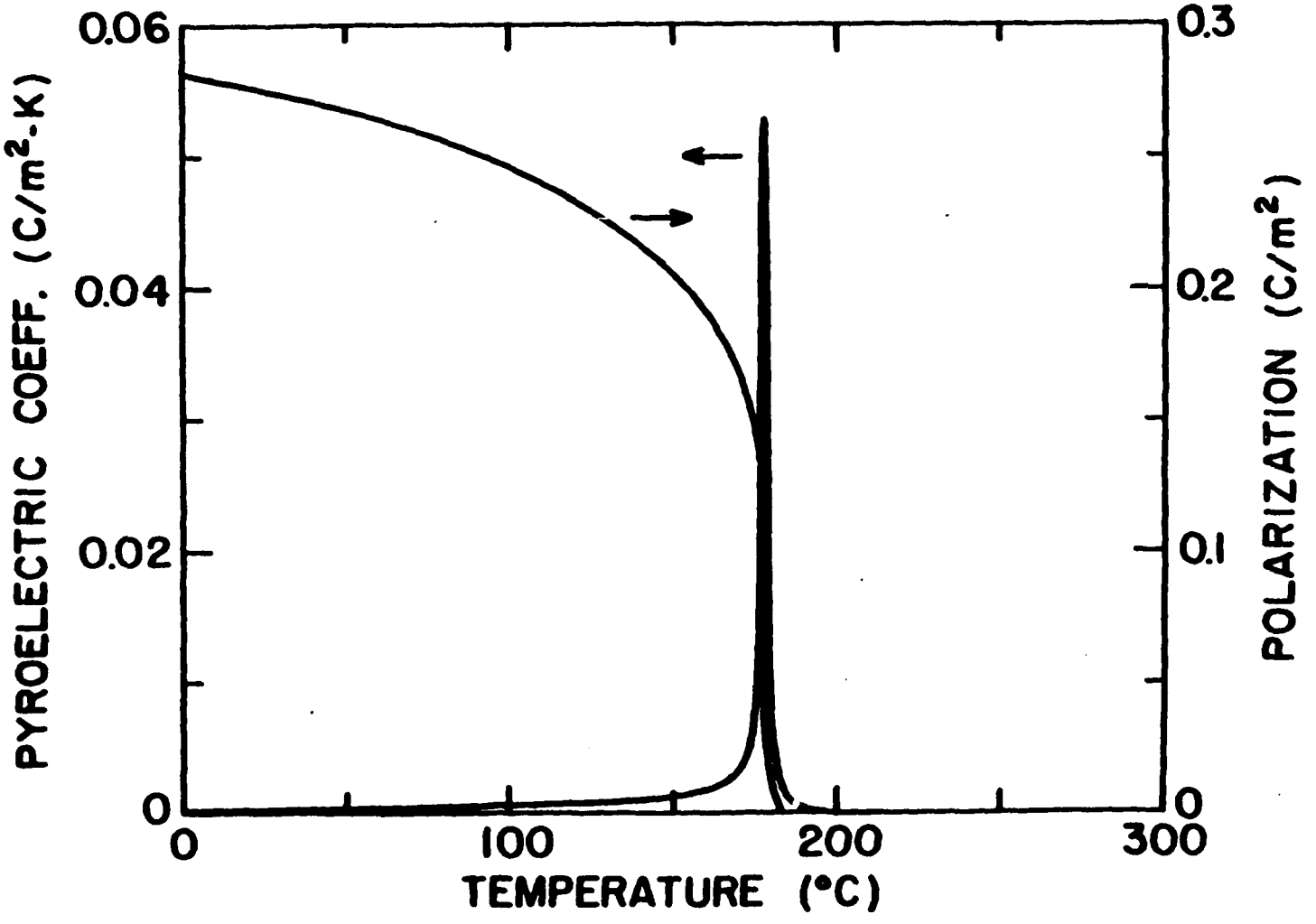
0.06
0.04
0.02
0
PYROELECTRIC COEFF. (C/m²-K)
0.3
0.2
0.1
0
POLARIZATION (C/m²)
0
100
200
300
TEMPERATURE (°C)

Fig 7(c)

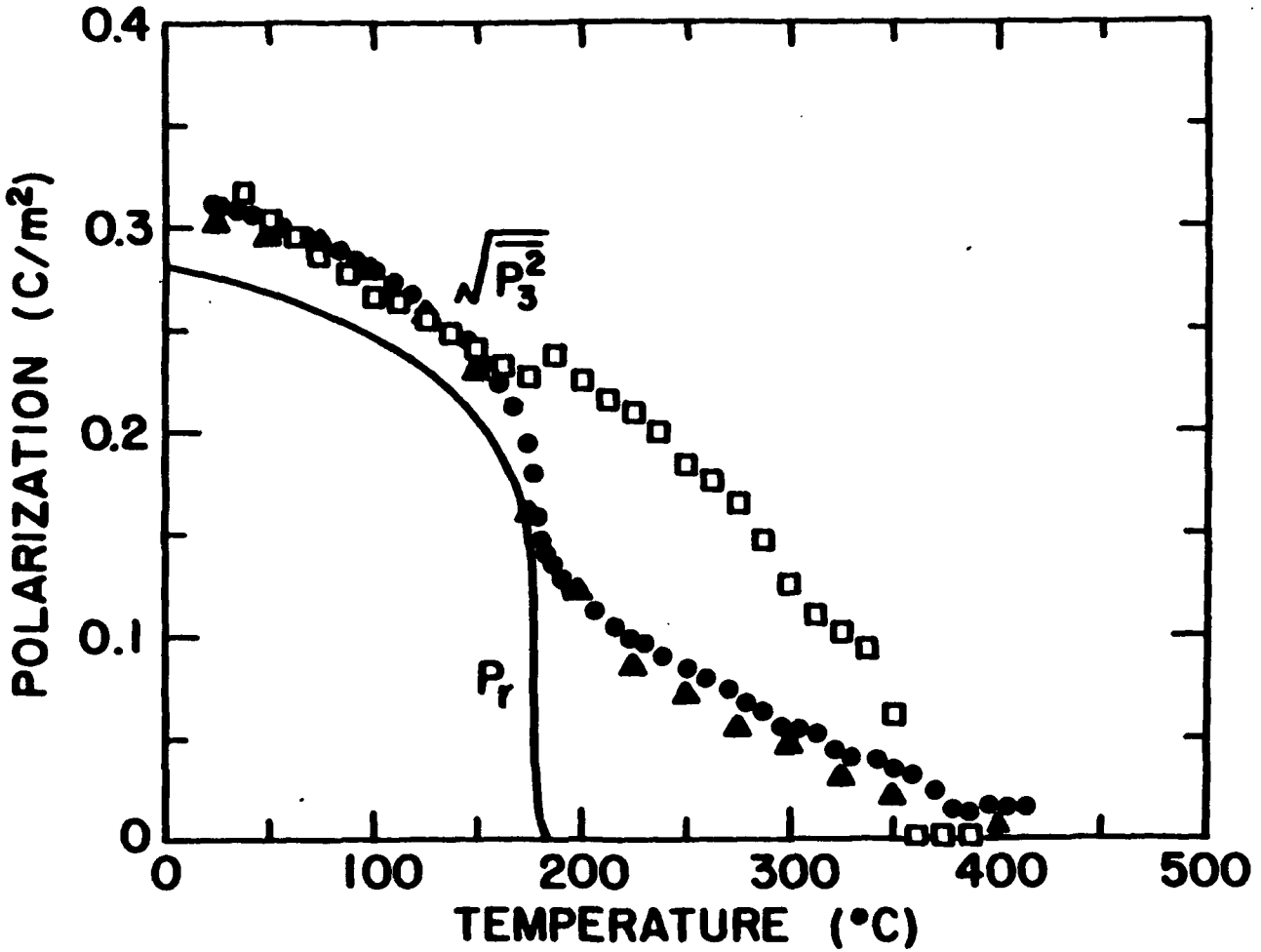
0.4
0.3
0.2
0.1
0
POLARIZATION (C/m²)
$\sqrt{\overline{P_3^2}}$
P_r
0
100
200
300
400
500
TEMPERATURE (°C)

Fig 7(d)

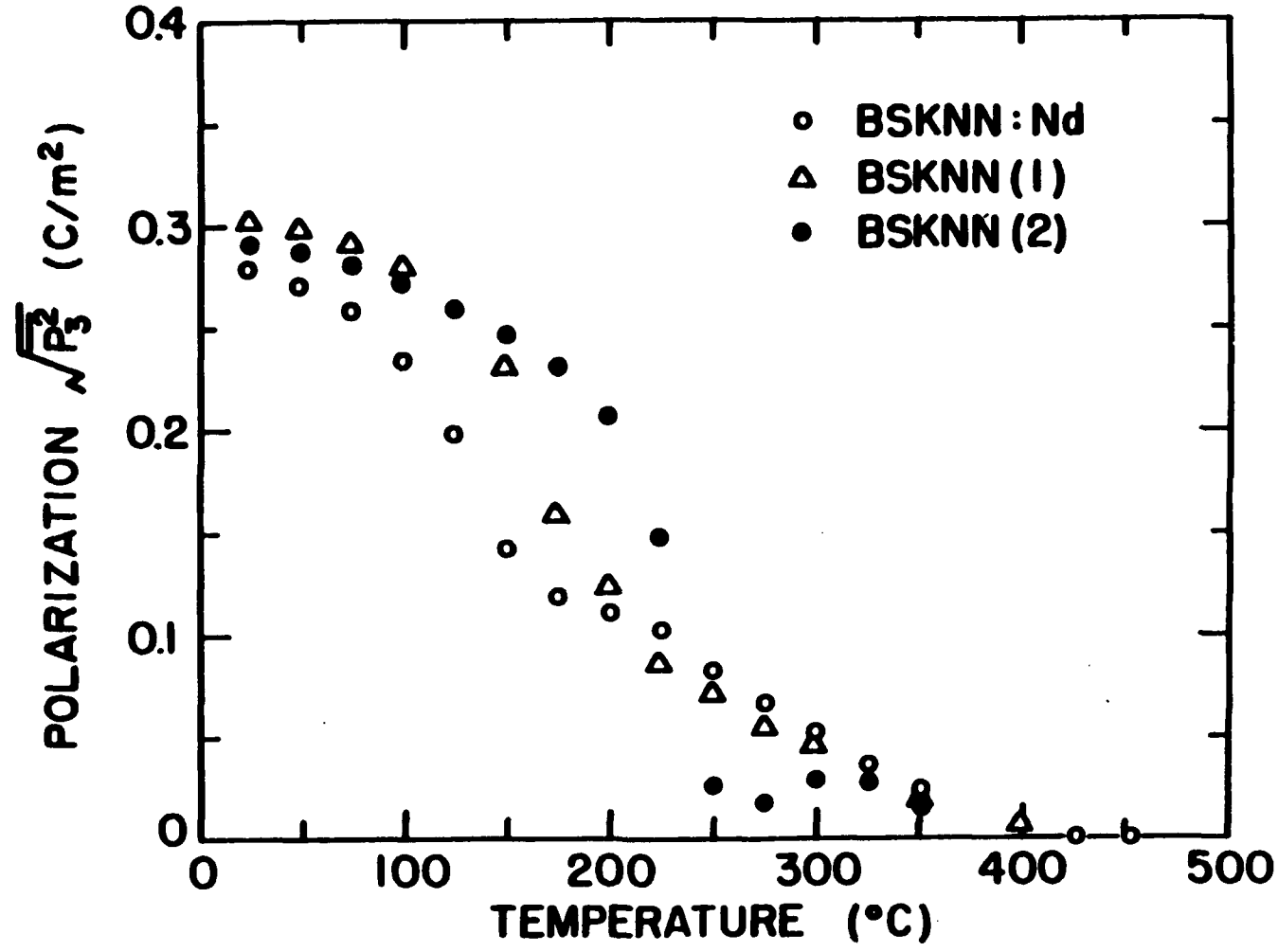
0.4
0.3
0.2
0.1
0
POLARIZATION $\sqrt{P_3^2}$ (C/m²)
BSKNN : Nd
BSKNN (1)
BSKNN (2)
0
100
200
300
400
500
TEMPERATURE (°C)

Fig. 8

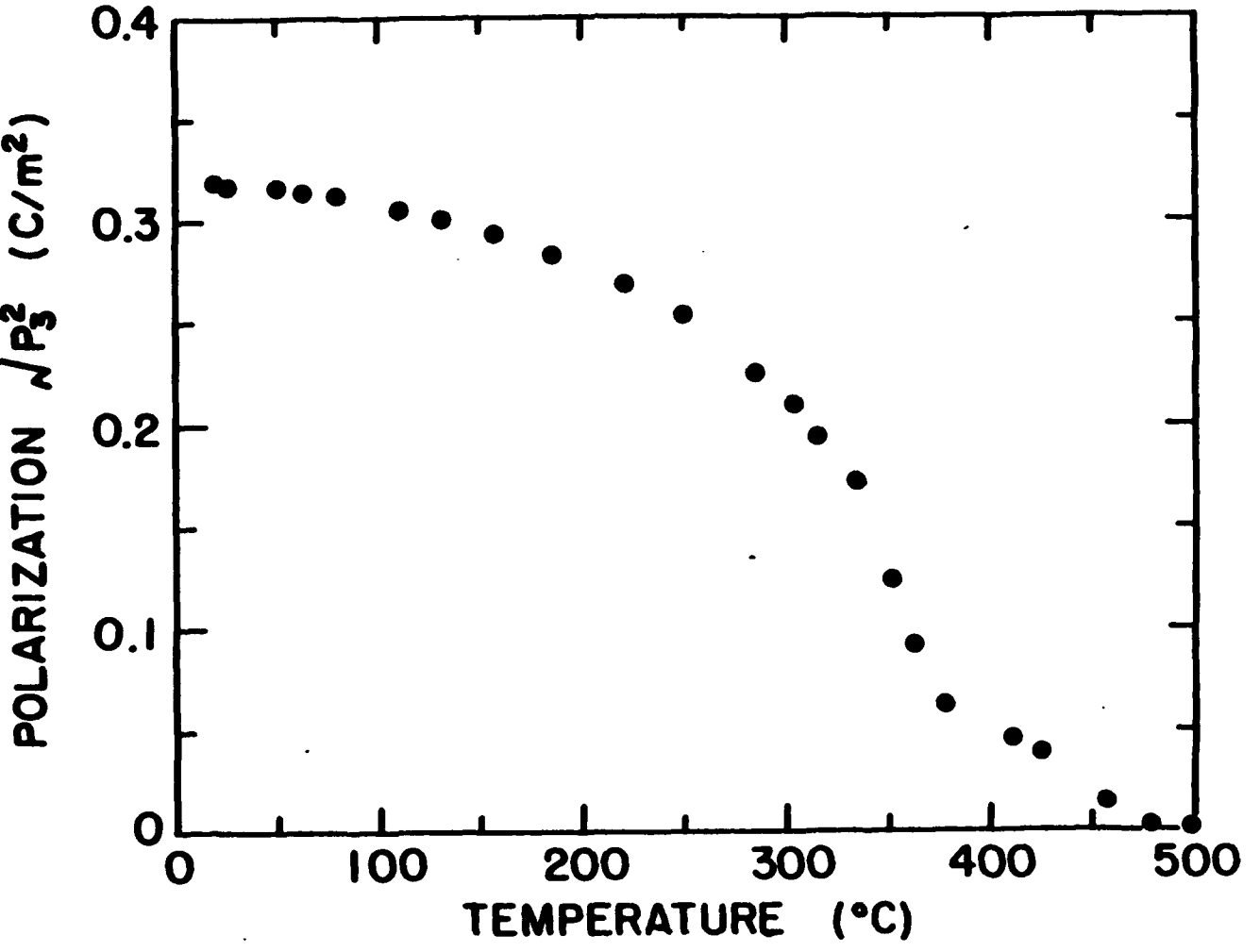
0.4
0.3
0.2
0.1
0
POLARIZATION $\sqrt{\overline{P_3^2}}$ (C/m²)
0
100
200
300
400
500
TEMPERATURE (°C)

Fig. 9

APPENDIX 2

RAMAN MEASUREMENTS OF THE FERROELECTRIC $Ba_{0.4}Sr_{0.6}Nb_2O_6$

G. Burns
F. H. Dacol
R.R. Neurgaonkar
A.S. Bhalla
R. Guo

RAMAN MEASUREMENTS OF THE FERROELECTRIC $Ba_{0.4}Sr_{0.6}Nb_2O_6$

G. Burns*, F. H. Dacol*, R. R. Neurgaonkar**, A. S. Bhalla***, and R. Guo***

* IBM T. J. Watson Research Center
P. O. Box 218
Yorktown Heights, NY 10598

** Rockwell International Science Center
Thousand Oaks, CA 91360

*** Materials Research Laboratory
The Pennsylvania State University
University Park, PA 16802

Using Raman spectroscopy, we have measured the A_1(TO) and E(TO) phonons in the tungsten bronze structured ferroelectric $Ba_{0.4}Sr_{0.6}Nb_2O_6$ (BSN). We observe phonon anomalies associated with T_c and also with a temperature $\approx$450°C. The latter is in the region where index of refraction measurements indicate the onset of a local polarization. By quenching the crystal from high temperatures, T_c can be shifted. We find that the phonon anomalies shift corresponding to the new T_c values.

For a crystal with the point group C_{4v}, a Raman spectrum with polarization x(zz)y gives the pure A_1 (TO) modes, and one with z(yz)x gives pure E(TO) modes. The A_1(TO) phonon modes are those that determine ε_c and the E(TO) phonon modes determine ε_a .

A_1 (TO) Raman modes - A complete A_1 (TO) spectrum is shown in Fig. 1 at three different special temperatures. In general, the spectra are similar to previous results[1]. Figure 2 shows the same data, but with an expanded frequency scale that emphasizes the low-energy modes and shows the results at more temperatures (measurements were taken at more temperatures but are not shown).

Consider the data in Fig. 2. At 23°C, the low-energy region is dominated by a mode at 88 cm^{-1}, which decreases in frequency as T_c($\approx$86 is approached. For example, at 70°C, this mode peaks at 81 cm^{-1}, at 90°C it is 72.5 cm^{-1}, and essentially retains this value to 250°C (data at 100°C and 300°C are shown in Fig. 2). Above 250°C there is an increase in damping, particularly at 400°C and above, as can be seen in the Figs. 1 and 2. From the Lyddane-Sachs-Teller (LST) relation, a frequency shift from 88 to 73 cm^{-1} would give a fractional change in the dielectric constant of $d\varepsilon_c/\varepsilon_c \approx 34\%$.

Just above T_c, a mode appears in the A_1(TO) spectrum at $\approx 110\,cm^{-1}$ as can be seen from the 100°C data in Fig. 2. This mode is not apparent below T_c; however, it is observable at 90°C, which is just above T_c, to the highest temperatures of our measurements.

The observed intensity of the Raman features have rather distinct behavior. The intensity of the low-energy features (Fig. 1) increases up to ≈450°C. However, the intensity of the high-energy features (260 and 640 cm^{-1} at room temperature and 243 and 623 cm^{-1} at 400°C and above, as in Fig. 1) decreases steadily to ≈ 250°C, then more slowly to 450°C, whereupon it decreases rapidly above 450°C. Normally, the intensity of Raman active modes should increase with increasing temperature due to the Bose-Einstein factor.

Thus, for the A_1 (TO) phonons, the low-energy spectra (Fig. 2) have anomalous behavior associated with T_c. Also, the entire spectra have an anomalous decrease of intensity above 450°C.

E(TO) Raman Mode - The high energy ($> 100\,cm^{-1}$) E(TO) phonon results (not shown) have weak features at 106, 172, and 848 cm^{-1} and a more dominant mode at ≈ 600 cm^{-1} (which is resolved into a triplet at 553, 596, and 630 cm^{-1}). The observed intensity of these modes drops markedly above 400°C, similar to the observation discussed above.

The low-energy spectra (Fig.3) also have interesting behavior. The room temperature, 82 cm^{-1} feature decreases in intensity up to T_c, and cannot be observed above that temperature. The intensity of the low-energy mode ($\approx 23\,cm^{-1}$) mode also decreases with temperature up to T_c. Above T_c another low-energy mode begins to appear (see Fig. 3), and at 600°C, it peaks at ≈35 cm^{-1}. Between room temperature and 84 K the broad low energy shoulder sharpens to show two distinct modes at $\approx 28 cm^{-1}$ and $\approx 43\,cm^{-1}$.

Discussion - Although we have not been able to observe any true soft modes, both the A_1(TO) and the E(TO) phonons show anomalies associated with T_c and with a temperature ~ 450°C. The temperature dependence of the A_1(TO) mode at $88\,cm^{-1}$ causes ε_c to increase by ≈14% between 23°C and T_c. The 450°C temperature is near the dipole temperature (T_d) determined from optic index of refraction measurements which is associated with the onset of local polarization[2].

Similar to previous experiments[3], we have quenched $Ba_{0.4}Sr_{0.6}Nb_2O_6$ (BSN60), $Ba_{0.25}Sr_{0.75}Nb_2O_6$ (BSN75), and (Ba,Sr,K,Na)Nb_2O_6 (BSKNN) and find shifts of T_c with

quenching temperature which are shown in Fig. 4. In these experiments the samples were held at a temperature for xx hours and then quenched to room temperature by removing the crystal from the furnace. As can be seen, for the first two crystals the effect is essentially the same and large. The effect for BSKNN is distinctly smaller. In the earlier experiment, T_c decreased with increased quenching temperature and this variation was thought to be associated with increased disorder quenched into the crystal[3]. However, the results for these crystals (Fig. 4) show the opposite variation and we are not sure of the reason. However, using the quenched BSN60 crystal, we compared the Raman results to the unquenched crystal. The same effects were observed in both samples, with the anomalies occurring at the T_c values independent of whether they are shifted or not. This shows that the shift of T_c with quenching is a bulk effect that is associated with the fundamental structure of the material.

1. G. Burns, J. D. Axe and D. F. O'Kane, Solid State Comm. 7, 933 (1969). G. Burns, Appl. Phys. Lett. 20, 230 (1972). R. Clark and D. Siapkas, J. Phys. C 8, 377 (1975). D. Siapkas and R. Clark, Phys. Stat. Sol. (b) 62, 4377 (1974).
2. G. Burns and F. H. Dacol, this issue.
3. G. Burns and D. F. O'Kane, Phys. Letters 28A, 776 (1969).

Fig. 1 Raman spectra showing the A_1(TO) phonons.

Fig. 2 The same as Fig. 1, but showing the low-energy phonon spectra in more detail and at more temperatures.

Fig. 3 The low-energy Raman spectra which shows the E(TO) phonons.

Fig. 4 The T_c values as a function of quench temperature for the three samples as indicated. The dashed line is a guide to the eye. The three crystals BSN60, BSN75, and BSKNN have T_c values of 86, 58, and 188°C, respectively. Thus, we have added constants to the T_c scale (as indicated) so that the results are normalized to BSN60.

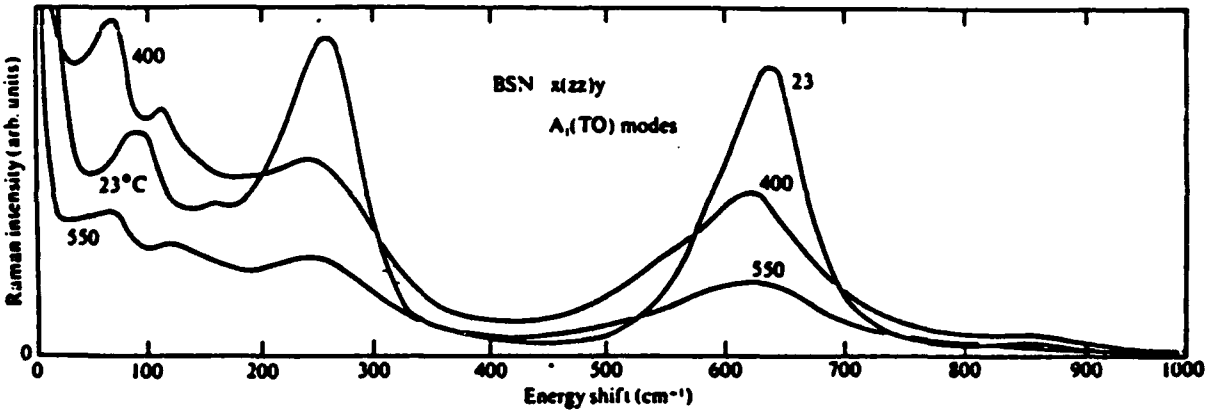
Raman intensity (arb. units)
400
23°C
550
BSN x(zz)y
A1(TO) modes
23
400
550
0
100
200
300
400
500
600
700
800
900
1000
Energy shift (cm⁻¹)

Fig 1

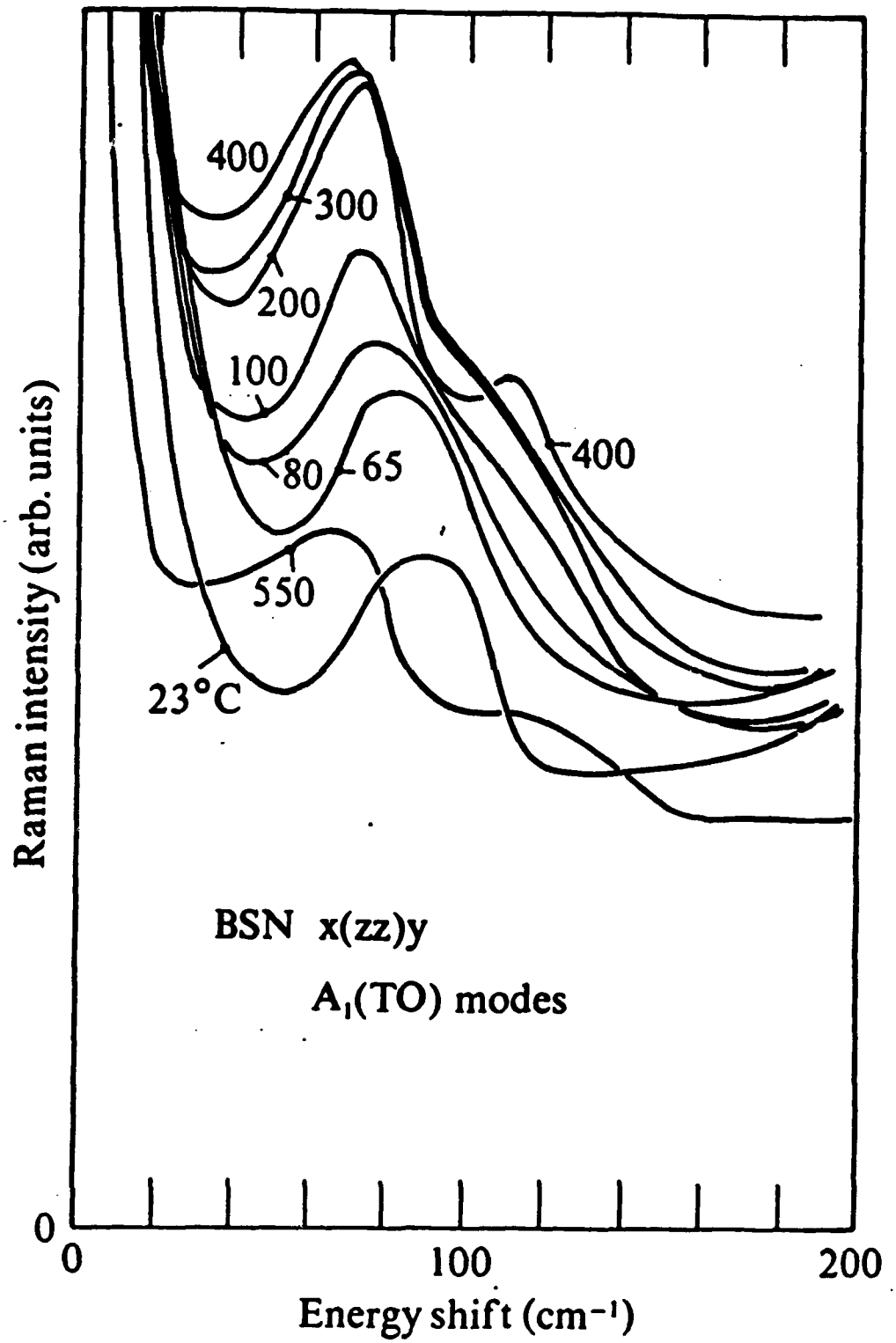
400
300
200
100
80
65
400
550
23°C
BSN x(zz)y
A_1(TO) modes
Raman intensity (arb. units)
0
0
100
200
Energy shift (cm^{-1})

Fig 2

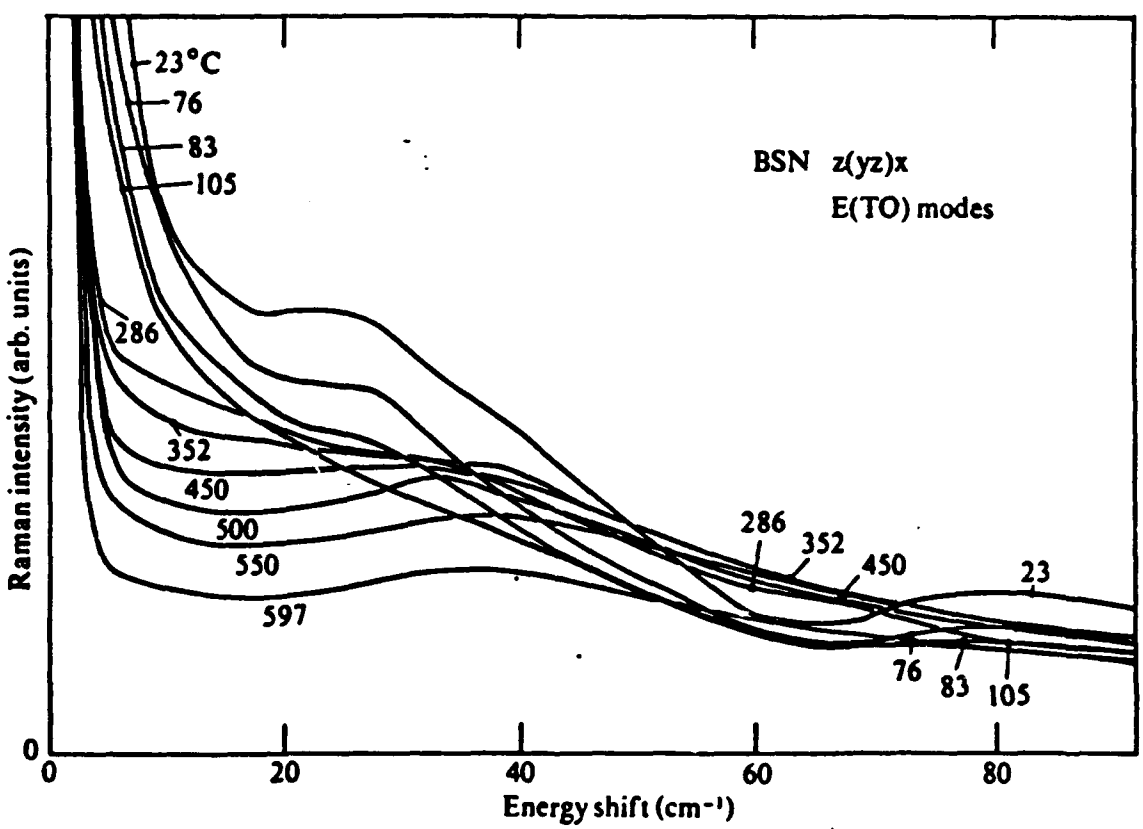
23°C
76
83
105
BSN z(yz)x
E(TO) modes
286
352
450
500
550
597
286
352
450
23
76
83
105
Raman intensity (arb. units)
0
0
20
40
60
80
Energy shift (cm⁻¹)

Fig 3

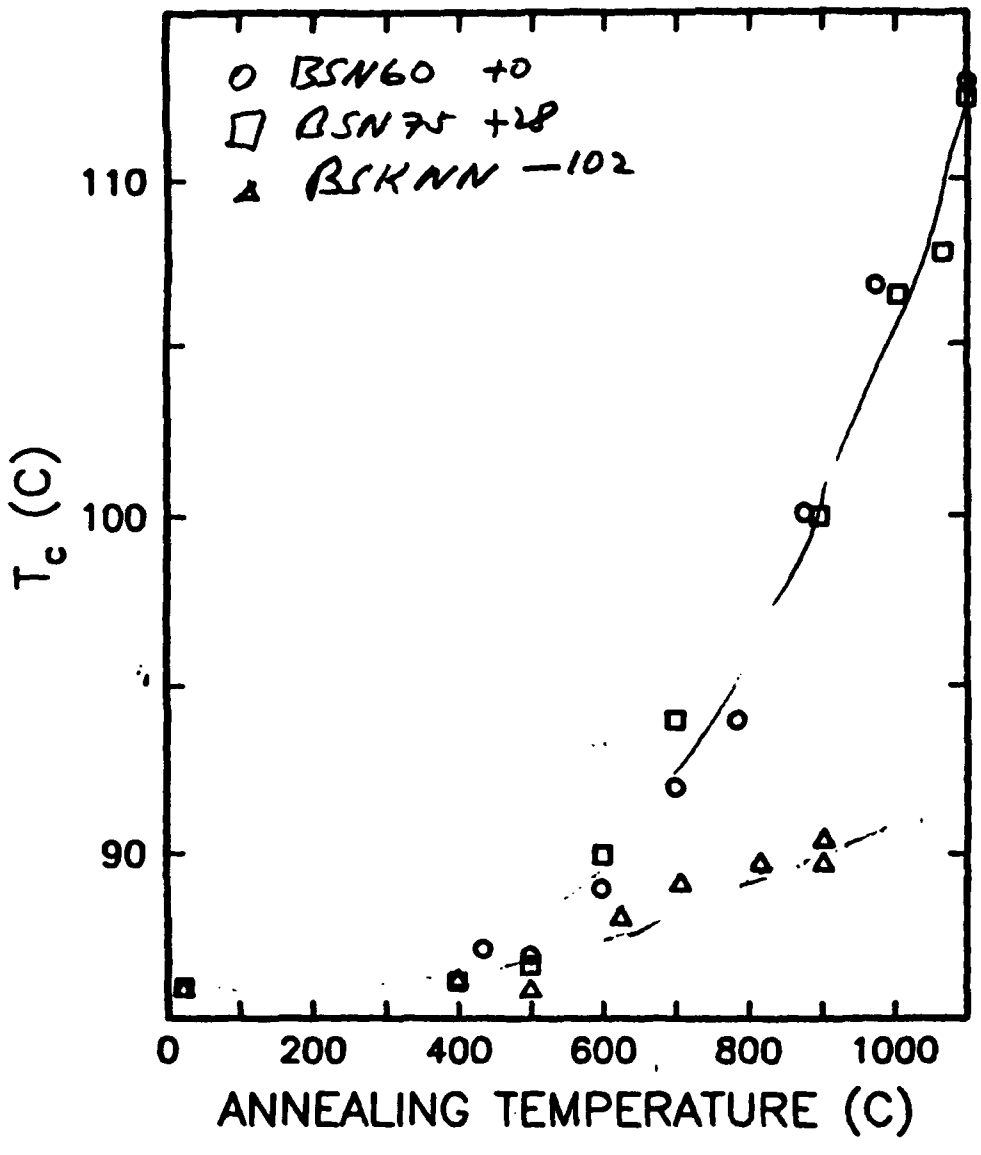
o BSN60 +0
□ BSN75 +28
△ BSKNN −102
110
100
90
T_c (C)
0
200
400
600
800
1000
ANNEALING TEMPERATURE (C)

APPENDIX 3

LOW TEMPERATURE DIELECTRIC AND PYROELECTRIC STUDIES OF THE MORPHOTROPIC PHASE BOUNDARY LEAD BARIUM NIOBATE (PBN) SINGLE CRYSTALS

R. Guo
A. S. Bhalla
C. A. Randall
L. E. Cross

LOW TEMPERATURE DIELECTRIC AND PYROELECTRIC STUDIES OF THE MORPHOTROPIC PHASE BOUNDARY LEAD BARIUM NIOBATE (PBN) SINGLE CRYSTALS

R.GUO, A.S. BHALLA, C. A. RANDALL and L.E. CROSS
Materials Research Laboratory
The Pennsylvania State University
University Park, PA 16802, USA

Lead barium niobate ($Pb_{1-x}Ba_xNb_2O_6$, PBN) is one of the oxide octahedron-type ferroelectrics with a tungsten bronze-type structure.[1,2,3] The crystal has a prototype symmetry of tetragonal 4/mmm at a temperature higher than T_c. At $T<T_c$, the crystal possesses either a ferroelectric tetragonal phase 4mm (for $1-x<0.63$) with a polarization vector along [001] direction or a ferroelectric orthorhombic phase m2m (for $1-x>0.63$) with a polarization vector along the [110] direction (referring to the prototype symmetry).[4,5] For a composition in the vicinity of $1-x\sim0.63$, a morphotropic phase boundary exists and separates two ferroelectric phases (tetragonal 4mm and orthorhombic m2m). It is reported when a composition is close to the MPB, many useful physical properties would be enhanced (e.g., dielectric constant[6,7], piezoelectric coefficient[7], and pyroelectric coefficient[8]) and are essentially temperature independent. It is thus of theoretical and practical significance to study MPB PBN compositions.

So far, no phase transition has been reported for PBN system at a temperature below the ferroelectric-paraelectric phase transition T_c. However, a strong low temperature dielectric dispersion behavior was found by Sankar et. al.(1987)[9]. This dielectric relaxation phenomena appeared at a low temperature (~-130°C) in an a-axis crystal with tetragonal symmetry ($Pb_{0.56}Ba_{0.44}Nb_2O_6$) and in a c-axis crystal with orthorhombic symmetry ($Pb_{0.65}Ba_{0.35}Nb_2O_6$). Knowledge about such 'unexpected' low temperature behavior, is very limited as far as the physical meanings of the phenomena are concerned. However, it is known that all relaxors have the possibility of more than one type of ions at identical crystallographic positions (Smolenskii and Isupov,1954)[10], as is the case for PBN where both Ba^{2+} and Pb^{2+} can occupy the same site A2 (15-coordinations). Also, relaxor ferroelectrics show similar dielectric relaxation properties at ferroelectric-paraelectric phase transition temperatures. So a thermally agitated dipole fluctuation model has been proposed (Cross,1987)[11] to interpret the

relaxor-type behavior of PBN. Further experimental evidence is desired to substantiate the validaty of the model.

In this paper, we report on the temperature and frequency dependences of dielectric properties of MPB PBN single crystal at low temperature range. We also report the results on low temperature pyroelectric properties of MPB PBN. More understanding about the nature of the morphotropic phase boundary is gathered from such studies.

Large dielectric relaxation phenomena has been encountered for MPB PBN single crystal in a non-polar direction at low temperature ($T<210K$) and over a broad frequency range (10^2-10^6Hz).

Low temperature properties of MPB PBN single crystals have been measured by direct charge measurement. A small polarization component has been detected in a non-polar direction at low temperature.

There is no evidence found for phase transition at low temperature in PBN system.

Chemical inhomogeneity destroys local translational symmetry, and hence perturbs direction of polarization away from macroscopic symmetry direction on a nanoscale (10^{-6} -10^{-9} m in linear dimension). Such perturbation is a thermally activated process and dynamic in nature. Thus, dielectric relaxation can be detected in a non-polar direction when thermal energy is comparable with potential barrier height of local polarization state. A thermally agitated polarization perturbation model has been suggested to explain the small "frozen-in" polarization component detected in a non-polar direction at very low temperature by pyroelectric techniques.

REFERENCES

1. V. A. Isupov & V. I. Kosiakov, Soviet Physks Tech. Phys., 3, 2002 (1958).
2. G. A. Smolenskii, V. A. Isupov & A. I. Agranovskaya, Soviet Phys. Solid State, 1, 400 (1959).
3. E. C. Subbarao, J. Amer. Ceram. Soc., 42, 448 (1959).
4. M. H. Francombe, Acta Cryst., 13, 131 (1960).
5. R. Guo, A. S. Bhalla, C. A. Randall, Z. P. Chang and L. E. Cross, Ferroelectrics, 93, 193 (1989).
6. T. R. Shrout & L. E. Cross, Ferroelectric Letters, 44, 325 (1983).
7. T. R. Shrout, H. Chen & L. E. Cross, Ferroelectrics, 74, 317 (1987).
8. R. Lane, D. L. Mack & K.R. Brown, Trans. J. Brit. Ceramic Soc., 71, 11 (1972).
9. S. G. Sankar, R. Guo, Z. P. Chang, A. S. Bhalla and L. E. Cross, Presented at 89th Annual Meeting of the American Ceramic Society, Apr. 26-30, Pittsburgh (1987).
10. G. A. Smolenskii and V. A. Isupov, Dokl. Akad. Nauk., SSSR, 97, 237 (1954).
11. L. E. Cross, Ferroelectrics, 76, 241 (1987).

APPENDIX 4

DIELECTRIC AND PYROELECTRIC PROPERTIES OF THE MORPHOTROPIC PHASE BOUNDARY LEAD BARIUM NIOBATE (PBN) SINGLE CRYSTALS AT LOW TEMPERATURE (10 - 300K)

R. Guo
A. S. Bhalla
C. A. Randall
L. E. Cross

DIELECTRIC AND PYROELECTRIC PROPERTIES OF THE MORPHOTROPIC PHASE BOUNDARY LEAD BARIUM NIOBATE (PBN) SINGLE CRYSTALS AT LOW TEMPERATURE (10 ~ 300K)

R.GUO, A.S. BHALLA, C. A. RANDALL and L.E. CROSS

Materials Research Laboratory

The Pennsylvania State University

University Park, PA 16802, USA

Abstract Low temperature (10~300K) dielectric and pyroelectric properties of morphotropic phase boundary lead barium niobate tungsten bronze ferroelectric single crystals have been investigated. Strong 'Debye-like' dielectric dispersion, along a non-polar direction (perpendicular to the polarization direction), has been observed and characterized by dielectric spectrum techniques. A direct charge measurement method has been used to study the low temperature pyroelectric properties in polar and non-polar directions. A 'frozen-in' polarization component in a non-polar direction is also reported. The low temperature relaxation effects are explained by the internal reorientation polarization perturbation and a thermally agitated local dipole fluctuation model.

INTRODUCTION

Lead barium niobate ($Pb_{1-x}Ba_xNb_2O_6$, PBN) is one of the oxide octahedron-type ferroelectrics with a tungsten bronze-type structure.[1,2,3] The crystal has a prototype symmetry of tetragonal 4/mmm at a temperature higher than T_c (see Table I.). At $T<T_c$, the crystal possesses either a ferroelectric tetragonal phase 4mm (for $1-x<0.63$) with a polarization vector along [001] direction or a ferroelectric orthorhombic phase m2m (for $1-x>0.63$) with a polarization vector along the [110] direction (referring to the prototype symmetry).[4,5] For a composition in the vicinity of $1-x\sim0.63$, a morphotropic phase boundary (MPB) exists and separates two ferroelectric phases (tetragonal 4mm and orthorhombic m2m). It is reported when a composition is close to the MPB, many useful physical properties would be enhanced (e.g., dielectric constant,[6,7] piezoelectric coefficient,[7] and pyroelectric coefficient[8]) and are essentially temperature independent. It is thus of theoretical and practical significance to study MPB PBN compositions.

So far, no phase tra tion has been reported for the PBN system at a temperature below the ferroelectric-paraelectric phase transition T_c. However, a strong low temperature dielectric dispersion behavior was found by Sankar et. al..[9] This dielectric relaxation phenomena appeared at a low temperature (~-130°C) in an a-axis crystal with tetragonal symmetry ($Pb_{0.56}Ba_{0.44}Nb_2O_6$) and in a c-axis crystal with orthorhombic symmetry ($Pb_{0.65}Ba_{0.35}Nb_2O_6$). Knowledge about such 'unexpected' low temperature behavior is very limited as far as the physical meanings of the phenomena are concerned. However, it is known that all relaxors have the possibility of more than one type of ion at identical crystallographic positions,[10] as is the case for PBN where both Ba^{2+} and Pb^{2+} can occupy the same site A2 (15-coordination). Also, relaxor ferroelectrics show similar dielectric relaxation properties at ferroelectric-paraelectric phase transition temperatures. So a thermally agitated dipole fluctuation model has been proposed[11] to interpret the relaxor-type

behavior of PBN. Further experimental evidence is desired to substantiate the validity of the model.

In this paper, we report on the temperature and frequency dependences of dielectric properties of MPB PBN single crystals in a temperature range from 10 to 300K. We also report the results on pyroelectric properties of MPB PBN in the same temperature range. More understanding about the nature of the morphotropic phase boundary is gathered from such studies.

EXPERIMENTAL PROCEDURE

Single crystal specimens used for this investigation were several millimeters in size and of optical quality. These crystals were grown by a Czochralski pulling technique. The chemical compositions of the crystals were characterized by electron microprobe analysis. PBN65, PBN61.5, and PBN57 were chosen as representatives for this study. The composition quoted in the text, tables, and figures is as PBN(1-x)% where (1-x)% is the mole percent of $PbNb_2O_6$ in $Pb_{1-x}Ba_xNb_2O_6$ composition. Several physical properties measured for these specimens are listed in Table I. Crystal specimens were oriented, cut, polished, and electroded with sputtered Au for dielectric and pyroelectric measurements.

Measurements of dielectric constant and loss tangent as functions of temperature (80K - 300K) at discrete frequencies (ranging from 100Hz to 100KHz) were made by using a computer interfaced automatic measuring system LCR meter (HP4274A, Hewlett-Packard) by standard techniques. Complex dielectric constants were obtained from impedance and phase angles measured in a range of frequencies (10 to 10^7Hz) and at discrete temperatures ranging from 10K to 300K using a RF impedance analyzer (HP4192A, Hewlett-Packard). The real and imaginary parts of the dielectric permittivity were calculated based on a simple parallel RC circuit model by using a separate computer program.

Low temperature pyroelectric measurements were carried out by using a direct charge measurement technique.[12] Figure 1. shows the experimental arrangement for the pyroelectric measurement. To achieve accurate measure of pyroelectric charge, a low leakage and low dielectric absorption polystyrene capacitor C_{FB} (≈0.2μF) is connected across an operational amplifier of an electrometer (Keithley 619) through a shielded feedback loop. The pyroelectric charge Q released by a previously poled sample (typically, at a field of >3KV/cm) as the temperature increases is instantaneously transferred to the feedback capacitor and this maintains zero-field conditions across the amplifier input. The output voltage $V_{out} = Q/C_{FB}$ gives a direct measure of the pyroelectric charge Q and hence the change of the spontaneous polarization, ΔP_s, as $\Delta P_s = Q/A$, where A is the electrode area of the sample. Since the field across the crystal is zero, the conduction current through the crystal is zero and the measurement is not affected by the crystal resistance, then,

$$V_{out} = A(\Delta P_s)/C_{FB} = Ap(\Delta T)/C_{FB} \quad (1)$$

where $p = (\Delta P_s)/(\Delta T)$ is the pyroelectric coefficient. Hence we have

$$(\Delta P_s) = V_{out}C_{FB}/A \quad (2)$$

$$p = V_{out}C_{FB}/A(\Delta T) \quad (3)$$

A cryogenic refrigeration system (APD, Cryogenics Inc.) has been used for low temperature measurements. The sample mounted inside an expander module was kept in vacuum (~10^{-5}torr). Temperatures as low as 10K can be achieved. A linear heating rate of 6°C/min has been used throughout the pyroelectric measurement. To eliminate the effect of space charge, samples were short circuited for at least 30 minutes at starting temperature prior to measurement.

RESULTS AND DISCUSSION

Dielectric Spectrum

a) Temperature Behavior

Dielectric constant and loss factor tanδ of single crystals PBN57, PBN65, and PBN61.5 as functions of temperature and discrete frequencies are shown in Figures 2, 3, and 4 respectively with the x-axis drawn as temperature. It is clear that for the MPB composition crystals, there is a profound dielectric dispersion along a non-polar direction at low temperatures far below the main ferroelectric-paraelectric phase transition. For PBN57 (tetragonal 4mm), the polarization vector is parallel to the [001] direction; thus a large dielectric relaxation is found for crystal directions perpendicular to [001], Figure 2. For PBN65 (orthorhombic m2m), the polarization vector is parallel to the [110] direction but a large dielectric relaxation can be found along the [001] direction, Figure 3. Figure 4 shows a dielectric relaxation behavior similar to Figure 3 since like PBN65, PBN61.5 belongs to orthorhombic symmetry at low temperature. In general, we find a strong resemblance between the low temperature dielectric relaxation behavior of PBN and a Debye-type relaxation in that the dielectric maximum shifts to higher temperatures at higher frequencies. Same results were obtained by using different electrode assemblies (e.g. sputtered gold or air-dry silver paste), that indicates such relaxation phenomena are essentially irrelevant to the contact resistance and capacitance.

The activation energies of such relaxation processes have been estimated by using a Debye model. According to the condition of maximum dissipation factor and dependence of relaxation time on the activation energy in Debye theory, the values of 0.130eV, 0.242eV, and 0.246eV for PBN57, PBN65, and PBN61.5 are obtained respectively.

b) Frequency Behavior

Figures 5(a) and 5(b) show the components of the complex dielectric constant of an a-axis PBN65 single crystal (orthorhombic) versus log(freq.). As can be seen at very low temperature (T<30K), K' is almost independent of either frequency or temperature. At a much higher temperature (T>210K), K' again is independent of frequency, except for the high frequency end which we believe is due to the influence of piezoelectric resonance.

The very low frequency end is mostly due to the superimposing of direct conductivity and a relaxation contribution. At the temperature range from 50K to about 190K, strong anomalous dispersion in K' (Figure 5(a)) and broad maxima of K" (Figure 5(b)) are observed. It is clear that this relaxation is clamped at both low and high temperatures.

A Cole-Cole plot is shown in Figure 6 for an a-axis crystal of PBN57 (tetragonal). The broad Cole-Cole 'circular-arc' indicates a broad distribution of relaxation times if the Debye relaxation concept is invoked.

Low Temperature Pyroelectric Properties

Spontaneous polarization changes in the temperature range 10K to 300K for three different samples (PBN57, PBN61.5, and PBN65) in six different orientations (parallel and perpendicular to the polar directions) are shown in Figure 7. Note that for all three compositions at temperatures well below 300K, polarization changes parallel to the polar axis are an order of magnitude smaller than those perpendicular to the axis, with no obvious discontinuities reflecting ferroelectric transitions. Also, along the non-polar direction, there is a continuous build-up of polarization when cooling at temperature below ~140K, and this varies with composition. Pyroelectric coefficients have been calculated for each crystal orientation according to Equation (3), as plotted in Figure 8. It is evident that pyroelectric coefficients for crystals from polar directions are basically flat and at least an order of magnitude smaller than those in non-polar directions. Although the pyroelectric coefficient in a non-polar direction is larger compared with that of a polar direction, it is still much smaller than that of a polar direction near a ferroelectric-paraelectric phase transition. Most importantly, the polarization onset in the non-polar direction occurs at a similar temperature to where the dielectric relaxations are found (Figures 5 and 6).

The pyroelectric measurement results (by direct charge measurement) have been cross checked by using Byer-Roundy[13] and Chynoweth[14] methods in the temperature

range from ~80K to ambient temperature. It appears that the pyroelectric coefficient values deduced from different techniques agree fairly well.

At very low temperatures, all dipoles are practically frozen and there is no contribution to the pyroelectric coefficient. However, a small peak in pyroelectric coefficient can be found for every sample at about 30K. The mechanisms of this behavior is not clear. A theoretical discussion related to this phenomenon may be found in the work of Glass and Lines.[15]

Possible Origins of Low Temperature Dielectric and Pyroelectric Behavior

At very low temperatures, all ferroelectric domains are frozen. So there is little possibility of domain wall movement contributing to the low temperature dielectric relaxation.

Hopping charges of either electronic or ionic nature may give rise to very similar dielectric behavior with the orientation of permanent dipoles. The important distinction lies in the degree of localization of these carriers: an electron or an ion confined to hopping between two preferred positions is indistinguishable from a dipole.[16] However, as we are going to point out below, the relaxation phenomena at low temperatures cannot be of a simple dipolar reorientational kind owing to the large dipole moment predicted and that it also implies that the hopping distance must be too large to be realistic. Thus the charge hopping model has been excluded.

The simplest form of dielectric response, and prototype for many discussions, is the behavior of Debye-type.[17] It is apparent that our results of dielectric dispersion have very broad distributions of relaxation times if Debye relaxation model is used. However, by a simple calculation using a double well energy model, one can find that the Debye model is not suitable in this case. Under an electric field E, the energy barrier for a dipole moment, $q\delta$, where δ is the separation between the negative and the positive charge q, is $(H-q\delta E)$ where H is the activation energy in absence of a field. At a temperature T', where T' is defined at $(\Delta P/\Delta T)_{T'}$ maximum, we can make the approximation $(H-q\delta E)$ -

kT', where k is the Boltzmann constant. Then the dipole displacement, δ, can be deduced. Taking PBN57 as an example for which an activation energy H=0.130eV was already derived from dielectric measurements, under a poling field of E=3KV/cm, for T'~100K, one then gets δ~400nm (too large for a Debye-type description) if taking q as the charge of an electron. So a relaxor ferroelectric-type approach rather than a conventional dipolar model is needed.

Polarization Fluctuation Model

We suggest a thermally agitated local polarization fluctuation model in order to give satisfactory explanation for the low temperature dielectric and pyroelectric properties in MPB PBN single crystals. This model is based strongly on the concept of the superparaelectric relaxor as suggested by both Smolenskii[10] and Cross[11].

In general, we consider the single domain state of a ferroelectric as having an uniform polarization. However, here we are considering the influence of nanoscale chemical inhomogeneity in the Ba^{2+} and Pb^{2+} distribution within the PBN. Since we are considering a macro-composition close to a MPB which separates two orthogonal orientations of polarization, the local chemical fluctuations of Ba^{2+} or Pb^{2+} content are sensitive to the perturbation of the polarization. This perturbation of the polarization is not only a change in magnitude but also an orientation deviation. The orientation deviation resulting from the two orthogonal polarization orientations can occur at either side of the MPB.

These perturbations give rise to local polarization states about the macro-polarization state within the single domain. So spatially there is a modulation of slightly differing polarization throughout a domain.

Figure 9 shows the schematic model of the domain state as described above. An angle θ(T) can be regarded as a measure of angular deviation of the polarization vector

compared to the macro polarization orientation. As one may expect, $\theta(T)$ is very small. A simple evaluation from the experimental data shows that $\theta(T)$ is less than two degrees.

The local polarization states differ slightly from the macro-polarization state. Activation energies H_i separate those local polar states in energy wells superimposed upon the macro-polarization energy well. At high temperatures these barriers are insignificant to the bulk thermal energy. However, at lower temperatures ($30K<T<210K$ approximately), these activation barriers are comparable to thermal energy kT. This allows for relaxation processes to be thermally excited from one perturbed polarization state to another. Owing to the distribution of activation energies, H_i, the dielectric relaxation (internal reorientations of dipole groups) will have broad relaxation time distributions and yield broad Cole-Cole plots.

Applications of an external electric field, E, parallel to the non-polar orientation allows a poling to exist within the local polarization states. The external electric field deepens the perturbation energy wells in one direction allowing for a component of polarization to be 'frozen-in' along a non-polar orientation of PBN. This is schematically represented in Figure 9(b), and accounts for the pyroelectricity in the non-polar orientation at low temperature.

We wish to emphasize that PBN is a different type of relaxor ferroelectric. Usually, the relaxor is considered as having local polar microregions (10-1000nm) in a paraelectric matrix. However, here we are considering a polar matrix which has local perturbations. At higher temperatures, there is a ferroelectric-paraelectric phase transition which has long-range cooperative interactions between dipoles to form macrodomains. But, at lower temperatures, perturbations from the original polar direction allow for thermally excited relaxations to occur and give dielectric anomalies and pyroelectric coefficients in unexpected non-polar directions and thus qualitatively explain the results presented here.

SUMMARY

Large dielectric relaxation phenomena has been encountered for MPB PBN single crystal in a non-polar direction at low temperature (T<210K) and over a broad frequency range (10^2-10^6Hz).

Low temperature properties of MPB PBN single crystals have been measured by direct charge measurement. A small polarization component has been detected in a non-polar direction at low temperature.

There is no evidence found for ferroelectric phase transitions at low temperature in the PBN system.

Chemical inhomogeneity destroys local translational symmetry, and hence perturbs the direction of polarization away from the macroscopic symmetry direction on a nanoscale (10^{-6} -10^{-9} m in linear dimension). Such perturbation is a thermally activated process and dynamic in nature. Thus, dielectric relaxation can be detected in a non-polar direction when thermal energy is comparable with potential barrier height of the local polarization state. A thermally agitated polarization perturbation model has been suggested to explain the small 'frozen-in' polarization component detected in a non-polar direction at very low temperature by pyroelectric techniques.

ACKNOWLEDGEMENT

This research was funded by the Office of Naval Research and Defence Advanced Research Project Agency.

REFERENCES

1. V. A. Isupov & V. I. Kosiakov, Soviet Physks Tech. Phys., 3, 2002 (1958).
2. G. A. Smolenskii, V. A. Isupov & A. I. Agranovskaya, Soviet Phys. Solid State, 1, 400 (1959).
3. E. C. Subbarao, J. Amer. Ceram. Soc., 42, 448 (1959).
4. M. H. Francombe, Acta Cryst., 13, 131 (1960).
5. R. Guo, A. S. Bhalla, C. A. Randall, Z. P. Chang and L. E. Cross, Ferroelectrics, 93, 193 (1989).
6. T. R. Shrout & L. E. Cross, Ferroelectrics Letters, 44, 325 (1983).
7. T. R. Shrout, H. Chen & L. E. Cross, Ferroelectrics, 74, 317 (1987).
8. R. Lane, D. L. Mack & K.R. Brown, Trans. J. Brit. Ceramic Soc., 71, 11 (1972).
9. S. G. Sankar, R. Guo, Z. P. Chang, A. S. Bhalla and L. E. Cross, 89th Annual Meeting Abstracts, p165 (American Ceramic Society, Westerville, 1987).
10. G. A. Smolenskii and V. A. Isupov, Dokl. Akad. Nauk., SSSR, 97, 237 (1954).
11. L. E. Cross, Ferroelectrics, 76, 241 (1987).
12. A. M. Glass, J. Appl. Phys., 40, 4699 (1969).
13. R. L. Byer and C. B. Roundy, Ferroelectrics, 3, 333 (1972).
14. A. G. Chynoweth, J. Appl. Phys., 27, 78 (1956).
15. A. M. Glass and M. E. Lines, Phys. Rev., B13, 180 (1976).
16. A. K. Jonscher, Physics of Dielectric Solids 1980, Inst. Phys. Conf. Ser. 58, 22 (1980)
17. P. Debye, Polar Molecules, (Chemical Catalog Co., New York, 1929).

TABLE I. Some physical properties measured for $Pb_{1-x}Ba_xNb_2O_6$ (PBN) specimens.

	Composition	Symmetry of ferroelectric phase	T_c (dielectric maxima at 1 kHz)	Polar vector orientation
PBN57	$1-x=0.57$	Tetragonal	316 °C (589 K)	‖[001]
PBN61.5	$1-x=0.615$	Ortho. ($T\sim 300$ K)		‖[110]
		Tetra. ($T>390$ K)	288 °C (561 K)	‖[001]
PBN65	$1-x=0.65$	Orthorhombic	282 °C (555 K)	‖[110]

FIGURE CAPTIONS

FIGURE 1. Experimental arrangement for the pyroelectric measurement.

FIGURE 2. Temperature dependence of dielectric constant (K') and loss factor (tanδ) for PBN57 single crystal along [100] direction at various frequencies ([100] a non-polar direction).

FIGURE 3. Temperature dependence of dielectric constant (K') for PBN65 single crystal along [001], [010] and [100] direction at various frequencies ([001] a non-polar direction). Also shown in dashed lines are the temperature dependence of loss factor (tanδ) along [001] direction.

FIGURE 4. Temperature dependence of dielectric constant (K') for PBN61.5 single crystal along [001], [110] and [100] direction at various frequencies ([001] a non-polar direction at low temperature). Also shown in dashed lines are the temperature dependence of loss factor (tanδ) along [001] direction.

FIGURE 5. The complex components of the dielectric constant of an a-axis PBN65 single crystal (orthorhombic) versus log(freq.) at different temperatures: (a) the real part (K') and (b) the imaginary part (K").

FIGURE 6. Cole-Cole plot for an a-axis crystal of PBN57 (tetragonal) at different temperatures.

FIGURE 7. Spontaneous polarization changes in temperature range 10K to 300K for three different samples (PBN57, PBN61.5, and PBN65) in (a) parallel, and (b) perpendicular to the polar directions.

FIGURE 8. Pyroelectric coefficients in temperature range 10K to 300K for three different samples (PBN57, PBN61.5, and PBN65) in (a) parallel, and (b) perpendicular to the polar directions.

FIGURE 9. A schematic drawing of the thermally agitated local polarization fluctuation model.

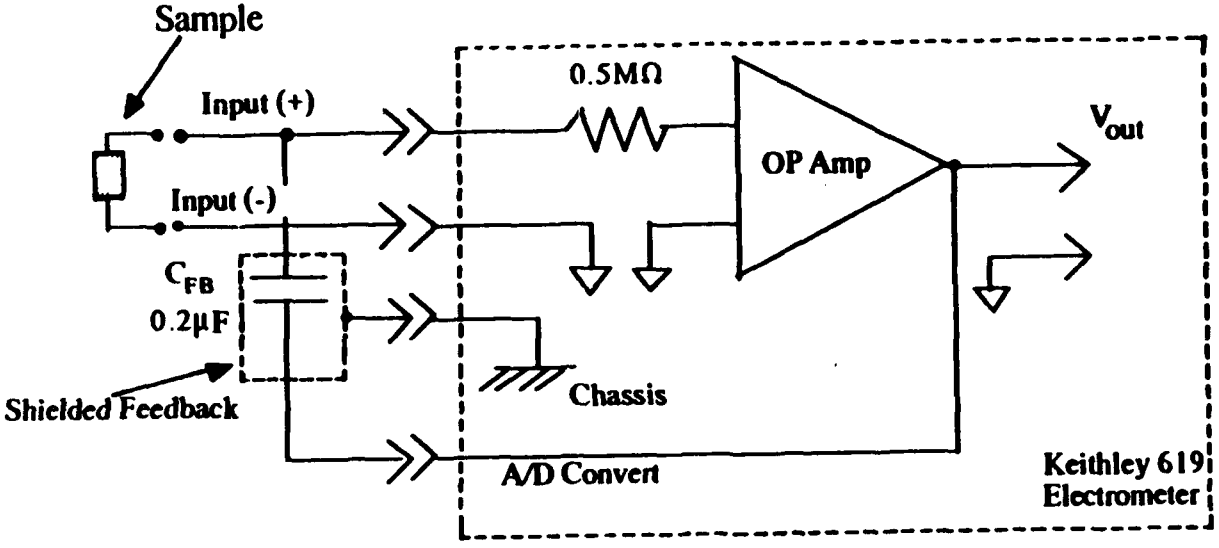
Sample
Input (+)
Input (-)
0.5MΩ
OP Amp
V_{out}
C_{FB}
0.2μF
Shielded Feedback
Chassis
A/D Convert
Keithley 619
Electrometer

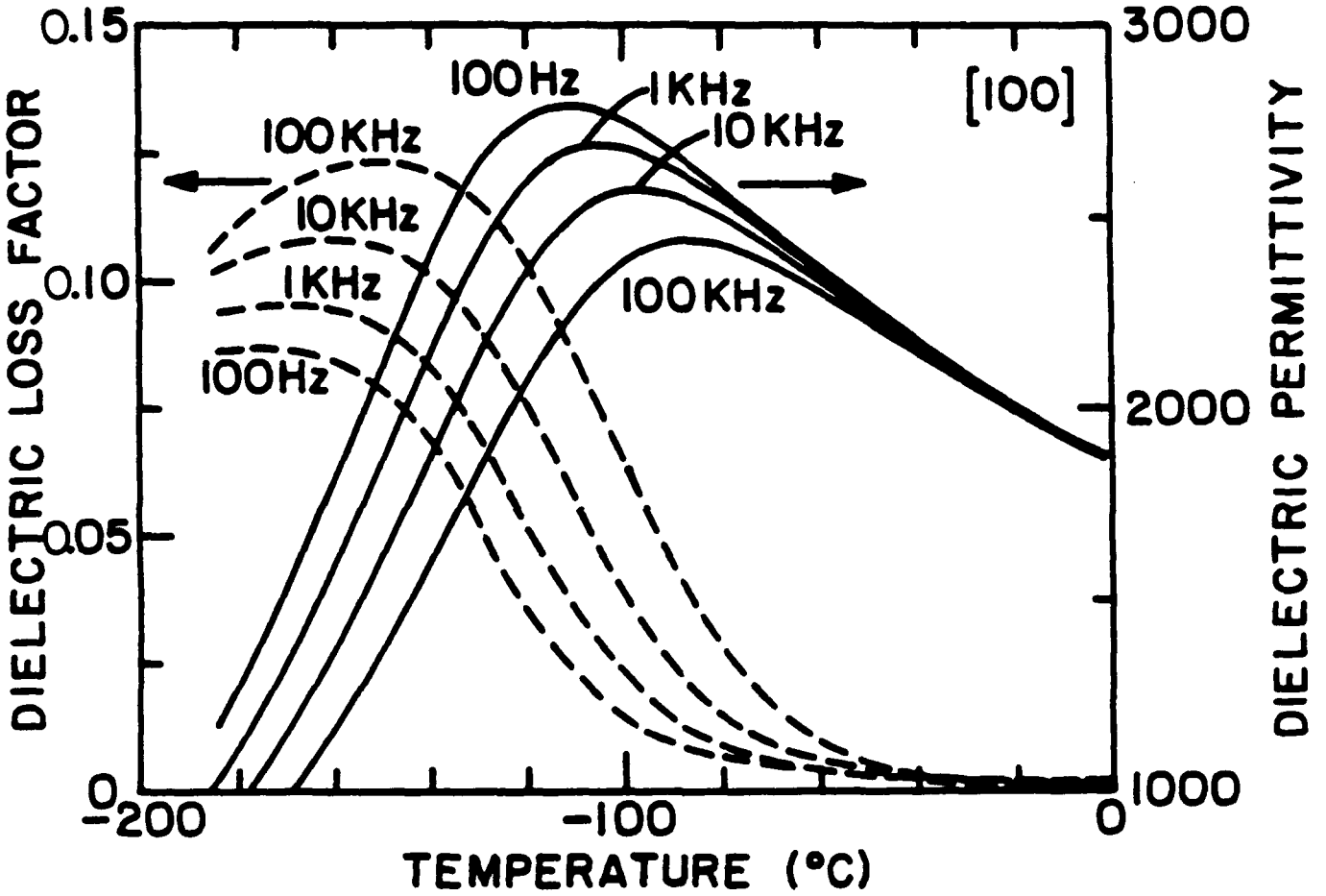
0.15
0.10
0.05
0
3000
2000
1000
-200
-100
0
100Hz
1KHz
10KHz
100KHz
[100]
100KHz
10KHz
1KHz
100Hz
100KHz
DIELECTRIC LOSS FACTOR
DIELECTRIC PERMITTIVITY
TEMPERATURE (°C)

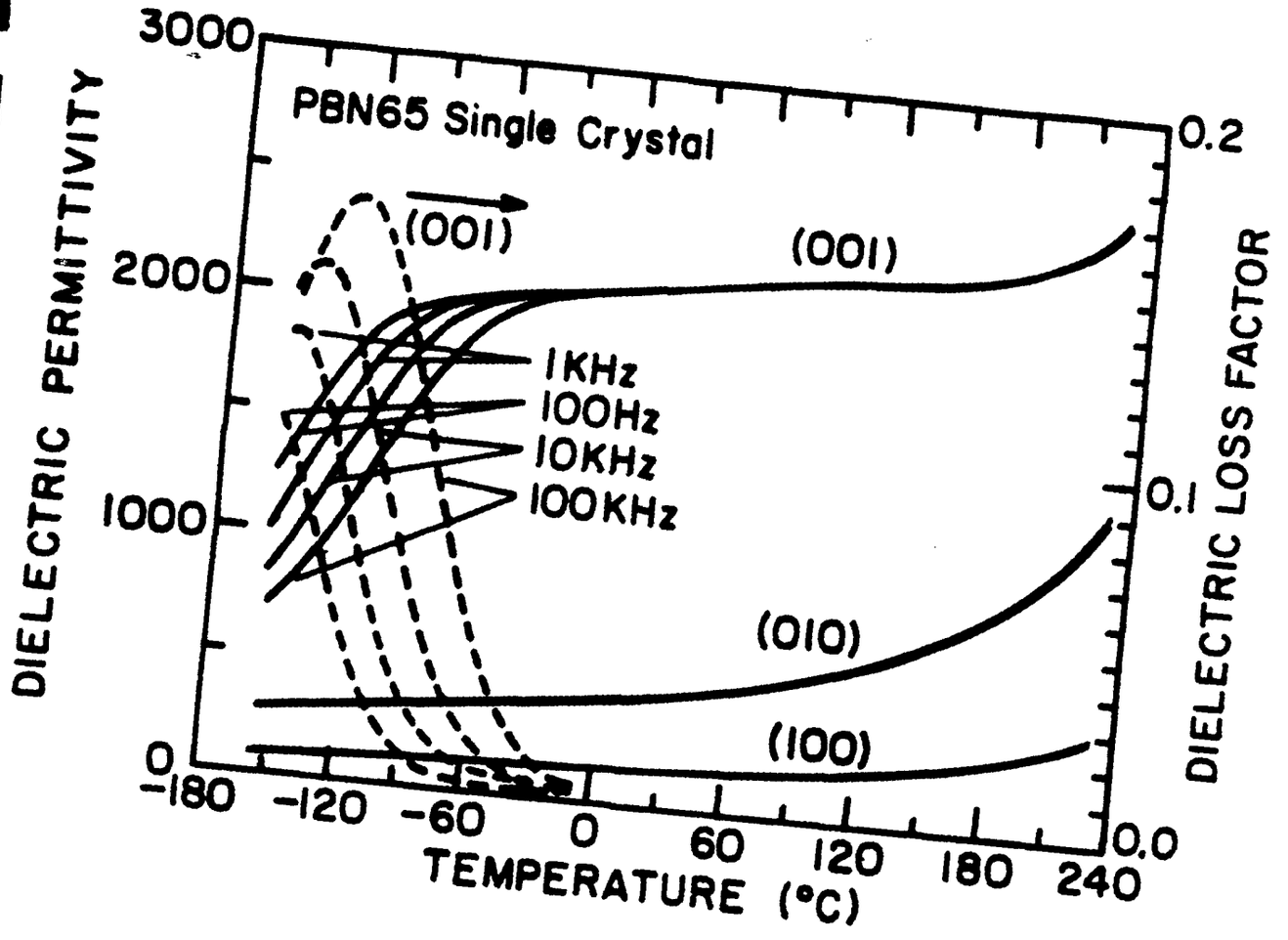
PBN65 Single Crystal
(001)
(001)
1KHz
100Hz
10KHz
100KHz
(010)
(100)
3000
2000
1000
0
0.2
0.1
0.0
-180
-120
-60
0
60
120
180
240
TEMPERATURE (°C)
DIELECTRIC PERMITTIVITY
DIELECTRIC LOSS FACTOR

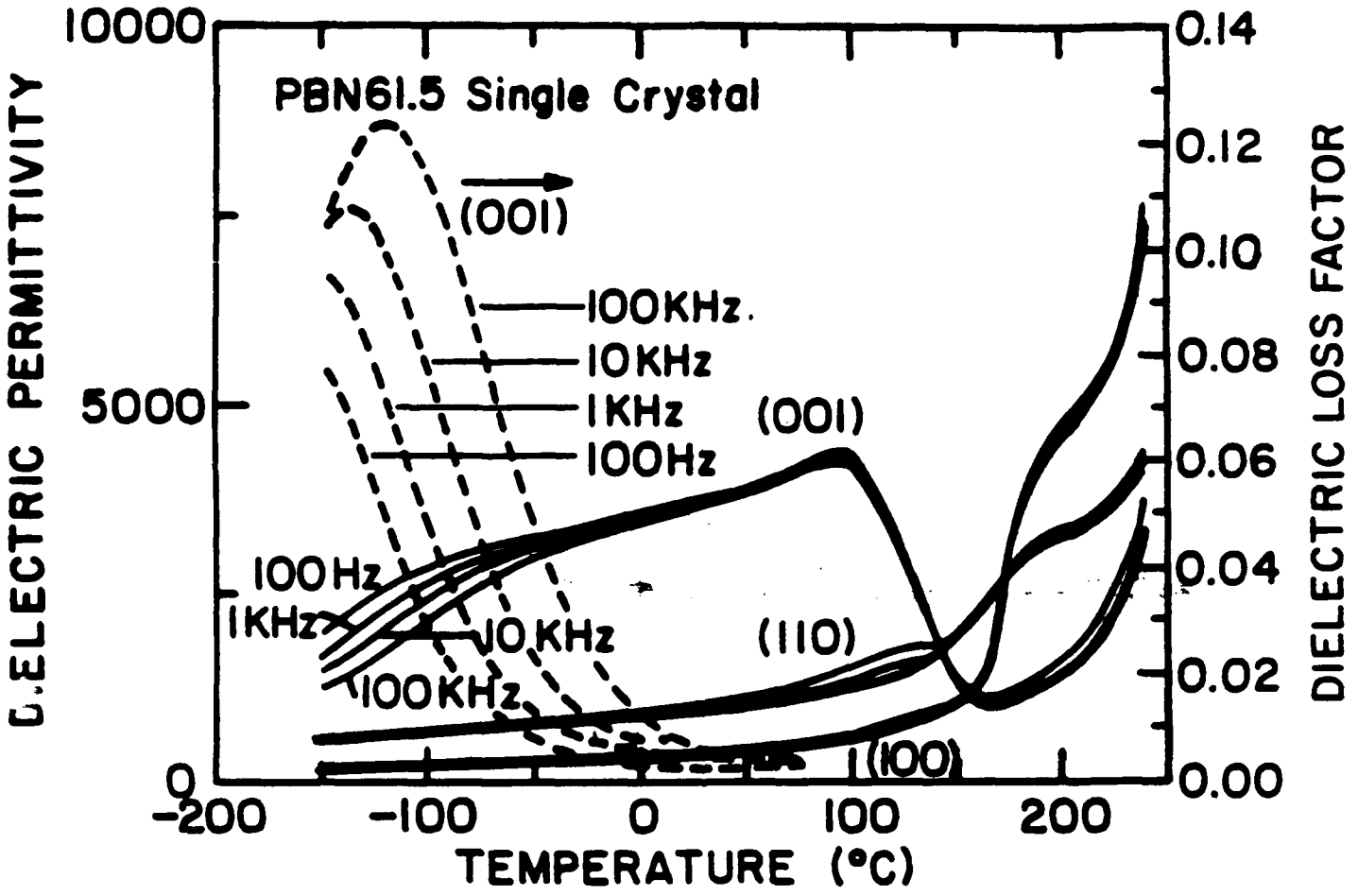
PBN61.5 Single Crystal
(001)
100KHz
10KHz
1KHz
100Hz
(001)
100Hz
1KHz
10KHz
100KHz
(110)
(100)
10000
5000
0
-200
-100
0
100
200
TEMPERATURE (°C)
0.14
0.12
0.10
0.08
0.06
0.04
0.02
0.00
DIELECTRIC LOSS FACTOR
DIELECTRIC PERMITTIVITY

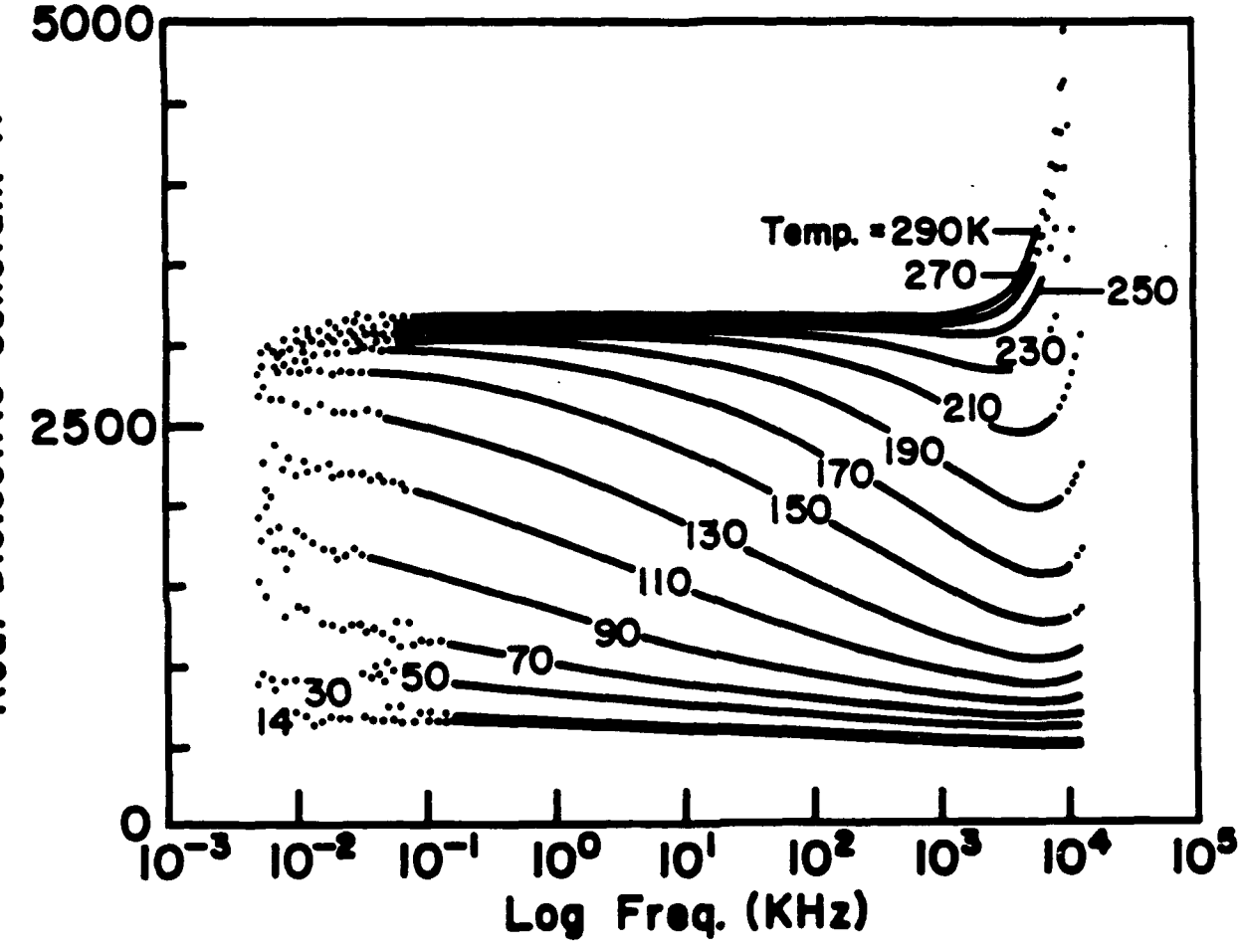
5000
2500
0
Real Dielectric Constant K'
Temp. = 290K
270
250
230
210
190
170
150
130
110
90
70
50
30
14
10^{-3} 10^{-2} 10^{-1} 10^{0} 10^{1} 10^{2} 10^{3} 10^{4} 10^{5}
Log Freq. (KHz)

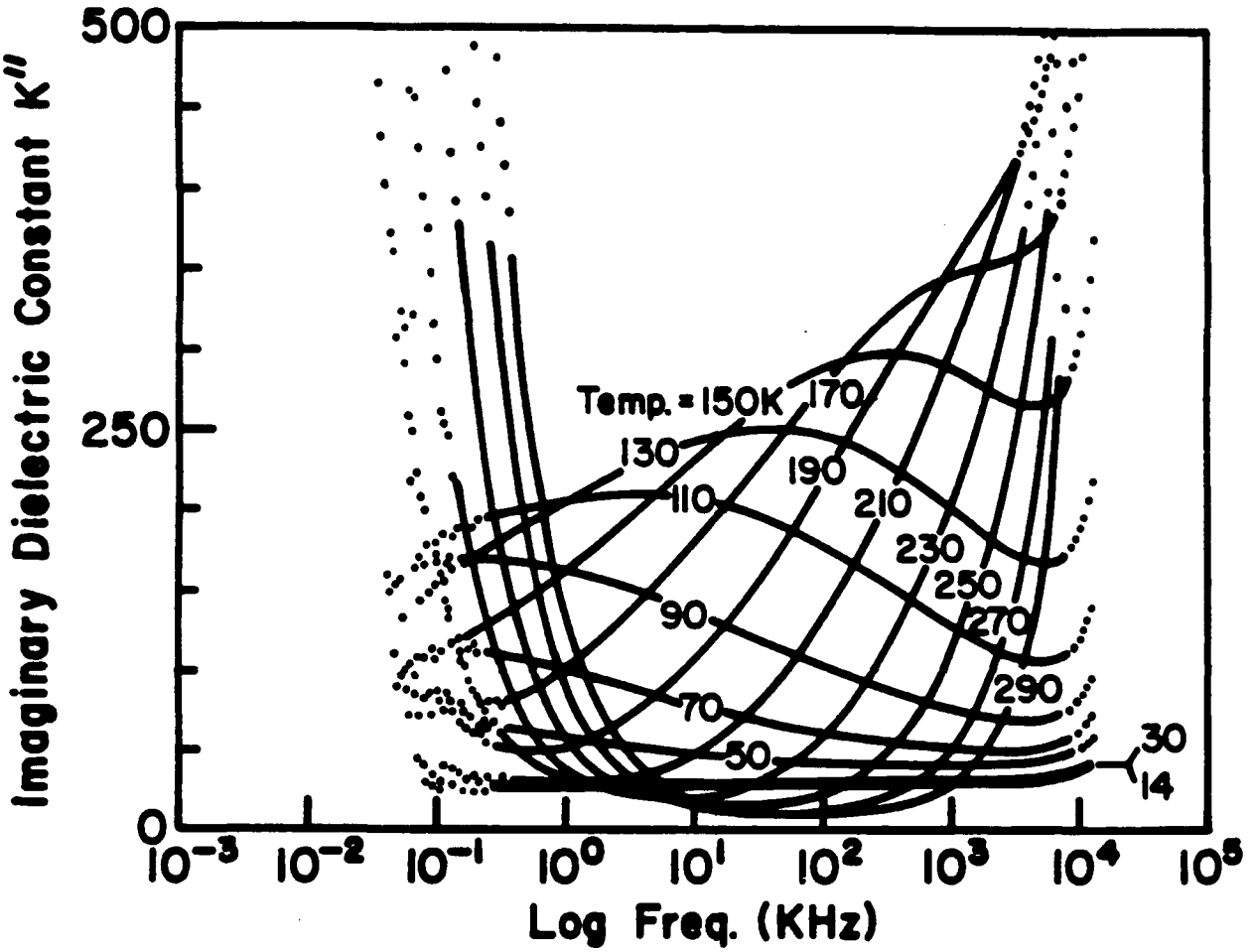
Imaginary Dielectric Constant K''
500
250
0
Temp. = 150K
170
130
190
110
210
230
250
90
270
290
70
30
50
14
10^{-3} 10^{-2} 10^{-1} 10^{0} 10^{1} 10^{2} 10^{3} 10^{4} 10^{5}
Log Freq. (KHz)

Fig 5(b)

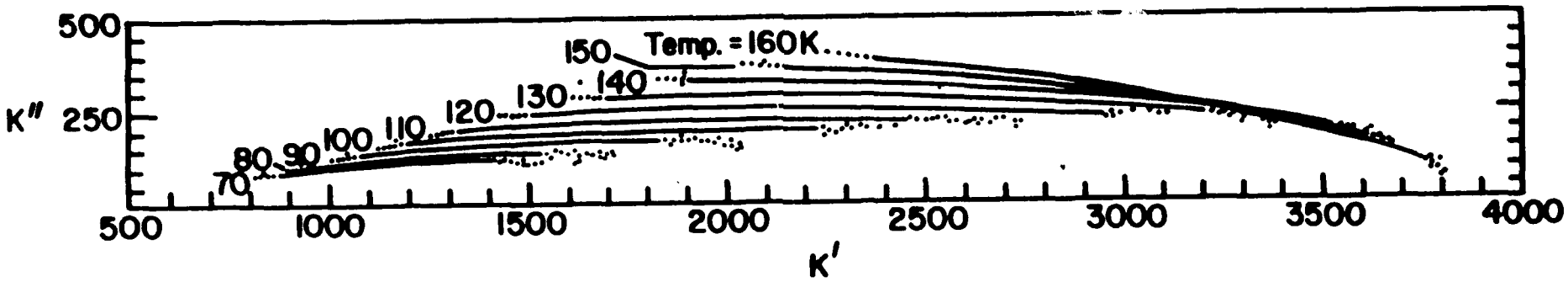
500
250
K''
150
Temp. = 160K
140
130
120
110
100
90
80
70
500
1000
1500
2000
2500
3000
3500
4000
K'

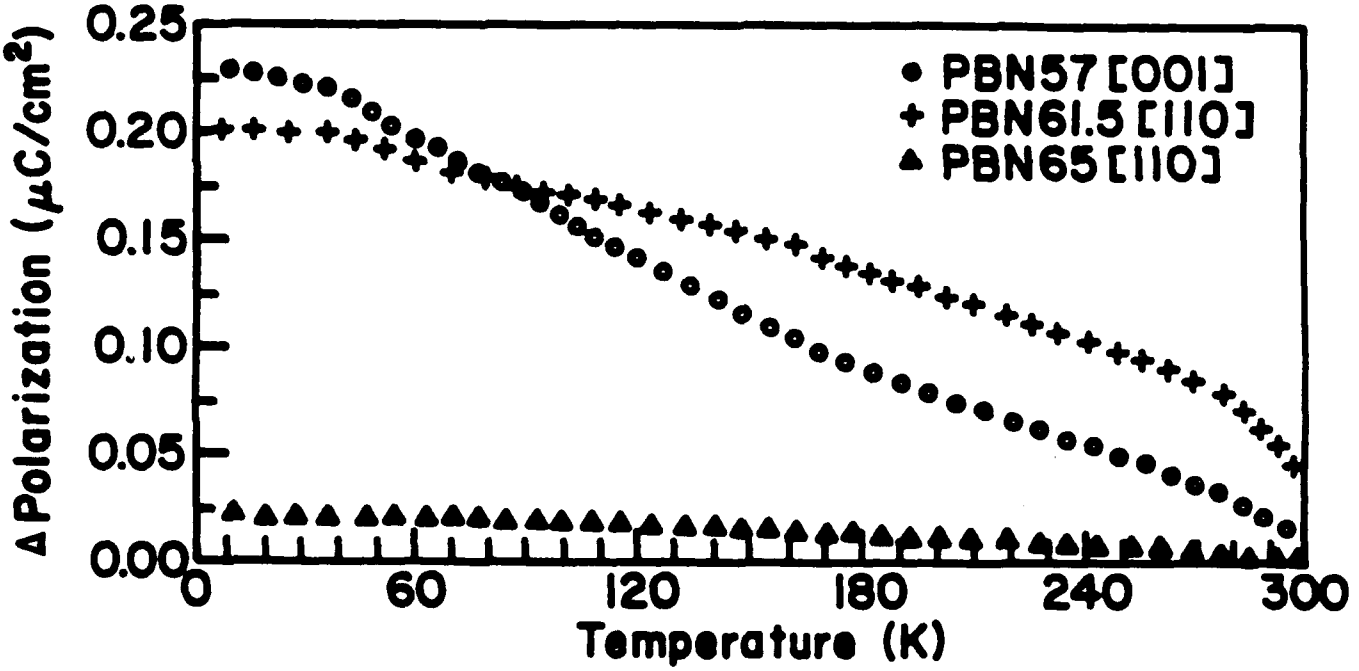
0.25
0.20
0.15
0.10
0.05
0.00
Δ Polarization (μC/cm²)
0
60
120
180
240
300
Temperature (K)
PBN57 [001]
PBN61.5 [110]
PBN65 [110]

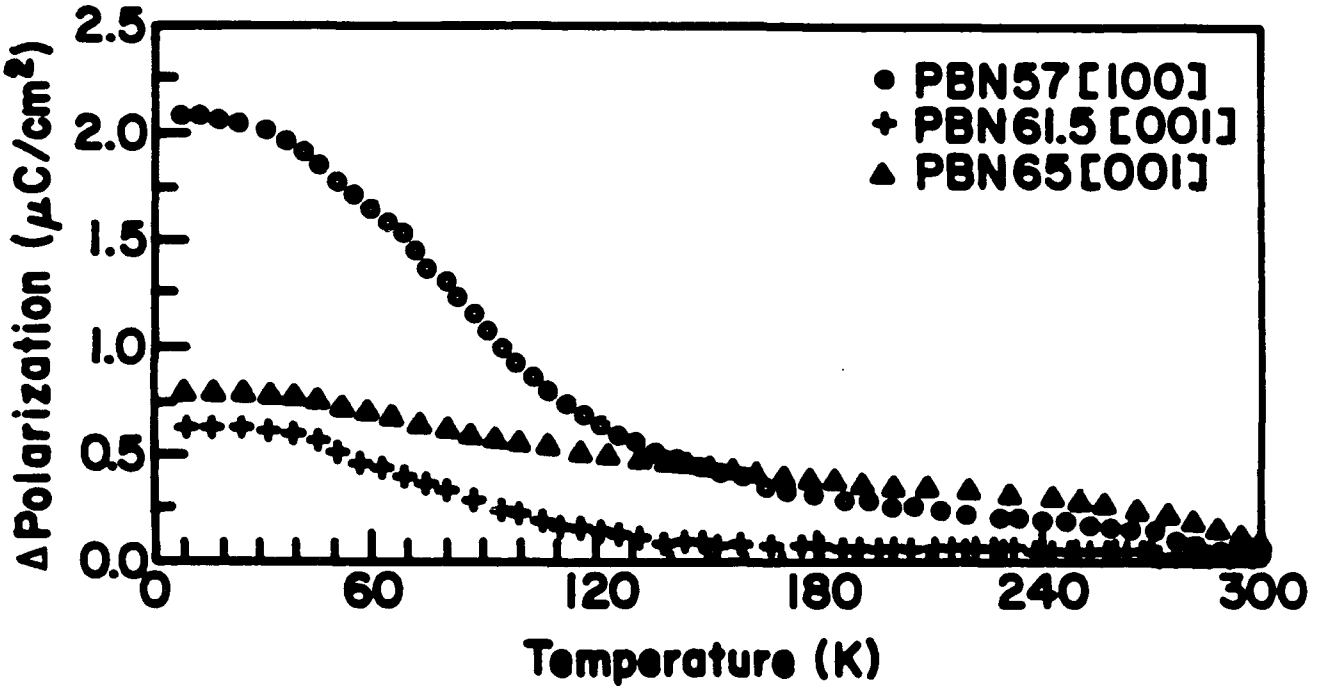
2.5
2.0
1.5
1.0
0.5
0.0
ΔPolarization (μC/cm²)
0
60
120
180
240
300
Temperature (K)
PBN57 [100]
PBN61.5 [001]
PBN65 [001]

Fig 7

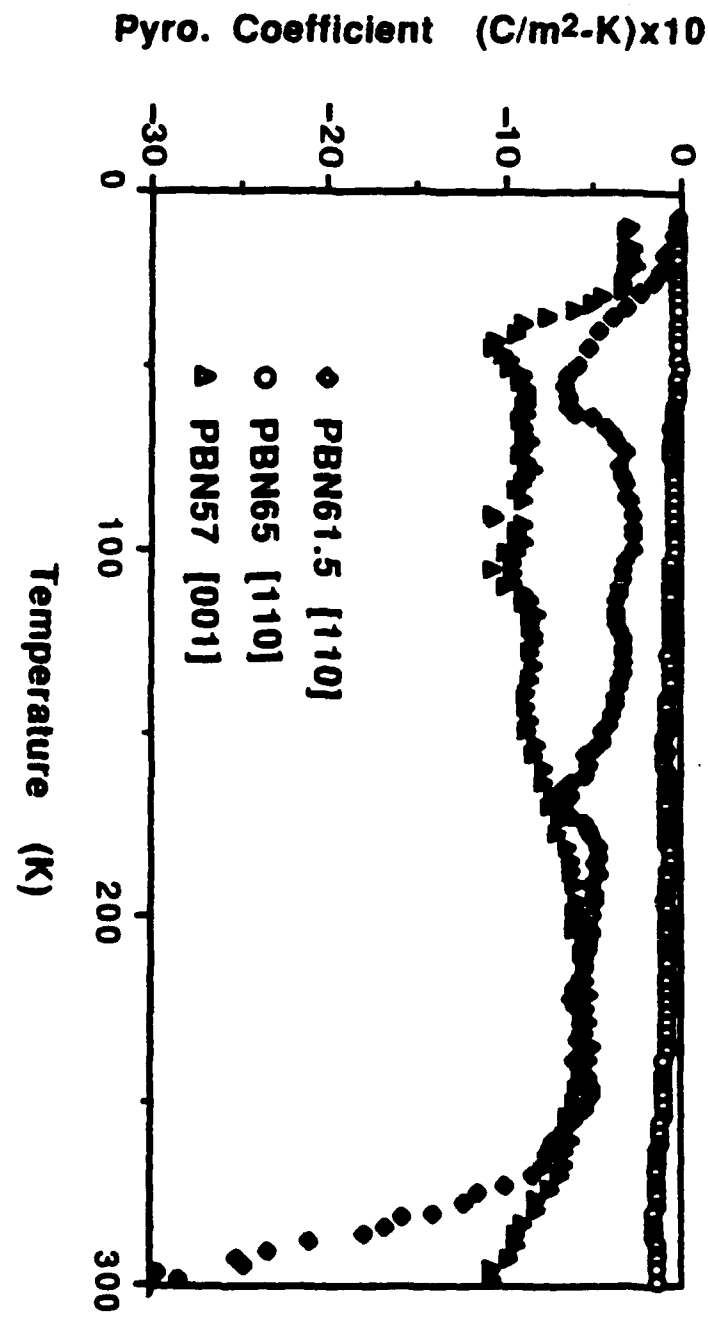
Pyro. Coefficient (C/m2-K)x10-6
-30
-20
-10
0
0
100
200
300
Temperature (K)
PBN61.5 [110]
PBN65 [110]
PBN57 [001]

Fig 8a

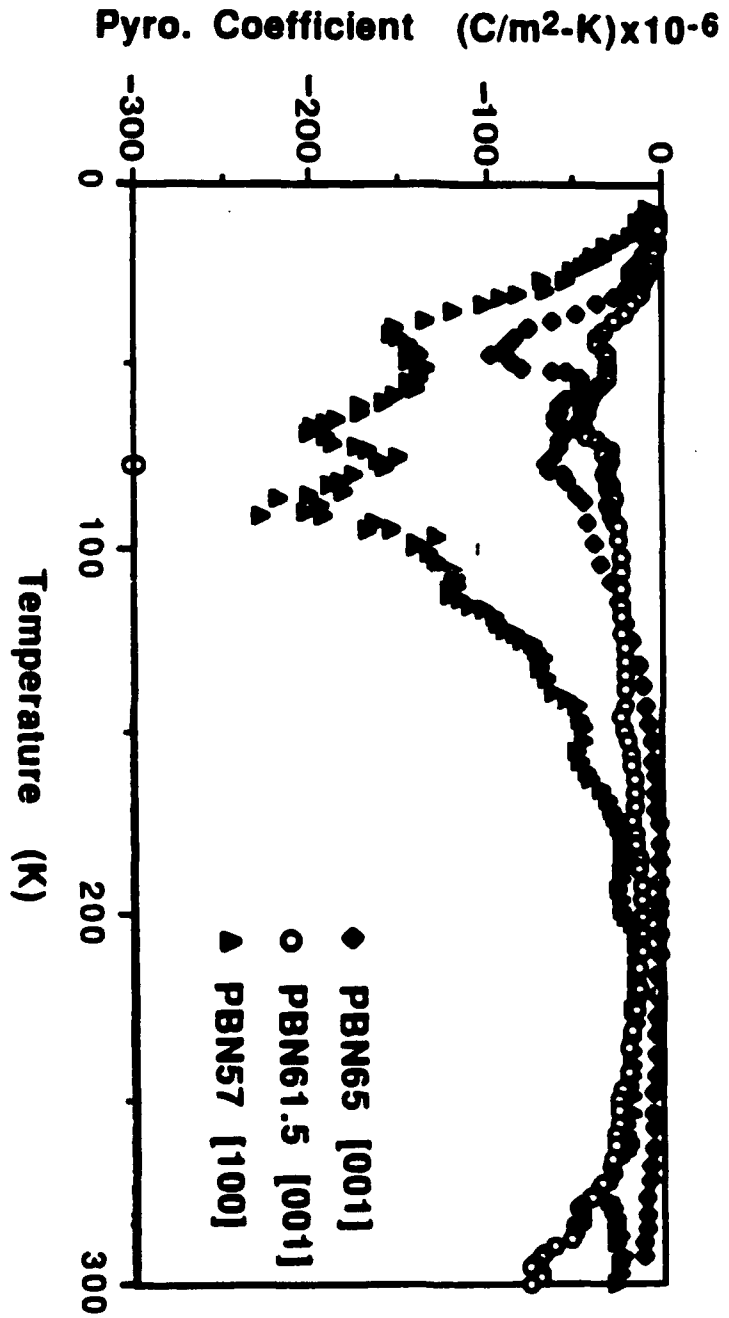
Pyro. Coefficient (C/m2-K)x10-6
-300
-200
-100
0
0
100
200
300
Temperature (K)
PBN65 [001]
PBN61.5 [001]
PBN57 [100]

Fig 2.

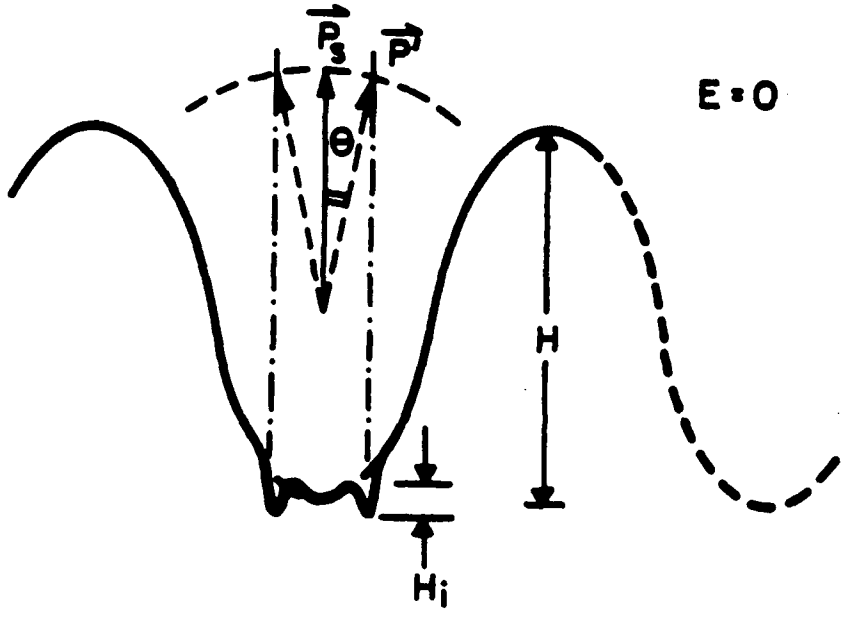

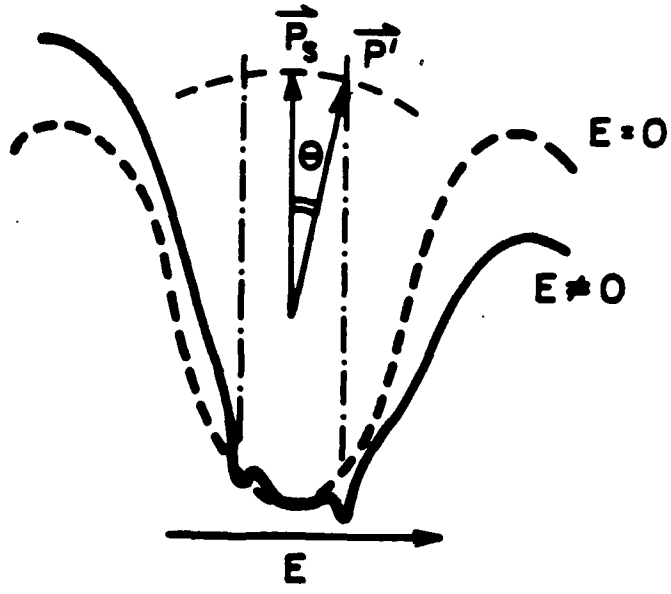

Fig. 9

APPENDIX 5

POLARIZATION MECHANISMS OF MORPHOTROPIC PHASE BOUNDARY LEAD BARIUM NIOBATE (PBN) COMPOSITIONS

R. Guo
A. S. Bhalla
C. A. Randall
Z. P. Chang
L. E. Cross

Polarization Mechanisms of Morphotropic Phase Boundary Lead Barium Niobate (PBN) Compositions

R. Guo, A.S. Bhalla, C.A. Randall, Z.P. Chang, and L.E. Cross

Materials Research Laboratory

The Pennsylvania State University

University Park, PA 16802

USA

ABSTRACT

Investigations of the polarization mechanisms in tungsten bronze relaxor ferroelectrics, $Pb_{1-x}Ba_xNb_2O_6$ (PBN[(1-x)%]) in particular, and of the morphotropic phase boundary compositions, have been carried out for both ceramics and bulk crystals by means of electrical, thermal, optical, and electron microscopic methods. Relations of phase transition behavior with compositional and polarizational fluctuations have been carefully studied. Instead of a sharp boundary composition, it is found that a rather wide composition range, $1-x \approx 0.63 \pm 0.03$ in $Pb_{1-x}Ba_xNb_2O_6$, corresponds to the orthorhombic and tetragonal morphotropic phase boundary. It is demonstrated with the help of optical conoscopic interference figures that for the near-morphotropic phase boundary single crystal PBN of tetragonal symmetry, the polarization vector can be switched orthogonally to an orthorhombic phase simply by the application of an electric field, which authenticates optically the 90 degree polarization rotation. Transmission electron microscope (TEM) study in the temperature range from -180°C to room temperature revealed the presence of incommensurate ferroelastic domains in the morphotropic phase boundary composition PBN crystals. In light of the above observed

experimental data, the polarization mechanisms of the morphotropic phase boundary compositions are discussed in terms of qualitative thermodynamics.

I. INTRODUCTION

Tungsten bronze ferroelectric lead barium niobate solid solution system, $Pb_{1-x}Ba_xNb_2O_6$ (PBN[(1-x)%]), has received considerable attention for a number of years after the initial investigation carried out in late 1950s.[1-7] However, ferroelectric PBN has recently become increasingly interesting, mainly because of its unique properties as being a tungsten bronze type ferroelectric relaxor with a morphotropic phase boundary (MPB) separating a tetragonal ferroelectric phase 4mm (with polarization dipole along [001]) and an orthorhombic ferroelectric phase m2m (with polarization dipole along [110]).[8-12] Extraordinarily large dielectric,[8,10] piezoelectric,[10] and pyroelectric[13] properties of morphotropic phase boundary PBN compositions have been reported confirming what is expected by applying Landau:Ginsburg:Devonshire thermodynamic phenomenology theory. It is of interest to investigate the characteristics of such morphotropic phase boundary composition PBN since a 90 degree polarization switch as well as other enhanced properties near the MPB could be of potential application in electro-optic, piezoelectric, and pyroelectric devices.

Work in this laboratory has included a comprehensive investigation of the polarization mechanisms in tungsten bronze type relaxor ferroelectrics, in particular of the morphotropic phase boundary composition PBN. In the present paper the results of electrical, thermal, and optic properties and TEM studies are described, and are interpreted in terms of the thermodynamic theories. An optical conoscopic interference pattern shows the electric field induced phase transition from one ferroelectric phase to the other. TEM studies reveal the coexistence of ferroelectric tetragonal and orthorhombic phases and the incommensurate ferroelastic domains. Full accounts of the individual details will be given in separate publications.

The composition quoted in the text, tables, and figures as PBN[(1-x)%] where

(1-x)% is the mole percent of $PbNb_2O_6$ in $Pb_{1-x}Ba_xNb_2O_6$ composition, refers to the post-growth analytical composition as determined by electron microprobe analysis. The crystal orientations used in this paper are based on the prototype tetragonal 4/mmm symmetry unless otherwise specified.

II. PREPARATION OF SPECIMENS

The ceramic specimens were prepared from high-purity chemicals using the conventional techniques of milling, prefiring, crushing, pressing, and firing. The specimens were prepared in the form of disks ~ 10 mm in diameter and ~ 1.2 mm thick. The final sintering temperature and time, which depended on composition, ranged from 1280°C to 1320°C for 1 to 6 hours. To compensate for the PbO loss during calcining, 3 wt% of excess PbO was added. Well reacted PBN ceramic pellets with 90 to 96% of theoretical density and 3 to 6 micrometer grain size were produced.

Single crystal specimens used for this investigation were prepared by the Czochralski pulling technique. Starting from high purity chemicals, the charge was heated in a Pt crucible by RF induction heating up to the melting temperature. Crystal was then withdrawn at a rate of 1 to 2 mm/hour along with rotations of crucible and the crystal boule. The crystal was slowly cooled to room temperature in 48 hours. Single crystals of the size of several millimeters of optical quality were thus grown even though there was some cracking problem during the slow cooling when they passed through the paraelectric to ferroelectric phase transition.

The chemical compositions of the specimens were characterized by electron microprobe. Three crystal compositions, PBN57, PBN61.5, and PBN65, had been chosen as representatives for this study. Ceramic and single crystal disk specimens were electroded by vacuum sputtered Au (or Pt in the case of high temperature measurements) after orientating, cutting, and polishing for electrical measurement. Bar shaped samples

from single crystal were also prepared for thermal expansion measurement. For TEM study single crystal samples were prepared by ion-beam thinning.

III. MEASUREMENT TECHNIQUES

A. Dielectric Properties

Measurements of permittivity and loss tangent at low field were made using a computer interfaced automatic measuring system LCR meter (Model HP4274A, Hewlett-Packard) over wide temperature (-180°C ~ 500°C) and frequency (10^2 ~ 10^5 Hz) ranges. A Delta design environment chamber covers the temperature range -180°C to +240°C. A vertical tube Kanthal wound furnace was used for the temperature range from room temperature to 500°C.

B. Thermal Expansion

Thermal expansion measurements were carried out from room temperature up to about 500°C by using a high sensitivity linear variable differential transformer (LVDT) dilatometer (Model 7/24DCDT-250, Hewlett-Packard). Heating/cooling rate of 0.5°C/min was chosen and regulated by a microprocessor based temperature controller. The specimen was mounted inside a fused silica holder which was set upright in a vertical furnace, and the thermal strains were measured by LVDT and recorded on an X-Y recorder.

C. Optical Measurement

A Leitz polarizing microscope was used for the optical measurement. To observe the conoscopic interference figure, an objective lense of numerical aperture 0.50 was used. White light was used as light source. The PBN57 crystal was oriented so that its optic axis [001] was parallel to the transmitted plane polarized light. Sputtered Au electrodes on (110) face of the crystal were deposited and fine silver wire were soldered to the faces and then connected to an DC power supply. Interference figures were observed through the eyepiece and recorded by camera.

IV. PROPERTIES OF MPB PBN

A. Dielectric Properties and Phase Diagram

The permittivity-temperature curves for various compositions near the MPB are given in Figure 1. These curves show that a maximum in permittivity and a minimum in the Curie temperature (represented by the temperature at which the permittivity peak occurs at 1KHz) are in the vicinity of 1-x = 0.63. Decreases in permittivity and/or increases in Curie temperature can be seen when the $PbNb_2O_6$ content in PBN is away from 63 mole percent. The variation of the permittivity as well as the phase transition temperature with composition is consistent with the results reported previously.[2,7] It is revealed by x-ray diffraction pattern (not shown here) that as the lead niobate content is increased up to 63 mole percent (compare to 60 mole percent reported by Smolenskii[2] and Baxter et al.[4] and 65 mole percent by Subbarao[3]), the orthorhombic distortion starts to dominate. With a further increase in the lead niobate content, the tetragonal symmetry (4mm) is then changed to an orthorhombic (m2m) distortion, as described by Francombe[5]. However, over the range where $PbNb_2O_6$ content is 60 to 66 mole percent, it is evident by x-ray that the two structures coexist and appear nearly equal in ratio at 63 mole percent of $PbNb_2O_6$.

Since the dielectric properties shown in Figure 1 are average properties measured on ceramic samples, it is more desirable to know the dielectric behavior along different orientations of PBN single crystals. Figures 2(a), (b), (c), and (d) show the dielectric properties for three crystals of the compositions close to the morphotropic phase boundary. Each conveys unique information about the typical dielectric behavior in different symmetry systems. Since there is no coupling between four-fold and two-fold axes in the prototype 4/mmm symmetry, different modes of polarization are seen in orthorhombic m2m symmetry (Figure 2(a), Curie temperature T_{c1} ~290°C) and in tetragonal 4mm symmetry (Figure 2(b), Curie temperature T_{c3} ~320°C) respectively. Figure 2(c) and 2(d) show the

crystal PBN61.5 actually goes through a phase transition from ferroelectric m2m to ferroelectric 4mm as temperature increases up to about 120°C and then eventually to a paraelectric state at T_c (≈ 290°C).

Hence $PbNb_2O_6$-$BaNb_2O_6$ phase diagram can be redrawn by adding our experimental data into the previously reported phase diagram[3] as shown in Figure 3 in which a curved morphotropic phase boundary into the Ba-rich side between ferroelectric m2m and ferroelectric 4mm has been indicated.

Large thermal hysteresis in dielectric properties has been observed for both single crystal and ceramic samples at the ferro-para phase transitions, and such hysteresis tends to be maximum when the composition is near the MPB particularly from the orthorhombic side. Figure 4 shows the hysteresis of dielectric permittivity for the single crystal PBN65 (measured along <110> direction) as an example. As can be seen in Figure 4, heating and cooling cycles reveal quite different characteristics of the crystal properties, with the cooling cycle showing much more dispersive behavior. The large hysteresis is believed to be due to the coexistence of two ferroelectric phases which have very close free-energies. Large dispersion of the dielectric constants observed for MPB PBN samples is suggestive of the relaxor-type phase transition. The chemical compositional distributions and micro polar regions merging into macro polar regions give rise to a frequency dependence of the dielectric constants.

B. Thermal Expansion

Thermal strain measurements of single crystal PBN61.5 are shown in Figure 5. As mentioned earlier in this paper, PBN61.5 is orthorhombic m2m at room temperature, tetragonal 4mm at temperatures above about 120°C and tetragonal 4/mmm in a paraelectric phase at temperatures above Curie temperature which is about 290°C, as determined by the dielectric measurement. A fairly good correspondence can be found between dielectric and thermal expansion measurements. When heated from room temperature, spontaneous strain built up along the c-axis and along the [110] direction it started to reduce slowly.

When heating continuously up to 120°C, large contraction can be observed for both the [001] and [110] directions while x_1 remains almost constant, whereas x_1 and x_3 start to increase when $x_{[110]}$ is almost constant until the ferroelectric-paraelectric phase transition temperature is reached. Large thermal hysteresis can be seen very clearly in Figure 5(a) where the orthorhombic distortion is not dominant until down to room temperature. Poling along c-axis can generate strain in [110] direction and make the orthorhombic to tetragonal phase transition to take place at a lower temperature as shown in Figure 5(c).

C. Optic Conoscopic Interference Pattern

Figure 6(a) shows the interference figure of the PBN57 single crystal at room temperature without any applied electric field. It is a typical uniaxial interference pattern consisting of cross isogyres concentric with a series of circles of isochromes and perpendicular to x and y, the principal vibration axes respectively (a reference for details of interference figure can be found, e. g. Ref.14). As expected for tetragonal systems, the crystal is always at extinction position under the crossed polarized light.

By applying a DC field up to 20 KV/cm on to the crystal in a direction parallel to [110], a biaxial interference figure was observed while rotating the stage, as shown in Figure 6(b). The trace of optic plane can be seen lying in [110] direction with the two melatopes indicating the outcrop of light rays that traveled along the optic axis while inside the crystal.

Depending on the applied electric field as well as the poling history of the sample, the melatope position changes along the [110] direction at different distance away from the center of the crossed Nicols. As shown in Figure 7, from 7(a) to 7(d), by reducing the poling field gradually, a systematic change of the melatope positions can be observed. Applying electric field again, but in [001] direction, the crystal can be switched back to its original tetragonal state, but incompletely. A thermal annealing at 550°C for 5 hours can bring the crystal essentially back to the original tetragonal state.

The optical conoscopic study shows that it is possible to switch the electrical polarization vector P_3 //[001] of tetragonal phase to a P_1//[110] of PBN57 single crystal. We believe this is the first report which suggests the possibility of orthogonal switching of the electric polarization associated with the crystallographic phase change of the MPB composition crystals. It is evident from this study that the direction of the polarization vector in the MPB composition crystals can be controlled by the application of externally applied field and such features may be explored for new optical devices.

D. TEM Study

TEM study was done by using diffraction contrast techniques and a liquid nitrogen cooled stage. The domain microstructures were deduced for PBN compositions across the phase diagram. Figure 8 shows 180° domain in tetragonal PBN, and Figure 9 shows 90° twins and 180° domains in orthorhombic PBN. For compositions close to the morphotropic phase boundary these macrodomains are found to coexist with some micro-aligned domains ~ 100Å separation which may be associated with the perturbation of the tetragonal and orthorhombic polar directions owing to the local symmetry effects, but further work is required. Dark-field imaging shows the discommensurations which are associated with an octahedral rotation in [110] directions to be coupled to the ferroelectric displacements in the orthorhombic ferroelectric symmetries. Figure 10 shows discommensuration microstructures in orthorhombic PBN75.

The TEM study reveals the manner in which the polarization manifests itself in the various ferroelectric symmetries. There exists only 180° ferroelectric domains in 4mm, and in m2m there exists both 90° twin like domains and 180° domains in the a-b plate. An incommensurate phase similar to those discovered in the other tungsten bronzes BNN ($Ba_2NaNb_5O_{15}$)[15] and SBN ($Sr_{1-x}Ba_xNb_2O_6$)[16] exists in both ferroelectric phases in PBN. These incommensurates exist at room temperature in tetragonal and orthorhombic ferroelectric phases, however, the discommensuration density is much lower and better defined on the orthorhombic side of the phase diagram. The origin of the

incommensuration is improper-ferroelastic and related to a superlattice involving octahedral tilts as represented schematically in Figure 11. The discommensuration structures seem to be coupled to the 90 degree ferroelectric domains in the m2m phase.

V. DISCUSSION

These studies have enabled us to find the relations among the electrical, thermal, and optical effects and the crystal structure of PBN.

For ferroelectric tetragonal PBN, $1-x < 0.60$ as shown in Figure 2(b), the sudden drop in dielectric permittivity K_3 when heating above the Curie temperature is achieved through an abrupt contraction in the [001] direction as indicated in Figure 5(a). Cooling below the Curie temperature, a mirror plane perpendicular to [001] direction in prototype 4/mmm is lost presumably because of the Nb^{5+} (as well as Pb^{2+} /Ba^{2+} in A1 and A2 positions) displacement along [001] direction from the surrounding oxygen ions, in a manner similar to $Sr_{1-x}Ba_xNb_2O_6$[17], creating a ferroelectric polarization in the [001] direction. A replacement of Sr^{2+} by Pb^{2+}, as in this case, necessarily increases the feedback action among cations and surrounding oxygens and raises the transition temperature evidently.[18]

As the $PbNb_2O_6$ content increased, the inhomogeneous distortion of the irregular shaped octahedron (compared to the ones in perovskite structure), enhanced by the packing effect of Pb^{2+} into A2 site (15 coordination site) and the puckering of the NbO chains in both [001] and [110] directions, destabilizes the tetragonal structure.

For ferroelectric orthorhombic PBN, $1 - x > 0.65$, the point group of the crystal structure is m2m with its [010] (in orthorhombic symmetry notation) direction in the [110] direction of the prototype tetragonal phase. Large ferroelastic strain has been detected for PBN orthorhombic structure in [001] and [110] directions as shown in Figure 5 for temperature lower than ~120°C. It is suggested that the measured thermal strain in [001]

direction is a collective puckering of the NbO_6 octahedron chains along the c-axis. Since the chains of octahedra are corner-linked the shear displacements are essentially in the opposite sense in successive c-layers and hence the c-repeat period is doubled, similar to the observation by Tendeloo et al.[19] using TEM on ferroelectric-ferroelastic $Ba_2NaNb_5O_{15}$. The successive shearing of octahedron eases the displacement of Nb^{5+} within the oxygen plane inside the octahedra, and no net polarization can exist along c-axis in orthorhombic structure. Instead, both spontaneous polarization and ferroelastic strain have been found in [110] directions.

The polarization and ferroelastic strain can be interpreted as follows:

As more Pb^{2+} replaces Ba^{2+} and occupies the A2 site, structural energy would be lower for a structure with lower symmetry (i.e., orthorhombic m2m in this case), when $PbNb_2O_6$ content reaches a critical ratio (i.e., ~ 63 mole% as determined experimentally). This is partly because of the size difference between Pb^{2+} (ionic radii=1.32Å) and Ba^{2+} (ionic radii=1.50Å) and partly because of the peculiar "lone electron pair" covalent bonding nature of Pb^{2+}, similar to the role of Pb^{2+} in $PbTiO_3$. NbO_6 octahedra are tilted or sheared in the manner mentioned above along the c-direction of the unit cell to minimize the electrostatic energy among cations and surrounding oxygen octahedra. In the same time, tilting of octahedra about c-axis in the direction parallel to [110] also happens in a corresponding way (because the O-Nb-O octahedral axes are not precisely parallel to the c-axis[17]), as shown in Figure 11. It is energetically favored that the unit cell would expand in <110> direction and contract in a perpendicular direction as we can see that this could be achieved by distorting the B1 octahedra (which is less distorted compared to B2 octahedral site) and empty C-sites permit such distortion to happen without structural difficulty. Such argument seems to agree well with our experimental results. Thermal expansion measurements on PBN61.5 showed the positive strain (expansion) built up in the [110] and [001] directions when the crystal system changes from tetragonal into orthorhombic as temperature drops, whereas there is almost no strain change in [100] direction. There is

also further evidence that TEM observed the incommensurate ferroelastic pattern which is associated with clockwise and counterclockwise rotation of octahedra about c-axis in [110] direction. Following such an argument, we can see (Figure 11) that the polar moment (Nb^{5+} displacement as well as the possible polarization contribution from Pb^{2+}) in perovskite-like groups would give rise to a net contribution in [110] direction, which is a polarization direction for orthorhombic structure.

It is anticipated that the shearing of the octahedra along c-direction and the rotation of the octahedra in [110] direction, are coupled even though there is no possibility of coupling in polarization modes in those two directions. The fact that poling along c-axis can actually induce large strain in [110] direction in PBN61.5 as shown in Figure 5(c) is an evidence of such elastic coupling between [001] and [110] directions in an orthorhombic structure. The structure itself is very sensitive to composition changes, however, the defect structure nature makes it behave as a buffer being able to accommodate the local chemical inhomogeneities. Even though there is no statistical compositional change in a crystal, the translational symmetry is interrupted due to the compositional fluctuations on a nanometer scale and a morphotropic phase boundary with certain composition variation ranges is found. The ferroelectric phases switching from one ferro phase to the other as a result of an applied electric field and observed by optical conoscopic interference figure can be explained by the suggested elastic coupling. Applying electric field in [110] direction of a tetragonal PBN crystal, would stabilize dipole along [110] direction first at locally Pb^{2+}-rich region and at the same time generate strain parallel to [110] direction. Coupling of the strain between [110] and [001] nucleates the crystal structure into orthorhombic, a biaxial optical figure is thus observed. Such electric field induced phase switch is fairly stable because of the ferroelastic strain built up in c-direction. That is also why thermal annealing is needed to revert the crystal back to the original symmetry.

The reason for large hysteresis in dielectric properties when the crystal is cooled through the ferroelectric to ferroelectric phase transition could be explained by thermodynamic theory:

The Gibbs' free energy of a crystal is given by

$$G = U - TS - EP - xX$$

where U, T, and S are internal energy, temperature, and entropy, respectively; EP is an electric term; xX is an elastic term. The electric term is divided into two parts, i.e. a ferroelectric part and a paraelectric part. Free energy change in the ferroelectric part is expressed by $-P_sE$. If the vector of P_s is antiparallel to the applied field, the free energy of the system increases. If the direction of spontaneous polarization is parallel to the applied field, the free energy of the system decreases. If the direction of spontaneous polarization is perpendicular to the applied field, the free energy of a system stays unchanged. A schematic drawing can be seen in Figure 12 to show the effects of the electric field applied on the free energy change, where FT and FO relate to the ferroelectric tetragonal and orthorhombic forms, respectively, and the subscripts 0, 1, and 2 correspond to the respective cases that the electric field strength is zero, parallel to the [001] direction and parallel to the [110] direction. When no electric field is applied, the free energy function curve as a function of composition x can be qualitatively given by FT_0 for the tetragonal and FO_0 for the orthorhombic phase. The intersection of FT_0 and FO_0 corresponds to the morphotropic phase boundary. When an electric field is applied parallel to the direction of [00i] of the tetragonal symmetry, the free energy curve can be expressed by FT_1 and $FO_1(FO_1=FO_0)$, by which the MPB can move to the barium-rich side (ξ_1). When the electric field is applied parallel to the direction of [110], the MPB can move to the lead-rich side (ξ_2) at the intersection of FT_2 ($FT_2=FT_0$) and FO_2. The above two cases are extremes. The two phases can coexist over a range of $\Delta\xi$ between these extreme cases. Applying electric field or mechanical stress in an appropriate direction can induce the

forthcoming phase transition which is metastable even after removal of the field since it must overcome stress produced between the host and the nucleus due to the growth.

At MPB compositions, the two ferroelectric phases intercept, which necessarily means that those two neighboring phases, orthorhombic m2m and tetragonal 4mm are energetically very much similar. A large thermal hysteresis on heating and cooling for thermal expansion, Figure 5, can then be understood because a first order phase transition can not take place until the latent heat stored is enough to accomplish the energy needed for rotation of polarization direction as well as for establishing the different elastic states.

In order to understand completely the ferroelectric polarization mechanisms of tungsten bronze PBN, detailed study on relation of atomic arrangement to ferroelectric polarization behavior is desired and the work in these directions are in progress.

ACKNOWLEDGEMENT

This research was funded by the Office of Naval Research and DARPA.

REFERENCES

[1]V. A. Isupov & V. I. Kosiakov, Soviet Physks Tech. Phys. 3, 2002 (1958).

[2]G. A. Smolenskii, V. A. Isupov & A. I. Agranovskaya, Soviet Phys. Solid State 1, 400 (1959).

[3]E. C. Subbarao, J. Amer. Ceram. Soc. 42, 448 (1959).

[4]P. Baxter & N.J. Hellicar, J. Amer. Ceram. Soc. 43, 578 (1960).

[5]M. H. Francombe, Acta Cryst. 13, 131 (1960).

[6]I. G. Ismailzade, Soviet Phys. Cryst. 4, 618 (1960).

[7]E. C. Subbarao, G. Shirane & F. Jona, Acta Cryst. 13, 226 (1960).

[8]T. R. Shrout & L. E. Cross, Ferroelectric Letters 44, 325 (1983).

[9]M. Adachi, S. G. Sankar, A. S. Bhalla, Z. P. Chang & L. E. Cross, Proc. 6th IEEE Inter. Symp. on Appl. of Ferroelectrics, p169 (Bethlehem, USA 1986).

[10]T. R. Shrout, H. Chen & L. E. Cross, Ferroelectrics 74, 317 (1987).

[11]J. R. Oliver, R. R. Neurgaonkar & L. E. Cross, J. Am. Ceram. Soc. 72(2), 202 (1989).

[12]L. E. Cross, Ferroelectrics 76, 241 (1987).

[13]R. Lane, D. L. Mack & K.R. Brown, Trans. J. Brit. Ceramic Soc. 71, 11 (1972).

[14]F. D. Bloss: *An Introduction to the Methods of Optical Crystallography* (Holt, Rinehart and Winston, 1961).

[15]R. Serneels, M. Snykers, P. Delavignette, R. Gevers, and S. Amelinckx, Phys. Stat. Sol. (b), 58, 277 (1973).

[16] L. A. Bursill and P.J. Lin, Acta Cryst., B43, 49 (1987).

[17]P. B. Jamieson, S. C. Abrahams & J. L. Bernstein, J. Chem. Phys. 48(11), 5048 (1968).

[18]A. R. Von Hippel : *Dielectrics and Waves* (John Wiley and Sons, 1954), p45.

[19]G. V. Tendeloo, S. Amerlinckx, C. Manolikas, and S. Wen, Phys. State. Sol. (a), 91, 483 (1985).

FIGURE CAPTIONS

Figure 1. Effect of composition on permittivity-temperature curves of PBN ceramics of formula $Pb_{1-x}Ba_xNb_2O_6$, a) 1 - x = 0.60 ~ 0.63; b) 1 - x = 0.63 ~ 0.66 at 1KHz.

Figure 2. (a): Dielectric property of single crystal PBN65 (mainly orthorhombic symmetry m2m when $T < T_c$); (b): Dielectric property of single crystal PBN57 (mainly tetragonal symmetry 4mm when $T < T_c$); (c) and (d): Dielectric property of single crystal PBN61.5 (mainly orthorhombic m2m when T < 120°C, and mainly tetragonal 4 mm when 120°C < T < T_c).

Figure 3. Phase diagram for $PbNb_2O_6$-$BaNb_2O_6$ solid solution system.

Figure 4. Hysteresis on heating and cooling for K vs T for single crystal PBN65 (110-face as an example).

Figure 5. Thermal strain vs temperature for PBN61.5 single crystal: a) x_3, b) x_1, and c) $x_{[110]}$.

Figure 6 (a) Conoscopic interference pattern for crystal PBN57 without poling and (b) Conoscopic interference figure for crystal PBN57 after poling 20 KV/cm in a direction parallel to [110].

Figure 7. Conoscopic interference pattern of PBN57 under different electric field a) 17, b) 1.3, c) 0.8, and d) 0KV/cm.

Figure 8. 180° ferroelectric domains in tetragonal PBN with dipole aligned along the <001> directions at room temperature.

Figure 9. 90° and 180° ferroelectric domains in orthorhombic PBN.

Figure 10. Dark field image at room temperature of incommensurate phases reveals discommensuratic microstructures in orthorhombic PBN. The contrast here reveals coupling between incommensurate phases and 90° ferroelectric domains.

Figure 11. 2-D projection of tungsten bronze type structure viewed onto (001) plane showing the octahedral tilting in the <110> directions about c-axis. (showing the ferroelectric polarization and its relation with strains in orthorhombic m2m).

Figure 12. Schematic presentation of free energy versus composition.

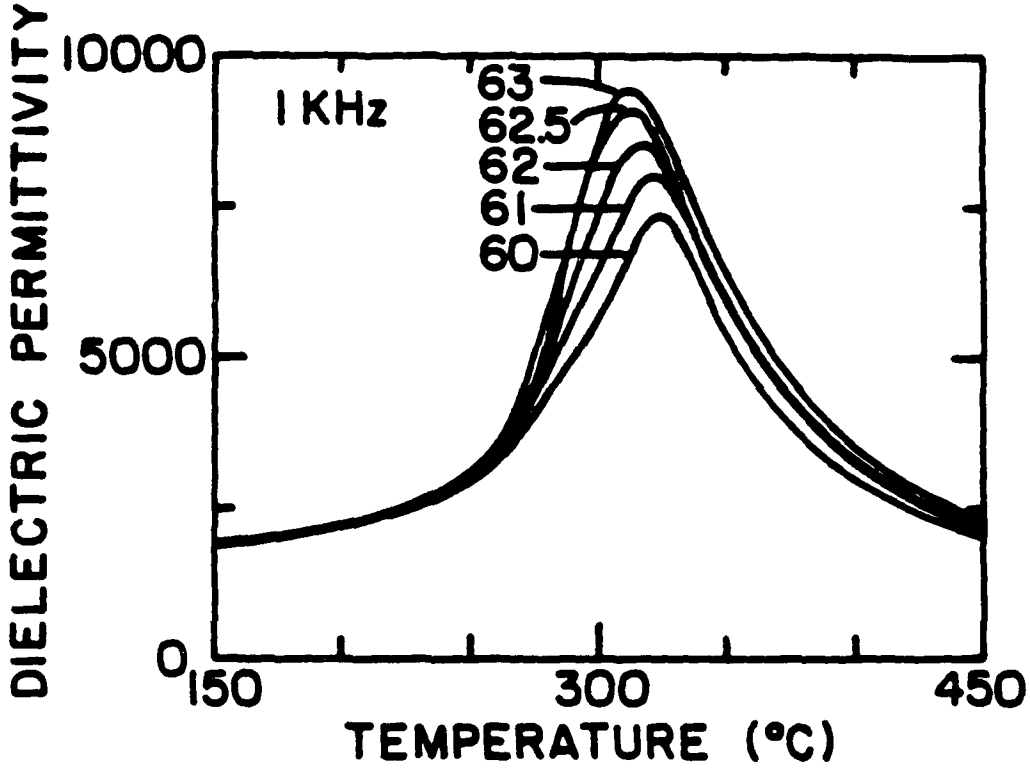
DIELECTRIC PERMITTIVITY
10000
5000
0
1 KHz
63
62.5
62
61
60
150
300
450
TEMPERATURE (°C)

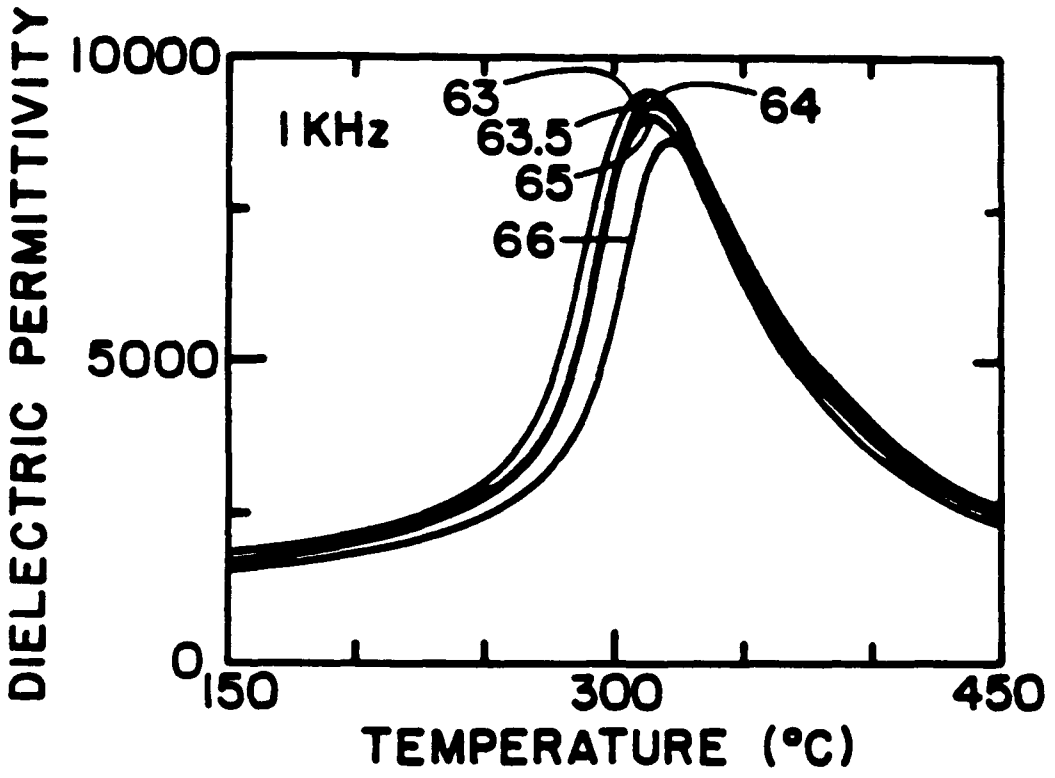
DIELECTRIC PERMITTIVITY
10000
5000
0
1 KHz
63
63.5
65
66
64
150
300
450
TEMPERATURE (°C)

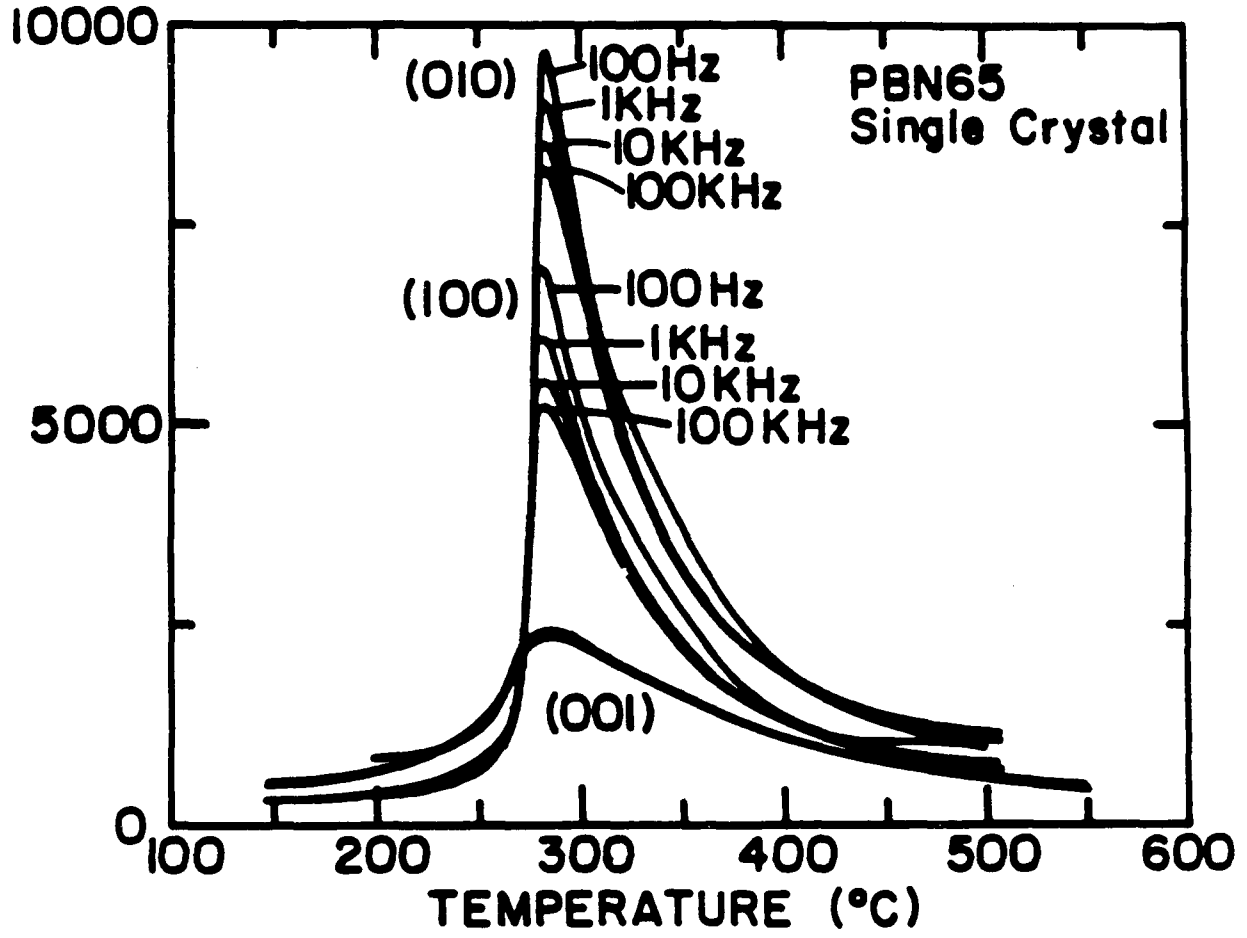
10000
5000
0
DIELECTRIC PERMITTIVITY
(010)
100Hz
1KHz
10KHz
100KHz
PBN65
Single Crystal
(100)
100Hz
1KHz
10KHz
100KHz
(001)
100
200
300
400
500
600
TEMPERATURE (°C)

Fig.

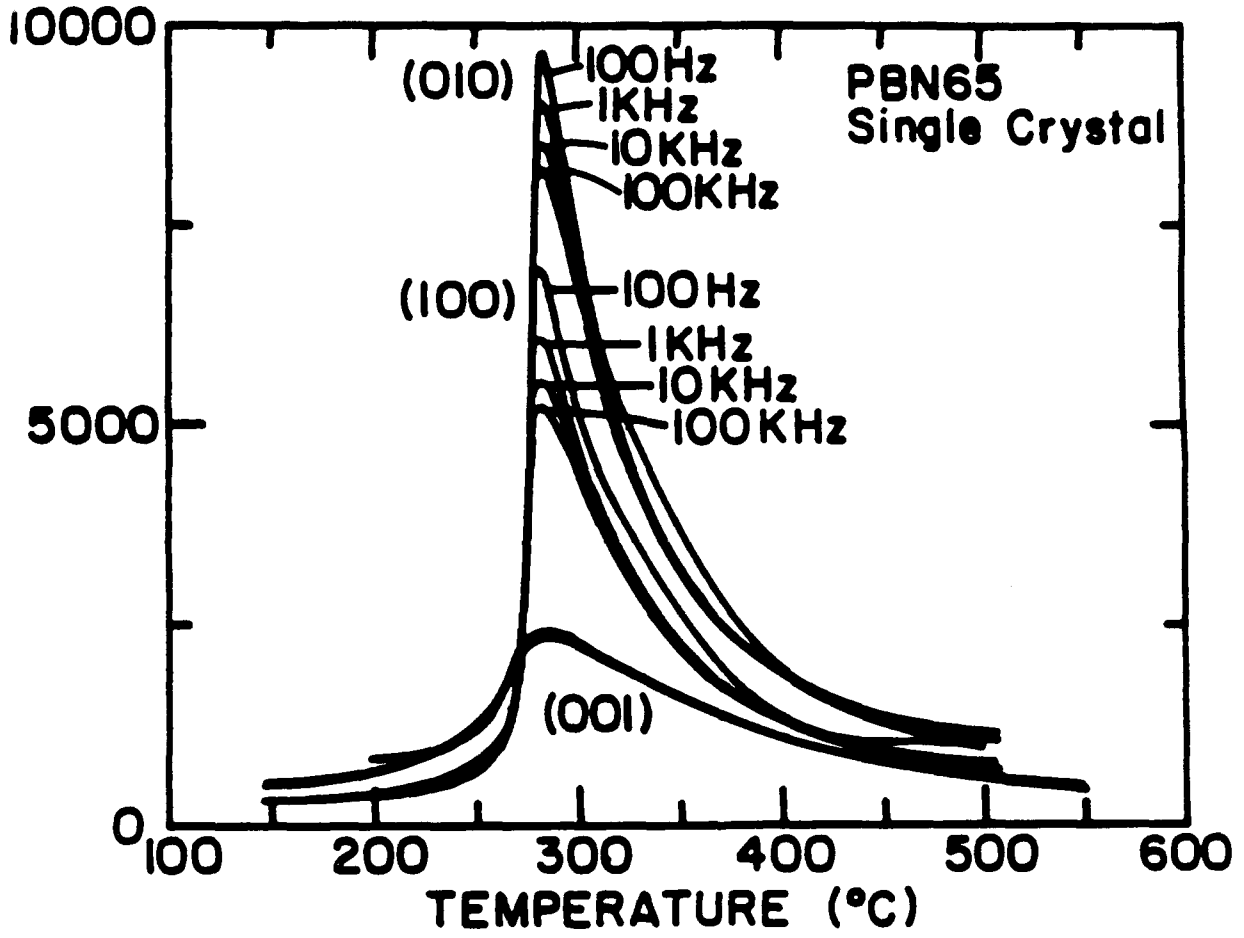
10000
5000
0
DIELECTRIC PERMITTIVITY
(010)
100Hz
1KHz
10KHz
100KHz
PBN65
Single Crystal
(100)
100Hz
1KHz
10KHz
100KHz
(001)
100
200
300
400
500
600
TEMPERATURE (°C)

Fig.

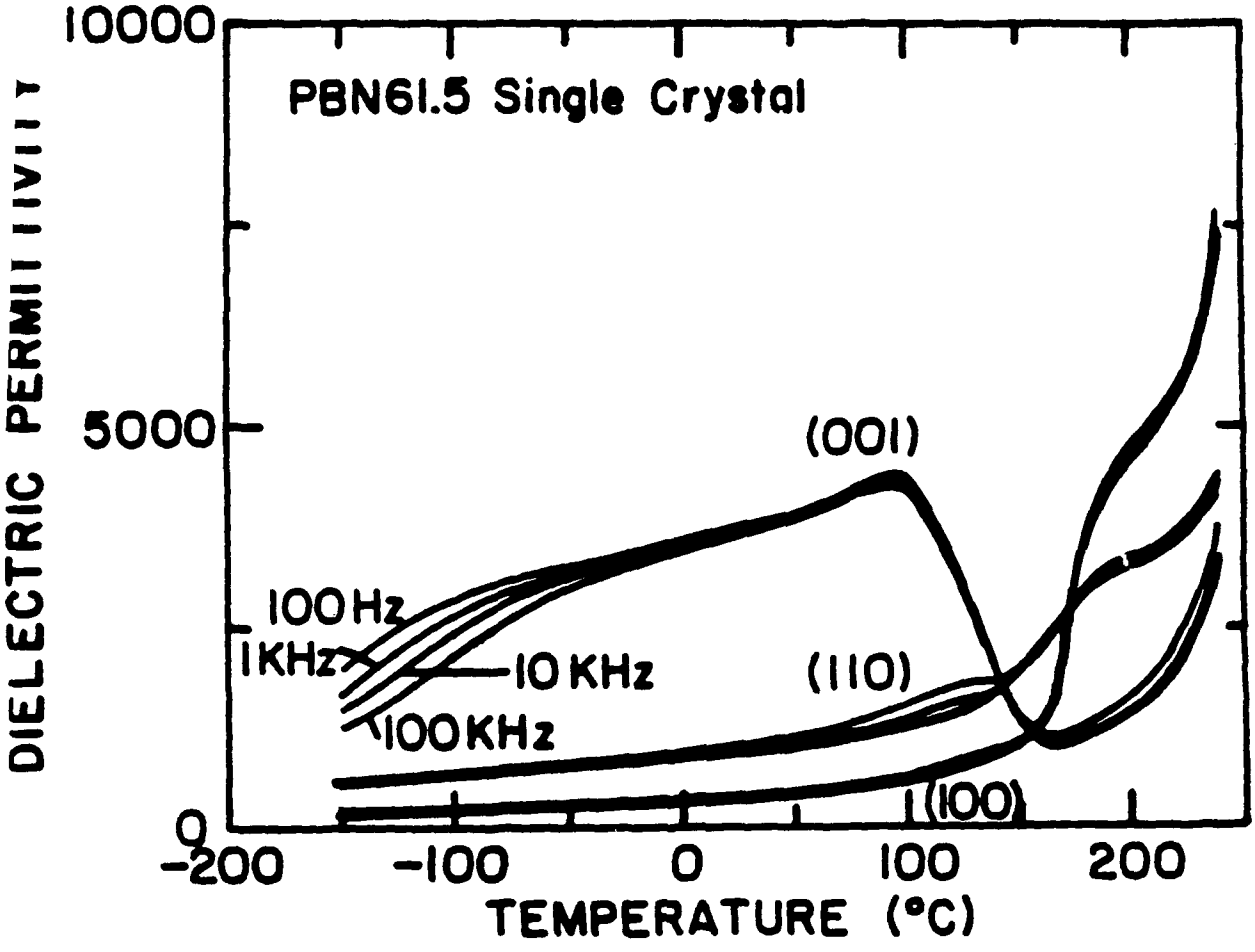
10000
5000
0
PBN61.5 Single Crystal
(001)
(110)
(100)
100Hz
1KHz
10KHz
100KHz
-200
-100
0
100
200
TEMPERATURE (°C)
DIELECTRIC PERMITTIVITY

Fig.

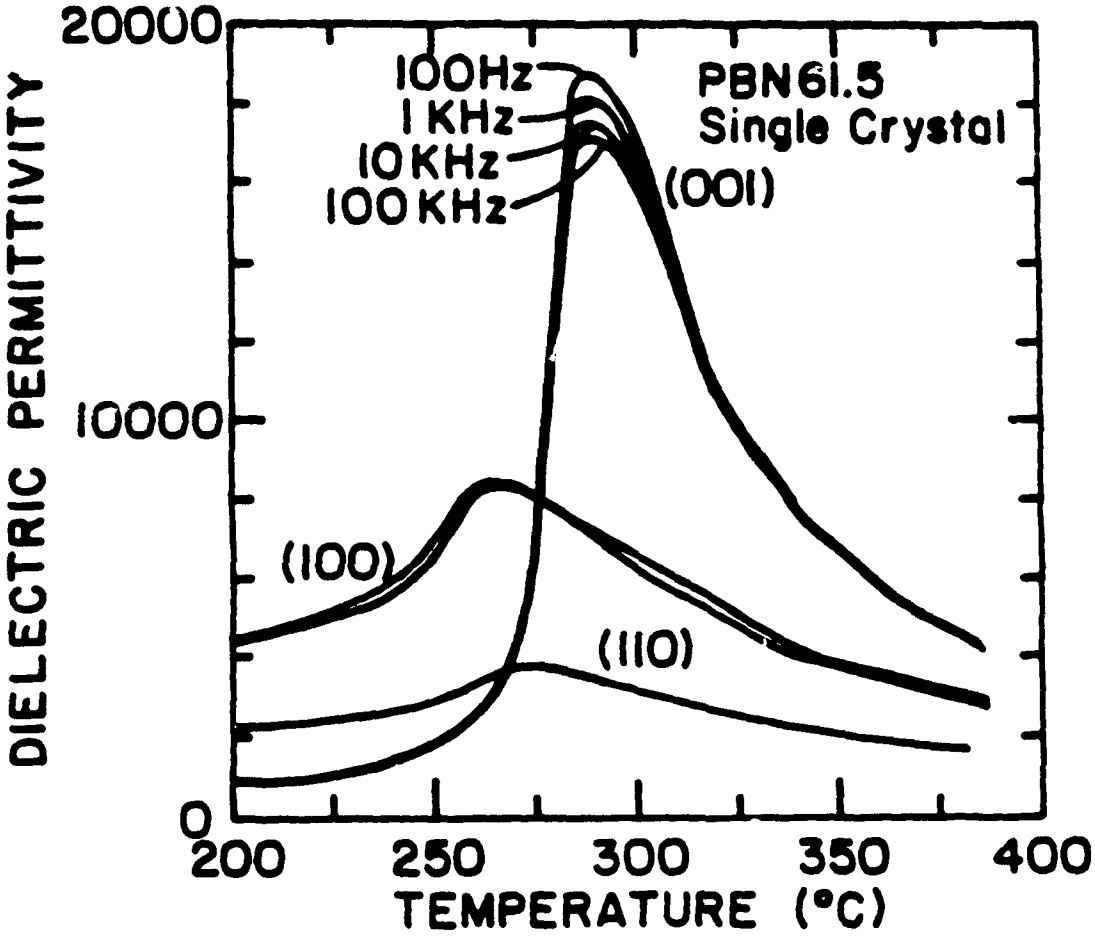
20000
10000
0
DIELECTRIC PERMITTIVITY
100Hz
1 KHz
10 KHz
100 KHz
PBN61.5
Single Crystal
(001)
(100)
(110)
200
250
300
350
400
TEMPERATURE (°C)

Fig. 4

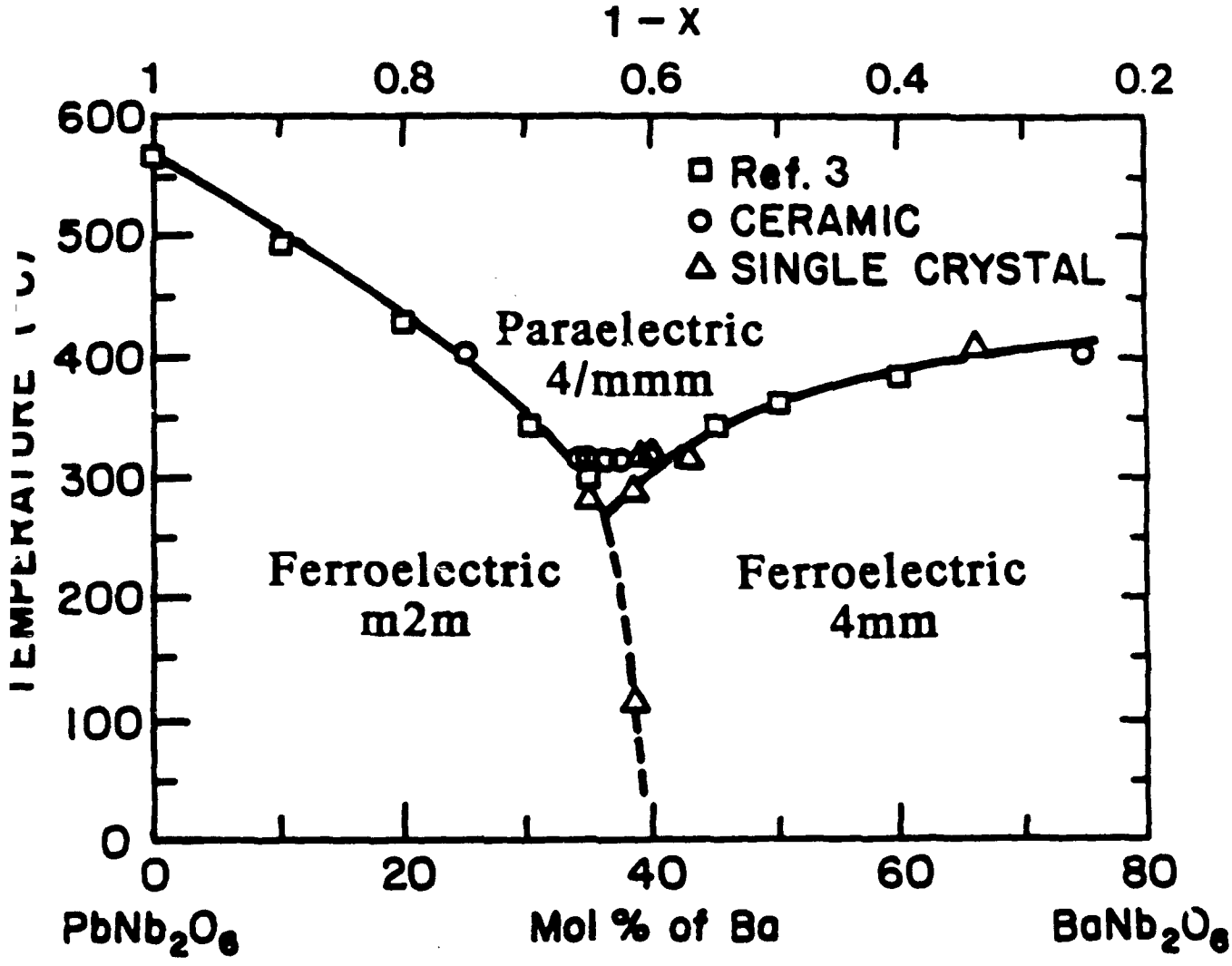
1 − X
1
0.8
0.6
0.4
0.2
600
500
400
300
200
100
0
TEMPERATURE (°C)
Ref. 3
CERAMIC
SINGLE CRYSTAL
Paraelectric
4/mmm
Ferroelectric
m2m
Ferroelectric
4mm
0
20
40
60
80
PbNb2O6
Mol % of Ba
BaNb2O6

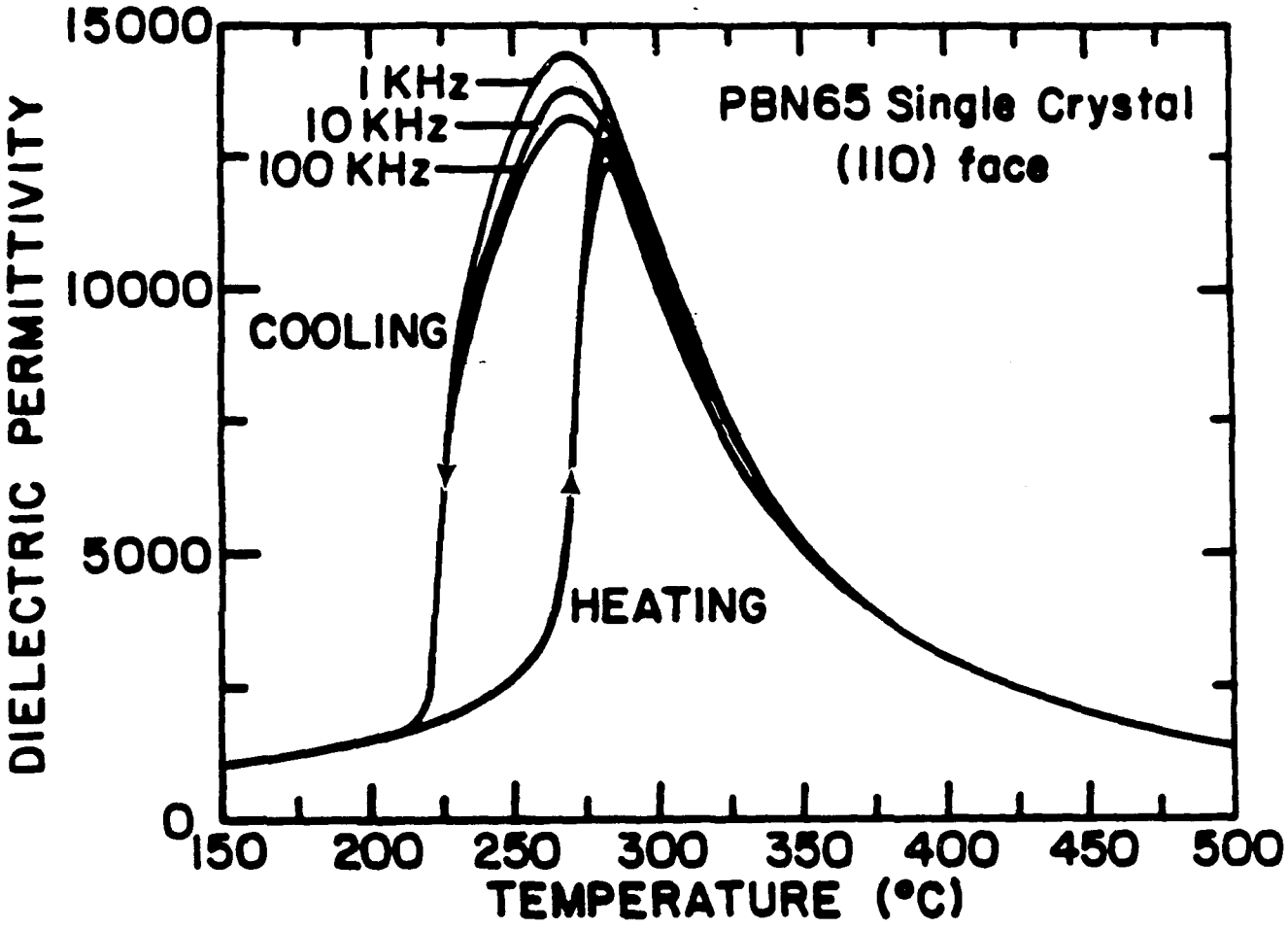
15000
10000
5000
0
DIELECTRIC PERMITTIVITY
1 KHz
10 KHz
100 KHz
PBN65 Single Crystal
(110) face
COOLING
HEATING
150
200
250
300
350
400
450
500
TEMPERATURE (°C)

Fig 4

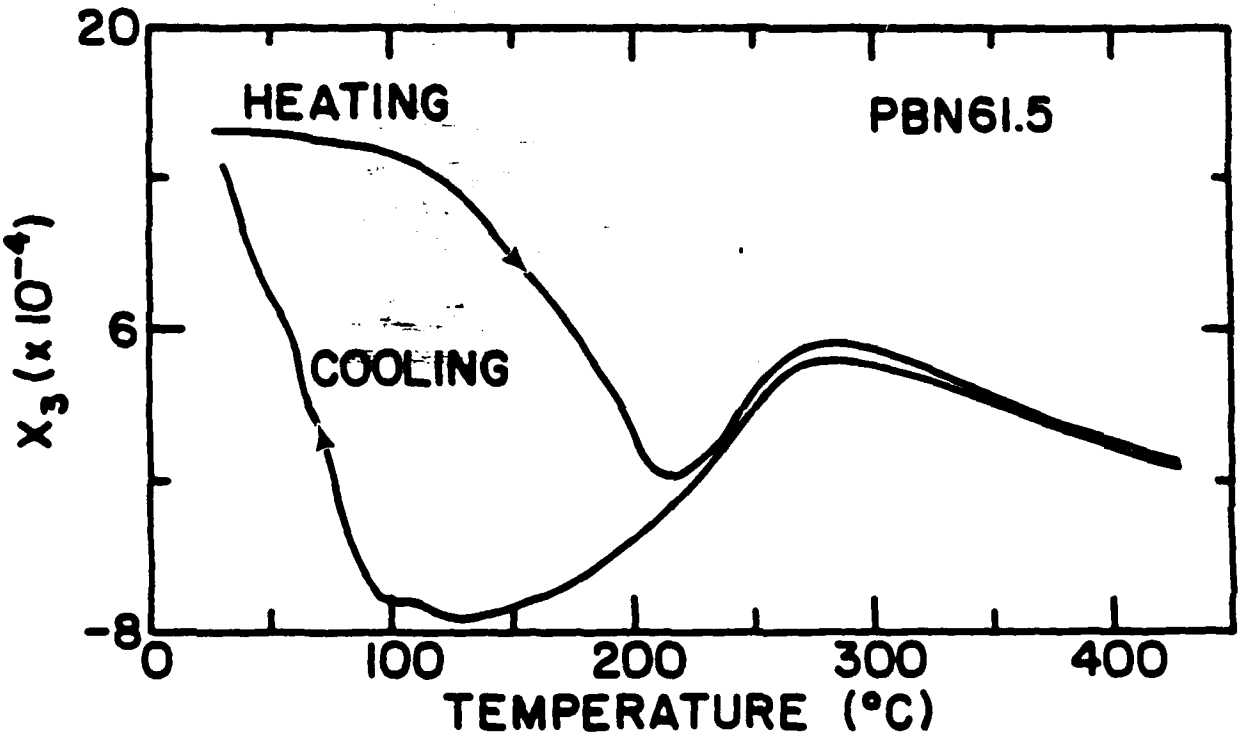
20
6
-8
HEATING
PBN61.5
COOLING
X_3 ($\times 10^{-4}$)
0
100
200
300
400
TEMPERATURE (°C)

Fig 5

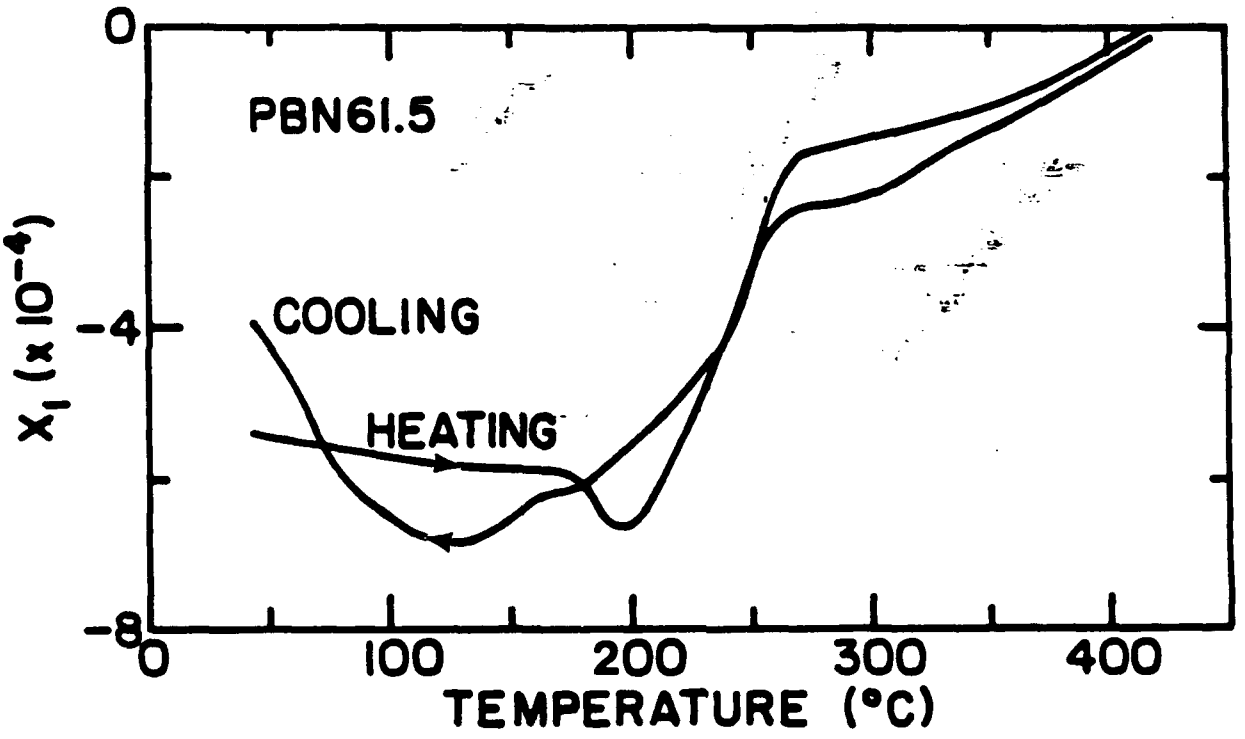
0
-4
-8
PBN61.5
COOLING
HEATING
X_1 (x 10^{-4})
0
100
200
300
400
TEMPERATURE (°C)

Fig 5 (c
C...
R-5

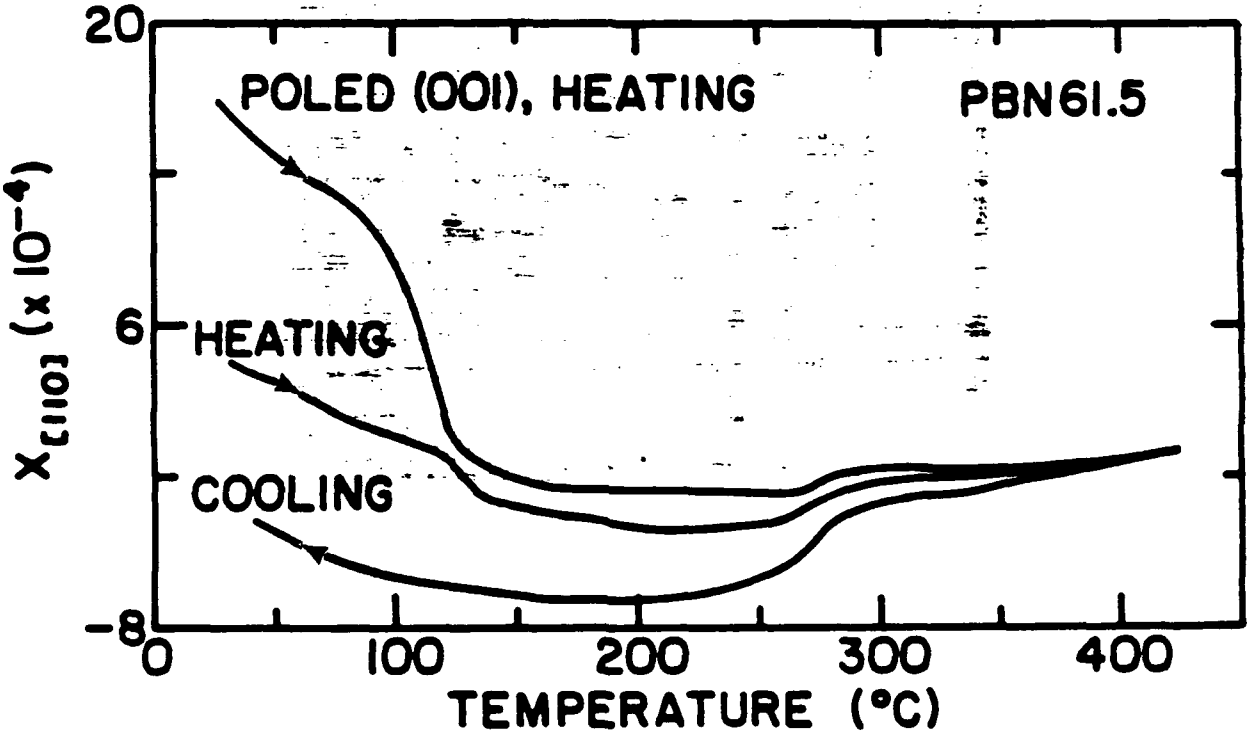
POLED (001), HEATING
PBN61.5
HEATING
COOLING
20
6
-8
0
100
200
300
400
TEMPERATURE (°C)
$x_{[110]}$ (x 10^{-4})

Fig 5(c)

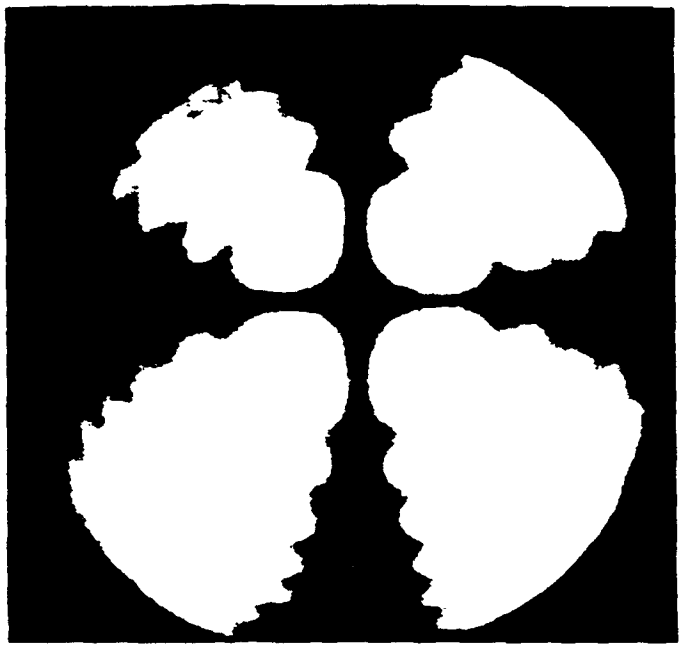

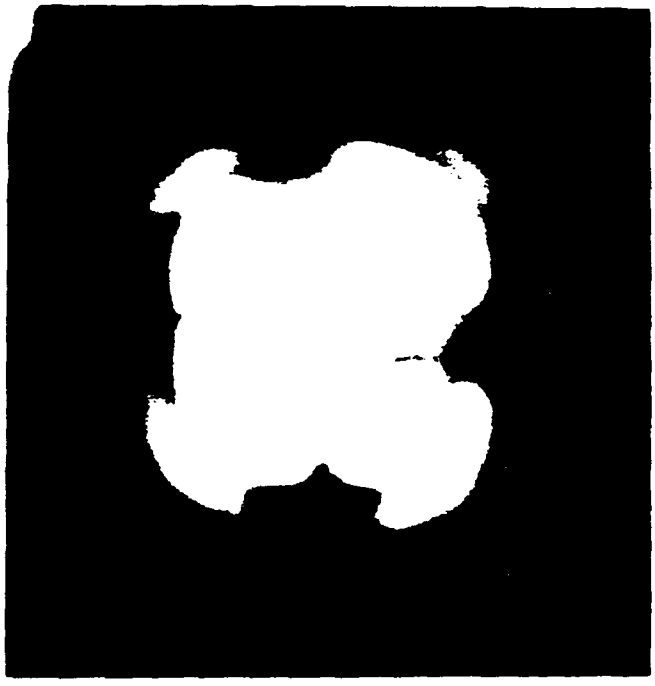

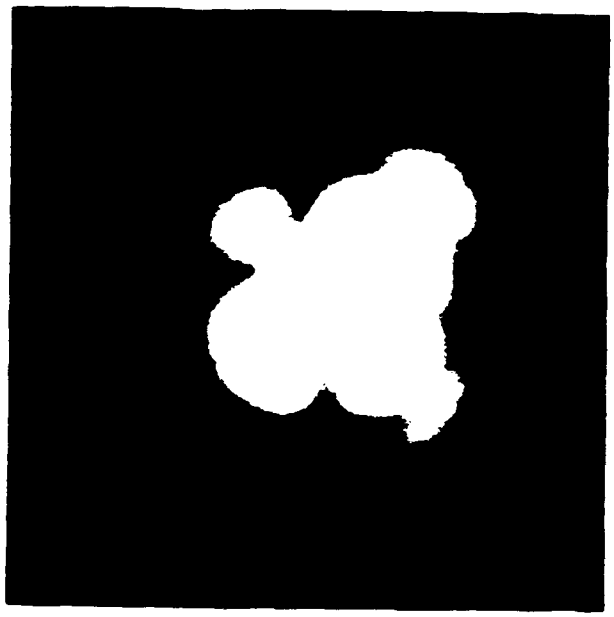

a.

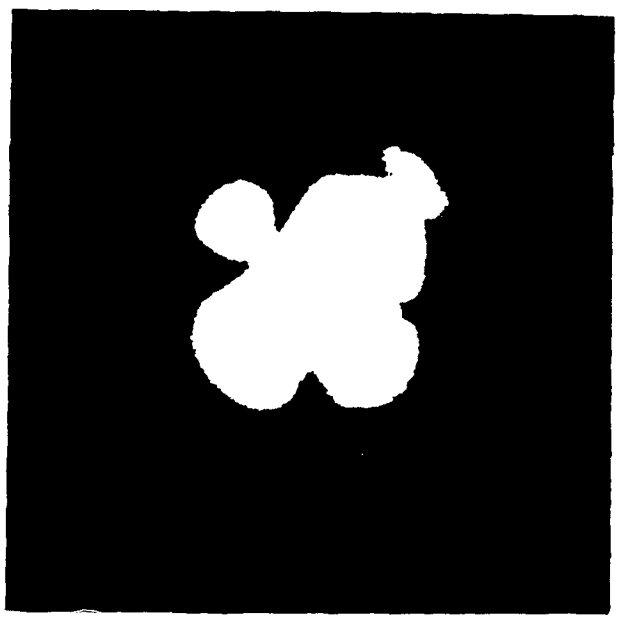

b

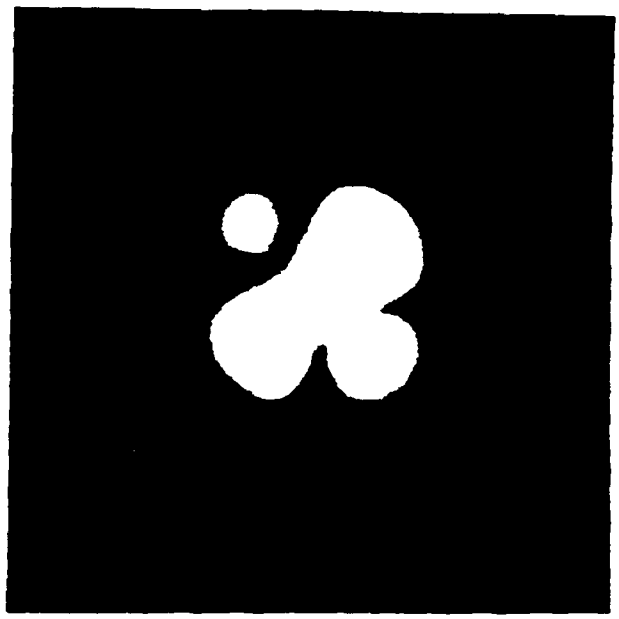

c

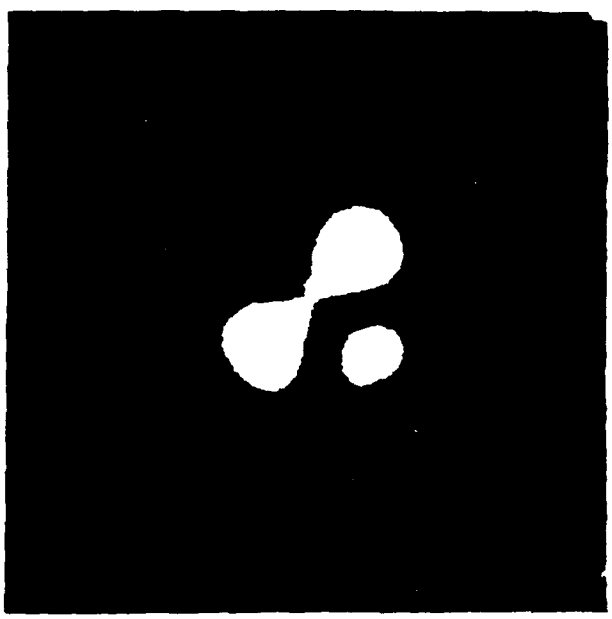

d

DF
0·1 μ

Fig 3

Fig 2

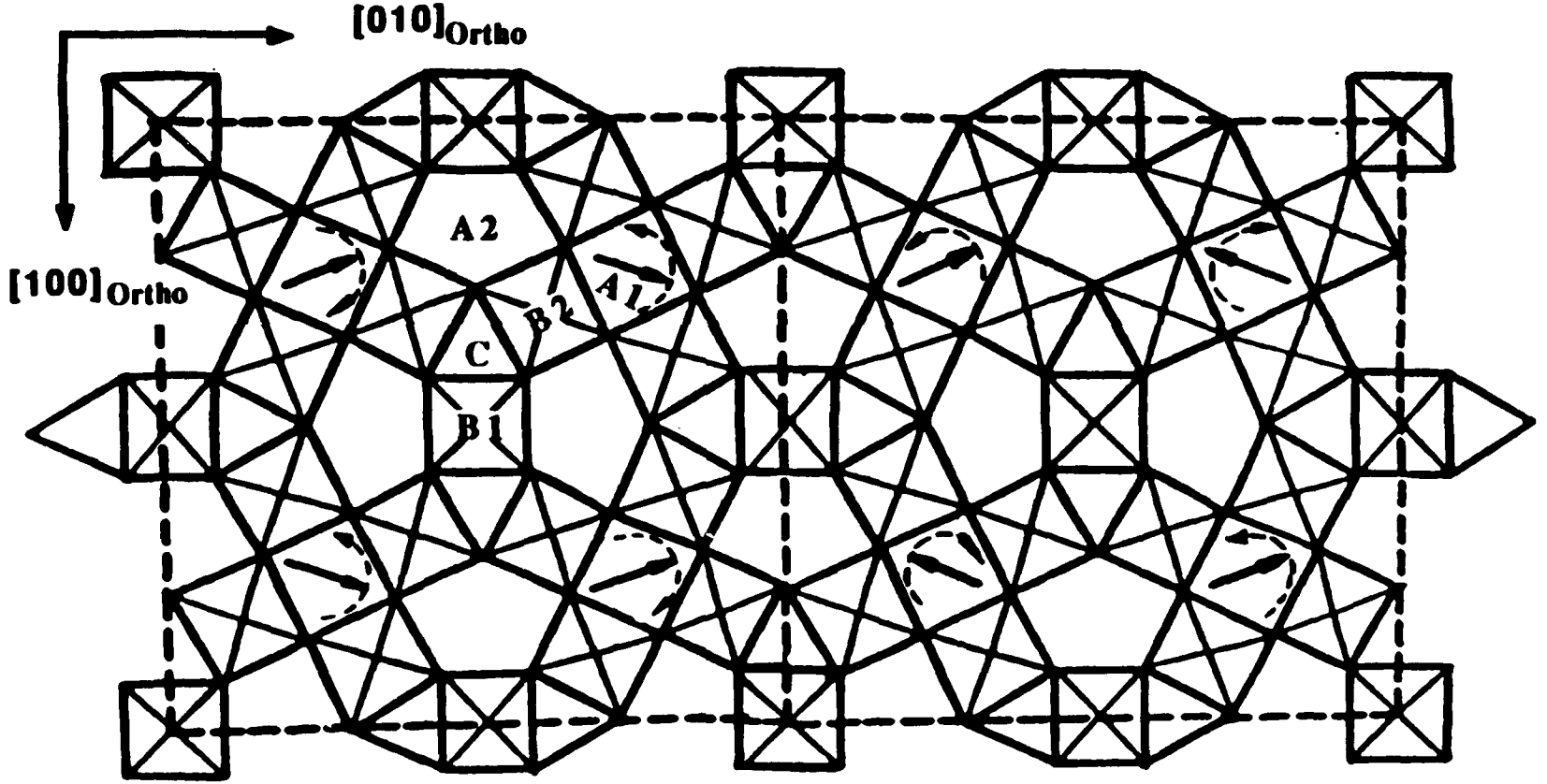
[010]Ortho
[100]Ortho
A2
A1
B2
C
B1

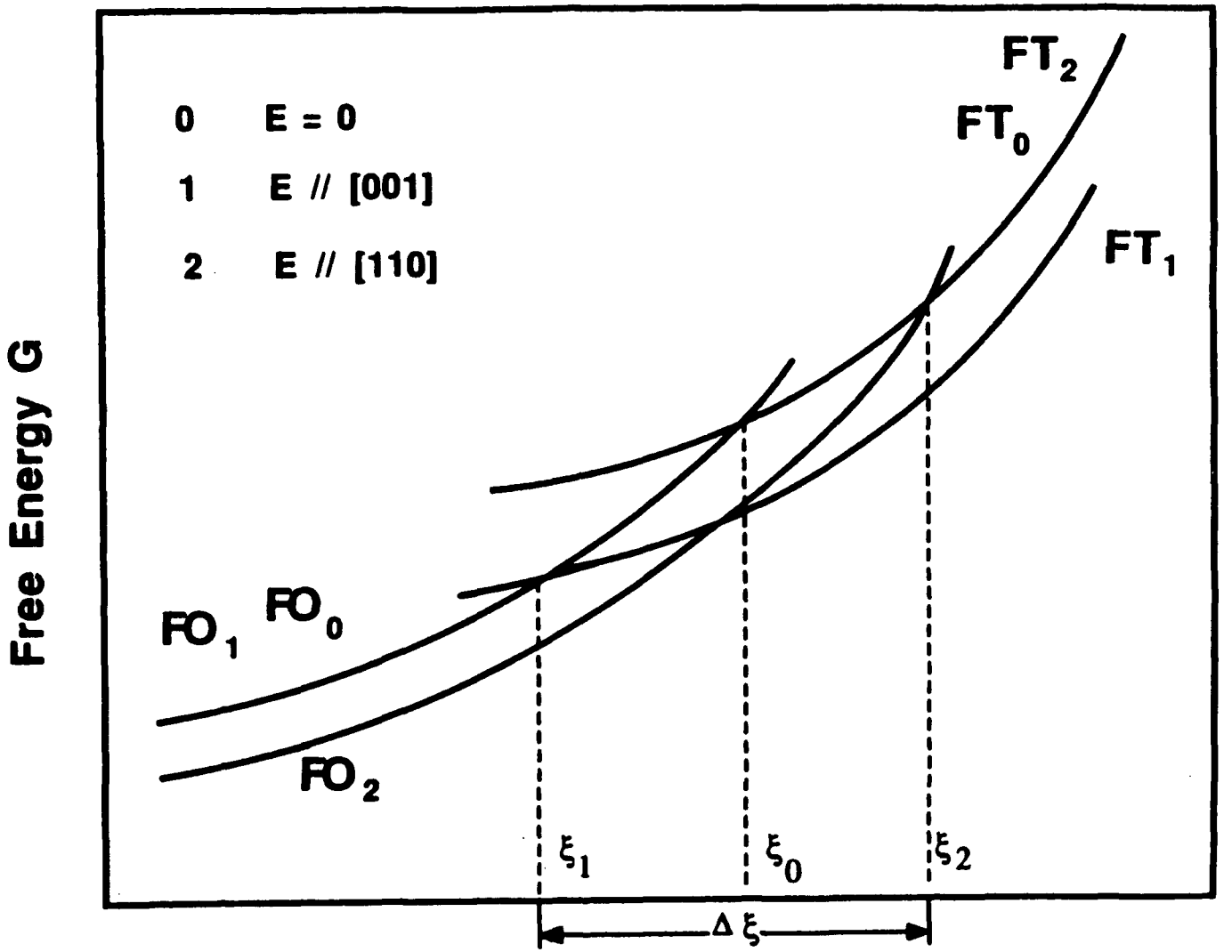
0 E = 0
1 E // [001]
2 E // [110]
FT2
FT0
FT1
FO1 FO0
FO2
ξ1
ξ0
ξ2
Δ ξ
Free Energy G
Composition (mol % of Pb)

APPENDIX 6

FABRICATION OF OPTICALLY TRANSPARENT LEAD MAGNESIUM NIOBATE POLYCRYSTALLINE CERAMICS USING HOT ISOSTATIC PRESSING

N. C. Kim
D. A. McHenry
S. J. Jang
T. R. Shrout

J. Am. Ceram. Soc., 73 [0] 000-000 (1990)

Fabrication of Optically Transparent Lead Magnesium Niobate Polycrystalline Ceramics Using Hot Isostatic Pressing

Namchul C. Kim,* Dean A. McHenry,* Sel-Joo J. Jang,* and Thomas R. Shrout*

Materials Research Laboratory, The Pennsylvania State University, University Park, Pennsylvania 16802

The physical, dielectric, and optical properties of hot isostatically pressed lead magnesium niobate polycrystalline ceramics modified with ½ mol% La_2O_3, $Pb_{1-3/2x}La_x\square_{x/2}(Mg_{1/3}Nb_{2/3})O_3$, have been investigated. Methods used to characterize the ceramics included determination of the dielectric permittivity, optical transmittance, and refractive index dispersion. The materials exhibited relaxor ferroelectric type behavior with a peak dielectric constant $K > 14000$ and average $T_c \sim -35$°C. Various sintering, hot isostatic pressing, and annealing conditions were examined to produce highly dense and optically transparent materials. Through the use of hot isostatic pressing, densities more than 99.5% theoretical and transmittance greater than 50% at 633-nm wavelength were obtained. Hot isostatic pressing technique appears to be a good alternative to hot uniaxial pressing without the associated problem of PbO volatility, reactivity with the pressure vessels, and geometrical constraints. [Key words: hot isostatic pressing, niobates, lead, optical materials, polycrystalline materials.]

I. Introduction

The ferroelectric relaxor lead magnesium niobate $Pb(Mg_{1/3}Nb_{2/3})O_3$, hereafter designated PMN, was first investigated by soviet workers in the late 1950's.[1] Since that time, PMN and its solid solution with $PbTiO_3$ have been extensively studied for various applications such as multilayer capacitors,[2] electrostrictive actuators,[3-5] piezoelectric transducers,[7] and pyroelectric bolometers.[8] These applications are based on the exceptionally superior dielectric and electrostrictive properties exhibited by these materials.[3,4]

Relaxor ferroelectrics, such as PMN-based materials, are characterized by a diffuse paraelectric–ferroelectric phase transition due to effects related to compositional micro inhomogeneity,[9-11] resulting in a broad Curie range rather than a distinct Curie temperature in the dielectric behavior. In addition, the position of the dielectric constant maxima versus temperature curve is strongly frequency dependent in the radio frequency range, being shifted towards higher temperature with increasing frequency as shown in Fig. 1.

Recently, PMN-based relaxor ferroelectrics prepared by hot uniaxial pressing (HUP)[12] have been investigated for possible use in electrooptic applications. Their good electrooptic response, fast switching time, and low half-wave voltage, $V_{1/2}$[13,14] make these materials viable alternatives to the (Pb,La)(Zr,Ti)O_3 (PLZT) compositions conventionally used in electrooptic devices such as optical shutters, modulators, displays, color filters, and image storage devices.[15-18] In addition to their device potential, optical property measurements on relaxors can generate information concerning the onset and degree of polarization of microdomains, leading to a better understanding of their diffuse dielectric behavior.[19]

In the utilization of HUP, however, the highly volatile and reactive nature of PbO with the pressure vessel (rams, dies, etc.) generally requires the addition of excess PbO, which results in nonuniform grain growth and dielectric aging.[20] The closed pressure vessel also effectively provides poor PbO atmosphere control, resulting in trapped PbO at the grain boundaries and triple points.[21] In addition, the pressure vessel is such that it limits the possibility of various sample geometries.

The purpose of this study was to prepare optically transparent polycrystalline ceramics of PMN by hot isostatic pressing (HIP). By first conventionally sintering PMN ceramics to closed porosity (~92% theoretical) in a well-controlled PbO atmosphere, final densification by HIP could be made without encapsulants, PbO control, or geometrical constraints. To further enhance densification and to control grain growth, a small amount of La_2O_3 (½ mol%) was added.[22] Characterization of the samples included density, dielectric, and optical property determinations.

II. Experimental Procedure

(1) Sample Preparation

Polycrystalline ceramic samples with the formula $(Pb_{1-3/2x}La_x)(Mg_{1/3}Nb_{2/3})O_3$ were prepared by solid-state reaction, using the appropriate amounts of high-purity (>99.99%) lead oxide (PbO), magnesium carbonate ($MgCO_3$), niobium pentoxide (Nb_2O_5), and ½ mol% of lanthanum oxide (La_2O_3). It is important to note the significance of purity, in that samples prepared using reagent-grade raw materials did not result in sufficient transparency to allow optical property measurements.

Since perovskite PMN is difficult to prepare without the appearance of undesirable pyrochlore phase(s), which can be detrimental to dielectric and optical properties, the columbite precursor method[23] was employed. As shown in Fig. 2, the preparation of PMN:La consisted of two stages; the columbite, $MgNb_2O_6$, was first synthesized and then mixed with stoichiometric amounts of PbO and La_2O_3 to form the perovskite structure. A small amount of excess PbO (about 1 mol%) was added to compensate for PbO volatility during calcination and the preliminary sintering stage. Both the columbite and subsequent calcined PMN:La powders were examined by X-ray diffraction to ensure phase purity. Less than ~2% pyrochlore phase was observed in the calcined powder.

Disks were prepared using poly(vinyl alcohol) (PVA) binder followed by burnout. Pellets were placed on platinum foil in closed alumina crucibles and sintered at temperatures of 1100° and 1200°C for 4 h. The desired PbO-rich atmosphere was maintained by placing small amounts of an equimolar powder mixture of PbO and ZrO_2 in a small platinum boat. Once sintered, the specimens were hot isostatically pressed for 2 h at temperatures in the range of 1000° to ~1100°C in atmospheres of air or a mixture of argon/oxygen under a pressure of 3000 psi (20 MPa) using a HIP system* schematically shown in

G. Haertling—contributing editor

Manuscript No. 198291. Received July 3, 1989; approved October 20, 1989.
*Member, American Ceramic Society.

*Model HIP 3000, Leco Co., St. Joseph, MI.

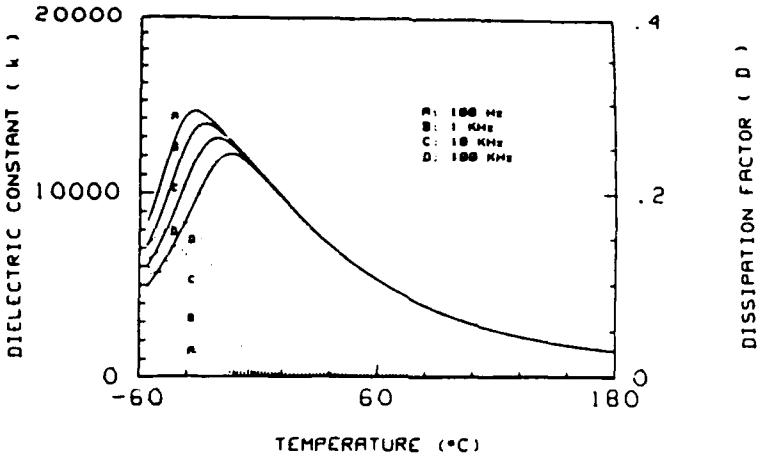

Fig. 1. Dielectric permittivity and dissipation factor of PMN:La as a function of frequency and temperature (1200°C/4 h sintered and 1100°C/2 h hot isostatically pressed in air).

Fig. 3. During HIP, no PbO control was required, as a result of the reduced volatility achieved by presintering the samples and the relatively low HIP temperatures used. To further reduce the level of PbO in the grain boundaries or triple points, samples were annealed at 900°C for 1 to 4 h.

Characterization of the hot isostatically pressed samples included determination of density using the Archimedes technique and grain size by scanning electron microscopy (SEM) of thermally etched surfaces.

(2) Dielectric Properties

The dielectric properties were determined on both sintered and hot isostatically pressed samples. Prior to the measurements, the samples were ground and electroded with sputtered gold. An air-dry silver paste was also applied on the sputtered surface to ensure good electrical contact. The dielectric measurements were carried out using an automated system consisting of a temperature control box[1] and LCR meter.[2] Relative dielectric permittivity and dissipation factor were measured pseudocontinuously at various frequencies (0.1, 1, 10, and 100 kHz) as the samples were heated from −60° to 180°C at a rate of 2° to 4°C/min. The relative degree of dielectric aging was determined by comparing the room-temperature dielectric permittivities during heating and cooling runs.

(3) Optical Transmittance

The surfaces of hot isostatically pressed ceramic samples were ground and optically polished with diamond paste to provide a mirrorlike surface. The optical transmittance was measured as a function of wavelength using a spectrophotometer[3] in the range of visible and near-IR (300- to 800-nm wavelength).

(4) Refractive Index (n)

Dispersion of the refractive index in the visible was measured by the minimum deviation method on an optical spectrometer described previously.[12] Prisms were cut and polished from the hot-pressed pellets and had apex angles of approximately 20°. After optical polishing, the prisms were annealed for 30 min at 700°C to relieve any residual polishing strains from within the samples. Several wavelengths were measured from various sources (H 486.1 and 656.3 nm, He 587.6 and 667.8 nm, and Hg 435.1 and 546.1 nm spectral lamps, HeNe

[1]Model 2300, Delta Design.
[2]Models 4274A and 4275A, Hewlett-Packard Co

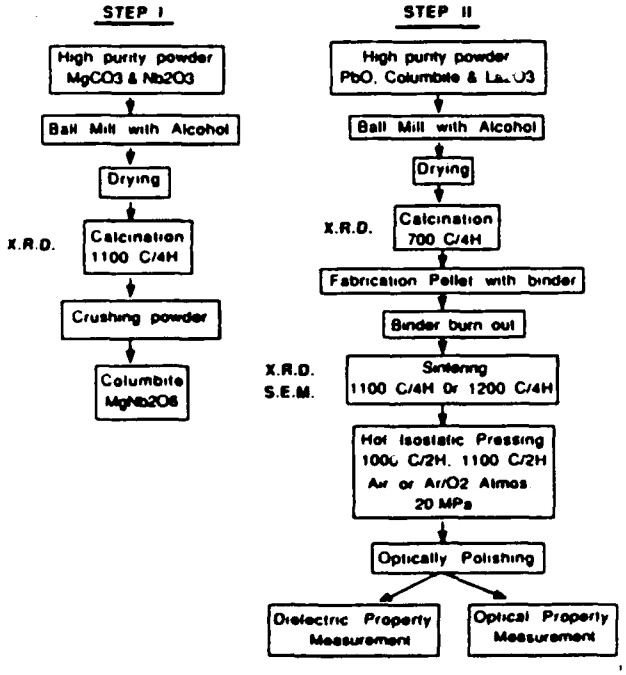

Fig. 2. Processing flow chart for the fabrication of PMN:La ceramics.

[3]2300, Cary.

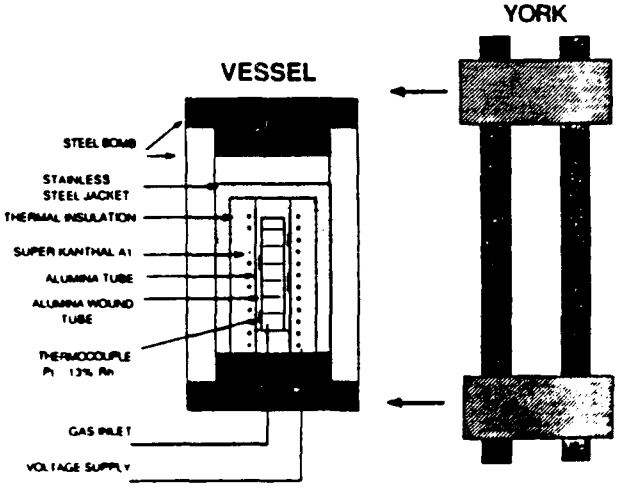

Fig. 3. Schematic representation of the HIP system.

Table I. Physical and Dielectric Characteristics of La-Modified Lead Magnesium Niobate

Sinter	HIP Conditions* Temp	Atm	Anneal	ρ (g/cm³)	% Theor.†	Grain size (μm)‡	T_c (°C at 1 kHz)	K_{max} at 1 kHz
1100°C, 4 h	1000°C, 2 h	Air		8.05	98.8	0.7–0.9	−25	10 500
1100°C, 4 h	1100°C, 2 h	Air		8.1	99.3	0.9	−25	11 000
1200°C, 4 h	1000°C, 2 h	Air		8.1	99.3	2.0–2.5	−33	13 600
1200°C, 4 h	1100°C, 2 h	Air	900°C, 1 h	8.12	99.6	2.0–2.5	−34	14 300
1200°C, 4 h	1100°C, 2 h	Ar/O_2	900°C, 1 h	8.12	99.6	2.0–2.5	−33	14 200
1200°C, 4 h	1100°C, 2 h	Air	900°C, >4 h	8.14	99.7	2.0–2.7	−35	14 800

*Hot isostatic pressing 3000 psi (20 MPa). †Theoretical density of PMN–0.01 La ~ 8.15 g/cm³. ‡Thermal etched surfaces (1000°C for 30 min).

laser (632.8 nm), and GreNe[5] laser (543 nm)). Uncertainties for the index measurements are within $\pm 3 \times 10^{-4}$.

III. Results and Discussion

(1) Physical and Dielectric Properties

The various physical and dielectric properties of La-modified PMN as a function of sintering and HIP conditions are reported in Table I. As tabulated, the density improved with increasing firing temperature. Upon HIP, the density increased from 95% theoretical density (ρ_{theo} ~ 8.15 g/cm³) for conventional sintering to more than 99.5%. Densification through HIP was similar to that achieved using HUP.[20] The densities of samples hot-pressed in air or a mixture of argon/oxygen atmosphere were similar.

Increasing the sintering temperature also resulted in grain growth. No differences in grain size before and after the HIP processing stage were observed. After HIP, the resultant average grain sizes of the samples were 0.7 to 0.9 μm for 1100°C and 2.0 to 2.5 μm for 1200°C firing, as compared to the very large (10 to 50 μm) and nonuniform grain sizes commonly found for hot uniaxially pressed PMN-based materials[20] and 2- to 10-μm grain sizes reported for PLZT.[24,25] It is believed that the small grain size and uniformity of hot isostatically pressed PMN:La ceramics are due to the addition of La, which inhibits grain growth. No explanation as to why the addition of La inhibits grain growth can be given at this time. Figure 4 shows representative microstructures of La-modified PMN ceramics.

The dielectric permittivity as a function of temperature and frequency for La-modified PMN is shown in Fig. 1. As presented, PMN:La exhibits relaxor type behavior with an average T_c ~ −35°C at 1 kHz with a maximum dielectric permittivity K > 14000. As previously reported, La has the effect of shifting T_c downward −25°C/mol%.[22] As presented in Table I, T_c was found to be higher for samples with relatively small grain sizes, reflecting a more diffuse phase transition. The dielectric permittivity was found to increase with increasing grain size. The grain size dependency of both T_c and K has been observed for other relaxor systems.[26] Upon HIP, the relative dielectric permittivity further increased because of the elimination of porosity. Post hot isostatically pressed annealing also enhanced the dielectric permittivity. It is believed that excess PbO exists in the grain boundaries and affects dielectric constant. In terms of aging, little if any was observed, unlike that found for hot uniaxially pressed samples.[20]

(2) Transmittance

The primary objective of the present work was the optical transparency. The transparency of ceramics as a function of sintering and HIP conditions is presented in Table II. As reported, conventionally sintered samples (at 1100°C) were not optically transparent. However, after HIP, the specimens were transparent enough to measure optical properties (see Figs. 5 and 6). The optical transmittance was found to increase with increasing firing and HIP temperature. In this work, the specimens which were fired at 1200°C and then hot isostatically pressed at 1100°C showed relatively high transmittance (more than 50%, for thicknesses of less than 0.3 mm at 632.8-nm wavelength). As shown in Fig. 7, if one takes into account surface reflection, according to the Fresnel formula, $R = (n-1)^2/(n+1)^2$, where R is the reflection coefficient in air from a single surface at normal incidence of light and n is the index of refraction, the transmittance is effectively even higher, being comparable to that of hot uniaxially pressed specimens[12–14] and PLZT.[15,16] The atmosphere, air or a mixture of argon/oxygen, used for the HIP process did not appear to significantly affect sample transparency. However, annealing after HIP was found to improve the optical transmittance. It appears that the amorphous grain-boundary phase, believed to be PbO-based, affects transparency. The measured optical transmittances as a function of wavelength from 300 to 800 nm are shown in Fig. 6. For most of these materials, the intensity of the transmitted light begins to increase abruptly at just below 380 nm (the absorption edge is near

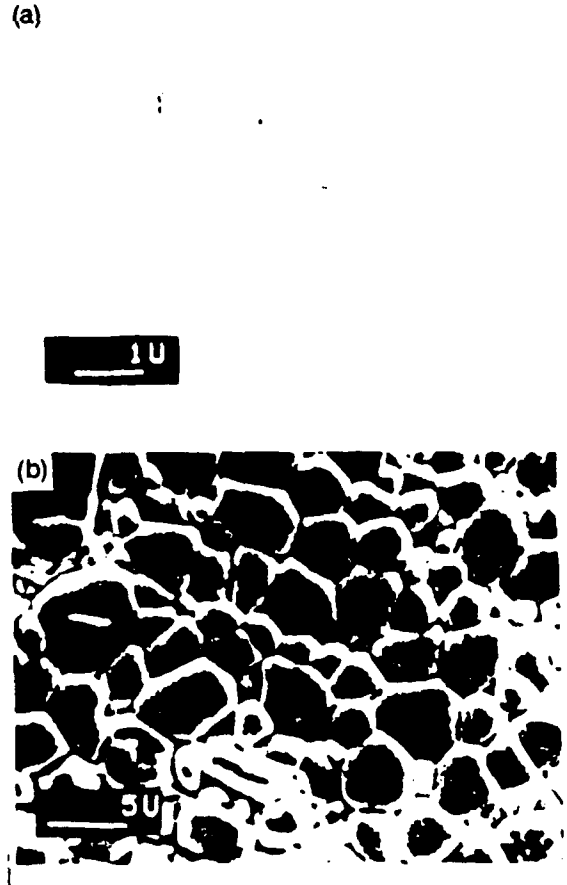

Fig. 4. Microstructure of PMN:La ceramics polished and thermally etched at 1000°C for 30 min: (a) 1100°C/4 h sintered and 1100°C hot isostatically pressed; (b) 1200°C/4 h sintered and 1100°C hot isostatically pressed.

[5]Melles Griot Co., Carlsbad, CA.

Table II. Optical Transmittance of La-Modified Lead Magnesium Niobate

Sinter	HIP conditions* Temp	Atm	Anneal	Optical transmittance†
1100°C, 4 h	1100°C, 2 h	Air		
1100°C, 4 h	1100°C, 2 h	Air		21%, 0.2 mm thick
1200°C, 4 h	1000°C, 2 h	Air		27%, 0.38 mm thick
1200°C, 4 h	1100°C, 2 h	Air	900°C, 1 h	44%, 0.32 mm thick
1200°C, 4 h	1100°C, 2 h	Ar/O_2	900°C, 1 h	37%, 0.34 mm thick
1200°C, 4 h	1100°C, 2 h	Air	900°C, 4 h	45%, 0.37 mm thick

*Hot isostatic pressing 3000 psi (20 MPa). †632.8-nm wavelength and uncorrected for reflection loss.

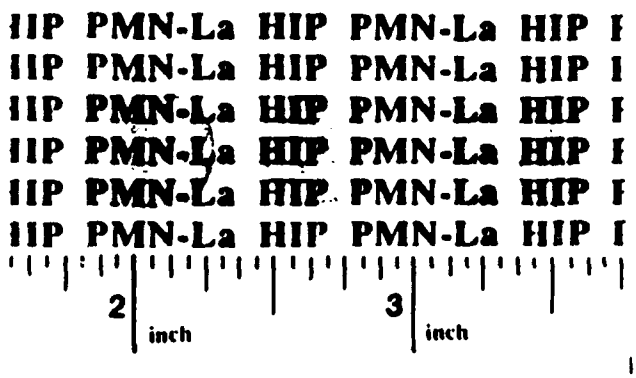

Fig. 5. Transparency of polished plates of hot isostatically pressed PMN:La (plates from left to right are 0.27, 0.32, and 0.2 mm thick).

376 nm) and then increases gradually at wavelengths above 450 nm. This gradual increase in transmittance continues into the near-IR without any noticeable absorption bands being observed as in PLZT.[15–17] However, specimens sintered at 1100°C and then hot isostatically pressed (20 MPa, 1000°C for 4 h in air) showed an abnormal transmittance curve (Fig. 6), which indicates that scattering or absorption of the incident light strongly dominated in the range of shorter visible wavelengths in the fine grain size (~0.9 μm) specimens. As reported in Table II and shown in Fig. 6, the measured optical transmittance varied with specimen bulk density and grain size. As with PLZT, grain boundaries, porosity, and impurities at which scattering or absorption of light occurs affect the overall optical transmittance.[17,18]

(3) *Refractive Index (n) Dispersion*

A representative refractive index dispersion curve for PMN:La ceramic prisms is shown in Fig. 8. Refractive index dispersion data below the band gap have been shown to be effectively described by a single-term Sellmeier oscillator equation[27]

$$n^2 - 1 = \frac{S_o\lambda_o^2}{\left(1 - \frac{\lambda_o^2}{\lambda^2}\right)} = \frac{E_dE_0}{E_o^2 - E^2} \quad (1)$$

where λ and E are the wavelength and energy of the incident light, respectively. E_o and λ_o are averaged oscillator positions characteristic of the material and related to its optical band gap. An averaged oscillator strength, S_o, accounting for all the optical interband transitions in the energy band structure and a parameter, E_d, known as the dispersion energy are also defined in Eq. (1).

The parameters in Eq. (1) can be obtained from experimental refractive index measurements by plotting $1/(n^2 - 1)$ vs $1/\lambda^2$. Figure 9 is the appropriate plot for our data. Tabulated Sellmeier parameters are given in Table III for PMN:La ceramics as well as for single-crystal PMN. It can be seen that the parameters for our ceramics with only 1% La addition are not greatly different from those for pure PMN. These materials, like other Pb perovskite oxides, have large refractive indexes and are quite dispersive in the visible because they contain a dense packing of highly polarizable cations (e.g., Pb^{2+} and Nb^{5+}). The refractive index dispersion parameter, E_o/S_o, is within the predicted range of $6.0 \pm 0.5 \times 10^{-14}$ eV·m^2. Values of E_d, the dispersion energy in La-containing glasses, have been found to be considerably higher than those of other glasses.[28] This trend of increasing E_d with La addition is consistent with our refractive index measurements,

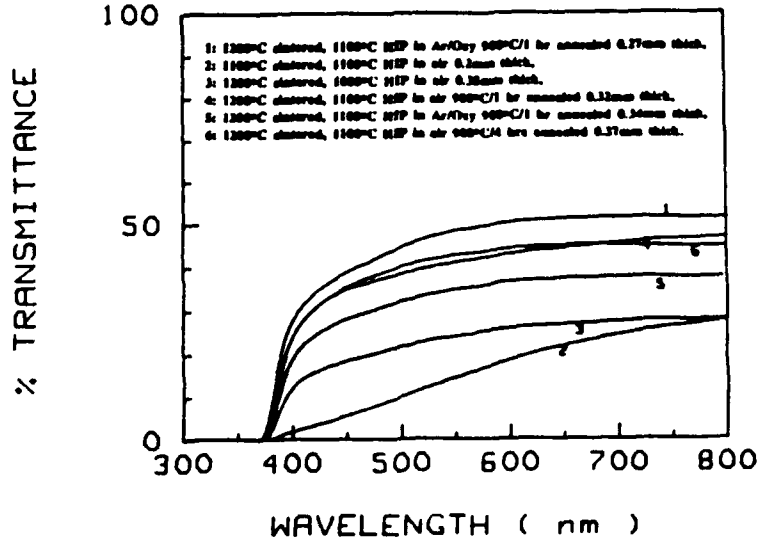

Fig. 6. Optical transmittance versus wavelength for PMN:La ceramics as a function of sintering and HIP conditions.

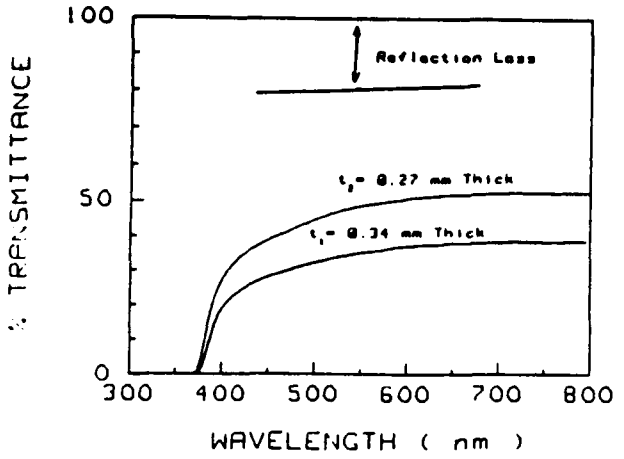

Fig. 7. Optical transmittance and reflection loss versus wavelength (1200°C sintered, 1100°C hot isostatically pressed in Ar/O_2, and 900°C/4 h annealed specimen).

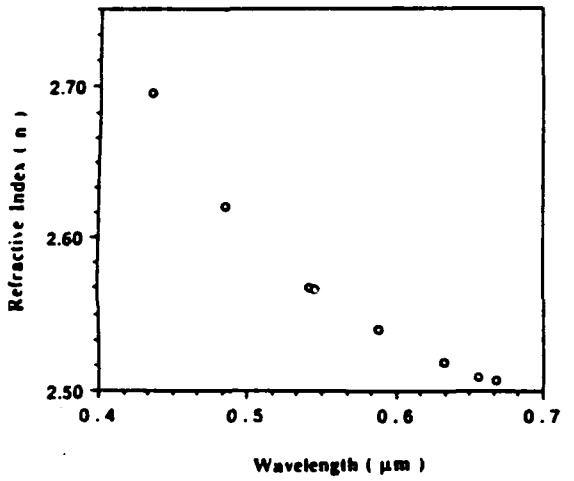

Fig. 8. Dispersion of refractive index (n) for PMN:La in the visible wavelength region.

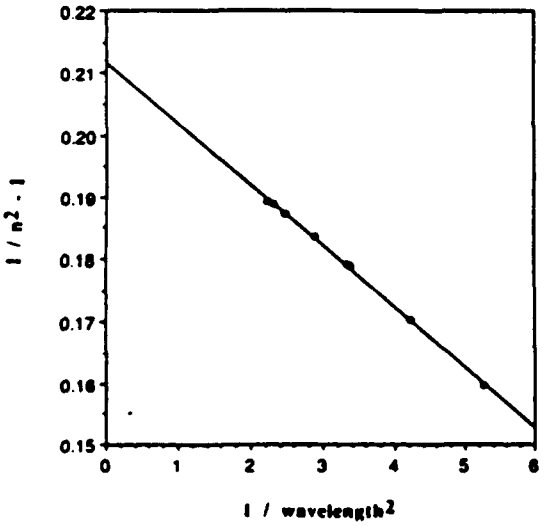

Fig. 9. Sellmeier parameters from the plot of $1/(n^2 - 1)$ versus $1/\text{wavelength}^2$ for PMN:La.

Table III. Sellmeier Refractive Index Parameters for PMN:La Ceramics and PMN (See Eq. (1))

Parameter	PMN:La	PMN*
n at 632.8 nm	2.5185	2.5219
λ_o (μm)	0.2152	0.216
S_0 ($\times 10^{14}$ m^{-2})	1.020	1.013
E_o (eV)	5.76	5.73
E_d (eV)	27.27	27.22
E_o/S_o ($\times 10^{-14}$ eV·m^2)	5.64	5.66

*Reference 29.

although higher La doping levels will be needed to confirm it more substantially.

IV. Summary

By the use of hot isostatic pressing (HIP), La-modified PMN polycrystalline ceramics have shown more than 99.5% theoretical density and fine grain size (0.7 to 0.9 μm for 1100°C, 2.0 to 2.5 μm for 1200°C sintered) without the associated problem of PbO volatility, reactivity with the pressure vessel (rams, die, etc.), and the geometrical constraints as compared with samples prepared by hot uniaxial pressing. Also, the addition of La promotes densification and inhibits grain growth during sintering.

The relative dielectric permittivity of the samples prepared by HIP increased because of the removal of porosity. The addition of La shifted the transition temperature (T_c) to lower temperatures (20° to 25°C/mol% of La) without affecting the relaxor type ferroelectric behavior as reported in previous work.

Optically polished thin plates of hot isostatically pressed PMN:La polycrystalline ceramics have shown more than 50% transmittance in the visible and near-IR region, and a high refractive index ($n > 2.7$ for wavelength < 430 nm), being comparable with that of PLZT ceramics.

Acknowledgments: The authors would like to express their gratitude to the following people for their contributions to this research effort: G. Shawver for assisting in the HIP process, J. R. Giniewicz for optical polishing, and B. Jones for sample preparation.

References

[1]G. A. Smolenskii and A. I. Agranovuskaya, "Dielectric Polarization of a Number of Complex Compounds," *Sov. Phys.—Solid State (Engl. Transl.)*, 1, 1429–37 (1959).

[2]T. R. Shrout and A. Halliyal, "Preparation of Lead-Based Ferroelectric Relaxor for Capacitor," *Am. Ceram. Soc. Bull.*, 66 [4] 704–11 (1987).

[3]S. J. Jang, "Electrostrictive Ceramics for Electrostrictive Applications"; Ph.D. Thesis. Pennsylvania State University, University Park, PA, 1979.

[4]S. J. Jang, K. Uchino, S. Nomura, and L. E. Cross, "Electrostrictive Behavior of Lead Magnesium Niobate Based Ceramic Dielectrics," *Ferroelectrics*, 27, 31–34 (1980).

[5]K. Uchino, "Electrostrictive Actuators: Materials and Applications," *Am. Ceram. Soc. Bull.*, 65 [4] 647–52 (1986).

[6]K. Uchino, S. Nomura, L. E. Cross, R. E. Newnham, and S. J. Jang, "Electrostrictive Effect in Perovskites and Its Transducer Applications," *J. Mater. Sci.*, 16, 569–78 (1981).

[7]S. Takahashi, A. Ochi, M. Yonezawa, T. Yano, T. Hamatsuki, and I. Fukui, "Internal Electrode Piezoelectric Ceramic Actuator," *Ferroelectrics*, 50, 181–90 (1983).

[8]R. E. Whatmore, P. C. Osbond, and N. M. Shorrocks, "Ferroelectric Materials for Thermal IR Detectors," *Ferroelectrics*, 76, 351–67 (1987).

[9]N. Setter and L. E. Cross, "The Role of B-site Cation Disorder in Diffuse Phase Transition Behavior on Perovskite Ferroelectrics," *J. Appl. Phys.*, 51 [8] 4356–60 (1980).

[10]L. E. Cross, "Relaxor Ferroelectrics," *Ferroelectrics*, 76, 241–67 (1987).

[11]G. Schmidt, "Diffusive Phase Transition," *Ferroelectrics*, 78, 199–206 (1988).

[12]D. McHenry, J. Giniewicz, S. J. Jang, A. Bhalla, and T. R. Shrout, "Optical Properties of Hot-Pressed Relaxor Ferroelectrics"; to be published in *Ferroelectrics*.

[13]D. McHenry, J. Giniewicz, S. J. Jang, T. R. Shrout, and A. S. Bhalla, "Electrical and Optical Properties of Relaxor Ferroelectrics" to be published in *Ferroelectrics*.

[14]D. McHenry, J. R. Giniewicz, S. J. Jang, T. R. Shrout, and A. S. Bhalla, "Optical and Electro-Optical Properties of Lead Magnesium Niobate-Lead

Titanate"; to be published in *Ferroelectrics*.

[15]G. H. Haertling and C. E. Land, "Hot-Pressed (Pb,La)(Zr,Ti)O_3 Ferroelectric Ceramics for Electrooptic Applications," *J. Am. Ceram. Soc.*, 54 [1] 1–11 (1971).

[16]G. H. Haertling, "Improved Hot-Pressed Electrooptic Ceramics in the (Pb,La)(Zr,Ti)O_3 System," *J. Am. Ceram. Soc.*, 54 [6] 303–309 (1971).

[17]R. C. Buchanan, Ceramic Materials for Electronics; pp. 154–222. Marcel Dekker, New York, 1986.

[18]L. M. Levinson, Electronic Ceramics Properties, Devices, Applications; pp. 371–492. Marcel Dekker, New York, 1987.

[19]G. Burns, "Crystalline Ferroelectrics with a Glassy Polarization Phase," *Phase Transitions*, 5, 261–76 (1983).

[20]J. Giniewicz, D. McHenry, S. J. Jang, and T. R. Shrout, "Hot Pressing of Relaxor Ferroelectrics"; to be published in *Ferroelectrics*.

[21]A. D. Hilton; Ph.D. Thesis. Essex University, U.K. 1989.

[22]N. C. Kim, W. Heubner, S. J. Jang, and T. R. Shrout, "Dielectric and Piezoelectric Properties of Lanthanum Modified Lead Magnesium Niobium–Lead Titanate Ceramics"; to be published in *Ferroelectrics*.

[23]S. L. Swartz and T. R. Shrout, "Fabrication of Perovskite Lead Magnesium Niobate," *Mater. Res. Bull.*, 17, 1245–50 (1982).

[24]K. Okazaki and K. Nagata, "Effect of Grain Size and Porosity on Electrical and Optical Properties of PLZT Ceramics," *J. Am. Ceram. Soc.*, 56 [2] 82–86 (1973).

[25]I. Matsuyama and S. Jyomura, "Grain Size Dependence of Optical Transmission in 7.6/70/80 PLZT," *J. Am. Ceram. Soc.*, 58 [7–8] 347–48 (1975).

[26]D. N. Huang, Z. W. Yin, and L. E. Cross, "Electrical Properties of Grain Growth PLZT Ceramics"; to be published in *Ferroelectrics*.

[27]M. DiDomenico, Jr., and S. H. Wemple, "Oxygen-Octahedra Ferroelectrics. I. Theory of Electro-Optical and Nonlinear Optical Effects," *J. Appl. Phys.*, 40 [2] 720–34 (1968).

[28]S. H. Wemple, "Refractive-Index Behavior of Amorphous Semiconductors and Glasses," *Phys. Rev. B: Solid State*, 7 [8] 3767–77 (1973).

[29]O. Yu Korshunov, P. A. Markovin, and R. V. Pisarev, "Refraction of Light in $PbMg_{1/3}Nb_{2/3}O_3$: A Ferroelectric with Diffuse Phase Transition," *Sov. Phys.— Solid State Engl. Transl.*, 25 [7] 1228–31 (1983).

APPENDIX 7

OPTICAL PROPERTIES OF HOT PRESSED RELAXOR FERROELECTRICS

D. A. McHenry
J. Giniewicz
S. J. Jang
A. Bhalla
T. R. Shrout

Ferroelectrics, 1989, Vol. 93, pp. 351–359
Reprints available directly from the publisher
Photocopying permitted by license only

© 1989 Gordon and Breach Science Publishers S.A.
Printed in the United States of America

OPTICAL PROPERTIES OF HOT PRESSED RELAXOR FERROELECTRICS

D. A. MCHENRY, J. GINIEWICZ, S. J. JANG, A. BHALLA and T. R. SHROUT

Materials Research Laboratory, The Pennsylvania State University, University Park, PA 16802 USA

(Received August 29, 1988)

The optical properties of hot pressed transparent ceramics based on the relaxor ferroelectric (1-x)Pb($Mg_{1/3}$,$Nb_{2/3}$)O_3-xPbTiO_3 (known as PMN-PT) solid solution system have been examined in the visible region. We report transmission as a function of wavelength, refractive indices as a function of temperature and wavelength, and quadratic electro-optic coefficient data for the 632.8 nm HeNe laser wavelength. For our particular ceramic compositions, .93($Pb_{0.99}La_{0.01}$)($Mg_{1/3}$,$Nb_{2/3}$)O_3-.07PbTiO_3 and .90 PMN-.10 PT, the refractive index dispersion is well described by a single term Sellmeier equation. The observed temperature dependence of the refractive indices $n(T)$ can be discussed in terms of polar microregions which alter the refractive indices in these ceramics via the quadratic electro-optic effect. Transverse quadratic electro-optic coefficients measured were in accord with those reported for other Pb containing perovskite oxides.

INTRODUCTION

A study of the optical properties of transparent (1-x) Pb($Mg_{1/3}$,$Nb_{2/3}$)O_3-xPbTiO_3 (hereafter PMN-PT) ceramics is of interest both for possible insight into the physical nature of relaxor ferroelectrics as well as for making practical extension of its several present applications to include usage in electro-optic devices. Present applications take advantage of (1-x) PMN-xPTs singularly excellent dielectric, low thermal expansion, and electrostrictive properties.[1,2] Ceramics with the composition .90 PMN-.10 PT have been used in surface deformable mirror technology and unlike $Pb_{1-x}La_x(Zr_yTi_{1-y})O_3$ (PLZT x/y/1-y) can be prepared as a stoichiometric "fully-stuffed" compound without aliovalent defects and concomitant dielectric aging effects.[3]

PMN is the classic example of a relaxor ferroelectric. It has the perovskite structure with Pb^{2+} ions on the cation A-site and Mg^{2+} and Nb^{5+} ions in a disordered setting for the cation B-site. This disorder is believed to lead to "glassy" polarization behavior observable in the temperature dependence of the refractive index.[4] The weak field dielectric permittivity as a function of temperature exhibits a broad frequency dependent (i.e., dispersive) maximum characteristic of a diffuse phase transition. Studies of the optical birefringence have revealed that PMN samples when cooled to low temperatures evidence no optical anisotropy which would be indicative of a macro-volume change to a polar phase.[5] The quadratic polarization-optic coefficients which have been reported ($g_{11} - g_{12} = .015$ m^4/C^2 and $g_{44} = .008$ m^4/C^2) are not very temperature dependent and are about an order of magnitude smaller than those of non-Pb-containing oxygen-octahedra ferroelectrics.[6] It is believed that Pb^{2+} ions on the A-site cause high refractive indices

and lowered g coefficients. The refractive index dispersion and its temperature dependence have also been reported.[7,8]

$PbTiO_3$ is also a perovskite ferroelectric but in contrast to PMN it undergoes a displacive first order phase transition at about 492°C. Optically, $PbTiO_3$ is uniaxial negative, has high refractive indices, and possesses an anomalous birefringence increase which disappears prior to the ferroelectric–paraelectric phase transition. $PbTiO_3$ is a good non-linear optical material with a large reversible polarization. $PbTiO_3$ has a value of only $g_{11} - g_{12} = +.003$ m^4/C^2 at room temperature and is unusual in this regard even among Pb perovskites.[6]

It is the purpose of this paper to report on the optical properties of two relaxor ferroelectric compositions, $.93(Pb_{0.99}La_{0.01})(Mg_{1/3}Nb_{2/3})O_3$-$.07PbTiO_3$ and .90 PMN-.10 PT. Sample preparation for these hot pressed ceramics are detailed in Reference 9 along with other physical and dielectric measurements. Lanthanum addition to PMN or PZT enhances densification and thus improves transparency. The effect of La^{3+} addition on the dielectric properties of PMN is reported in Reference 10. It will be of interest to see what effect adding small amounts of La_2O_3 and $PbTiO_3$, a normal displacive ferroelectric, to form a solid solution with a relaxor ferroelectric like PMN will have on the optical properties.

TRANSMISSION

Ferroelectric hot pressed samples to be employed in optical and electro-optical devices must be made sufficiently transparent in the visible and near IR region. Optical transmission measurements were made as a function of wavelength using a Cary 2300 spectrophotometer upon electrically unpoled optically polished plates. Figure 1(a,b) shows the measured percent transmission as a function of wavelength (300 nm–800 nm). For both of these materials the percentage of transmitted light begins to rise abruptly at just below 380 nm and then increases only gradually with wavelength above 450 nm. This gradual increase in transmittance continues into the near IR at least through 1500 nm without any noticeable absorption bands being observed. The reflection loss line is drawn in from the calculated reflection $R = (n - 1)^2/(n + 1)^2$ values using the measured refractive indices from the next section.

The .90 PMN-.10 PT hot pressed sample is especially transparent (31.7%T @ 450 nm and 57.1%T @ 680 nm). The maximum value for the dielectric permittivity in this material is $Tc \cong 45$°C at 1 KHz. Ferroelectric regions are of pseudocubic symmetry for the PMN-rich compositions in this solid solution. The $.93(Pb_{0.99}La_{0.01})(Mg_{1/3}Nb_{2/3})O_3$-$.07PbTiO_3$ composition is well into the paraelectric region at room temperature ($T_c \sim 9$°C at 1 KHz). In PLZT it has been shown that the pseudocubic 9/65/35 composition is considerably more transparent than either the rhombohedral 7/65/35 or tetragonal 12/40/60 ferroelectric compositions, especially for shorter visible wavelengths where absorption and light scattering dominate.[11] Light scattering from domain walls and grain boundary scattering will occur in La-doped PMN-PT ceramics as well and lower the optical transparency. The addition of $PbTiO_3$ to PMN seems to cause the thermal stabilization of polar

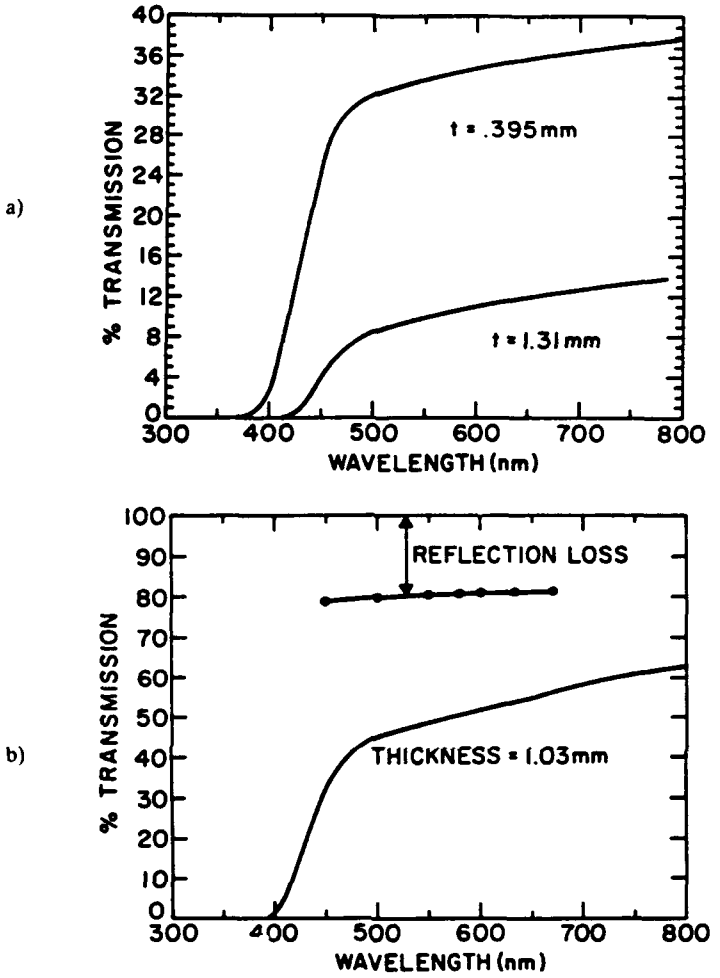

FIGURE 1 Percent transmission as a function of wavelength for hot pressed optically polished plates for ceramic compositions. a) .93($Pb_{0.99}La_{0.01}$)($Mg_{1/3}$,$Nb_{2/3}$)O_3-.07$PbTiO_3$ excess; b) .90 PMN-.10 PT.

microferroelectric regions in these ceramics. Further improvements in transparency for these ceramics may be achieved by optimizing the processing and sintering conditions.

REFRACTIVE INDEX DISPERSION

The refractive indices for several visible wavelengths were measured by the method of minimum deviation. Prisms with apex angles of between 20°–30° were cut and polished from the bulk ceramics. The prisms were then annealed for 30 min at

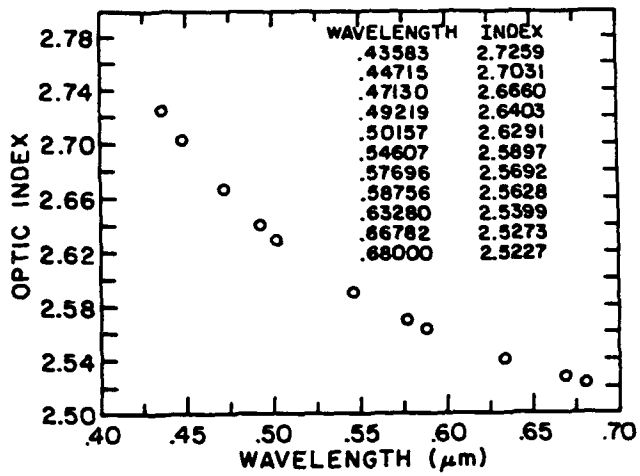

FIGURE 2 Refractive index dispersion for $.93(Pb_{0.99}La_{0.01})(Mg_{1/3},Nb_{2/3})O_3$-$.07PbTiO_3$ in the visible region.

525°C in order to relieve polishing strains. The prism apex angles and minimum deviation angles were determined using a Gaertner optical spectrometer with a smallest vernier reading of 20″. Reproducibility and calibration of the spectrometer readings lead us to estimate that errors for the reported index values are within $\pm 3 \times 10^{-4}$.

A representative dispersion curve for prisms with composition $.93(Pb_{0.99}La_{0.01})(Mg_{1/3},Nb_{2/3})O_3$-$.07PbTiO_3$ is shown in Figure 2. These polycrystalline materials clearly have a very high refractive index (>2.7 for $\lambda < 450$ nm) which is mainly attributable to their having a high density of polarizable ions such as Pb^{2+}, Ti^{4+}, and Nb^{5+}. Also, the refractive index is quite dispersive in the visible region, characteristic of the optical spectrum on the long wavelength side of UV absorption peaks. Wemple and Didomenico have shown that the dispersion of the index is frequently well described by a single-term Sellmeier dispersion formula of the form[12]

$$n^2 - 1 = \frac{S_o\lambda_o^2}{\left(1 - \frac{\lambda_o^2}{\lambda^2}\right)} = \frac{E_dE_o}{E_o^2 - E^2} = \frac{f}{E_o^2 - E^2} \tag{1}$$

where λ, E = wavelength and energy of the incident light, respectively
λ_o, E_o = average oscillatory position and energy, respectively
S_o, $f = E_oE_d$ = average oscillator strength
E_d = dispersion energy.

The Sellmeier constants in Equation (1) are determined by plotting $n^2 - 1$ vs. λ^{-2} to a straight line least squares fit. Figure 3 shows this type of plot for

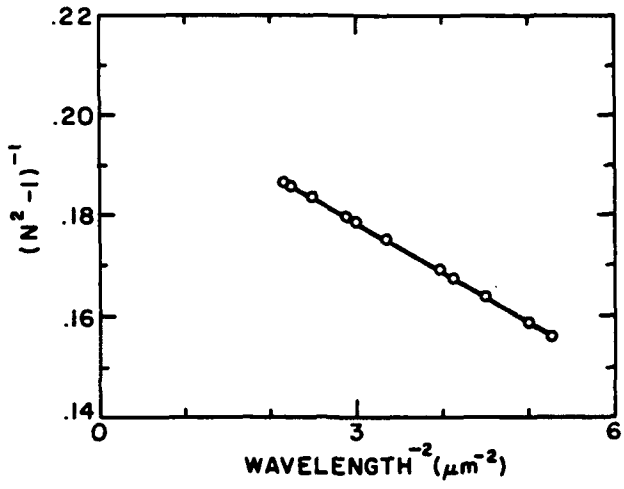

FIGURE 3 Plot of $1/n^2$-1 vs. $1/\lambda^2$ for $.93(Pb_{0.99}La_{0.01})(Mg_{1/3},Nb_{2/3})O_3$-.07$PbTiO_3$ in order to determine Sellmeier parameters.

$.93(Pb_{0.99}La_{0.01})(Mg_{1/3}Nb_{2/3})O_3$-.07$PbTiO_3$. The tabulated Sellmeier parameters for our measurements as well as for the system end members PMN and $PbTiO_3$ are given in Table I.

Addition of $PbTiO_3$ appears to 1) raise the refractive index; 2) raise the dispersion energy E_d; and 3) lower E_o (a quantity related to the energy band gap) as compared to pure single crystal PMN. The addition of small amounts of La^{3+} and associated A-site vacancies in place of the Pb^{2+} ions would be expected to lower the refractive index values. The values for $PbTiO_3$ in the table are single crystal values averaged for a ceramic index.[13]

TABLE I

Refractive index parameters for the PMN-PT system

	PMN[6]	$.93(Pb_{0.99}La_{0.01})(Mg_{1/3},Nb_{2/3})O_3$-.07$PbTiO_3$	.90 PMN-.10 PT	$PbTiO_3$[10]
n @ 632.8 nm	2.5219	2.5399	2.5455	2.688
λ_o (μm)	0.216	0.218	0.220	0.222
S_o($\times 10^{-14} m^{-2}$)	1.013	1.012	1.00	1.09
E_o (eV)	5.73	5.69	5.64	5.59
E_d (eV)	27.2	27.40	27.31	30.0
f (eV)^2	156	155.9	154	168
E_o/S_o ($\times 10^{-14}$ eV m^2)	5.66	5.62	5.64	5.13

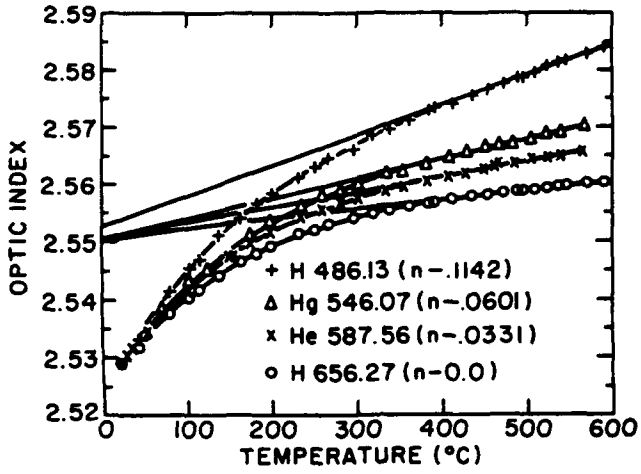

FIGURE 4 Temperature dependence of the refractive index for $.93(Pb_{0.99}La_{0.01})(Mg_{1/3},Nb_{2/3})O_3$-$.07PbTiO_3$ at four spectral wavelengths in the visible from 20°C–600°C.

REFRACTIVE INDEX TEMPERATURE DEPENDENCE

A small oven was constructed and mounted on the spectrometer to enable us to measure refractive indices in the range 20°C–600°C. Temperatures were measured using a pair of thermocouples located above and below the prisms. Control of the temperature was maintained within ±2°C for the indicated temperature readings.

The temperature dependence of the refractive index was measured at four common spectral wavelengths (H 486.13 nm, Hg 546.07 nm, He 587.56 nm, and H

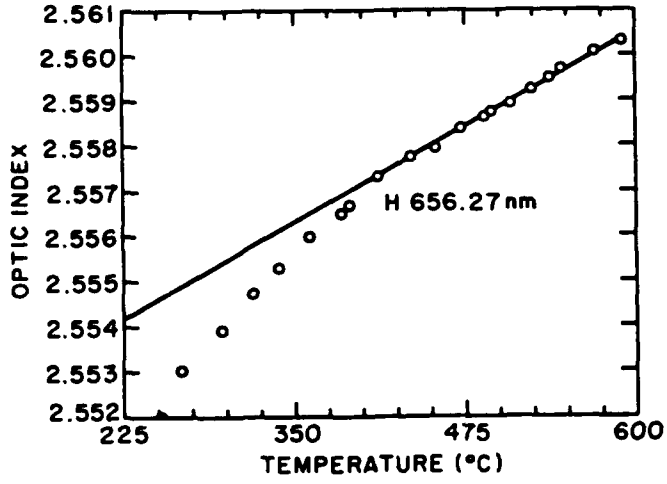

FIGURE 5 Expanded view of $n(T)$ for composition $.93(Pb_{0.99}La_{0.01})(Mg_{1/3},Nb_{2/3})O_3$-$.07PbTiO_3$ @ H 656.27 nm in order to ascertain T_d value.

656.27 nm). Figure 4 shows the measured $n(T)$ curves at the listed wavelengths for $.93(Pb_{0.99}La_{0.01})(Mg_{1/3},Nb_{2/3})O_3$-$.07PbTiO_3$. It should be noted that subtractions have been made as marked on the top three graphs in order to show all four curves on the same high resolution scale. A few features of these $n(T)$ curves should be pointed out. First, the high temperature region of the curves is given approximately by a straight line fit to the data in this region. The dn/dt values determined by the slopes of these lines increase for shorter wavelengths nearer to the energy band gap and range from 5.36×10^{-5}/°C for H 486.13 nm down to 1.69×10^{-5}/°C for H 656.27 nm. Secondly, the departure from linearity occurs at a point often called T_d[4] which is several hundred degrees above the regular Curie temperature ($Tc \cong$ 9°C). No major change in the refractive indices would then be expected to occur at T_c.

Figure 5 shows an expanded view of the H 656.27 nm curve in order to show more clearly this departure from linearity. The value of T_d was determined as being approximately 390°C for each of the four wavelengths. T_d is therefore seemingly independent of wavelength.

QUADRATIC ELECTRO-OPTIC COEFFICIENTS

The transverse quadratic electro-optic coefficients were measured using an AC Senarmont compensator method using phase sensitive lock-in amplifier detection. A HeNe laser with a 632.8 nm output was used as a light source. The values for the electro-optic coefficients as a function of temperature (20°C–250°C) were determined under low frequency (<50 KHz) unclamped conditions. At room temperature, the quadratic electro-optic coefficients in terms of polarization (polarization-optic) were, $g_{11} - g_{12} = 0.08 \pm 10\%$ m^4/C^2 and in terms of electric field $R_{11} - R_{12} = 2.25 \times 10^{-16}$ m^2/V^2 $\pm$ 10% for $.93(Pb_{0.99}La_{0.01})(Mg_{1/3},Nb_{2/3})O_3$-$.07PbTiO_3$. The electro-optic g coefficients increase weakly with temperature and level off so that an average value of $g_{11} - g_{12} \cong .012$ m^4/C^2 is found for the 20°C–250°C temperature range.[14]

DISCUSSION

The $n(T)$ behavior in relaxor ferroelectrics (as found in our samples Figures 4 and 5) is often explained as follows. At temperatures higher than T_d the refractive index is primarily controlled by thermal expansion and thus changes linearly with temperature. Below T_d, the departure from linear behavior occurs due to the presence of microregions of local polarization which causes a change Δn in the refractive index proportional to the square of the polarization by the quadratic electro-optic effect.[4,15]

For randomly oriented crystallites as found in our unpoled ceramics, the appropriate observed change in refractive index is given by[16]

$$\Delta n = \frac{\Delta n_{\parallel} + 2\Delta n_{\perp}}{3} = \frac{-(n^o)^3}{2}\left[\frac{g_{33} + 2g_{13}}{3}\right]P_d^2 \qquad (2)$$

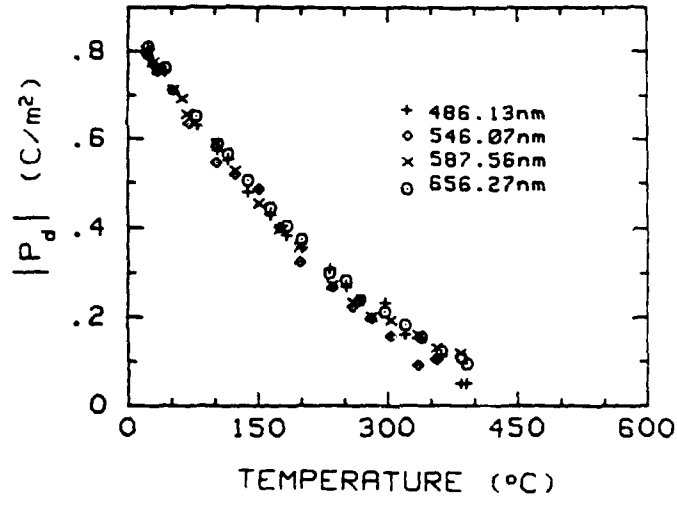

FIGURE 6 $|P_d|$ as a function of temperature for $.93(Pb_{0.98}La_{0.01})(Mg_{1/3}Nb_{2/3})O_3$-.07$PbTiO_3$ calculated from $n(T)$ data.

where n^o is the undeviated refractive index as given by the straight line, the g's are the appropriate combination of electro-optic coefficients, and P_d is the local polarization present. Since we know Δn, n^o, and can approximate the electro-optic coefficients by our measured value ($g_{11} - g_{12} \cong .012$ m⁴/C²), we can invert Equation (2) to find the magnitude of local polarization, $|P_d|$. This is shown in Figure 6 for the four wavelengths at which $n(T)$ was measured.

Temperature dependent Sellmeier parameters have also been calculated based upon the four frequency measurements of $n(T)$. From a primarily linear graph of E_o vs. T we have determined $dE_o/dT = -6.48 \times 10^{-4}$ eV/°C. This quantity represents a change in the energy of the effective oscillator which can be correlated to the temperature variation of the band gap (quite close to $dE_{gap}/dT \cong -6.7 \times 10^{-4}$ eV/°C for indirect bandgaps).[7] P_d exists to much higher temperatures and is a great deal larger than the measured reversible polarization. The comparatively large values for P_d may be due to grain boundaries in the ceramic inhibiting polarization reversal.

The value of $T_d \sim 390$°C (as shown in Figures 4 and 5) is larger than has been measured for PMN single crystals[7] with $T_d \sim 344$°C. This increased value may have been caused by the addition of $PbTiO_3$. Further studies are underway to establish the cause of such an enhancement of T_d in these ceramics compared with single crystal PMN.

SUMMARY

We have prepared hot pressed optically transparent relaxor ferroelectric samples and have measured some of the important linear optical properties. Transmission measurements verify that PMN-PT based ceramics can be made optically trans-

parent in the visible range. Refractive index dispersion has been successfully modeled by a single term Sellmeier equation. Quadratic electro-optic coefficients were measured and used to interpret the $n(T)$ behavior of these ceramic samples according to a theory of micropolar regions applicable to relaxor ferroelectrics.

Future work to follow up this investigation will include examining a further series of La^{3+} modified PMN-PT and PST hot pressed transparent ceramics for electro-optic related properties.

ACKNOWLEDGEMENTS

The authors gratefully acknowledge Frank Ainger of Plessey Co. for his guidance during the hot pressing and DARPA for their support of the Nanocomposite Project.

REFERENCES

1. S. J. Jang, Ph.D. Thesis, The Pennsylvania State University (1979).
2. S. J. Jang, K. Uchino, S. Nomura and L. E. Cross, *Ferroelectrics*, **27**, 31 (1980).
3. W. Pan, E. Furman and L. E. Cross, *Journ. Mater. Sci. Lett.*, **5**, 647 (1986).
4. G. Burns and F. Dacol, *Phase Transitions*, **5**, 261 (1985).
5. L. E. Cross, *Ferroelectrics*, **76**, 241 (1987).
6. P. D. Thatcher, *Journ. Appl. Phys.*, **41**, 4790 (1970).
7. O. Yu Korshunov, P. A. Markovin and R. V. Pisarev, *Sov. Phys. Solid State*, **25** (7), 243 (1983).
8. G. Burns and F. H. Dacol, *Solid State Commun.*, **48** (10), 853 (1983).
9. J. Giniewicz, D. A. McHenry, S. J. Jang and T. R. Shrout, ECAPD-1, ISAF '88, Paper U12, Zurich, Switzerland (1988).
10. N. Kim, S. J. Jang and T. R. Shrout, ECAPD-1, ISAF '88, Paper U9, Zurich, Switzerland (1988).
11. G. Haertling, "Electronic Ceramics: Properties, Devices, Applications," ed., L. M. Levinson, Marcel Dekker, pp. 371–492 (1987).
12. M. DiDomenico, Jr. and S. H. Wemple, *Journ. Appl. Phys.*, **40** (2), 720 (1968).
13. P. D. Thatcher, *Applied Optics*, **16**, 3210 (1977).
14. D. A. McHenry, W. Pan, Q. M. Zhang, S. J. Jang and A. S. Bhalla, Unpublished work.
15. A. S. Bhalla, R. Guo, L. E. Cross, G. Burns, F. Dacol and R. R. Neurgaonkar, *Phys. Rev. B*, **36** (4), 2030 (1987).
16. G. Burns and F. H. Dacol, *Phys. Rev. B*, **28** (5), 2527 (1983).

APPENDIX 8

CHARACTERIZATION OF (1-x)$Pb(Mg_{1/3}Nb_{2/3})O_3$ - (x)$PbTiO_3$ AND $Pb(Sc_{1/2}Ta_{1/2})O_3$ TRANSPARENT CERAMICS PREPARED BY UNIAXIAL HOT-PRESSING

J. R. Giniewicz
D. A. McHenry
T. R. Shrout
S. J. Jang
A. S. Bhalla
F. W. Ainger

CHARACTERIZATION OF (1-x)Pb(Mg1/3Nb2/3)O3 - (x)PbTiO3 AND Pb(Sc1/2Ta1/2)O3 TRANSPARENT CERAMICS PREPARED BY UNIAXIAL HOT-PRESSING

J.R. GINIEWICZ, D.A. MCHENRY, T.R. SHROUT, S.-J. JANG and A.S. BHALLA

Materials Research Laboratory, The Pennsylvania State University, University Park, PA U.S.A.

F. W. AINGER, Plessey Research (Caswell) Limited, Caswell Towcester, U.K.

Abstract Transparent relaxor ferroelectric ceramics of (1-x)Pb(Mg1/3Nb2/3)O3-(x)PbTiO3 and Pb(Sc1/2Ta1/2)O3 have been prepared by low temperature uniaxial hot-pressing. The ceramics are highly dense (> 99.5 % theor.) and transmit throughout the visible. The addition of excess PbO and La2O3 and post-pressing heat treatment are found to enhance transparency. The ceramics have been characterized for phase purity, development of microstructure, dielectric behavior and optical transmission in order to determine optimum conditions.

INTRODUCTION

Considerable interest is currently focused on the optical and electro-optical character of relaxor ferroelectric materials. The excellent electro-optic response, switching time, and half-wave voltages, $V\pi$, distinguish these materials as promising candidates for a variety of electro-optic device applications.[1] Further, optical / electro-optical property measurements on transparent relaxor compositions provide important new data useful for a more thorough understanding of the material's diffuse nature.[2,3] Transparent relaxor ferroelectric ceramics have been prepared for this investigation by hot uniaxial pressing (HUP). The ceramics have been characterized for phase purity, microstructure, dielectric behavior, and optical transmission.

SAMPLE PREPARATION AND EXPERIMENTAL PROCEDURE

Polycrystalline specimens transparent enough for optical / electro-optical measurements possessing desirable characteristics such as uniform microstructure, high density, and phase purity are not easily produced by conventional sintering methods. The samples examined in this investigation were prepared by means of hot uniaxial pressing. The powders of Pb(Mg1/3Nb2/3)O3, [PMN], (1-x)Pb(Mg1/3Nb2/3)O3 - (x)PbTiO3, [PMN-PT], (x = 0.7) and Pb(Sc1/2Ta1/2)O3, [PST] were prepared from reagent grade and optically pure starting oxides by the columbite / wolframite [4] precursor method [5] in order to produce phase - pure compositions. The compositions of interest were prepared stoichiometrically and with excess PbO and / or La2O3 as indicated in Table I so as to allow for a range of hot-press conditions and to enhance transparency.

The samples were prepared for hot-pressing in the form of disks 38 mm or 64 mm in diameter. The disks were pressed at a pressure of ≈38 MPa for 6 hours at a temperature in the range 900 °C to 1200 °C. Flowing O2 was used during the heating cycle. The specific

conditions for each sample investigated are given in Table I. The samples were embedded in coarse alumina sand to prevent reaction with the silicon nitride rams.

The uniaxially hot-pressed samples were initially characterized for phase-purity, density, and average grain size. It was determined by x-ray diffraction that all specimens were phase pure. The order parameters, Ω, of the PST specimens were also evaluated as described in the next section by means of x-ray diffraction. Sample densities as determined by the Archimedes technique and average grain size as evaluated by means of the line intercept method on scanning electron micrographs of fractured surfaces are recorded in Table I.

The samples were sliced into Top, Bottom, and Parallel sections, as shown in Figure 1, and the sections annealed in air at 900 °C for 8 hours in order to elimate excess PbO. The sample surfaces were then ground with Al2O3 grinding media and coated with a sputtered gold electrode for dielectric measurement.

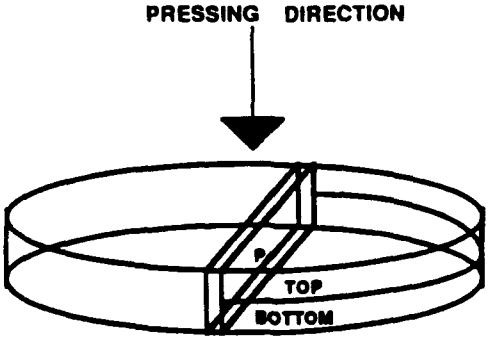

FIGURE 1 Test plates sliced from the hot uniaxially pressed ceramic.

Samples prepared for optical transmission measurement were taken as adjacent slices (arbitrary direction) from the original hot-pressed disk. One of the slices was annealed in air at 900 °C for 8 hours before it was optically polished, while the other slice was polished with no post-pressing heat-treatment. Optical transmission measurements were made on a Cary 2300 spectrophotometer.

RESULTS AND DISCUSSION

All the samples under investigation are of high density with most higher than 99.5 % theoretical density as indicated in Table I. The average grain size, as determined by the line intercept method on scanning electron micrographs of fracture surfaces, appears to depend upon the processing conditions and compositional modifications (Table I); it is observed that both excess PbO and higher hot-press temperatures encourage grain growth. In all cases, no variation in average grain size is observed with position (i.e.– top or bottom sections) within the sample. In general, the microstructures are found to be uniform with well-formed, equiaxed grains.

TABLE I Processing conditions and physical properties of test samples.

SAMPLE	PbO	La2O3	T (°C)	∂ (%theor.)	Ave Grn Size (μm)
PMN					
PMN	- -	- -	1100	99.7	2
PMN-PT					
PMNTA	- -	- -	900	99.6	2
PMNTB	- -	- -	1050	99.7	10
PMNTC	2 wt%	- -	1100	99.6	20
PMNTD	2 wt%	1 mol%	900	99.1	5
PMNTE	2 wt%	1 mol%	1100	99.6	15
PST					
PSTA	10 wt%	- -	1050	99.8	5
PSTB	2 wt%	- -	1200	98.9	5
PSTC	2 wt%	- -	1250	99.8	5

TABLE II Dielectric properties [10 KHz].

SAMPLE	SECTION	K	T (°C)	Ω	b 3/4 (°C)
PMN	T	10600	-14		62
	B	10200	-15		62
	P	11200	-15		62
PMNTA	T	14300	37		66
	B	11400	37		65
	P	15700	36		60
PMNTB	T	25000	35		35
	B	24000	34		35
	P	19100	15		57
PMNTC	T	20600	31		40
	B	21500	35		40
	P	30800	34		40
PMNTD	T	20800	13		52
	B	13900	12		58
	P	17600	15		52
PMNTE	T	17300	14		50
	B	21600	13		50
	P	25100	13		38
PSTA					
	N	6077	25	0.9	25
	P	7342	23	0.9	20
PSTB					
	N	7862	21	0.9	25
	P	7093	22	0.9	20
PSTC					
	N	8576	21	0.9	25
	P	8051	22	0.9	20

TABLE III Optical transmission.

SAMPLE	*(Anneal)	t (mm)	% Transmission 470 (nm) (blue)	560 (nm) (green)	760 (nm) (red)
PMN	Before	0.8	<1	<1	<1
	After	0.8	<1	<1	<1
	After	0.5	<1	<1	2
PMNTA	Before	0.8	<1	<1	<1
	After	0.8	<1	<1	<1
PMNTB	Before	0.9	<1	<1	<1
	After	0.9	<1	<1	<1
PMNTC	Before	0.7	2	2	3
	After	0.7	2	2	3
PMNTD	Before	0.8	<1	<1	5.6
	After	0.6	12	19	26
	After	0.5	18	35	45
PMNTE	Before	1.3	7	10	13
	After	0.9	12	17	22
	After	0.4	35	42	45
PSTA	Before	0.8	<1	2	20
	After	0.4	30	45	50
PSTB	Before	0.9	<1	<1	<1
	After	0.9	<1	<1	<1
PSTC	Before	- -	- -	- -	- -
	After	0.4	20	22	22

The dielectric response of the various samples, which have undergone post-pressing heat-treatment, at a frequency of 10 KHz is recorded in Table II. The particular slice of the sample as indicated in Figure 1 is designated by the labels T, B, and P for each specimen. The quantity (b 3/4) is a measure of the diffuseness of the permittivity as a function of temperature,[6] representing the width of K(T) at 3/4 the value of K(max). The order parameter, Ω, is relevant to the PST samples only which exhibit order / disorder variations as a function of temperature and thermal history.[6,7] It is defined by the ratio of the x-ray diffraction intensities of peaks corresponding to the normal and superstructure lattices. A completely ordered material has a value $\Omega = 1$.[7]

The dielectric response K(T) at various frequencies within the range 100 to 100,00 Hz was measured over a temperature range of -60 to 200 °C for each sample. The dielectric constant as a function of temperature is diffuse and strongly frequency-dependent for both PMN and PMN-PT specimens, characteristic of the relaxor ferroelectrics. The K(T) for PST is sharp and only slightly diffuse at the transition, indicative of the high degree of structural order.

The general effect of varying hot-press temperatures and of the various chemical modifications on the dielectric response is outlined in Table II. Based on the data presented, some basic tendencies can be deduced. It is seen that the largest K(max) values at 10 KHz are observed for samples prepared at higher pressing temperatures with the highest K(max), in the PMN-PT series, occurring for samples that were batched with excess PbO and 1 mol% La2O3. There is some correlation between the average grain size and the higher dielectric constants with specimens of larger average grain sizes exhibiting the highermagnitudes of K consistent with the previously reported grain-size dependence of the dielectric response of PMN.[8] Addition of 1 mol% La2O3 is seen to effectively reduce the temperature of the maximum dielectric constant by more than 20 °C again in agreement with prior investigation on PMN transparent ceramics.[9] The variation of the diffuseness of the K(T) as indicated by (b 3/4) in Table II for the various pressing temperatures and chemical modifications is also largely a function of grain size. The diffuseness (b 3/4) of the PST samples is not at all affected by the pressing temperature variations implemented in this investigation. This is further reflected in the constant value of the order parameter, $\Omega = 0.9$, for all the PST specimens. It should be noted that the high degree of ordering obtained for these samples is generally not easily achievable by the conventional means of preparing ordered PST ceramics [10] which generally requires an additional long, high temperature annealing under controlled atmosphere to induce structural ordering. Since the HUP temperatures employed to produce these dense PST ceramics are well below the order/disorder transition temperature (≈1475 °C) [10], highly ordered ceramics may be produced. Further, the degree of order is not affected by the low temperature post-pressing anneal conducted here since the annealing temperature in this case is well below the temperature at which a disordered PST ceramic becomes ordered (≈1050 °C). [10]

There is observed for all samples some anisotropy of the dielectric response with respect to the pressing direction as well as a gradient of the response between top and bottom portions of the ceramic. The PMN sample exhibits the least variation with direction and location within the ceramic of all the speicmens examined. The anisotropy observed in the PST samples appears to become slightly less for higher pressing temperatures. The large anisotropy of PSTA may also be related in part to the rather high PbO content of this specimen. The anisotropy with respect to pressing direction for all the PMN-PT samples except PMNTD is considerable. There is no clear correlation between the "polarity" of the anisotropy (i.e. - the direction of the higher magnitude) and the compositional and pressing temperature variations. Further, all PMN-PT specimens exhibit a significant difference in K between the top and bottom sections, again with no definite correlation with the compositional and pressing temperature variations.

Since in most cases, no clear correlation can be made between the dielectric anisotropy and the modifications made, it seems likely that the source of the variations of K(Max) throughout the sample arises in the initial, pre-pressing stages of sample preparation (e.g.-- mixing, forming, etc.) and that the resulting anisotropy and gradients between top and bottom are enhanced by the final HUP process. It is suggested that the macroscale inhomogeneities introduced in the early stages of sample preparation lead to a non-uniform distribution of PbO thereby making conditions favorable for the formation of Pb-rich phases, in particular at the grain boundaries, during the uniaxial hot-pressing procedure. The formation of such intergranular phases in relaxor ferroelectric ceramics produced by various methods has been extensively reported.[11,12,13] Although no second phases were detected by means of XRD or by routine SEM investigation of the microstructure in this investigation, a very thin intergranular phase may be present in these materials which, as previous research has demonstrated,[13] can significantly affect the dielectric response of the material. The largely intergranular fracture of the ceramics as observed in SEM micrographs suggests the existence of such a grain boundary layer. Further, a considerable amount of aging was observed for PMN-PT samples prepared both stoichiometrically and with excess PbO and La2O3. Although it is beyond the scope of the present work and will not be presented here, this aging is worthy of note since the aging phenomenon in PMN has been found to be very closely related to variations in stoichiometry due to an excess or deficiency of PbO in the material.[14] The results obtained in this study suggest that such a variation in stoichiometry may occur non-uniformly throughout the specimen as a result of the processing procedure. A more thorough investigation of possible grain boundary phases and local variations in stoichiometry is required.

The percent transmission at various wavelengths across the visible spectrum are recorded in Table III for samples before and after post-pressing annealing and for selected specimens at two sample thicknesses. Reflection losses, as calculated by means of the Fresnel formula, are about 30% assuming an average refractive index of 2.5 at room temperature for the samples

under consideration. In general, it appears that higher temperatures and, in the case of the PMN-PT series, additions of both excess PbO and 1 mol% La_2O_3 significantly enhance the transparency of the ceramics, conditions which were shown to also encourage grain growth and high dielectric response. Post-pressing annealing is also seen to further enhance transmission across the entire visible spectrum due likely to the liberation of excess PbO.

SUMMARY

Hot uniaxial pressing of chemically modified relaxor ferroelectric compositions is an effective means of producing dense, transparent ceramics with a high dielectric response. Transparent PST ceramics may be produced with an extremely high degree of ordering due to the low hot-pressing temperatures employed. Some variations in dielectric response and the appearance of dielectric aging suggest the formation of intergranular Pb-rich phases and/or local variations in stoichiometry induced by the HUP process. Further investigation into the nature of these irregularities and the mechanism of their formation is required to optimize samples prepared by this procedure.

ACKNOWLEDGEMENTS

The authors are grateful to Mick Latimer and Dave Roberts of Plessey Research, U.K. for their help in the preparation of the samples. The authors also wish to ackowledge the research funding provided by the Office of Naval Research.

REFERENCES

1. D.A. McHenry, J. Giniewicz, S.-J. Jang, A. Bhalla and T.R. Shrout, Ferroelectrics, 93, 351 (1989).
2. G. Burns and F. Dacol, Phase Transitions, 5, 261 (1983).
3. L.E. Cross, Ferroelectrics, 76, 241 (1987).
4. JCPDS #24-1017 $ScTaO_4$.
5. S.L. Swartz and T.R. Shrout, Materials Research Bulletin, 18, 663 (1983).
6. C.G.F. Stenger, F.L. Scholten, and A.J. Burggraaf, Solid State Communications, 32, 989 (1979).
7. N. Setter, Ph.D. Thesis, Pennsylvania State University, (1980).
8. T.R. Shrout, U. Kumar, M. Megherhi, N. Yang and S.-J. Jang, Ferroelectrics, 76, 479 (1987).
9. N. Kim, W. Huebner, S.-J. Jang and T.R. Shrout, Ferroelectrics, 93, 341 (1989).
10. C.G.F. Stenger and A.J. Burggraaf, physica status solidi (a), 61, 275 (1980).
11. E. Goo, T. Yamamoto, K. Okazaki, Journal of the American Ceramic Society, 69 [8], C-188 (1986).
12. J. Guha, D.J. Hong and H.U. Anderson, Journal of the American Ceramic Society, 71 [3], C-152 (1988).
13. K.Z. Baba-Kishi and D.J. Barber, Ferroelectrics, 93, 321 (1989).
14. T.R. Shrout, W. Huebner, C.A. Randall and A.D. Hilton, Ferroelectrics, 93, 361 (1989).

APPENDIX 9

NANOSTRUCTURAL-PROPERTY RELATIONS IN COMPLEX LEAD PEROVSKITES

C. A. Randall
A. S. Bhalla

JAPANESE JOURNAL OF APPLIED PHYSICS
VOL. 29, NO. 2, FEBRUARY, 1990, pp. 327-333

Nanostructural-Property Relations in Complex Lead Perovskites

C. A. RANDALL and A. S. BHALLA

Materials Research Laboratory, The Pennsylvania State University, University Park, PA 16802, USA

(Received July 4, 1989; accepted for publication November 18, 1989)

From transmission electron microscopy studies on several complex lead perovskite compounds $Pb(B'B'')O_3$, and their solid solutions a classification can be obtained based on B-cation order. This classification divides the complex lead perovskites into three subgroups; random occupation or disordered, nanoscale or short coherent long-range order and long coherent long-range order of B-site cations. A correlation between the nanoscale B-site order and relaxor on glassy ferroelectric behavior is found in these lead perovskites. An hypothesis is suggested which relates 0-3 polar connectivity to 0-3 order-disorder connectivity. This hypothesis is discussed with relation to present theories [G. A. Smolenskii: J. Phys. Soc. Jpn. (1970) Suppl., p. 26, L. E. Cross: Ferroelectrics 76 (1987) 241, T. L. Renieke and K. L. Ngai: Solid State Commun. 18 (1973) 1543] and reported experimental results of the perovskite relaxor ferroelectrics.

KEYWORDS: relaxor materials, dielectric properties, nanocomposite, electron microscopic study, model for relaxor behavior

§1. Introduction

1.1 *Ferroelectric background*

For the past thirty years there has been much work, both pure and applied, on the oxide ferroelectric materials and their properties.[1-3] One of the most complex ferroelectrics class is those characterized by a diffuse and dispersive phase transition of the so-called relaxor ferroelectrics.[4,5] The permittivity (ε') and tan δ ($\varepsilon''/\varepsilon'$) vs temperature show a diffuse phase transition over a so-called Curie range. There is a Curie maximum temperature, which is frequency dependent over a wide frequency range, and increases in temperature with increasing frequency. Also, the maximum in the permittivity (ε') does not correspond with the maximum in the dielectric loss (tan δ). Figure 1 shows a typical permittivity vs temperature for a relaxor ferroelectric. This transition behavior is very different from the 'normal-like' ferroelectrics which usually shows a sharp 1st or 2nd order phase transition.

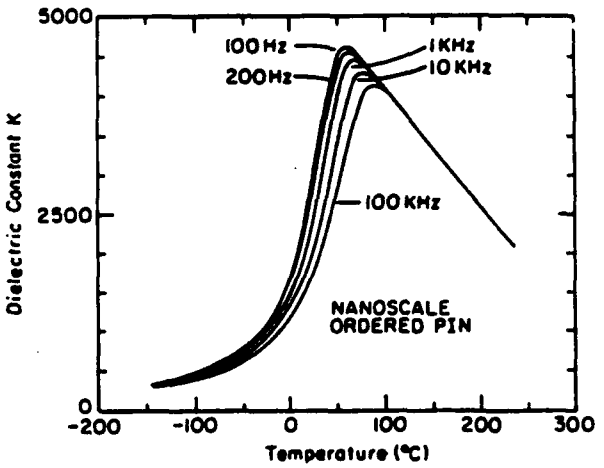

Fig. 1. A schematic representation of the permittivity versus temperature relationship for a complex lead perovskite relaxor.

The most widely accepted models for the understanding of the relaxor ferroelectrics have come from Smolenskii[4] and Cross.[5] The Smolenskii model notes that ferroelectric relaxors have a common characteristic where two or more cations occupy equivalent crystallographic sites. It is the distribution of these cations which gives rise to chemical microregions with various compositions and in turn differing Curie temperatures. The summed distribution of these microregions give the broad phase transition. As a relaxor ferroelectric crystal is cooled, these microregions undergo the paraelectric→ferroelectric phase transition and local polar microregions are created (~ 100 Å).

The Smolenskii model[4] is a very successful model but it has its weaknesses:

1) There is no discrimination between compounds and solid-solutions with mixed cation sites and their tendency to show relaxor or normal dielectric characteristics.
2) With a Gaussian distribution of chemical microregions with their differing Curie temperatures there must exist very subtle changes in chemical compositions from area to area for the major volume of the crystal. This would not appear to give sufficient gradients necessary for the localization of polar microregions or clusters.

Two independent studies on the order-disorder perovskite, $Pb(Sc_{1/2}Ta_{1/2})O_3$, were performed by Setter and Cross[6,7] and also Stenger and Burgraaff[8] in which the key role of the cation distribution and its effect on the dielectric properties was demonstrated.

An understanding of the relaxor dielectric properties was enhanced by the superparaelectric theory as suggested by Cross.[5] Basically, the superparaelectric theory describes the relaxor and its localized polar microregions analogous to the spin cluster behavior in superparamagnets. Considering two polarization states, +P and −P, superparaelectric potential, as illustrated in Fig. 2, these polarization states of a polar microregion are separated by an activation barrier. The height of the

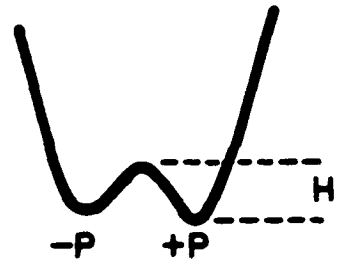

Fig. 2. Schematic representation of a superparaelectric potential describing the polarization states +P and −P.

barrier, H, is directly proportional to the volume of the polar microregion itself. This indicates thermal energy, $k_B T$, and the frequency of polarization flipping, v, are related in a simple relation:

$$v = v_D \exp\left(\frac{-H}{k_B T}\right)$$

where,

H is the activation height between −P and +P,
k_B is the Boltzmann constant,
T is the absolute temperature,
v is the flipping frequency between −P and +P,
and v_D is the Debye frequency ($\sim 10^{11}$–10^{13} Hz).

However, for low thermal energies the polarization will 'lock-in' to a particular orientation, thus forming a polar microdomain or a polar cluster. This feature distinguishes the polar microregion from the polar microdomain (which is static and not a strong frequency dependent feature).

The superparaelectric concept accounts for many of the observed properties of the ferroelectric relaxor such as the frequency dependence of the permittivity, the dielectric aging,[9,10] and also the metastable switching from micro→macrodomain.[11-13] It also reflects the nonlinear behavior of the thermal and optical properties as observed in these materials.[14-16]

1.2 *Cation order background*

Within a given crystal structure the arrangement of various cations and point defects on particular crystallographic sites depends on the relative magnitude of the interaction energy for possible configurations. If this interaction is sufficiently low there are no detectable correlations between the occupancy of neares neighbor sites. However, if there exists a diffuse but distinct superlattice reflection the cations have long range order (LRO) between unlike cations on nearest neighbor sites. Since, in this study the scale of this LRO is important to observed physical properties we describe a coherence length based on the size of ordered domains as imaged with transmission electron microscopy (TEM). A short coherence length of LRO is associated with order domain in a range ~20–800 Å in diameter, and long coherence lengths corresponding to order domains much greater than 1000 Å. For excellent reviews on cation order see Cowley (1976) and Reynaud (1982).[17,18]

As discussed above in §1.1 and 1.2, there is a need to better understand the nanostructure property relationship in these important class of ferroelectric materials. In view of this we carried out studies on a wide selection of important and well characterized complex lead perovskites (single crystals and ceramics). Based on our TEM observations a new insight is gained in the understanding of the nanostructure of these relaxor materials. In this paper we present an approach relating B-site cation order to the ferroic properties in complex lead perovskites. This approach has been discussed in light of present theories and satisfies experimental results.

§2. Results and Discussion

The results discussed here on the structural ordering are made from TEM analysis. Major advantages of this technique include: small coherence length of high energy electrons, the very strong scattering power of electrons with atom ($\sim 10^4$ times greater than X-rays) and also direct imaging of nanostructures with contrast and high resolution methods.

Within the complex perovskites $Pb(B'_xB''_{1-x})O_3$ ($x = 1/2$) family many of the compounds have shown long-range B-site ordering of the cations, as documented by Galasso.[19] The ordering of B-site cations in these systems gives rise to an F-centered $2a_0 \times 2a_0 \times 2a_0$ superstructure, see Fig. 3(a). This additional symmetry consideration gives a set of superlattice lines/spots, F-spots in electron diffraction. However, if the B-cations are randomly occupying the lattice there is no superstructure and the ordinary perovskite cell $a_0 \times a_0 \times a_0$ describes the compound in the paraelectric state, see Fig. 3(b).

Examples of some of the TEM results obtained from complex lead perovskites: Fig. 4(a) shows a weak-diffuse but distinct F-spots in $Pb(Sc_{1/2}Ta_{1/2})O_3$ (PST); 4(b) shows the corresponding dark-field image revealing the contrast of the nanoscaled ordered domains; and 4(c) demonstrates long-range order in normal PST being broken by an antiphase boundary. Figure 5 shows strong F-spot in ⟨211⟩ zone axis pattern from $Pb(Co_{1/2}W_{1/2})O_3$ corresponding to an ordered grain also observed are incommensurate satellite reflections. Nanoscale order domains in PMN:PT (0.9/0.1) and the corresponding ⟨110⟩ zone axis pattern with superstructural F-spots is shown in Figs. 6(a) and 6(b) respectively.

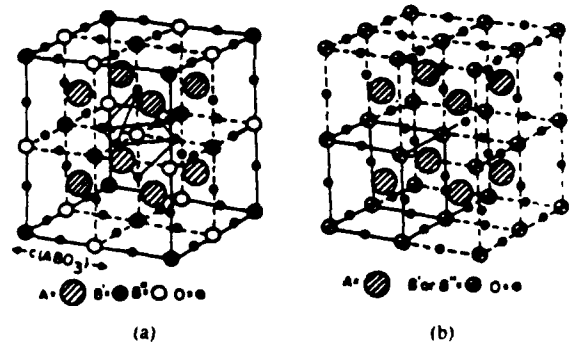

Fig. 3. (a) Ordered B-site superstructure of $Pb(B'_xB''_{1-x})O_3$ ($x = 1/2$) complex perovskite; (b) disorder B-site with primitive perovskite ...

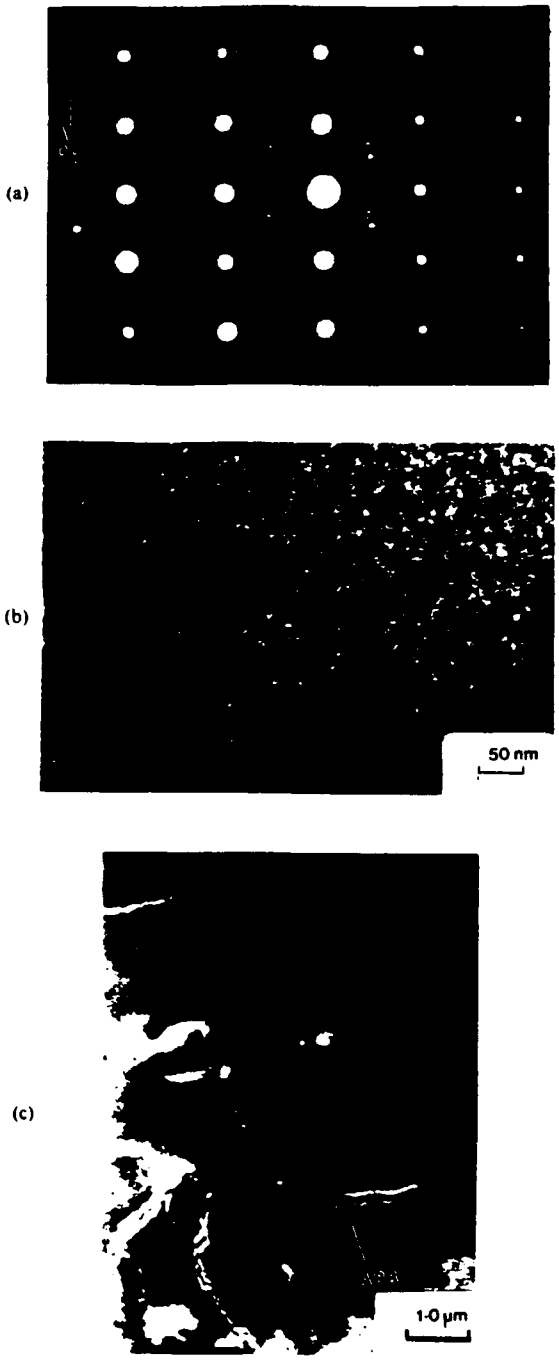

Fig. 4. (a) ⟨110⟩ zone axis pattern from relaxor $Pb(Sc_{1/2}Ta_{1/2})O_3$, the diffuse and weak but discrete order spots are marked F-spots; (b) corresponding dark field image with nanoscale order domains (bright contrast); and (c) long-range order being broken by antiphase boundaries in normal $Pb(Sc_{1/2}Ta_{1/2})O_3$.

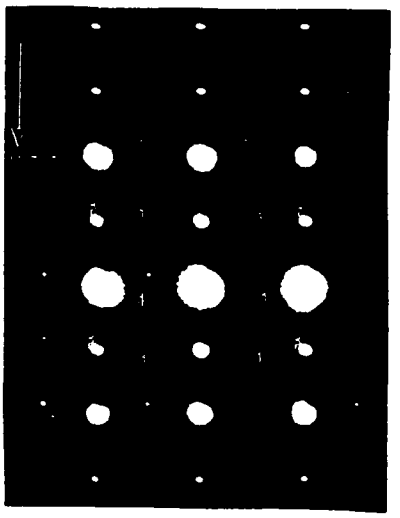

Fig. 5. ⟨211⟩ zone axis pattern in $Pb(Co_{1/2}W_{1/2})O_3$ taken at −160°C; a strong order F-spot is indicated along with incommensurate satellites (I).

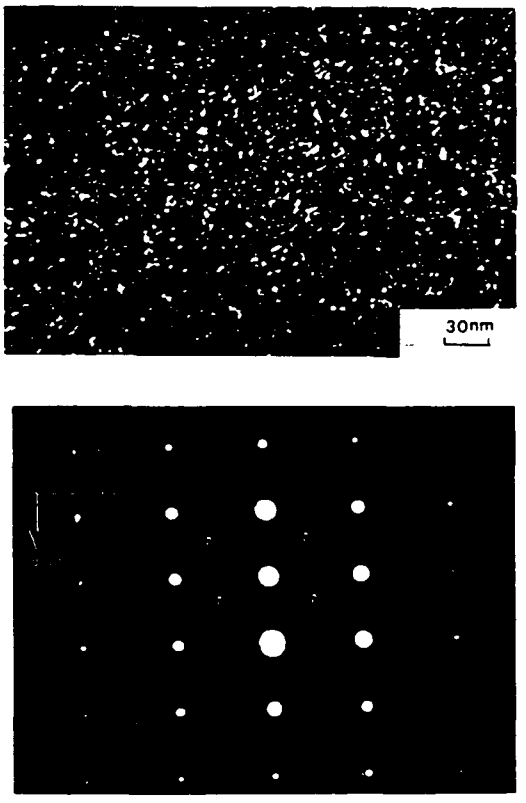

Fig. 6. (a) ⟨110⟩ zone axis diffraction pattern from 0.9 PMN-0.1 PT showing an order spot (F) and (b) the corresponding dark field image reveals nanoscale order domains (~100 Å).

So within the complex lead-perovskites $Pb(B'_{1/2}B''_{1/2})O_3$ ($x=1/2$) systems there are several examples where the B-site cations B′ and B″ have a driving force sufficiently large from valence and ionic radii differences as to order the cations and give superstructure. For instance, $Pb(Co_{1/2}W_{1/2})O_3$, has a strong driving force and grows with almost complete ordering between Co^{+2} and W^{+6} cations. Perovskites such as PST and $Pb(In_{1/2}Nb_{1/2})O_3$ (PIN) have lower driving forces close to the critical limit of disorder and order occupancy of the B-sites. This is inferred by various annealing, quenching, and growth condition effects which shows differing scales (LRO).[8,9] In

Table I. Property differences between relaxor and normal perovskite ferroelectrics.

Property	Normal	Relaxor
permittivity temperature dependence $\varepsilon=\varepsilon(T)$	sharp 1st or 2nd order transition about Curie temperature	broad-diffuse phase transition about Curie maxima (T_{max})
permittivity temperature and frequency dependence $\varepsilon=\varepsilon(T, \omega)$	weak frequency dependence	strong frequency dependence
remanent polarization	strong remanent polarization	weak remanent polarization
scattering of light	strong anisotropy (birefringent)	very weak anisotropy to light (pseudo-cubic)
diffraction of X-rays	line splitting owing to spontaneous deformation from paraelectric→ ferroelectric phase	no X-ray line splitting giving a pseudo-cubic structure

the $x=1/2$ ordered perovskites there is an average B-site valence of +4 in the superstructure which gives rise to so-called stoichiometric ordering.

In the complex lead-perovskites $Pb(B'_{1/3}{}^{+2}B''_{2/3}{}^{+5})O_3$ ($x=1/3$) systems there is a LRO with short coherence length of a 1:1 non-stoichiometric ordering between cations which gives an average valence not equal to +4. The local field and charge compensation mechanisms associated with non-stoichiometric order is not well understood in these systems, but the fact remains that the nanoscale order domains ~100 Å do exist in $x=1/3$ systems, as observed by a number of authors.[20-24]

In our TEM study we are able to classify a number of complex perovskites based on their B-site cation order and respective dielectric, X-ray, and optical properties. The compounds and solid-solutions are then assigned to the normal ferroelectrics (antiferroelectrics) or relaxor ferroelectrics (Table I) as based on their characteristics outlined by Cross.[5] The relations of the cation order in the complex lead perovskites to the respective dielectric behavior (normal or relaxor) are summarized in Table II and in Fig. 7.

We observed that in the solid-solutions of $Pb(Mg_{1/3}Nb_{2/3})O_3$:$PbTiO_3$, (PMN:PT), and $Pb(Zn_{1/3}Nb_{2/3})O_3$:$PbTiO_3$, (PZN:PT), there is a gradual disappearance of the F-spot close to the morphotropic phase boundary which separates strong relaxor ferroelectric behavior from normal ferroelectric behavior in the phase diagram of solid solutions. So on the relaxor side of the phase diagram there exists nanoscale cation order and in the normal side of the diagram there is a cation distribution which is atomically random or disordered with no distinct superstructure. Also, we have included $Pb(Fe_{1/2}Nb_{1/2})O_3$ (PFN) and $Pb(Fe_{1/2}Ta_{1/2})O_3$(PFT) as "normal" ferroelectrics in Table II and Fig. 7. In a number of studies on these compounds with both ceramics and single crystals the results point towards a normal ferroelectric behavior despite a broad phase transition in the permittivity versus temperature data.[25] X-ray, birefringence, and D.T.A. (differential-thermal-analysis) point to normal behavior.[26,27] Brunskill *et al.*[26] and Brixel *et al.*[27] have extrapolated from the temperature dependence of spontaneous birefringence, a polarization order parameter in PFN and PFT respectively. This, as Brixel *et al.* concludes, suggests these materials behave like normal or proper ferroelectrics. So those complex lead perovskites $Pb(B'_xB''_{1-x})O_3$ and solid solutions which have classical relaxor behavior also possess nanoscale B-site order. This strong correlation is thought to be very

Table II. Analysis of order and their corresponding dielectric behavior in a number of $Pb(B'_xB''_{1-x})O_3$ systems.

Compound	Relative coherence length of B-site long range order	Dielectric description
$Pb(Fe_{1/2}Nb_{1/2})O_3$ (PFN)	disordered	normal
$Pb(Fe_{1/2}Ta_{1/2})O_3$ (PFT)	disordered	normal
$Pb(Mg_{1/3}Nb_{2/3})O_3$ (PMN)	short	relaxor
0.9 PMN:0.1 PT ($PT-PbTiO_3$)	short	relaxor
0.8 PMN:0.2 PT	short	relaxor
0.7 PMN:0.3 PT	short	relaxor
0.6 PMN:0.4 PT	disordered	normal
$Pb(Zn_{1/3}Nb_{2/3})O_3$ (PZN)	short	relaxor
0.915 PZN:0.085 PT	short	relaxor
0.9 PZN:0.1 PT	short	relaxor
0.885 PZN:0.115 PT	disordered	normal
$Pb(Ni_{1/3}Nb_{2/3})O_3$ (PNN)	short	relaxor
$Pb(Sc_{1/2}Ta_{1/2})O_3$ (PST)	short	relaxor
$Pb(Sc_{1/2}Ta_{1/2})O_3$	long	normal
$Pb(In_{1/2}Nb_{1/2})O_3$ (PIN)	short	relaxor
$Pb(In_{1/2}Nb_{1/2})O_3$	long	normal
$Pb(Mg_{1/2}W_{1/2})O_3$ (PMW)	long	normal
$Pb(Co_{1/2}W_{1/2})O_3$ (PCW)	long	normal
$Pb(Cd_{1/3}Nb_{2/3})O_3$ (PCN)	short	relaxor

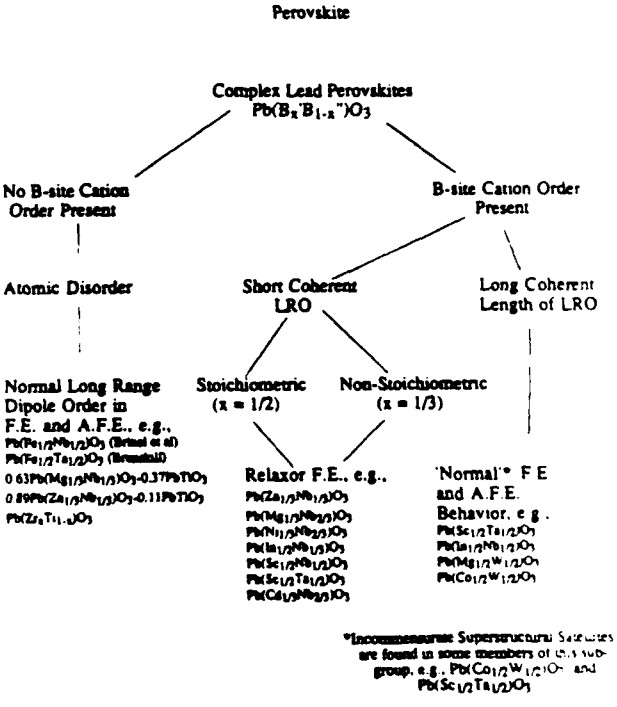

Fig. 7. Flow diagram showing the classification of complex lead perovskites with respect to B-site cation order and dielectric behavior.

important in localizing polar regions or clusters as will be discussed below.

The complex lead-perovskite $Pb(B'_xB''_{1-x})O_3$ ($x=1/2$) and long coherence cation (LRO) and having ferroelectric or antiferroelectric properties are traditionally regarded as normal ferroelectrics or normal antiferroelectrics with long range co-operative interactions between the dipoles. However, the authors here are cautious on this point in light of new experimental evidence of incommensurate satellite reflections observed in TEM studies on some of these materials.[28] Some of those compounds found in this subgroup such as PCW, PST, and PIN have subtle incommensurate dipole modulations associated with the paraelectric→ferroelectric phase transition; these may not strictly be classified as normal ferroelectrics or normal antiferroelectrics. More research is on-going within this interesting subgroup of long-range B-site order lead-based perovskites in order to classify these materials.

2.1 *An hypothesis for the relaxor ferroelectrics as a nanocomposite*

Let us introduce the perovskite relaxor ferroelectrics in terms of a nanocomposite. These relaxor compounds as nanocomposites can be considered by two differing but fundamentally related ways.

(i) We may consider the relaxor nanocomposite through its chemical connectivity.[29] According to the above results the nanoscale LRO has a 0–3 connectivity within a 3-dimensionally interconnected disordered matrix, as schematically represented by Fig. 8.

(ii) We can also consider the relaxor nanocomposite on its mixing of polar and non-polar regions. The connectivity of these two phases is very much a question of the temperature of the system. At higher temperatures, $T>T_0$, (T is a temperature where the total crystal is paraelectric) then we have a material which is chemically heterogeneous as described in (i) but electrically homogeneous (or paraelectric). However, lower temperatures below T_0, optical and thermal expansion experiments indicates the on-set of a polarization through non-linear index of refraction and thermal strain effects:[14–16]

$$\Delta\eta_{ij} \propto g_{ijkl} P^2_{kl}$$
$$\Delta x_{ij} \propto Q_{ijkl} P^2_{kl}$$

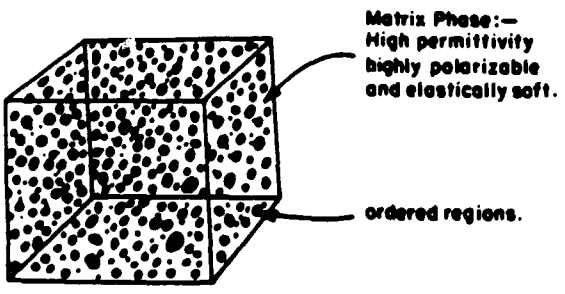

Fig. 8. Schematic representation of nanoscale order domains (dark regions) in a disordered matrix in the form of a 0–3 connected nanocomposite.

Where $\Delta\eta$ is the optical birefringence, g_{ijkl} the quadratic electro-optic coefficients, P^2 mean square polarization, Δx_{ij} thermal strain and Q_{ijkl} are electrostrictive coefficients of the material.

At temperatures in the range ($T<T_0$), the nonpolar-polar connectivity is described in 0–3. At lower temperatures ($T\ll T_0$) as more and more of the crystals volume becomes ferroelectric, the connectivity may change to other forms e.g., 3–3, 3–0, etc. The mechanisms of the kinetics involving stabilizing and equilibration of dynamic polar regions and clustering of neighboring polar regions through local strain and local electric field effects in the matrix phase is not well understood. But, a direct freezing in of the polar microdomain in the cold-stage TEM studies on 8.2/70/30 PLZT has been observed by Randall *et al.*[13,30] indicating the existence of such polar domains. Also, the 'in-situ' switching of the polar microdomains to an aligned macrodomain state confirming their metastable phase transition in relaxors.

The new hypothesis suggests an intimate connection between the 0–3 chemical order distribution (i) and 0–3 polar distribution (ii) in the complex lead perovskites at high temperatures $T<T_0$, provided the chemically ordered regions are associated with a much higher transition than the surrounding matrix.

In the following text we will test the 0:3 nanocomposite approach in relation to various existed models for explaining the relaxor behavior.

2.2 *Reneike-Ngai theory (1976)*[31]

This model was originally postulated with 'disorder' phonon modes originating at highly defective regions of the lattice and coupling with the matrix soft mode and locally perturbing the Curie temperature. This is suggested to give rise to 0–3 polar microregion distributions with various Curie temperatures and local polarization order parameters. One of the major objections to the Reneike-Ngai theory was discussed by Isupov.[32] He pointed out that the theory did account for the broad phase transition and described local polar microregions but it was based on a homogeneous crystal matrix with locally distributed defects. According to Isupov, a homogeneous matrix does not exist in relaxors and all microscopic parts of the crystal are inhomogeneous.

We suggest here that the Reneike-Ngai theory should be reconsidered in light of the present nanostructural observations. The new hypothesis suggests an disordered matrix surrounding nanoscale order-domains; it is conceivable that the order domains have additional phonon modes which could couple to the soft mode of the matrix. The strength of the coupling and its perturbation on the local soft mode transition give rise to local various Curie temperatures. This in turn may be related to the size of the cation order domains themselves.

2.3 *The superparaelectric model (1987)*[5]

The superparaelectric model (1987) satisfactorily accounts for the nature of the polarization behavior in polar microregions. The sites of cation order in the disordered matrix may give potential wells ~100 Å within the lattice in which to localize the superparaelectric poten-

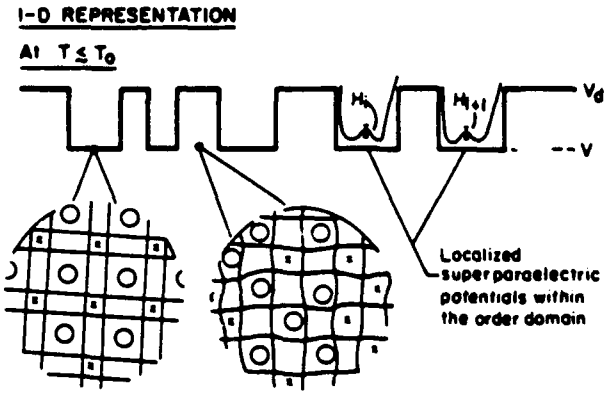

Fig. 9. Schematic representation demonstrating how nanoscale ordered regions giving rise to local strain barriers within the perovskite lattice. These barriers are the suggested sites to localize superparaelectric potentials of the polar regions at high temperatures.

tials, as schematically represented in Fig. 9. The lattice potential differences between LRO and disorder regions are owing to strain and electrostatic energy differences between these respective regions. This difference in lattice potential then can act as a barrier to localize short-range dipolar domains which, of course, are described by the superparaelectric model. Which in turn explains the dielectric, optical, X-ray, and thermal properties of relaxor ferroelectrics.

§3. Summary

In summary the present approach of cation order which is based on the TEM observations and the available experimental data on various complex lead oxide perovskites can be highlighted as follows:

(i) Separates the complex lead perovskite family into three subgroups based on B-site cation order:

a) random or fully disordered distributions,
b) short coherence LRO distributions,
c) long coherence LRO distributions.

(ii) The above approach links these discrete nanoscale order domains to the relaxor ferroelectrics in the complex lead perovskites. This change in B-site distribution from nanoscale order to random occupation is observed very close to the morphotropic phase boundary in solid solution PZN:PT and PMN:PT. Also, scale of LRO accounts for the difference in the macroscopic behavior of PST and PIN. The disorder in PFN and PFT accounts for the normal characteristics in the temperature dependence of the spontaneous birefringence.

(iii) The nanoscale order domains are natural sites for localizing the superparaelectric polar clusters within a paraelectric matrix. This is supported by the work of Smolenskii and Cross who both predicted a size of ~100 Å for the polar microregion from the dielectric relaxations in the permittivity measurements.

(iv) However, despite the apparent successes of this qualitative hypothesis, there are still points of conjecture we wish to relay to the reader:

a) There is no knowledge of which part of the order-disorder 0–3 nanocomposite is ferroelectric and paraelectric at higher temperatures.
b) There is, so far, no statistical analysis of the scale of LRO distribution or volume percentage within these materials.
c) We have only a limited understanding of non-stoichiometric order in the $x=1/3$ complex lead perovskites.[33,34]

Acknowledgements

The authors wish to thank DARPA and ONR for their support of this study. Many thanks go to Professor L. E. Cross and Professor D. J. Barber, Dr. G. Burns, Drs. T. R. Shrout, K. Baba-Kishi and A. D. Hilton and many others for useful discussions and encouragement throughout this work. Thanks to Joyce Baney for typing this manuscript.

References

1) M. A. Lines and A. M. Glass: *Principles and Applications of Ferroelectrics and Related Materials* (Clarendon Press, Oxford, 1977).
2) B. Jaffe, W. R. Cook and H. Jaffe: *Piezoelectric Ceramics* (Academic Press, New York, London. 1971).
3) F. Jona and G. Shirane: *Ferroelectric Crystals* (Macmillan, New York, 1962).
4) G. A. Smolenskii: *Proc. 2nd Meet Ferroelectricity, Kyoto, 1969*, J. Phys. Soc. Jpn. **28** (1970) Suppl. p. 26.
5) L. E. Cross: Ferroelectrics **76** (1987) 241.
6) N. A. Setter and L. E. Cross: J. Mater. Sci. **15** (1980a) 2478.
7) N. A. Setter and L. E. Cross: J. Appl. Phys. **51** (1980b) 4356.
8) C. G. Stenger and A. F. Burgraaf: Phys. Status Solidi (a) **61** (1980) 275.
9) W. A. Schulze, J. V. Biggers and L. E. Cross: J. Mat. Sci. **15** (1978) 2478.
10) P. Wuyi, E. Furman, G. O. Dayton and L. E. Cross: J. Mater. Sci. Lett. **51** (1983) 3399.
11) V. A. Bokov and I. E. Myl'nekova: Sov. Phys. Solid State 3 (1961) 613.
12) X. Yao, Z. L. Chen and L. E. Cross: J. Appl. Phys. **54** (1984) 3399.
13) C. A. Randall, D. J. Barber, R. W. Whatmore and P. Groves: Ferroelectrics **76** (1987) 00.
14) G. Burns and B. A. Scott: Solid State Commun. **13** (1973) 417.
15) G. Burns and F. M. Dacol: Phys. Rev. **B28** (1980) 2527.
16) S. J. Jang, K. Uchino, S. Nomura and L. E. Cross: Ferroelectrics **27** (1980) 31.
17) J. M. Cowley: Advances in High Temperature Chemistry (Academic Press, London, New York, 1971) Vol. 3, p. 36.
18) F. Reynaud: Phys. Status Solidi (a), **72** (1982) 11.
19) F. S. Galasso: *Structure, Properties, and Preparation of Perovskite Type Compounds* (Pergamon Press, Oxford, London, Edinburgh, New York, Toronto, Sidney, Paris, Branschweig, 1969).
20) B. Krause, J. M. Cowley and J. Wheatley: Acta Cryst. A35 (1979) 1015.
21) A. D. Hilton, C. A. Randall and D. J. Barber: Inst. Phys. Conf. Series, No. 90 (1987) Chapter 9, 315.
22) A. D. Hilton, C. A. Randall, D. J. Barber and T. R. Shrout: Ferroelectrics **93** (1989) 379.
23) J. Chen, H. Chen and M. A. Harmer: J. Am. Ceram. Soc. 72 (1989) 593.
24) E. Hussan, M. Chubb and A. Morell: Mater. Res. Bull. 33 (1988) 357.
25) Landolt-Bornstein: *New Series III/16a*, ed. T. Mitsumi and S. Nomura (Springer-Verlag, Berlin, 1981).
26) J. H. Brunskill, H. Schmid and P. Tissot: Ferroelectrics 37 (1981) 547.

27) W. Brixel, J. P. Rivera and H. Schmid: Ferroelectrics **55** (1984) 181.
28) C. A. Randall, S. A. Markgraf, A. S. Bhalla and K. Baba-Kishi: Phys. Rev. B **40** (1989) 413.
29) R. E. Newnham, D. Skinner and L. E. Cross: Mater. Res. Bull. **13** (1978) 525.
30) C. A. Randall, D. J. Barber and R. W. Whatmore: J. Micro. **145** (1987) 235.
31) T. L. Renieke and K. L. Ngai: Solid State Commun. **18** (1973) 1543.
32) G. A. Smolenskii, V. A. Bokov, V. A. Isupov, N. N. Kranik, P. E. Pasyhkov and A. I. Sokolov: *Ferroelectrics and Related Materials*, ed. G. Taylor and G. A. Smolenskii (Gordon and Breach, New York, London, Paris, Montreux, Tokyo, 1984).
33) T. R. Shrout, W. Huebner, C. A. Randall and A. D. Hilton: Ferroelectrics **93** (1989) 361.
34) D. M. Smyth, M. P. Harmer and P. Peng: American Ceramic Society Meeting, Indianapolis, IN (1989).

APPENDIX 10

CRYSTALLIZATION OF NANOMETER SIZE COPRECIPITATED $PbTiO_3$ POWDERS

G. R. Fox
E. Breval
R. E. Newnham

CRYSTALLIZATION OF NANOMETER SIZE COPRECIPITATED $PbTiO_3$ POWDERS

G.R. Fox, E. Breval, and R.E. Newnham

Materials Research Laboratory

The Pennsylvania State University

University Park, Pa 16802

ABSTRACT

Crystallization of coprecipitated $PbTiO_3$ powder was studied by calcining as-precipitated powders at 400-800°C for up to 262hr. The coprecipitated powders were prepared from a solution containing a 1:1 molar ratio of $Pb(NO_3)_2$:$TiCl_4$ and a 1.1:1 molar ratio of H_2O_2:$TiCl_4$. The solution containing the lead and titanium complexes was slowly added to NH_4OH solution under constant pH = 10.00±0.05 conditions that induced precipitation. Transmission electron microscopy (TEM) and X-ray diffraction indicated that the calcined powders consisted of an intimate mixture of amorphous, cubic (or distorted tetragonal with $c_o/a_o<1.01$), and tetragonal ($c_o/a_o=1.065$) $PbTiO_3$ particles between 10 and 400nm, with both particle size and phase content depending on heat treatment. Powders exhibiting the cubic or distorted tetragonal phase consisted of particles between 20 and 200nm in diameter. Fully crystalline tetragonal $PbTiO_3$ powders consisting of 100-400nm particles were prepared.

INTRODUCTION

The purpose of this study was to observe the particle size, morphology, and crystallization behavior of coprecipitated $PbTiO_3$ powders. Previous reports on coprecipitated $PbTiO_3$ have described the coprecipitation process[1,2] and the dielectric properties[3,4] but little work has been completed on the crystallization behavior of coprecipitated $PbTiO_3$. Since the amorphous as-precipitated powders and the calcined crystalline powders display extremely high surface areas[1,2], it was of particular interest to determine whether a cubic $PbTiO_3$ phase is formed in calcined powders due to effects of particle size upon cubic to tetragonal transformation energies.

In previous work on sol-gel derived $PbTiO_3$[5], it was reported that an intermediate cubic phase is formed during the amorphous to tetragonal transformation but it is unclear whether the cubic phase is related to the small particle size of the powders. For $PbTiO_3$ prepared by the alkoxide method, a shift in the cubic to tetragonal transition temperature (T_c) toward lower temperatures was reported for particle sizes below 50nm[6]. One group of workers have also reported stabilization of a distorted cubic $PbTiO_3$ phase for 20nm powders prepared by the alkoxide method[7].

It has been suggested[8] that the decrease in T_c with decreasing particle size is due to an increase in pressure on the volume of the particle. This explanation assumes that the pressure on the volume is due to an "effective" surface tension and that the Laplace equation given by

$$P = \frac{2\delta}{r} \qquad (2)$$

δ = surface tension.
r = radius of particle.

is valid for a solid. Such a model also assumes that the shift in T_c is due only to pressure effects such as those reported by Sumara[9].

A second approach to interpreting the shift in T_c with size comes from the calculations of Batra et al, on ferroelectric thin films. In this model, the stability of the ferroelectric phase is lowered because of depolarization fields which arise from incomplete charge compensation at the ferroelectric surface. For free ferroeletric particles in air, complete charge compensation at the particle surface is not likely. Hence, depolarization fields will increase and the stability of the ferroelectric phase will decrease with decreasing particle size.[10]

Both of these models predict room temperature stabilization of the cubic non-ferroelectric state below a critical particle size, but some factors are not considered which could greatly effect this size dependence. Both models assume single domain states for the ferroelectric phase. The effects of lattice defects, which may significantly contribute to the free energy of a small particle, is also ignored.

In this paper we present evidence for a possible cubic phase in fine particle coprecipitated $PbTiO_3$. Transmission electron microscopy (TEM) can be used to differentiate between, cubic (Pm3m) and tetragonal (P4mm) $PbTiO_3$ phases by comparing converged beam microdiffraction (CBMD) patterns of individual powder particles. Since $PbTiO_3$ exhibits a large difference between the a_o and c_o unit cell parameters (c_o/a_o = 1.065), the 2-fold symmetry along tetragonal <100> can easily be identified by measuring the distance between the 100 and 001 spots of the CBMD pattern (see Figure 1). With a powder that contains both cubic and tetragonal phases, the fraction of each phase can be determined by observing the CBMD patterns of a large number of powder particles along <100> or <001> axes. Figure 2 shows the expected percentage of 2-fold and 4-fold CBMD patterns versus number fraction for powders containing both cubic and tetragonal particles. Using TEM with other supportive

experimental techniques, it is possible to determine the particle size, shape and phase content of coprecipitated $PbTiO_3$ as a function of calcination time and temperature.

EXPERIMENTAL PROCEDURE

Figure 3 outlines the preparation of coprecipitated $PbTiO_3$ powders. Hydrogen peroxide[a] was added to 14.15±0.02ml of $TiCl_4$[b] solution (2.65mol/l) in a 1.1:1 molar ratio of H_2O_2:$TiCl_4$. The mixture was then diluted with deionized water to give 1000ml solution and 37.50±0.02ml $Pb(NO_3)_2$[c] solution (1.00mol/l concentration) was added to give a 1:1 ratio of $Pb(NO_3)_2$:$TiCl_4$. Deionized water was added to the mixed solution to give a final volume of 1500ml solution. The solution was maintained at 43±2°C and constantly stirred. Precipitation was induced by pumping the heated solution at 10ml/min into a three neck flask containing NH_4OH[d] solution. Ammonium hydroxide solution was added to the three neck flask simultaneously with the $Pb(NO_3)_2/TiCl_4$ solution to maintain the pH in the flask at 10.00±0.05. The solution and precipitate formed in the three neck flask was stirred constantly and the temperature was maintained at 43±2°C. After adding all the $Pb(NO_3)_2/TiCl_4$ solution to the three neck flask, the precipitates were filtered and washed *with deinionized water to remove* Cl^- and NO_3^- (less than 0.1 mole percent of each species remained after washing). Concentrations of lead and titanium in the wash solutions were also monitored in order to confirm that neither lead nor titanium was leached from the precipitate. The precipitates were dried at 100°C and crushed

---

[a]. Aldrich Chemical Co., Hydrogen peroxide 30% by weight solution in water, A.C.S. reagent grade.

[b]. Aldrich Chemical Co., Titanium (IV) Chloride 99.9%.

[c]. Aldrich Chemical Co., Lead (II) Nitrate 99+% A.C.S. reagent grade.

[d]. Aldrich Chemical Co., Ammonium Hydroxide A.C.S. reagent grade.

to form a powder. Three gram samples of the dried as-precipitated powders were calcined at 400 - 800°C for 0 - 260hr in covered alumina crucibles.

The phase content of the calcined powders was determined by X-ray diffraction[e] using CuKα radiation at a scan rate of 1°2θ/min. Integrated diffraction peak areas were obtained using a scan rate of 0.1°2θ/min. All samples for X-ray diffraction were back loaded packed powder specimens. The specific surface area of each powder was measured by a nitrogen single point adsorption technique.[f] Transmission electron microscopy[g] (120kV) with energy dispersive spectroscopy was used to investigate powder particle size, morphology, and composition. The crystallographic structure of particles was determined using CBMD (20 and 40nm probe) and selected area electron diffraction (SAED). TEM specimens were prepared from dilute suspensions of $PbTiO_3$ powders in isopropanol. A drop of the suspension was placed on a carbon coated copper grid, dried, and carbon coated.

---

[e]. Scintag Pad V diffractometer, Santa Clara, CA.

[f]. Quantachrome monosorb, model MS-12, Syosset, NY.

[g]. Philips EM 420 transmission electron microscope with LINK EDS attachment, Mahwah, NJ.

RESULTS AND DISCUSSION

X-ray diffraction data of the as-precipitated powders and powders calcined at 400°C are presented in Figure 4. The as-precipitated powder is amorphous as indicated by the broad peak at d=3.0Å. Crystalline $PbTiO_3$ peaks are not observed in powders calcined at 400°C until they have been heat treated for 262hr. Powders calcined at 500°C exhibited crystalline $PbTiO_3$ peaks after 2hr at temperature (see Figure 5). For powders calcined above 500°C, the diffraction patterns were similar to the pattern at 500°C for 262hr.

A few of the diffraction patterns indicate that both amorphous and crystalline $PbTiO_3$ are present simultaneously as is demonstrated by the pattern for the sample heated at 400°C for 262hr. In order to quantify the fraction of crystalline $PbTiO_3$ present in each of the calcined powders, the integrated 111 peak intensities were measured and normalized to the integrated 111 peak intensity measured for a standard coprecipitated powder calcined at 800°C for 262hr. The concentration of crystalline $PbTiO_3$ increases markedly with increasing calcination temperature and time as shown in Figure 6. Fully crystalline tetragonal $PbTiO_3$ is obtained only for powders calcined at 800°C.

Specific surface area as a function of calcination time and temperature is shown in Figure 7. At 400°C and 500°C, the specific surface area decreases with increasing calcination time, indicating an increase in particle size and/or density. At 600°C, the specific surface area remains constant. A small decrease in specific surface area with increasing calcination time is observed again at 800°C, suggesting further increase in particle size or density.

TEM analysis of the powders provides further insight into the crystallization processes occurring during calcination (see Table 1). As-precipitated powders exhibit particle sizes less than or approximately equal to 10nm in diameter, but the primary particles are highly agglomerated as shown in Figure 8. Electron diffraction indicates that, powders calcined at

400°C for 262hr. and at 500°C and higher temperatures consist of combinations of crystalline and amorphous particles. The fraction of crystalline and amorphous particles depended upon calcination time and temperature, in agreement with the X-ray diffraction results. Examples of CBMD patterns for crystalline single particles are shown in Figure 9a and b. Figure 9a shows a 4-fold symmetry axis of either a tetragonal or cubic particle while Figure 9b shows the 2-fold symmetry axis of a tetragonal particle. Some powders calcined below 800°C exhibited more 4-fold symmetric CBMD patterns than would be expected statistically for a purely tetragonal material (as indicated in Figure 1). Since it is difficult to distinguish c_o/a_o ratios of less than 1.01 in these CBMD patterns some apparent 4-fold symmetry patterns may be 2-fold patterns of tetragonal particles with $c_o/a_o<1.01$. Hence, the partially crystallized powders consist of a tetragonal phase with $c_o/a_o=1.065$ and a cubic phase or tetragonal phase with $c_o/a_o<1.01$.

Powders calcined at 500°C for 10min. consist mostly of amorphous particles (as confirmed by X-ray and electron diffraction), but some groups of crystalline particles were observed as shown in Figure 10. The crystalline particles are equiaxed and are approximately 20-50nm in diameter. All <100> or <001> CBMD patterns of crystalline particles exhibited 4-fold symmetry, thus indicating a cubic phase or tetragonal phase with $c_o/a_o<1.01$.

The crystalline particles in powders calcined at 400°C for 262hr. and 500°C for 2hr. were similar to those shown in Figure 10. These powders also contained large quantities of amorphous particles surrounding regions of crystalline particles. More 4-fold than 2-fold symmetry CBMD patterns, for <100> or <001> directions, were observed for these powder particles. Further evidence indicating the presence of cubic or distorted tetragonal phases ($1.000<co/ao<1.065$) comes from asymmetry of the 002 and 200 X-ray diffraction peaks for the partially crystallized powders. Figures 11a and b shows the 002 and 200 diffraction peaks for fully crystallized powder calcined at 800°C for 262hr and powder calcined at 500°C for

2hr., respectively. By comparing the two patterns, one sees that the peaks in Figure 11b are broadened asymmetrically. The 002 peak is broadened more on the high angle side while the 200 peak is broadened more on the low angle side. This is the type of diffraction pattern expected for a powder containing a distribution of particles with c_o/a_o ratios between 1.000 and 1.065. Figure 11b also shows an average $c_o/a_o=d_{002}/d_{200}=1.050$ which is slightly smaller than the $c_o/a_o=1.065$ for large particle $PbTiO_3$ powders.

Micrographs of powders calcined at 500°C for 24hr are shown in Figure 12. Clusters of small amorphous particles are intimately mixed with larger crystalline particles. Necking between amorphous particles (10 - 30nm), which was also observed in the powders discussed above, indicates that the amorphous particles sinter before crystallizing. Crystalline particles are 20-200nm in diameter and are generally equiaxed. Powders calcined at 600°C for 10min show similar quantities and morphologies of amorphous and crystalline material, but the crystalline particle sizes range from 50-100nm. As shown by electron diffraction, both powders appear to contain a cubic phase of distorted tetragonal phase.

Figure 13 is a micrograph of powder calcined at 600°C for 2hr. A small number of amorphous clusters are found between the large crystalline grains. The amorphous clusters consist of 10-30nm equiaxed particles. Crystalline particles are equiaxed, faceted and 20 - 100nm in diameter. Powders calcined at 500°C for 262hr. and 600°C for 24hr. exhibit crystalline particles like those shown in Figure 13, but no amorphous particles were found.

At 800°C only crystalline particles were observed as shown in Figure 14. Both equiaxed and elongated particles were present. Particle sizes ranged from 100-200nm for 10min. to 200-400nm for 262hr calcination times. Particles also began to sinter at the longer calcination times.

None of the SAED ring patterns or CBMD patterns indicated the presence of $Pb_2Ti_2O_6$ or $PbTi_3O_7$ which are cubic structures that may possibly form within the calcined powders. Hence it was concluded that the powders exhibiting excessive amounts of 4-fold axes contain

cubic or distorted tetragonal (c_o/a_o<1.01) $PbTiO_3$. In all of the powders, especially those believed to contain a cubic $PbTiO_3$ phase, many of the small particles (≤100nm) contained what appeared to be dislocations or other lattice defects. Such defects may have large effects upon the free energies of the crystalline phases, therefore causing the formation of a cubic phase. With extended heat treatments, such defects would be depleted along with any phases stabilized by such defects. By considering the phase information from both X-ray and electron diffraction, a phase formation diagram as a function of calcination time and temperature can be constructed as shown in Figure 15. The broken lines used to separate phase fields signify that the exact position and shape of the boundaries have not been conclusively determined. Hence, the boundaries shown only indicate general trends in phase formation for increasing calcination time and temperature.

CONCLUSIONS

Crystallization of coprecipitated $PbTiO_3$ powders is complex in that several phases occur that are dependent upon heat treatment and particle size. Also, several particle morphologies occur which are dependent upon heat treatment. As-precipitated amorphous powders exhibit equidimensional particles approximately 10nm in size which sinter and grow to form equidimensional crystalline particles. Small equidimensional crystalline particles between 20-100nm primarily show cubic or distorted tetragonal ($1.000<c/a<1.065$) symmetry. With increasing calcination time and temperature, equidimensional crystalline particles grow in size (50-200nm) and transform to the tetragonal state (up to 400nm). Further calcination causes necking between crystalline tetragonal particles along with particle growth, pronounced faceting, and particle elongation.

The reason for the appearance of a cubic $PbTiO_3$ phase at room temperature may be due to lattice defects, size effects, charge compensation effects or a combination of many factors arising from the boundary conditions imposed by nanometer size particles. Investigations of materials containing higher quantities of cubic phases need to be completed before it can be determined which physical effects play a dominant role in stabilizing a room temperature cubic $PbTiO_3$ phase.

ACKNOWLEDGEMENTS

The authors would like to thank Ann Casciani who made the specific surface area measurements and Dr. Clive Randall for discussion concerning the TEM and electron diffraction data. Susan McKinstry, Dr. James Adair and Douglas Watson also provided helpful and stimulating discussion.

REFERENCES

1. G.R. FOX, J.H. ADAIR, R.E. NEWNHAM, accepted by J. Mat. Sci.

2. G.R. FOX, J.H. ADAIR, R.E. NEWNHAM, submitted to J. Mat. Sci.

3. Y.H. LEE, M.J. HAUN, A. SAFARI, R.E. NEWNHAM, Proc. IEEE Symp. on Applications of Ferroelectrics (ISAF), Lehigh University, (1986) 318.

4. M.H. LEE, A.H. HALLIYAL, R.E. NEWNHAM, Ferroelectrics **87** (1988) 71.

5. S.R. GURKOVICH, J.B. BLUM, Ferroelectrics **62** (1985) 189.

6. K. ISHIKAWA, K. YOSHIKAWA, N. OKADA, Phys. Rev. B **37** [10] (1988) 5852.

7. O. YAMAGUCHI, A. NARAI, T. KOMATSU, K. SHIMIZU, J. Am. Ceram. Soc. **69** [10] (1986) *C-256*.

8. K. UCHINO, E. SADANAGA, K. OONISHI, T. MOROHASHI, H. YAMAMURA, J. Am. Ceram. Soc. **72** [8] (1989) 1555.

9. G.A. SAMARA, Ferroelectrics **2** (1971) 277.

10. I.P. BATRA, P. WURFEL, B.D. SILVERMAN, J. Vac. Sci. Technol. **10** [5] (1973) 687.

FIGURE CAPTIONS

Figure 1 - Calculated appearance of CBMD patterns from simple zone axes in cubic and tetragonal $PbTiO_3$. For the tetragonal lattice c/a = 1.0651 will appear in the <100> CBMD pattern as $g_{010}/g_{001} = 1.0651$.

Figure 2 - Probability for observing 2-fold and 4-fold <001> and <100> CBMD patterns in a system containing cubic and tetragonal phases.

Figure 3 - Diagram for $PbTiO_3$ coprecipitation process.

Figure 4 - X-ray diffraction patterns indicating amorphous nature of as-precipitated powders and powders calcined at 400°C for 24hr. Powder calcined at 400°C for 262hr. exhibits tetragonal $PbTiO_3$ peaks.

Figure 5 - X-ray diffraction pattern of powder calcined at 500°C for 10min. exhibits an amorphous structure while powders calcined for longer times show tetragonal $PbTiO_3$ peaks.

Figure 6 - Relative concentration of crystalline $PbTiO_3$ as a function of calcination time and temperature.

Figure 7 - Specific surface area of calcined powders as a function of calcination time and temperature.

Figure 8 - Amorphous as-precipitated $PbTiO_3$ precursor powder.

Figure 9 - CBMD patterns of single particles in calcined powders.
a) cubic <100> direction or tetragonal <001> direction,
b) tetragonal <100> with a 1.06 ratio between the vertical and horizontal spots.

Figure 10 - Crystalline particles that exhibit only 4-fold symmetry along <001> or <100> axes in powders calcined at 500°C/10min.

Figure 11 - a) 002 and 200 X-ray diffraction peaks for powder calcined at 800°C/262hr., b) asymmetrically broadened 002 and 200 peaks with average $c_o/a_o=d_{002}/d_{200}=1.050$ for powder calcined at 500°C/2hr.

Figure 12 - Cluster of sintered amorphous particles (marked by arrow) and 100-200nm crystalline particles in powder calcined at 500°C for 24hr.

Figure 13 - Small 10-30nm amorphous particles (marked by arrow) between large 100nm crystalline particles calcined at 600°C for 2hr.

Figure 14 - Elongated and sintered tetragonal $PbTiO_3$ particles calcined at 800°C for 24hr.

Figure 15 - Formation diagram of $PbTiO_3$ phases as a function of calcination time and temperature. Dashed line boundaries indicate general trends and have not been determined exactly.

Table 1 - Phase Content and Particle Size of Calcined Powders

Calcination Temp. (°C)	Calcination Time (hr.)	%Amorphous Phase (±10%)	Cubic Phase	Tetragonal Phase
400	24	100 (10nm)		
400	262	95 (10-20nm)	yes (20-50nm)	yes (50-100nm)
500	0.2	85 (10-50nm)	yes (20-50nm)	
500	2	70 (20-50nm)	yes (20-50nm)	yes (50-100nm)
500	24	15 (10-20nm)	yes (20-75nm)	yes (100-200nm)
500	262	0		yes (100-200nm) (elongated)
600	0.2	50	yes (50-100nm)	yes (50-100nm)
600	2	15		yes (100nm)
600	24	0		yes (100nm)
800	0.2	0		yes (100-200nm) (elongated)
800	2	0		yes (150-200nm) (elongated)
800	24	0		yes (200-300nm) (elongated)
800	262	0		yes (200-400nm) (aggregated)

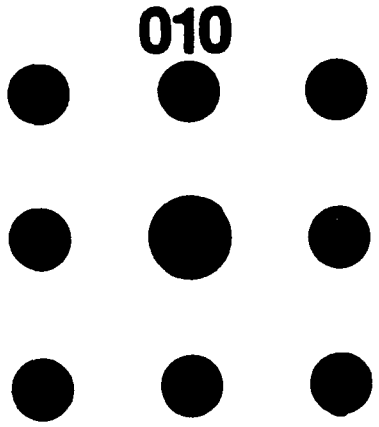

4-fold symmetry

<100> cubic or
<001> tetragonal

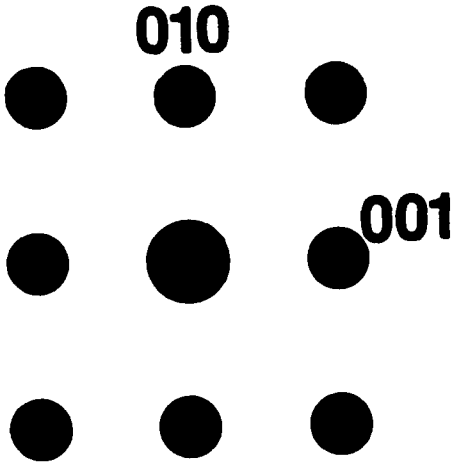

2-fold symmetry

<100> tetragonal

$$\frac{g_{010}}{g_{001}} = 1.0651$$

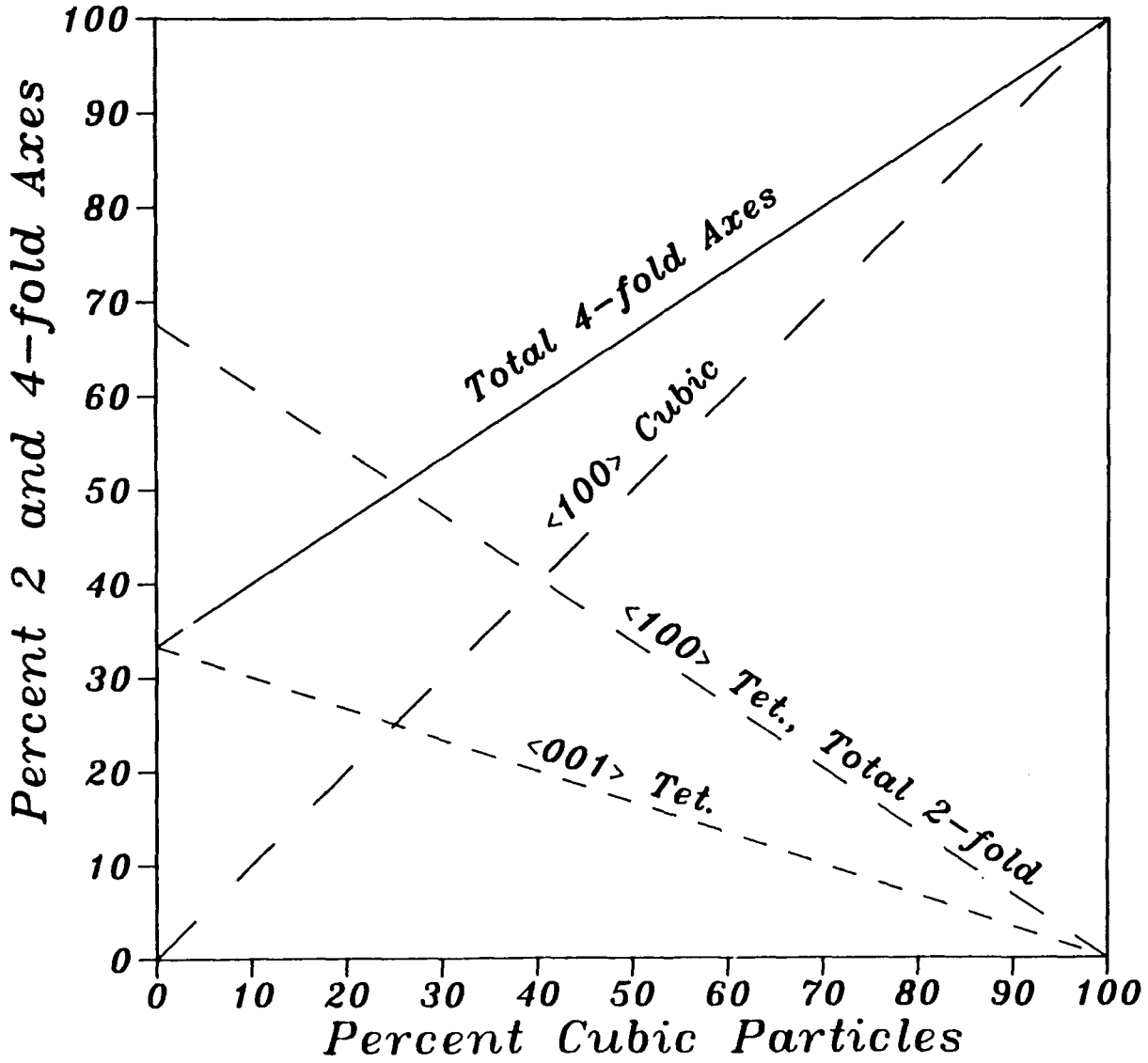
Percent 2 and 4-fold Axes
100
90
80
70
60
50
40
30
20
10
0
0
10
20
30
40
50
60
70
80
90
100
Percent Cubic Particles
Total 4-fold Axes
<100> Cubic
<100> Tet., Total 2-fold
<001> Tet.

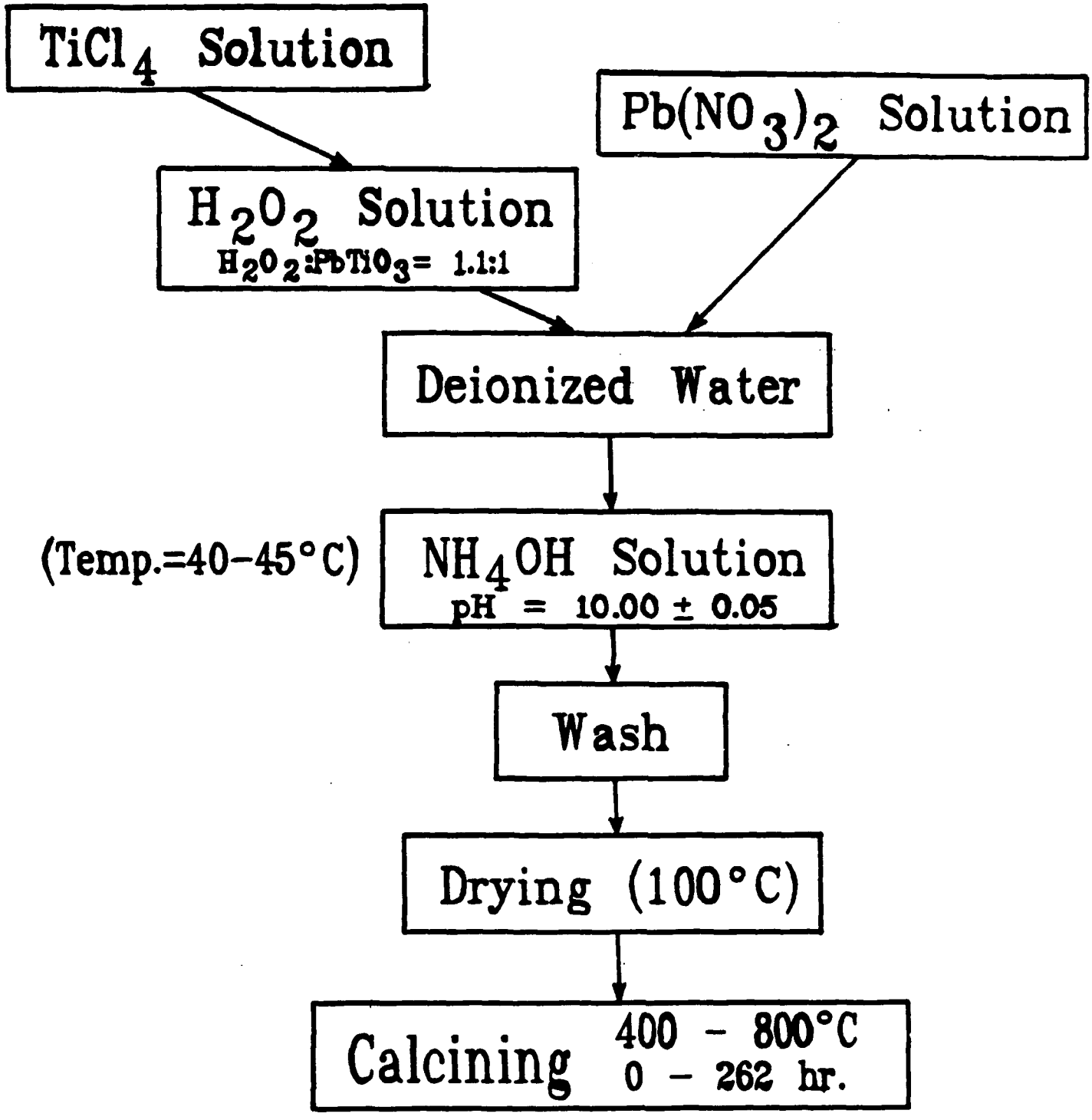
$TiCl_4$ Solution
$Pb(NO_3)_2$ Solution
H_2O_2 Solution
H_2O_2:$PbTiO_3$= 1.1:1
Deionized Water
(Temp.=40-45°C)
NH_4OH Solution
pH = 10.00 ± 0.05
Wash
Drying (100°C)
Calcining
400 - 800°C
0 - 262 hr.

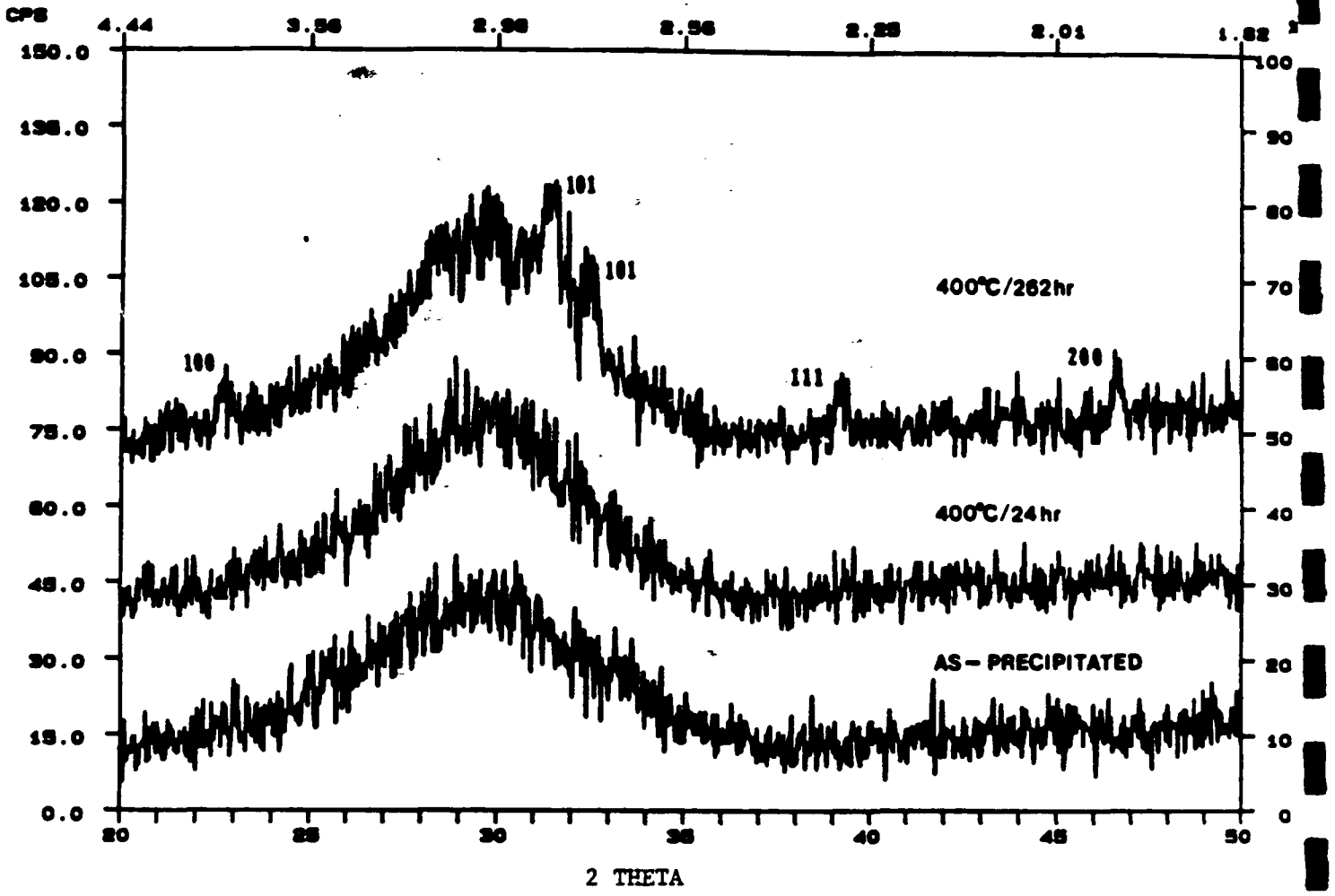
CPS
4.44
3.56
2.96
2.56
2.28
2.01
1.82
150.0
135.0
120.0
105.0
90.0
75.0
60.0
45.0
30.0
15.0
0.0
100
90
80
70
60
50
40
30
20
10
0
101
101
100
111
200
400°C/262hr
400°C/24hr
AS-PRECIPITATED
20
25
30
35
40
45
50
2 THETA

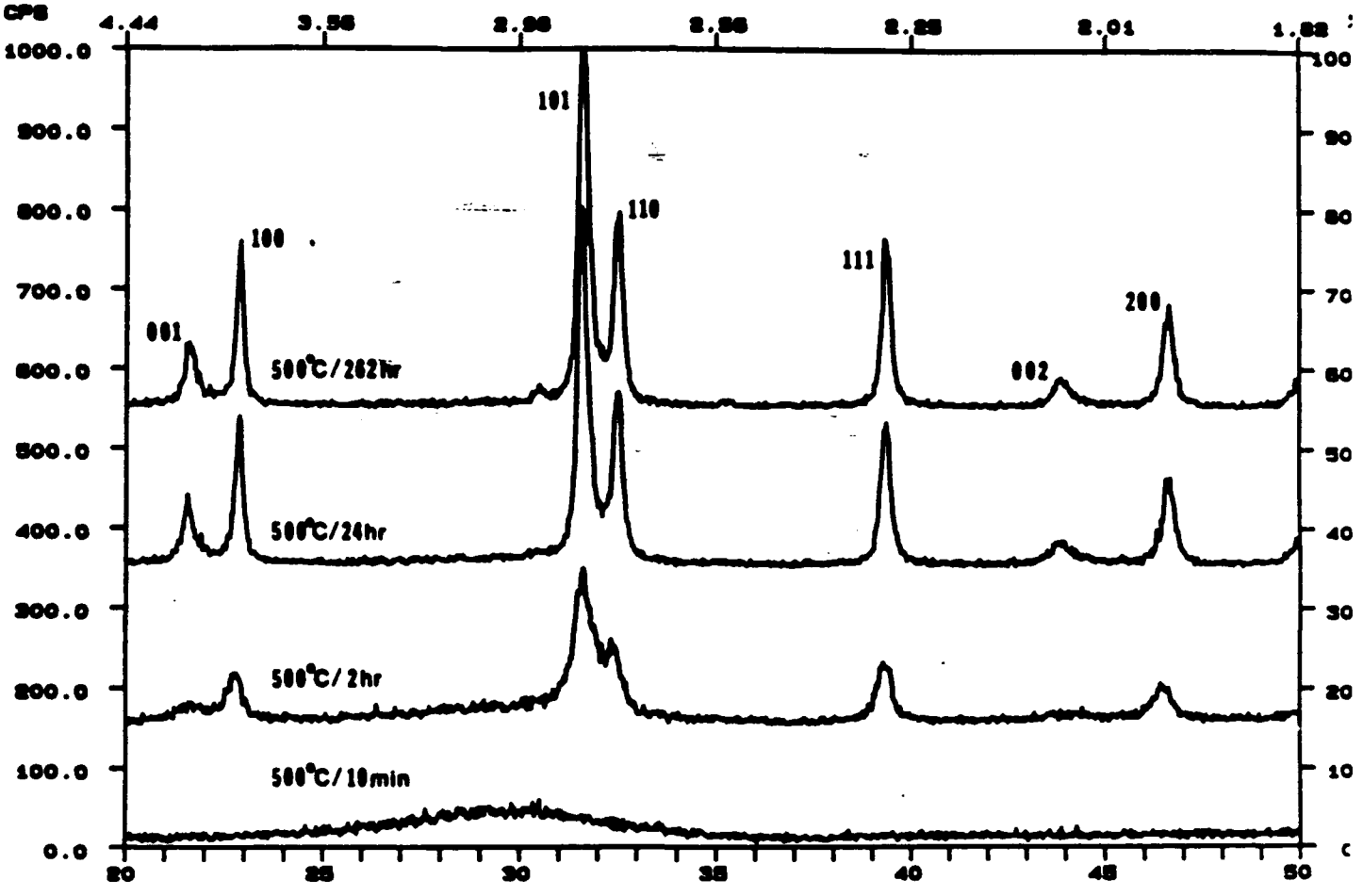
CPS
4.44
3.56
2.96
2.54
2.22
2.01
1.82
1000.0
900.0
800.0
700.0
600.0
500.0
400.0
300.0
200.0
100.0
0.0
100
90
80
70
60
50
40
30
20
10
0
001
100
101
110
111
002
200
500°C/20Hr
500°C/24hr
500°C/2hr
500°C/10min
20
25
30
35
40
45
50
2 THETA

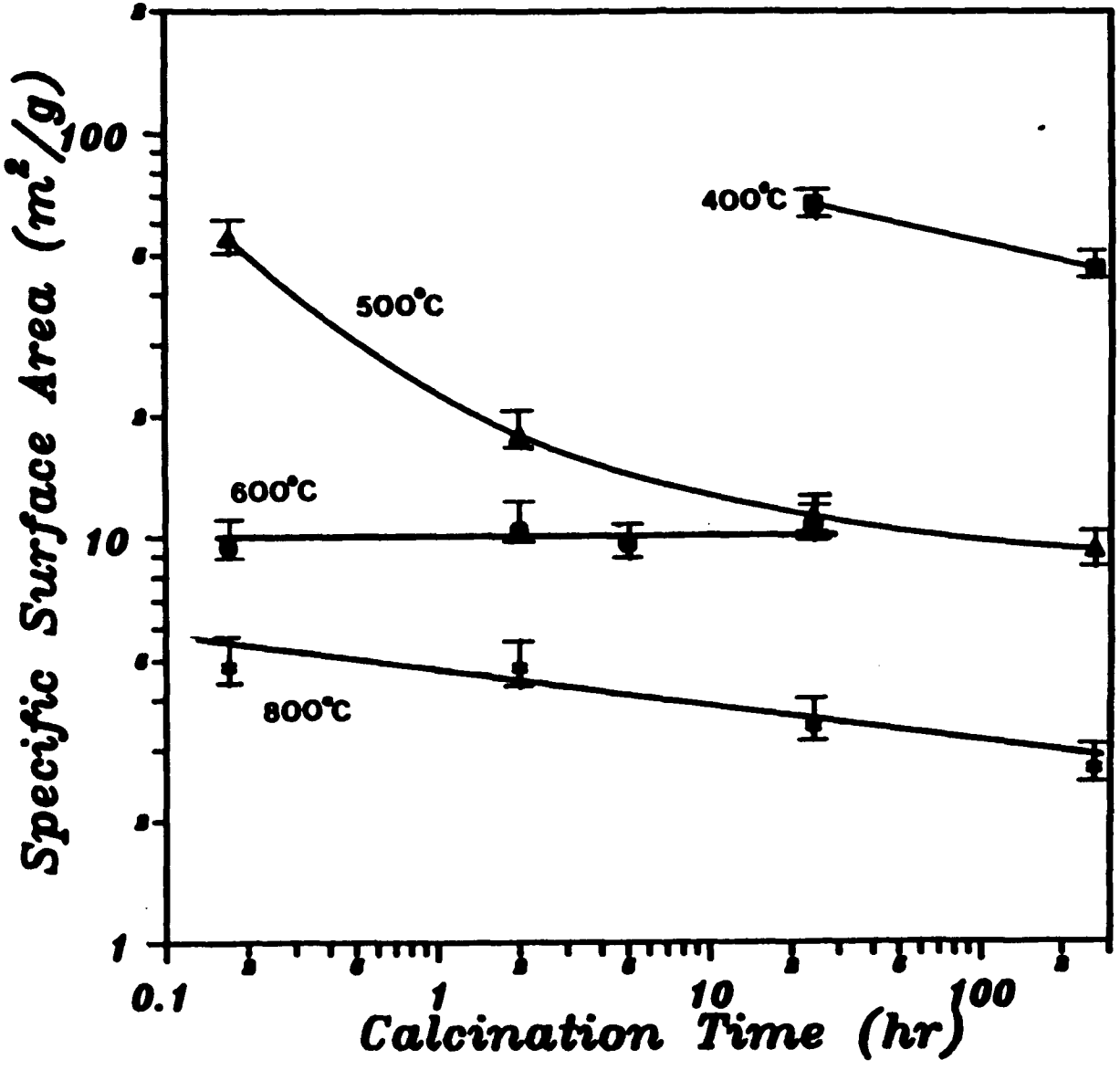
Specific Surface Area (m^2/g)
100
10
1
400°C
500°C
600°C
800°C
0.1
1
10
100
Calcination Time (hr)

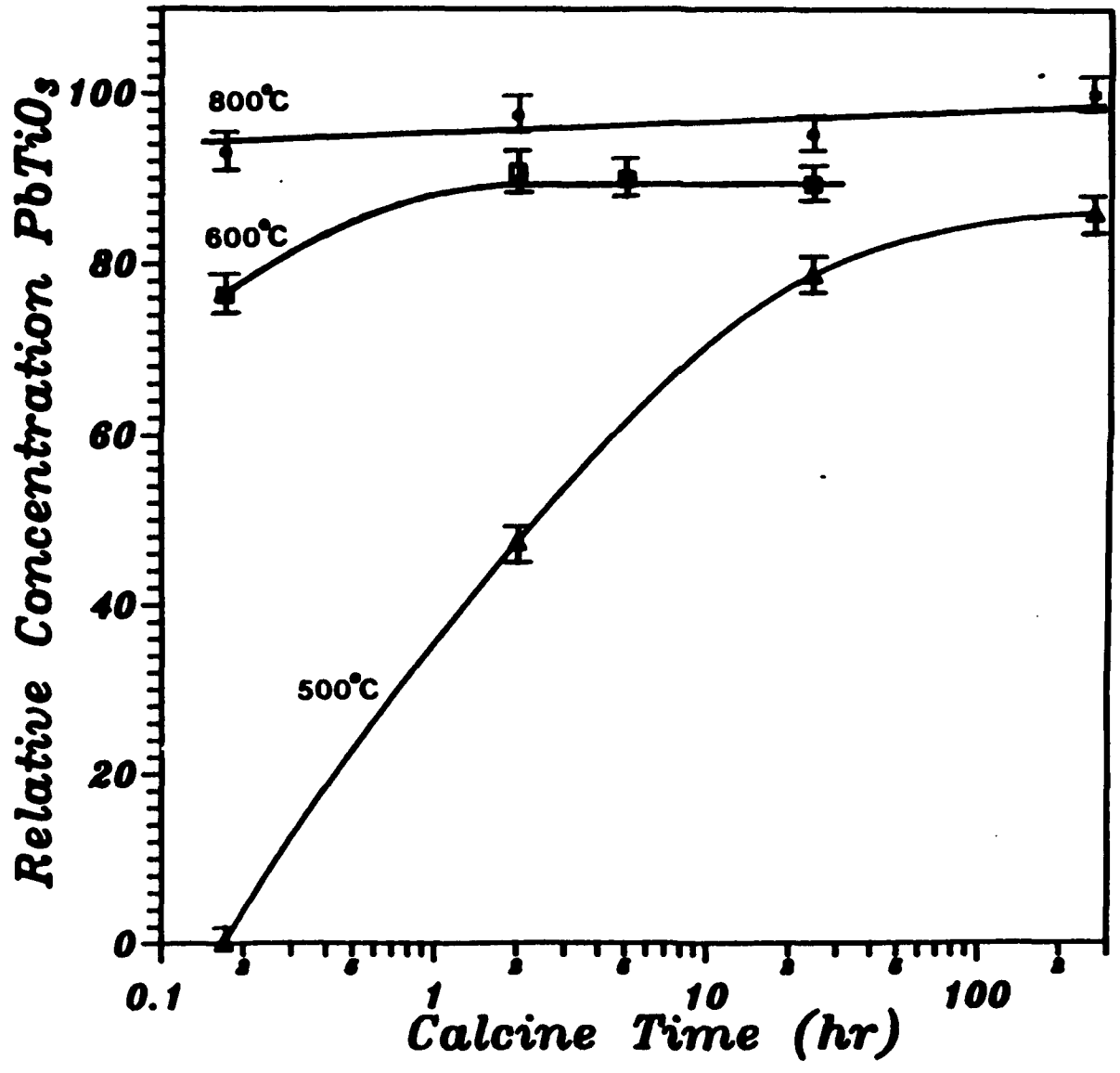
Relative Concentration $PbTiO_3$
100
80
60
40
20
0
800°C
600°C
500°C
0.1
1
10
100
Calcine Time (hr)

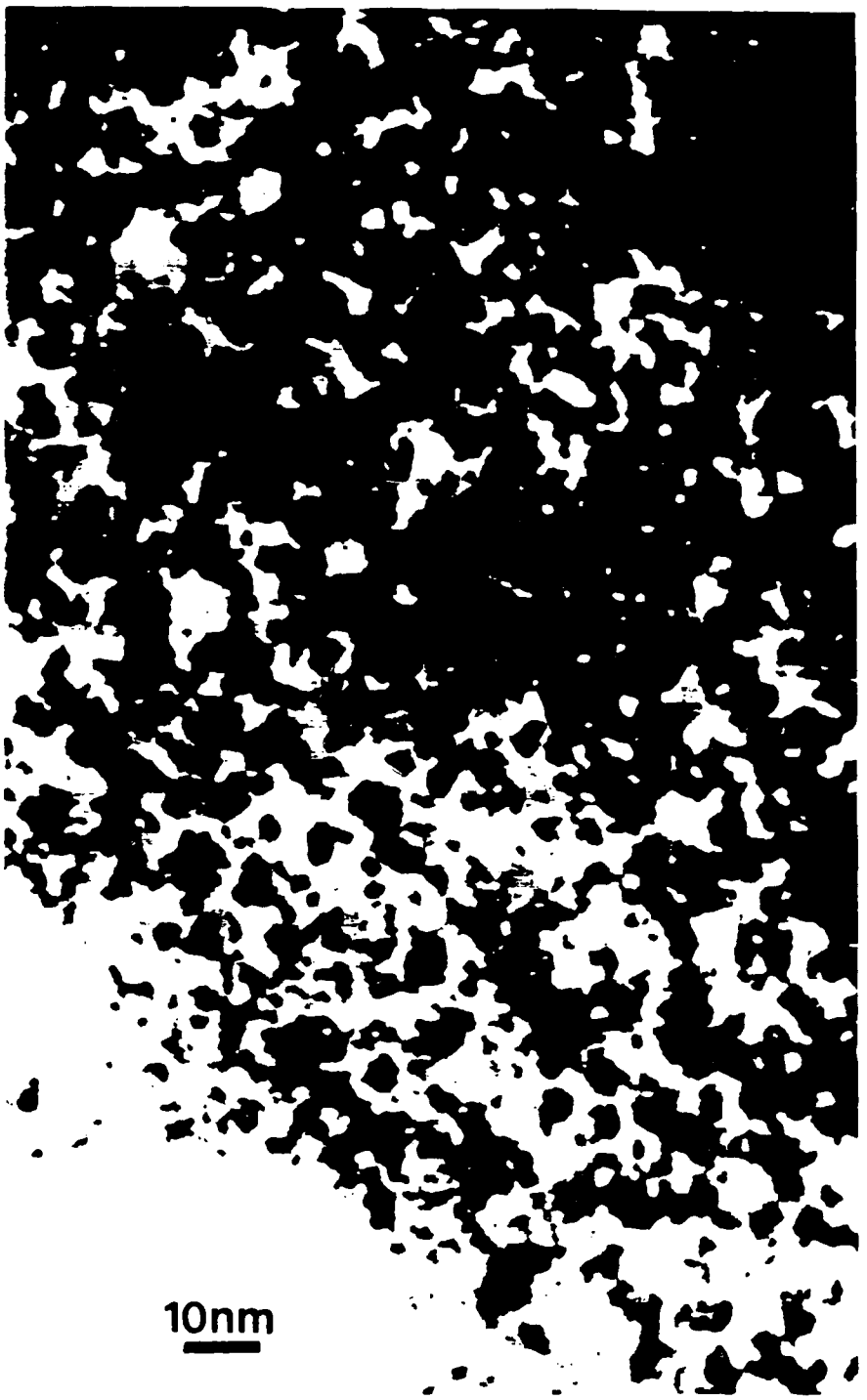
10nm

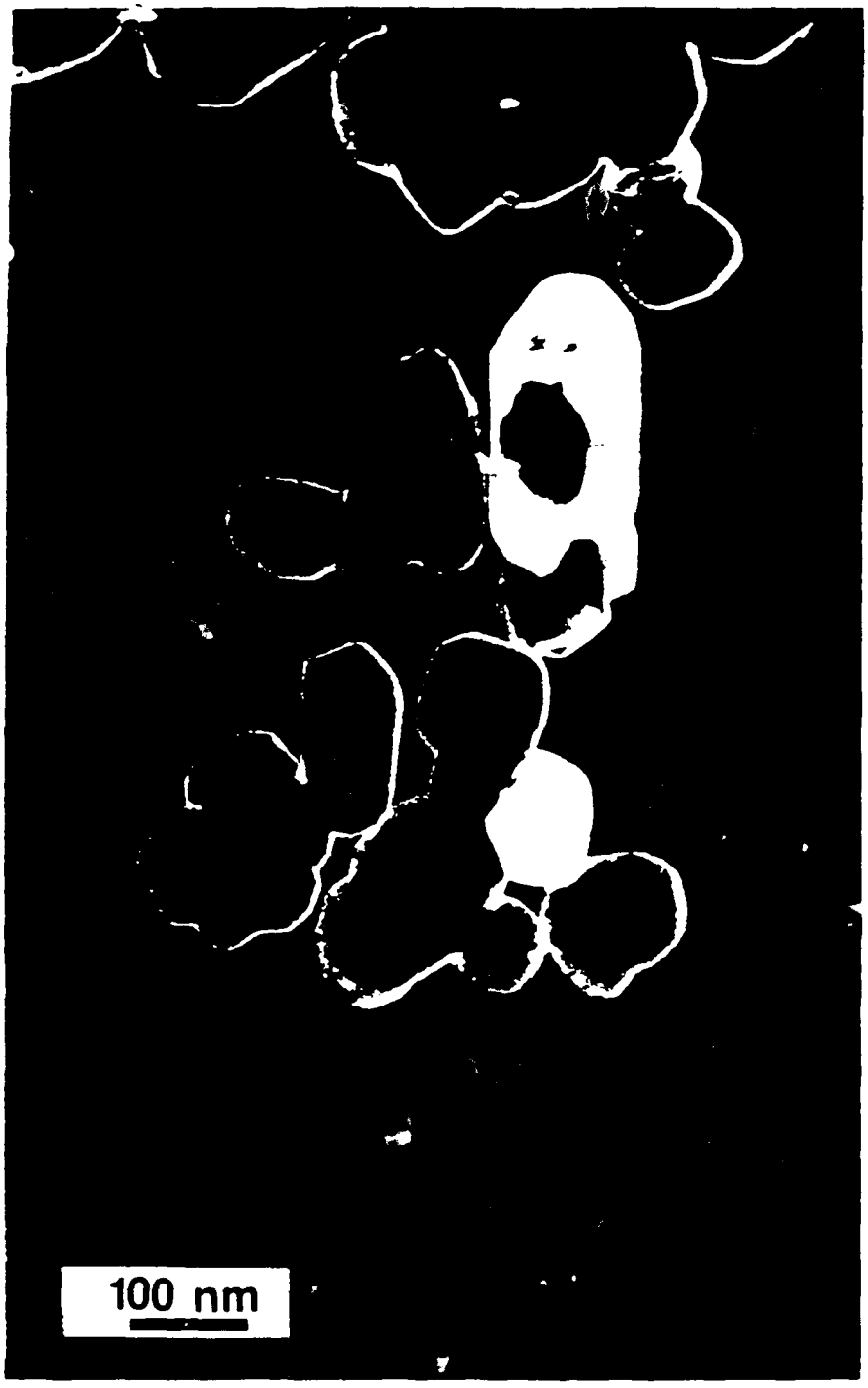
100 nm

50 nm

200 nm

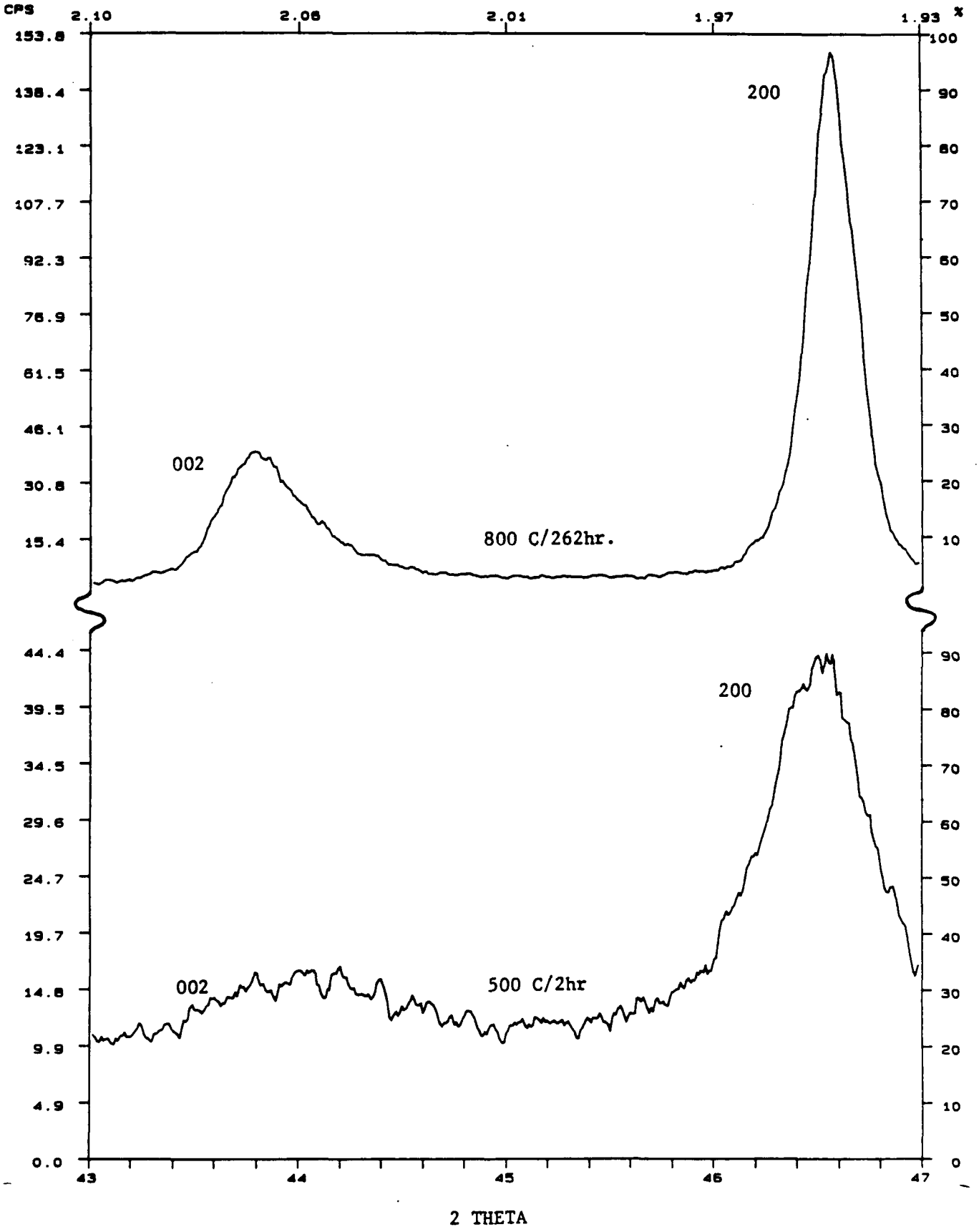
CPS
2.10
2.06
2.01
1.97
1.93
%
153.8
138.4
123.1
107.7
92.3
76.9
61.5
46.1
30.8
15.4
100
90
80
70
60
50
40
30
20
10
200
002
800 C/262hr.
44.4
39.5
34.5
29.6
24.7
19.7
14.8
9.9
4.9
0.0
90
80
70
60
50
40
30
20
10
0
200
002
500 C/2hr
43
44
45
46
47
2 THETA

50nm

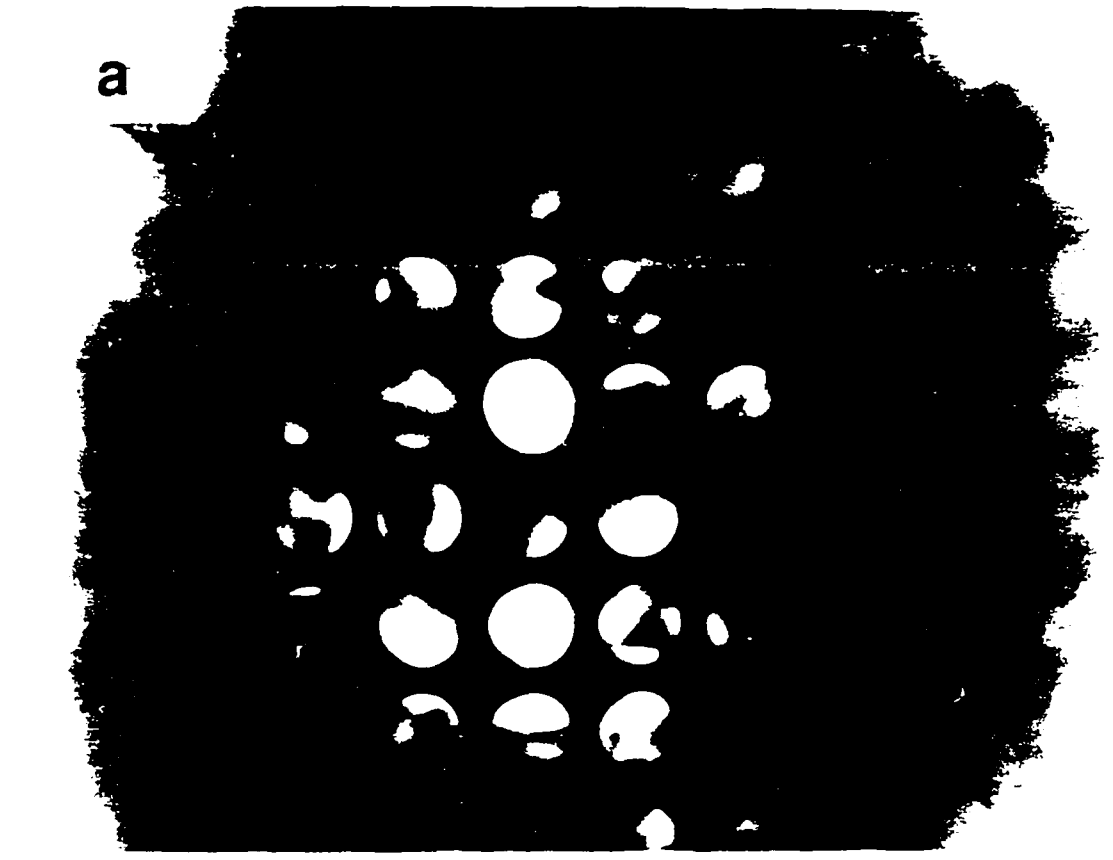
a

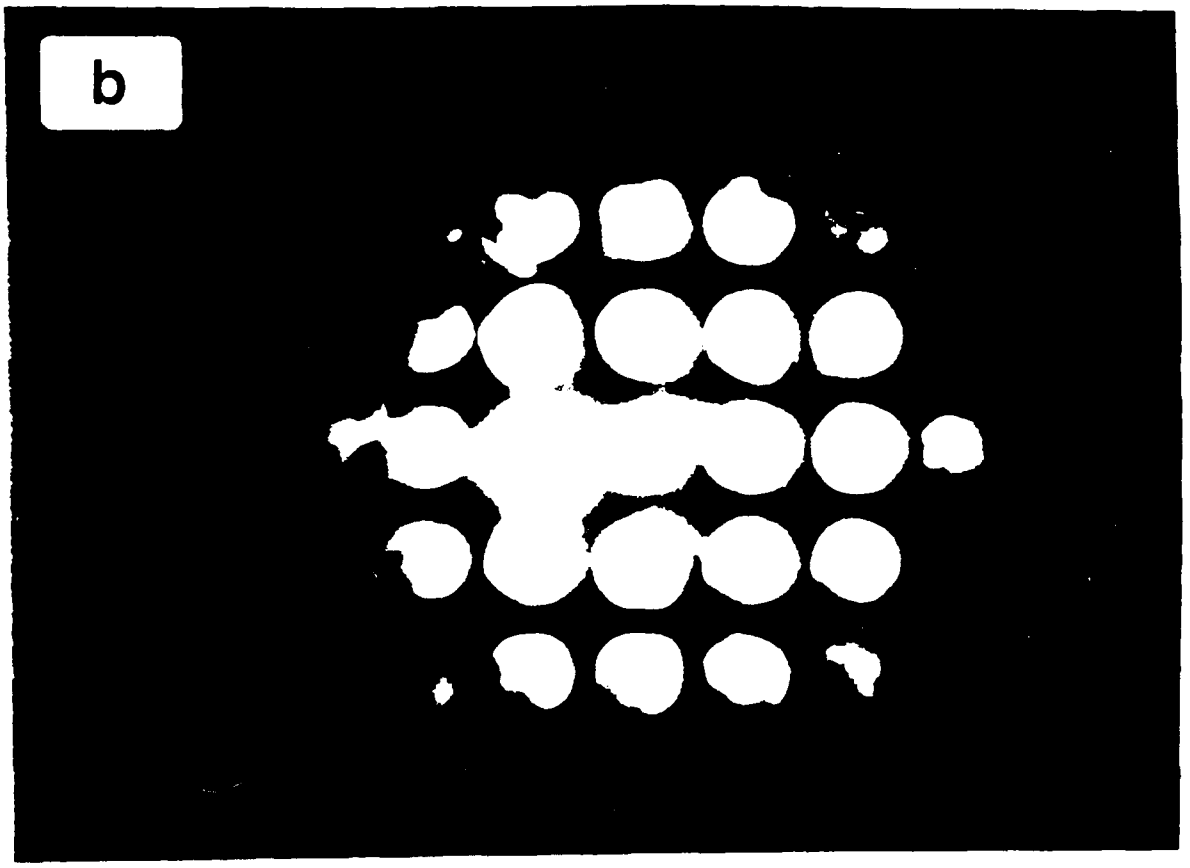
b

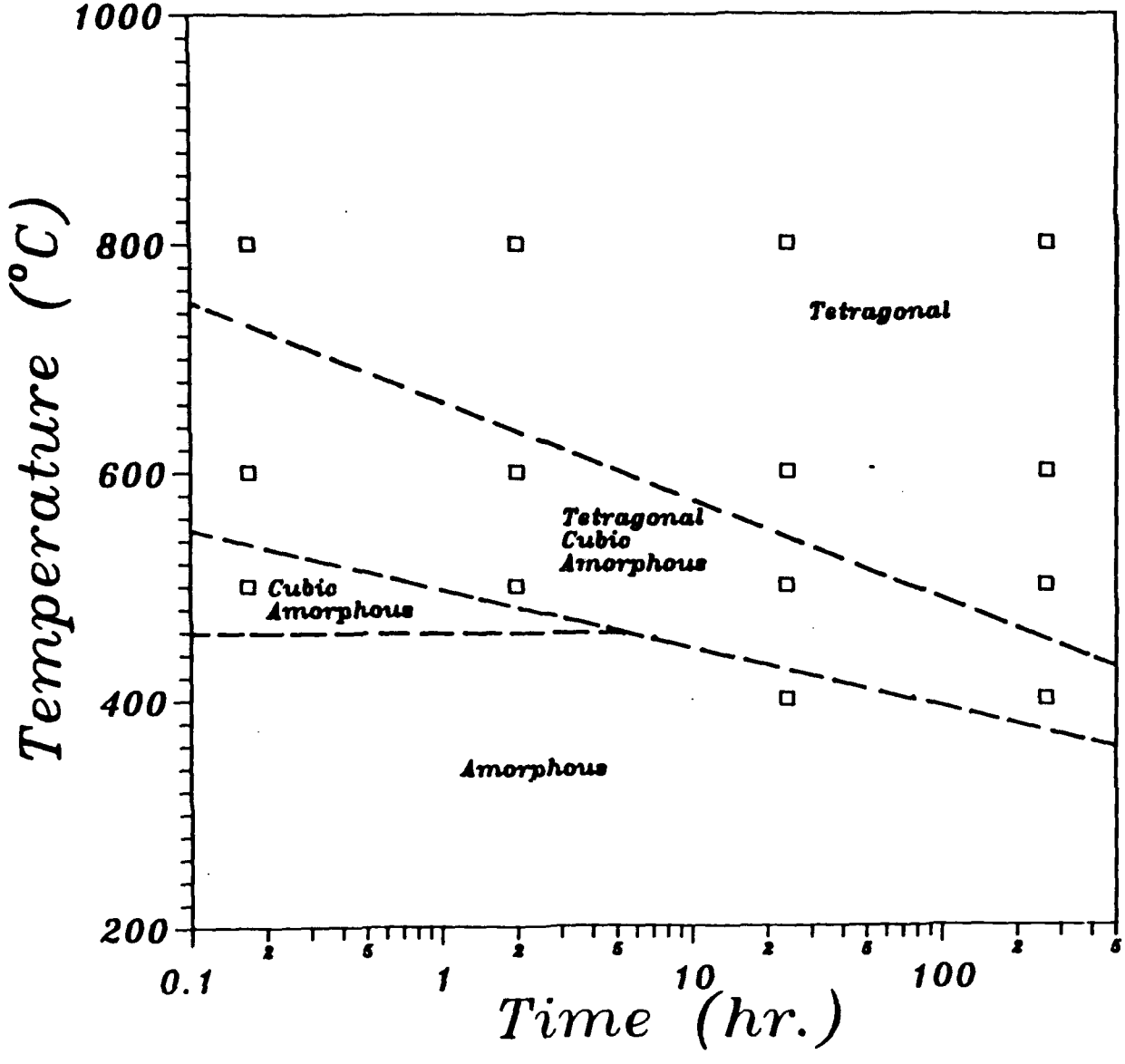
1000
800
600
400
200
Temperature (°C)
Tetragonal
Tetragonal
Cubic
Amorphous
Cubic
Amorphous
Amorphous
0.1
1
10
100
Time (hr.)

APPENDIX 11

STUDIES ON POLYMERIC $Pb(Mg_{1/3}Nb_{2/3})O_3$ GELS

P. Ravindranathan
E. Brevel
S. Komarneni
R. Roy

STUDIES ON POLYMERIC $Pb(Mg_{1/3}Nb_{2/3})O_3$ GELS

P. RAVINDRANATHAN, E. BREVAL, S. KOMARNENI [1] and R. ROY
Materials Research Laboratory, The Pennsylvania State University, University Park, PA 16802, USA

Received 20 March 1989; in final form 4 April 1989

Sol–gel method is gaining importance in the field of electronic ceramic materials. It is important to study the structure of the gels before processing to final product. Lead-, magnesium-, niobium- and titanium-containing gels of different composition have been prepared and characterized by TEM. The TEM study revealed that the as-prepared gels have a coarse texture and showed some crystallites of a few nanometer in size. Analyses by EDS and SAEDP indicated that phase separation exists on a very fine scale.

1. Introduction

Sol–gel processing is one of several methods currently under investigation for the preparation of electronic and high-technology ceramic materials. Due to the intrinsic nature of the synthetic schemes available, sol–gel processing offers significant advantages (e.g. higher purity, molecular homogeneity, reduced processing temperatures and unique fabrication opportunities) over conventional processing methods [1,2]. Recently we have reported the importance of the sol–gel process for the preparation of electronic ceramics in a review paper [3]. The importance and the application of the sol–gel process will be understood only if we know the chemistry of the precursor or gels. The chemistry of the gelation step normally involves the controlled hydrolyses of single- or multi-component alkoxides to form a three-dimensional network of metal–oxygen linkages. Part of the versatility of the sol–gel technique arises from the fact that soluble inorganic salts can be incorporated into these networks, either by actual chemical reaction or simple entrapment in the gelled matrix. Several groups have recently taken advantage of the solvating ability of 2-methoxyethanol to develop synthetic schemes for the preparation of a series of lead-containing perovskite materials in the PT, PLZT system using lead acetate as the precursor [4,5]. Dey et al. [6] have reported the structure of polymeric $PbTiO_3$ gels using transmission electron microscopy.

Previously we have reported [3] the sol–gel processing of lead magnesium niobate having perovskite structure. In the present investigation the physical structure of several gel compositions such as $Pb(Mg_{1/3}Nb_{2/3})O_3$ (PMN), $0.9Pb(Mg_{1/3}Nb_{2/3})O_3$–$0.1PbTiO_3$ (PT), and $0.65Pb(Mg_{1/3}Nb_{2/3})O_3$–$0.35PbTiO_3$ have been studied by transmission electron microscopy (TEM).

2. Experimental

Complex alkoxide of PMN (A) was prepared by reacting lead acetate, $Pb(CH_3COO)_2 \cdot 3H_2O$ with magnesium ethoxide, $Mg(OC_2H_5)_2$ and niobium ethoxide, $Nb(OC_2H_5)_5$, in methoxyethanol. Details of the complete reaction procedure are given for the PMN gels in our earlier paper [3]. In the preparation of 0.9PMN–0.1PT (B) and 0.65PMN–0.35PT (C) gels, titanium isopropoxide was used as titanium source. Titanium isopropoxide was added to the solution containing $Mg(OC_2H_5)$ and $Nb(OC_2H_5)_5$ in methoxyethanol to prepare PMN–PT gels. Complex alkoxide solution was hydrolysed with a stoichiometric amount of water mixed with methoxyethanol and allowed to gel at room temperature. The gels were heated at 325°C for 1 h and calcined at 775°C for 2 h to form the respective oxides.

[1] Also with the Department of Agronomy.

0167-577x/89/$ 03.50 © Elsevier Science Publishers B.V.
(North-Holland Physics Publishing Division)

Samples for TEM analysis were prepared from a diluted suspension of the as-prepared gel powder and from the ground calcined material in isopropanol. A drop of this suspension was transferred to a carbon-coated grid which was again carbon-coated after drying. The specimens were studied using TEM (Philips EM420, 120 kV) fitted with an energy-dispersive spectrometer (EDS, LINK). Care was taken not to intensify the electron beam on the specimen while studying the gels in TEM. Selected area electron diffraction patterns (SAEDP) were obtained to study the crystal structure and the crystallinity of the material. A semiquantitative EDS determination was used to get spectra of elemental analysis of the gels and was done either from many particles to give average composition or from single crystalline particles. Convergent beam electron diffraction (CBED) was also obtained to get diffraction patterns from the particles. The probe size both for EDS spectra and CBED patterns ranged from 20 to 40 nm. In some cases EDS spectra were obtained from regions of 100 to 500 nm. The reflections in the diffraction patterns were used to determine the phase distribution. The {001} and {110} reflection from the perovskite occurring at 4.1 and 2.8 Å, respectively, identified the perovskite phase while the pyrochlore phase was identified by its {222} reflection at 3.0 Å.

3. Results and discussion

Bulk gels of all the three samples were transparent and yellow in color. They were amorphous to X-rays and remained so even after heating the gel up to 400°C. Gels dried at room temperature and calcined at 775°C for 2 h were studied by TEM. Careful TEM investigations of the as-dried gel materials (A, B and C) showed amorphous nature giving a diffuse ring pattern at ≈ 3 Å and with a grain size of 5–10 nm. A typical TEM bright field image of the PMN gel is shown in fig. 1. The gel appears to be coarse in texture. Dark field image of the same gel shows scattered grains of a few nanometer in size in all specimens (A, B and C). An example of a dark field image of the PMN gel highlighting the crystallites is shown in fig. 2. Analysis by EDS indicated homogeneity of Pb, Mg and Nb on a fine scale in gel A, whereas in the other two gels (B and C), the crystallites contain

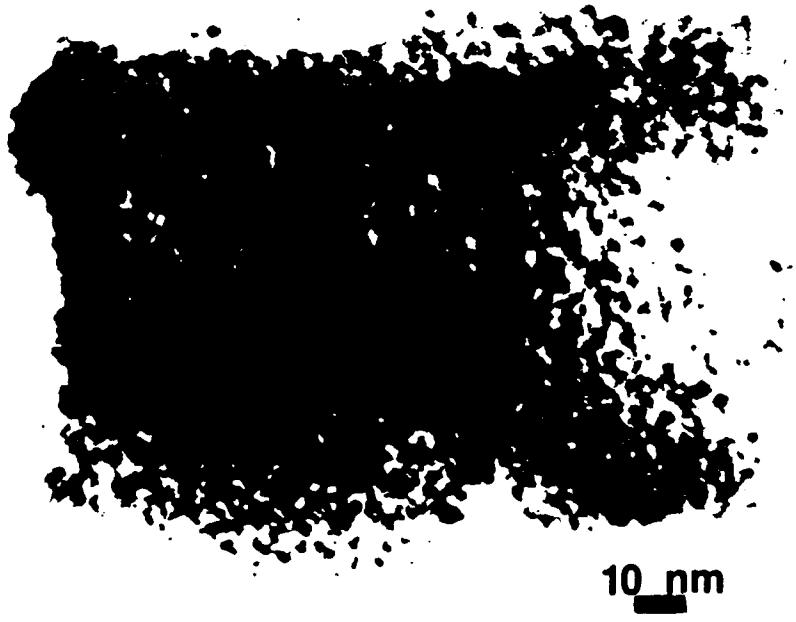

Fig. 1. TEM bright field image of PMN gel.

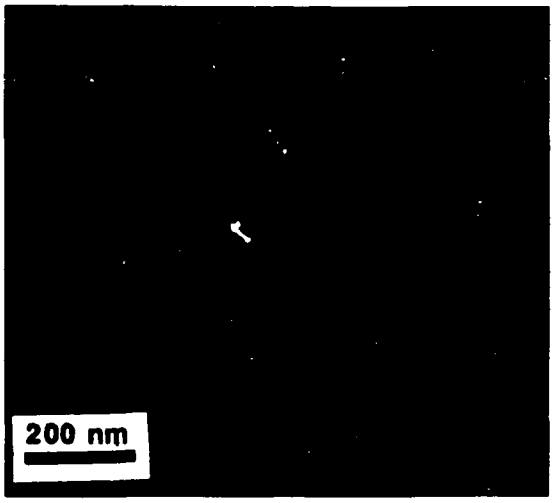

Fig. 2. TEM dark field image of 0.9PMN–0.1PT gel.

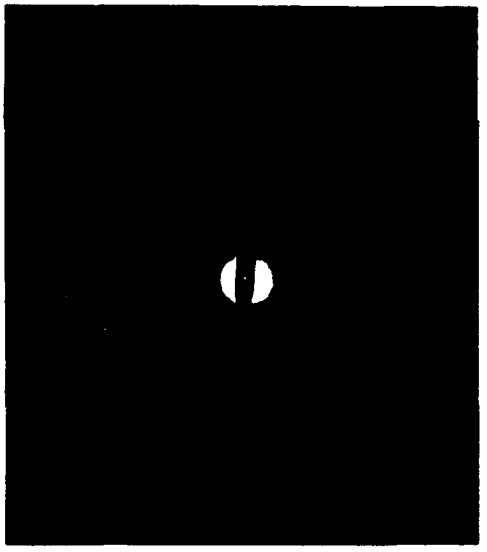

Fig. 3. Selected area diffraction pattern of PMN gel.

more titanium. Electron diffraction pattern for a typical as-prepared PMN gel (fig. 3) shows a diffuse ring at ≈ 3 Å from the amorphous material and a few spots from the scattered crystalline grains. Similar observations were made in $PbTiO_3$ gels prepared under basic conditions indicating inhomogeneous cation distribution on a fine scale [6]. Analysis by CBED from many single grains revealed that the largest "d" value to be observed was 4.2 Å corresponding to the {001} reflection of perovskite. The phenomenon of phase separation in gels was also observed by Schaefer and Keefer [7,8]. Recently, Low and McPherson [9] also reported phase separation which is attributed to the unfavorable free energy of mixing and/or the inherent polymerization and condensation of polymer species in gels. Brinker and Scherer [10] pointed out that hydrolysis conditions during the process of gelation favor phase separation in gels. They believed that the process of phase separation could be completely suppressed in acid-catalysed gels as observed by Brinker et al. [8] and Nogami and Moriya [11]. Acid-catalysed gels of A, B and C were prepared and the TEM study revealed that the chemical composition was homogeneous to a certain extent but phase separation persisted on a very fine scale. Hence it is very unlikely that phase separation in gels can be completely suppressed although its scale may be monitored to approach, but not reach, single phase.

When the gels were exposed to a strong electron beam for some time, a larger number of crystalline grains were seen in the dark field image of TEM. It may be due to the interaction of the electron beam with the gel which causes this effect. The SAEDP from the material exposed to electron beam for long time gave mainly perovskite lines while a few pyrochlore lines were also observed. When gel C is exposed to strong electron beam, the SAEDP gave only perovskite lines and pyrochlore lines were found neither in SAEDP nor in CBED (fig. 4). This may be due to the addition of PT, which stabilizes the formation of perovskite phase.

The calcined gels at 775°C were also examined by TEM and X-ray powder diffraction, which indicate the formation of perovskite phase with some pyrochlore phase. The calcined material from all three gel compositions consisted mainly of perovskite phase.

4. Conclusion

Studies of PMN–PT sol–gels by TEM reveal that phase separation occurs on a very fine scale due to differing hydrolysis rates of the chemical species involved.

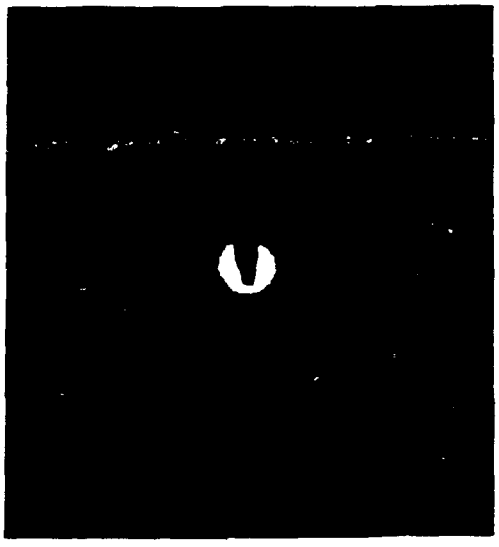

Fig. 4. Selected area diffraction pattern of 0.65PMN–0.35PT gel.

Acknowledgement

This research was supported by the Office of Naval Research Contract No. N00014-86-K-0767.

References

[1] S.P. Mukherjee, J. Non-Cryst. Solids 42 (1980) 477.
[2] H. Dislich, J. Non-Cryst. Solids 57 (1983) 371.
[3] P. Ravindranathan, S. Komarneni, S.C. Choi, A.S. Bhalla and R. Roy, Ferroelectrics 7 (1988) 810.
[4] J.B. Blum and S.R. Gurkovich, J. Mater. Sci. 20 (1985) 4479.
[5] K.D. Budd, S.K. Dey and D.A. Payne, Proc. Brit. Ceram. Soc. 36 (1985) 107.
[6] S.K. Dey, K.D. Budd and D.A. Payne, J. Am. Ceram. Soc. 70 (1987) C295.
[7] D.W. Schaefer and K.D. Keefer, in: Better ceramics through chemistry, eds. C.J. Brinker, D.E. Clark and D.A. Ulrich (North-Holland, Amsterdam, 1984) p.1.
[8] C.J. Brinker, K.D. Keefer, D.W. Schaefer and C.S. Ashley, J. Non-Cryst. Solids 48 (1982) 47.
[9] I.M. Low and R. McPherson, J. Mater. Sci. 23 (1988) 4141.
[10] C.J. Brinker and G.W. Scherer, J. Non-Cryst. Solids 70 (1985) 301.
[11] M. Nogami and Y. Moriya, J. Non-Cryst. Solids 37 (1980) 191.

APPENDIX 12

SOLID-STATE EPITAXIAL EFFECTS IN STRUCTURALLY DIPHASIC XEROGEL OF $Pb(Mg_{1/3}Nb_{2/3})O_3$

P. Ravindranathan
S. Komarneni
R. Roy

SOLID-STATE EPITAXIAL EFFECTS IN STRUCTURALLY DIPHASIC XEROGEL OF $Pb(Mg_{1/3}Nb_{2/3})O_3$

P. Ravindranathan*, S. Komarneni*+ and R. Roy*

Materials Research Laboratory
The Pennsylvania State University
University Park, PA 16802

J. Am. Ceram. Soc. Communications

*Member, American Ceramic Society
+Also with the Department of Agronomy

ABSTRACT

Lead magnesium niobate (PMN), $Pb(Mg_{1/3}Nb_{2/3})O_3$, with perovskite structure has been prepared using structurally diphasic PMN gels. Diphasic gels were made using various concentrations of perovskite PMN seeds. The unseeded gel calcined at 775°C for 2hr gave ~98% of perovskite PMN phase. The use of 1% PMN perovskite seed not only led to a pure perovskite phase but also lowered the crystallization temperature of these gels by about 75°C. These results show that the use of structural nanoheterogeneity helps to lower the crystallization temperature and to stabilize the perovskite phase.

[Key words: diphasic xerogel, epitaxy, lead magnesium niobate, crystallization.]

INTRODUCTION

Lead magnesium niobate, $Pb(Mg_{1/3}Nb_{2/3})O_3$ (PMN), is an important ferroelectric relaxor material. It has shown great promise for application in both capacitors and electrostrictive actuators (1,2). A significant problem, however, exists in the preparation of this material i.e., it is very difficult to prepare the phase with only perovskite structure. Usually, an unwanted pyrochlore phase also forms during the processing of PMN. The pyrochlore phase deteriorates the dielectric property. Depending upon the processing conditions, the amount of pyrochlore phase will vary. A few methods have been reported in the literature (3-5), in which perovskite PMN has been synthesized but the temperature of formation is high. Swartz and Shrout (3) prepared perovskite PMN at 800°C using columbite precursor, which was in turn prepared at 1000°C. Even with the above method a small amount (≤2%) of pyrochlore was observed.

It is well known that sol-gel method is widely employed to prepare ceramic oxides at low temperature. The other advantages are high purity, molecular homogeneity, better control of stoichiometry and formation of ultrafine powders. Recently, there is a considerable interest in making electroceramics by the sol-gel process. We have recently reported the importance and the preparation of perovskite PMN by sol-gel method (6). Our results showed that pure perovskite phase can be formed at a temperature as low as 775°C.

A recent innovation of the sol-gel process is to make maximally heterogeneous materials. The new concept has resulted in a family of nanocomposites, a new class of di- or multiphasic materials where the two or more phases may differ in composition (7-10) or in structure (11). These structurally diphasic materials with crystalline seeds in amorphous or semicrystalline gels of the same composition appear to be highly promising for densification and in radically lowering the ceramic processing temperatures. Our present experiments use the sol-gel route to make diphasic xerogels of PMN which are nanocomposites and which serve as precursors for making perovskite PMN at very low temperatures. In this paper, the effect of PMN seeds in lowering the crystallization temperature of PMN is reported.

EXPERIMENTAL PROCEDURE

Complex alkoxide solution was prepared by reacting lead acetate, $Pb(CH_3COO)_2 \cdot 3H_2O$,* with magnesium ethoxide, $Mg(OC_2H_5)_2$,* and niobium ethoxide, $Nb(OC_2H_5)_2$*. Water associated with lead acetate was removed by dissolving and refluxing lead acetate at 125°C in methoxyethanol in flowing argon atmosphere in a two neck reaction flask. Then a mixture of $Mg(OC_2H_5)_2$ and $Nb(OC_2H_5)_5$ in methoxyethanol was added and heated at 110°C for 12 hrs to form complex alkoxide. The resulting solution was hydrolyzed with water in methoxyethanol and allowed to gel at room temperature.

The PMN gel prepared by the above procedure was calcined at 775°C for 2 hrs with an intermediate heating step at 325°C for 1 hr to remove the organics. The calcined powders were characterized by x-ray powder diffraction (XRD) and transmission electron microscopy (TEM). These powders were used as seeds, by dispersing them in methoxyethanol in an ultrasonifier. The particles forming the stable sol are crystalline (perovskite PMN) and approximately 200 nm in size.

The PMN seed sol was added to the complex alkoxide solution and stirred vigorously. The gelation occurred within 24 hrs. The addition of seed to the solution prior to gelation led to the structurally diphasic gel. This diphasic PMN gel was dried at room temperature and calcined at different temperatures.

Since the crystallization of PMN does not lead to a clear exotherm during differential thermal analysis powder x-ray diffraction (XRD) was utilized to determine the temperature of crystallization. The XRD was carried out for the gel fired at various temperatures. The relative amount of pyrochlore and perovskite phases were determined by measuring their respective 100% intensity peaks [i.e. (110) for perovskite; (222) for pyrochlore]. The percentage of perovskite phase was calculated by using the following equation

$$\% \text{ perovskite} = \frac{I_{perovskite} \times 100}{(I_{perovskite} + I_{pyrochlore})}$$

* Aldrich, Milwaukee, Wisconsin.

RESULTS AND DISCUSSION

The as-dried unseeded gel powder was found to be amorphous by XRD. Differential thermal analysis of the gel showed an exotherm at 320°C which is due to the oxidation of organics present in the gel. The gel powder calcined in air at 775°C showed the formation of perovskite phase (~98%). Cubic pyrochlore phase was observed as an intermediate product below 700°C prior to the perovskite phase formation. With our earlier observation (6) and from other reports (2,3) it is concluded that formation of perovskite phase from pyrochlore phase may be a kinetic problem. In fact, pure perovskite phase was obtained at 700°C after heating the PMN gel for 120 hrs.

The percentage of perovskite phse formed from the structurally diphasic PMN gels with various concentration of seeds heated at various temperature is shown in Fig. 1. The data show that seeding with as little as 1% of PMN nuclei lowered the formation temperature of perovskite phase by about 75°C compared to the unseeded gel. With 5% seed, pure perovskite (100%) phase was prepared at a temperature as low as 675°C. The x-ray powder diffraction pattern of the structurally diphasic gel with 5% seeds and calcined at 675°C for 2 hrs is shown in Fig. 2. Figure 2 clearly shows the formation of pure perovskite phase. With increasing seed concentration, the amount of perovskite phase increased (Fig. 1). It is clear from these results that a significant lowering of the formation temperature occurred upon seeding by some form of solid-state epitaxial reaction. These results are in agreement with the concept of "nucleation and epitaxial growth," which is believed to govern the reactions occurring in isostructurally seeded gels (12). The expected equilibrium phase (perovskite) can grow from the gel matrix onto the provided nuclei along certain crystallographic directions. This type of heterogeneous nucleation eliminates the need for the system to exceed the activation energy required for the formation of the nuclei as in the case of a system with homogeneous nucleation. As a result, the perovskite phase can crystallize at a lower temperature (13).

The influence of 1% concentration of PMN seeds in structurally diphasic gels on the crystallization of perovskite PMN phase at 675°C has also been studied as a function of time and the results are plotted in FIg. 3. It is clear from Fig. 3 that it is possibel to get 100% perovskite

phase after heating the diphasic gel for 50 hrs. Thus, as pointed out above, isostructural seeding works via epitaxial growth on the nuclei provided, thereby lowering the crystallization temperature in the structurally diphasic gels.

CONCLUSION

This study has demonstrated that isostructural seeding not only lowered the formation temperature of perovskite PMN very substantially (≥75°C) but also stabilized the perovskite phase. The lowering of the crystallization (formation) temperature in structurally diphasic gels can be explained by an epitaxial growth mechanism.

REFERENCES

1. L.E. Cross, S.J. Jang, R.E. Newnham, S. Nomura and K. Uchino, "Large Electrostrictive Effects in Relaxor Ferroelectrics," Ferroelectrics 23 [3-4] 187-92 (1980).

2. M. Lejeune and J.P. Boilet, "$Pb(Mg_{1/3}Nb_{2/3})O_3$ (PMN) Multilayer Capacitors," J. De Physique, Colloque C1, C1-895-98 (1986).

3. S.L. Swartz and T.R. Shrout, "Fabrication of Perovskite Lead Magnesium Niobate," Mat. Res. Bull., 17 1245-50 (1982).

4. J.P. Guha and H.V. Anderson, "Preparation of Perovskite $Pb(Mg_{1/3}Nb_{2/3})O_3$ Using $Pb_3Nb_2O_8$ and MgO," J. Am. Ceram. Soc., 69 [11] C-287 - C-288 (1986).

5. Harold S. Horowitz, "Low Temperature Synthesis Route to $MgNb_2O_6$," J. Am. Ceram. Soc., 71 (5) C-250 - C-251 (1988).

6. P. Ravindranathan, S. Komarneni, A.S. Bhalla, R. Roy and L.E. Cross, "Sol-Gel Processing of Lead Magnesium Niobate (PMN) Powder and its Characterization," pp. 182-89 *in* Ceramic Transactions, Ceramic Powder Science, Vol. 1, Edited by G.L. Messing, E.R. Fuller, Jr. and Hans Hausner, Am. Ceram. Soc. (1988).

7. R.A. Roy and R. Roy, "Diphasic Xerogels: I. Ceramic-Metal Composites," Mat. Res. Bull., 19 169-177 (1984).

8. D. Hoffman, R. Roy and S. Komarneni, "Diphasic Ceramic Composites via a Sol-Gel Method," Mat. Lett., 2 245-47 (1984).

9. D. Hoffman, R. Roy and S. Komarneni, "Diphasic Xerogels, A New Class of Materials: Phases in the System Al_2O_3-SiO_2," J. Am. Ceram. Soc., 67 468-71 (1984).

10. D. Hoffman, S. Komarneni and R. Roy, "Preparation of a Diphasic Photosensitive Xerogel," J. Mat. Sci. Lett., 3 439-42 (1984).

11. R. Roy, Y. Suwa and S. Komarneni, "Nucleation and Epitaxial Growth in Diphasic (Crystalline + Amorphous) Gels," pp. 247-258 *in* Ulrastructure Processing of Ceramics, Glasses and Composites, Vol. 2, Edited by L.L. Hench and D.R. Ulrich, Wiley, New York (1986).

12. Gabriel Vilmin, S. Komarneni and R. Roy, "Crystallization of $ThSiO_4$ from Structurally and/or Compositionally Di-phasic Gels," J. Mat. Res., 2(4) 489 (1987).

13. R.A. Shellemarr and G.L. Messing, "Liquid Phase Assisted Transformation of Seeded γ-Alumina," J. Am. Ceram. Soc., 71 [5] 317-22 (1988).

FIGURE CAPTIONS

Figure 1. Percentage of perovskite phase vs. temperature for the PMN gel with various concentration of seeds.

Figure 2. X-ray powder diffraction pattern of diphasic gel calcined at 675°C, 2 hrs.

Figure 3. Percentage of perovskite phase vs. calcination time at 675°C for the 1% seeded PMN gel.

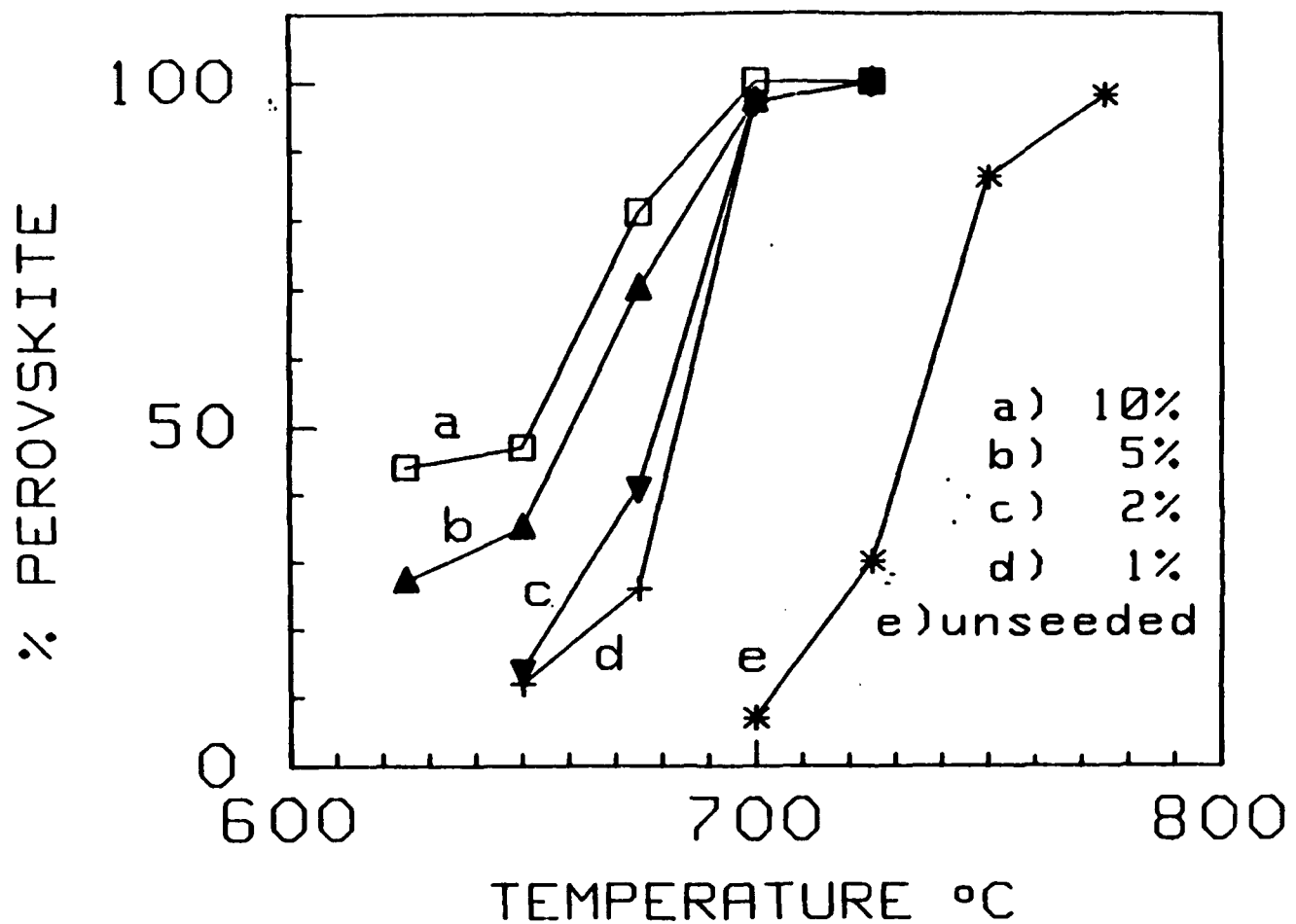
100
50
0
% PEROVSKITE
600
700
800
TEMPERATURE °C
a
b
c
d
e
a) 10%
b) 5%
c) 2%
d) 1%
e) unseeded

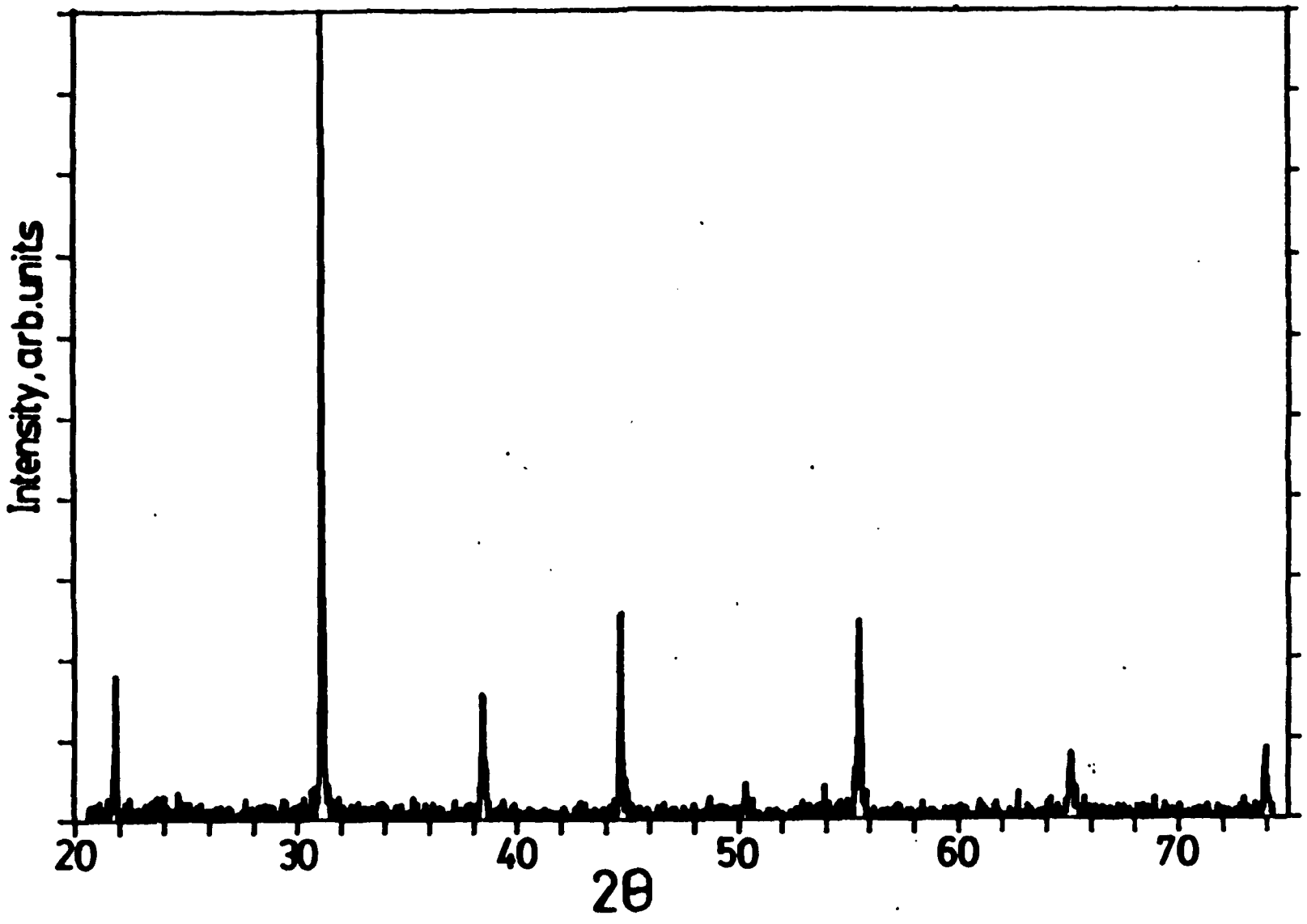
Intensity, arb.units
20
30
40
50
60
70
2θ

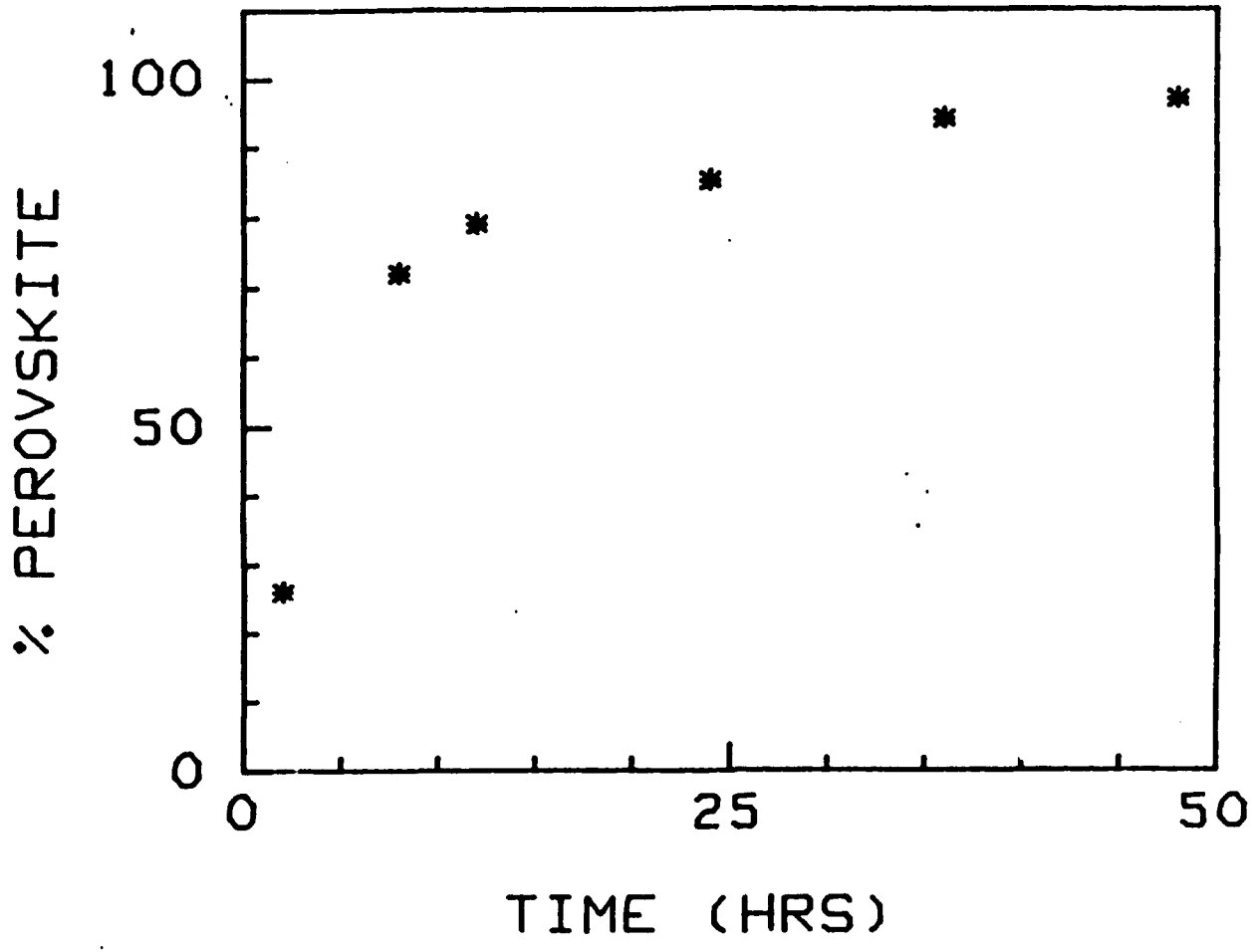
100
50
0
% PEROVSKITE
0
25
50
TIME (HRS)

APPENDIX 13

SYNTHESIS OF ULTRA-FINE AlN POWDERS BY THE REACTIVE ELECTRODE SUBMERGED-ARC METHOD (RESA)

T. Ono
P. W. Brown
J. H. Adair
P. Ravindranathan

SYNTHESIS OF ULTRA-FINE AlN POWDERS BY THE REACTIVE-ELECTRODE SUBMERGED-ARC METHOD (RESA)

Toru Ono, Paul W. Brown, James H. Adair and P. Ravindranathan
Materials Research Laboratory
The Pennsylvania State University
University Park, State College, PA 16802

The RESA method was applied to fabrication of ultra-fine aluminum nitride powders at low temperature. Pure aluminum rods were used for the electrodes and liquid nitrogen or liquid ammonia for the dielectric fluid. Powders formed in liquid nitrogen were a mixture of γ-aluminum oxide, aluminum and hexagonal aluminum nitride. Most of the particles were spherical, with sizes ranging from 5 to100 nm; a few small polyhedral particles were also observed. Powders formed in liquid ammonia were a mixture of hexagonal aluminum nitride and aluminum. The particles consisted of large polyhedral particles (30-100 nm) and super-fine particles (less than 10 nm).

INTRODUCTION

Ultra-fine ceramic powders are attractive for new applications. Komarneni et al. reported the controllability of the microstructure[1] and the lowering of crystallization temperature[2] by using ultra-fine particles. The phenomenon of atom movement in ultra-fine particles[3] is one of the unique characteristics they exhibit. A variety of methods, such as sol-gel processing,[4] plasma method[5] and spark erosion,[6] have been applied to the fabrication of ultra-fine powders. Kumar and Roy introduced a new method for the fabrication of ultra-fine ceramic powders, called RESA, Reactive-Electrode Submerged-Arc, and reported syntheses of various oxides[7] and carbides.[8] As a further step, we have applied RESA to the fabrication of ultra-fine

nitride particles. The synthesis of aluminum nitride is the subject of the investigation. Because of its high electrical resistivity, high thermal conductivity and translucency, aluminum nitride is one of most promising materials for electronic devices, especially for super integrated circuits which emit large amounts of heat.[9] In this paper, AlN powders fabricated using liquid nitrogen and liquid ammonia were analyzed using X-ray diffraction (XRD), transmission electron miroscopy (TEM), energy dispersive analysis of emitted X-rays with an ultra thin window for light elements (UTW), and surface area analysis.

EXPERIMENTAL

Apparatus

A schematic of RESA apparatus is shown in Fig. 1. Two high purity aluminum rods were used as the reactive-electrodes and submerged in liquid nitrogen or liquid ammonia in a thermally insulated glass container. A welding transformer, which produces a high AC current, is used as the power source for the arc. One of the electrodes can be moved by a linear actuator; the other is fixed. The applied current is detected by a current sensor and monitored. Automatic operation is possible by comparing the set current and the applied current. If the applied current is lower than the set current, the controller sends a signal to move the electrodes closer together to maintain the proper distance for a stable arc.

Synthesis of Powders

When an arc occurs between the electrodes, the temperature of the area around the arc becomes extremely high. Both the electrode metal and the dielectric fluid are locally evaporated, atomized and/or ionized, and react in certain temperature range. The products are rapidly cooled by the surrounding dielectric fluid. Fig. 2 shows an idealized arc spot. In the figure, isotherms are idealized as concentric circles, where 2743 K is the boiling point of aluminum, ≅2700 K is the decomposing point of aluminum nitride, 934 K is the melting point of aluminum, and 77 K is the boiling point of nitrogen under 1 atm.. Powders were readily synthesized in liquid ammonia. However, yields of powders synthesized in liquid nitrogen were extremely low.

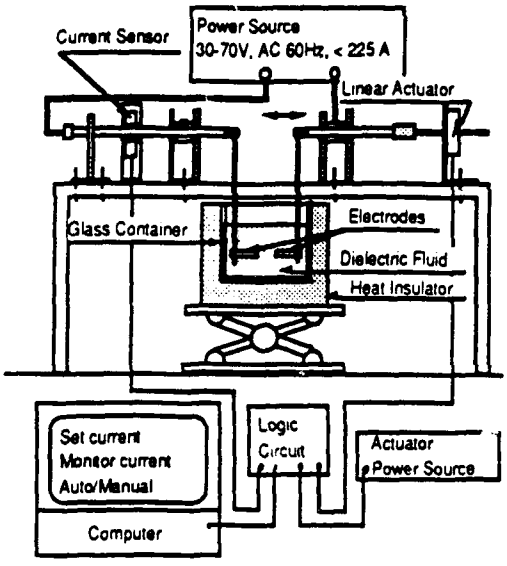

Fig. 1. Schematic of RESA apparatus.

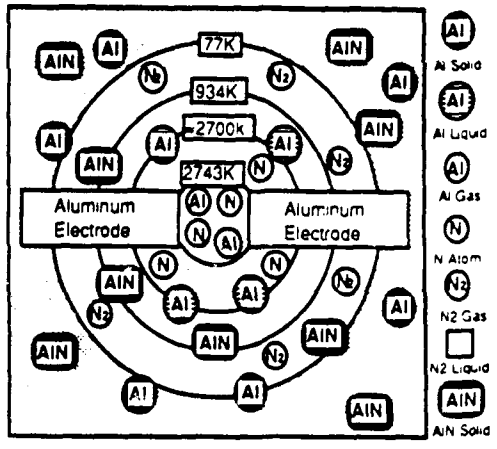

Fig. 2. An idealized arc spot.

Treatment of Powders

After the synthesis procedure was terminated, the remaining dielectric fluid was immediately evaporated, and the glass container washed to detach the powders from the container wall using low polarity liquid such as tertiary butyl alcohol. The powder-butanol slurry was sonicated. The samples for TEM and UTW were taken from this slurry and dropped directly on the sample holder. The rest of slurry was freeze-dried, and the powders collected. The powders are characterized by XRD, TEM, UTW, and surface area analysis.

RESULTS AND DISCUSSION

XRD

XRD patterns of powders obtained using liquid nitrogen and liquid ammonia are shown in Fig. 3 and 4, respectively. According to the JCPDS files, the common peaks in the figures result from aluminum metal (4-787) and aluminum nitride (25-1133). The extra peaks in Fig. 3 are very close to those of cubic aluminum nitride (34-678) or of γ-aluminum oxide (10-425), but it is impossible to identify the compounds responsible for these peaks by XRD alone.

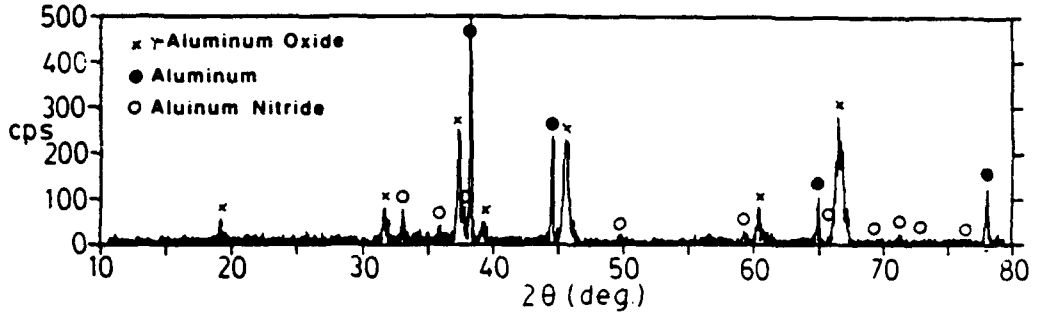

Fig. 3. XRD pattern of powders synthesized in liquid nitrogen.

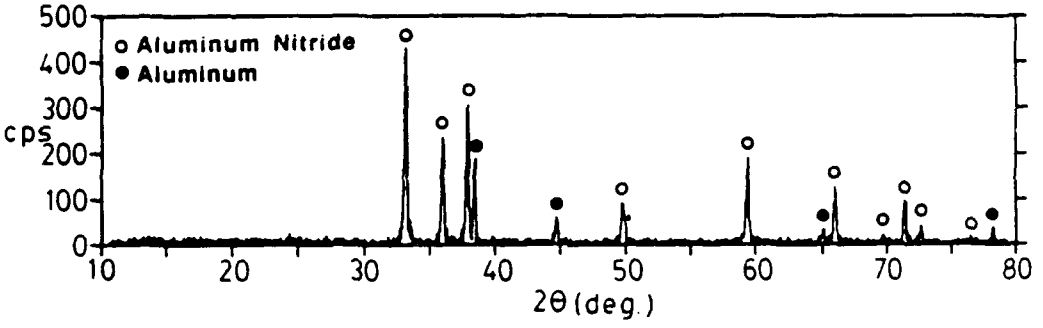

Fig. 4. XRD pattern of powders synthesized in liquid ammonia.

TEM

A TEM micrograph of powders from liquid nitrogen is shown in Fig. 5. The powders consist mostly of spherical particles with a few polyhedral particles also present. The range of diameters for the spherical particles is about 5-100 nm. The diffraction pattern shows some rings and obvious bright spots, which fit both γ-aluminum oxide (JCPDS#10-425) and cubic aluminum nitride (JCPDS#34-679). A TEM micrograph of powders obtained from liquid ammonia is shown in Fig. 6-(a). There are no spherical particles but, rather, larger (30-100 nm) polyhedral particles and smoke like concentrations of super-fine particles. A diffraction pattern taken from this region indicates hexagonal aluminum nitride. As shown in Fig. 6-(b), an amorphous pattern is observed in the super-fine particle region in the same sample.

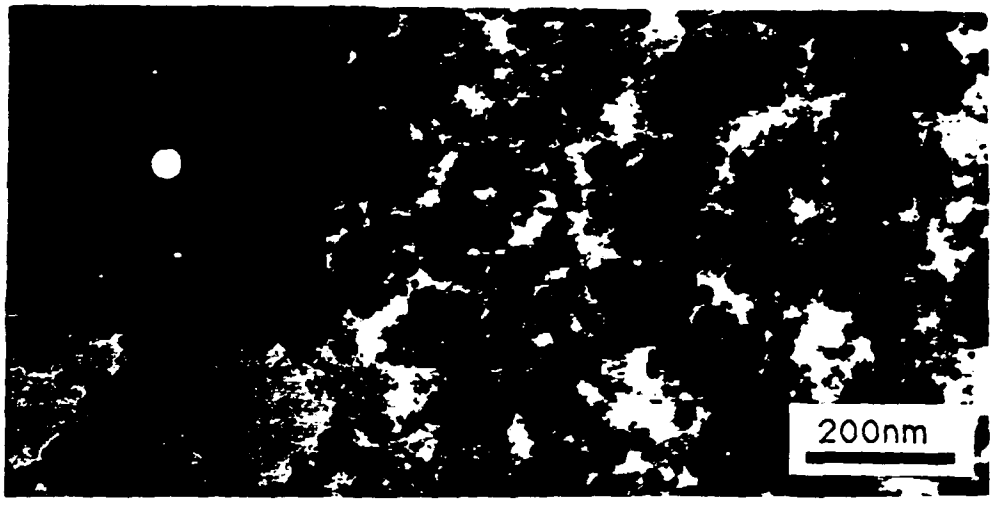

Fig. 5. TEM micrograph and diffraction pattern of powders formed in liquid nitrogen.

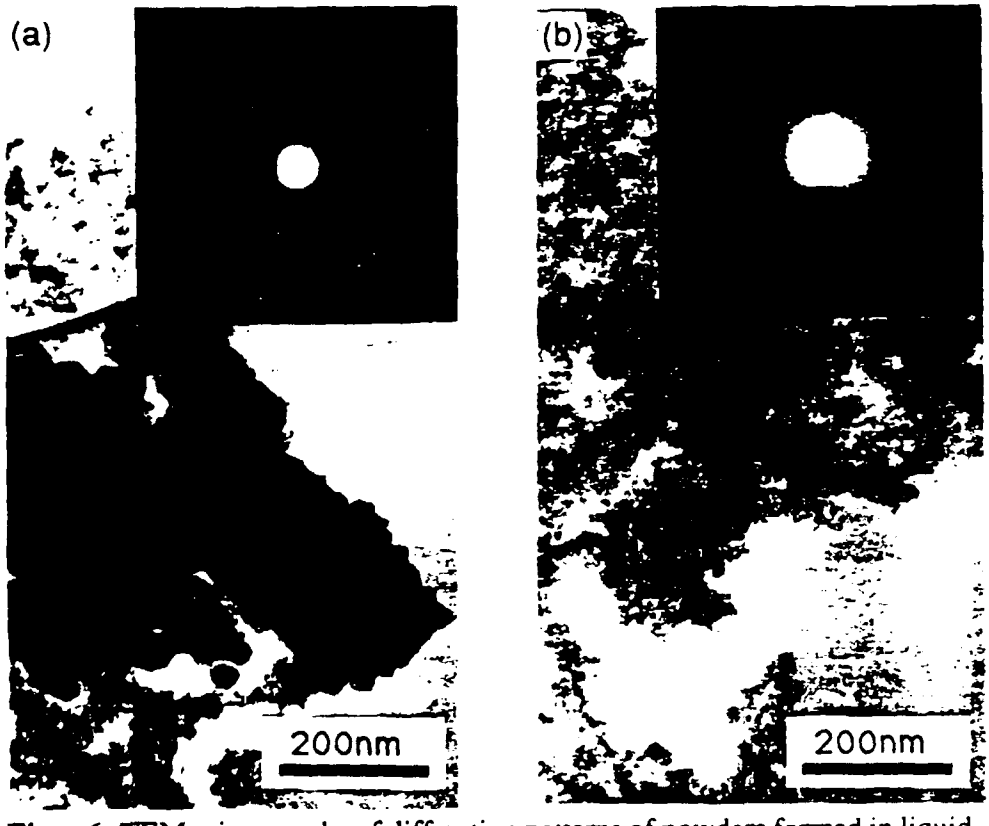

Fig. 6. TEM micrographs of diffraction patterns of powders formed in liquid ammonia: (a) rather large particles, and (b) super-fine particles.

UTW

Typical UTW patterns for powders prepared in nitrogen and ammonia are shown in Fig. 7 and 8, respectively. Powders synthesized in liquid nitrogen show few nitrogen counts. On the other hand, the powders prepared in ammonia contain significant nitrogen, although oxygen is also present.

The reason for presence of oxygen in the powders synthesized in liquid ammonia is currently being investigated. It may be associated with post-synthesis oxidation. These data suggest that the unassigned XRD peaks shown in Fig. 3 for powders prepared in liquid nitrogen are in fact γ-Al_2O_3 peaks. The very low yields of powder support the conclusion that AlN formation is not favorable in liquid nitrogen. The formation of γ-Al_2O_3 is associated with the presence of contaminant oxygen in the system. γ-Al_2O_3 also forms when water is used as the dielectric fluid.[7]

While this is evidence for the formation of hexagonal and amorphous AlN, the formation of the cubic polymorph reported by Kieffer et al.[10] has not been observed. That γ-Al_2O_3 forms in some instances combined with the coincidence of the γ-Al_2O_3 and cubic AlN diffraction peaks may warrant reconsideration of the existence of the latter.

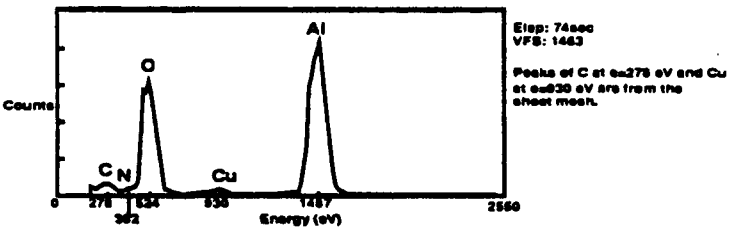

Fig. 7. UTW of powders formed in liquid nitrogen.

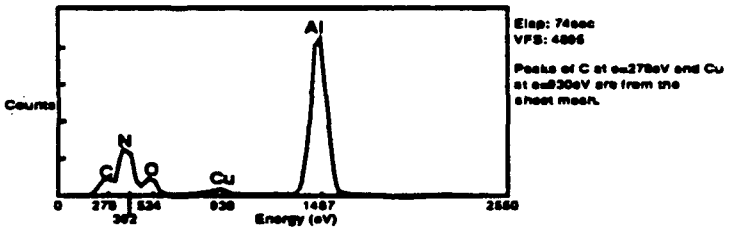

Fig. 8. UTW of powders formed in liquid ammonia.

SURFACE AREA ANALYSIS

The results of surface area analysis and calculated average diameters (assumed spheres) are shown in Table 1. For powders synthesized in liquid nitrogen, the calculated values of average diameter are in accord with sizes observed in the TEM micrographs. The calculated diameters of powders synthesized in liquid ammonia show intermediate values between large particles and super-fine particles observed in TEM. The large surface areas observed by surface area analysis are consistent with the formation of very fine and highly reactive particles.

Table 1. Specific surface area and calculated average diameter of powders

Powders Using Liquid Nitrogen		Powders Using Liquid Ammonia	
Surface Area (m^2/g)	Diameter (nm)	Surface Area (m^2/g)	Diameter (nm)
37.0	40.7(for 100% Al_2O_3) 60.0(for 100% Al) 50.7(for AlN)	278.8	8.0(for 100% Al) 6.7(for 100% AlN)

CONCLUSIONS

Powders synthesized using liquid ammonia are a mixture of hexagonal aluminum nitride and aluminum. They consist of rather large polyhedral particles (30-100 nm) and super fine particles (less than 10 nm).

Powders synthesized under liquid nitrogen are a mixture of γ-aluminum oxide, aluminum and hexagonal and amorphous aluminum nitride. Most of the particles are spherical, with sizes between 5-100 nm. A few smaller polyhedral particles are also present.

The presence of aluminum oxide in the powders made using liquid nitrogen is assumed to be caused by oxygen contamination, and the γ structure is as the same as that of the powder made using deionized water.

There was no evidence for the formation of cubic aluminum nitride.

FUTURE WORK

To eliminate sources of oxygen contamination.

To decrease the amount of residual aluminum metal.

To apply the RESA process to the fabrication of other nitrides.

ACKNOWLEDGMENTS

The authors wish to thank Dr. Masaaki Sugiyama and Nippon Steel Corporation for technical assistance on TEM observations and UTW analyses. The financial support of Nippon Steel Corporation and NSF, Grant DMR 8812824, is gratefully acknowledged.

REFERENCES

[1]Y. Suwa, R. Roy, and S. Komarneni, "Lowering crystallization temperatures by seeding in structurally diphasic Al_2O_3-MgO xerogels," *J. Am. Ceram. Soc.*, **68** [9] C-238-C-240 (1985)

[2]S. Komarneni, Y. Suwa, and R. Roy, "Application of compositionally diphasic xerogels for enhanced densification: The system Al_2O_3-SiO_2," *J. Am. Ceram. Soc.*, **69** [7] C-155-C-156 (1985)

[3]S. Iijima, "Structural fluctuation of metal clusters under the electron beam irradiation," *Nippon Kessho Kyokaishi*, **29** [4] 288-296 (1987)

[4]D. Hoffman, R. Roy, and S. Komarneni, "Diphasic ceramic composites via a sol-gel method," *Mater. Letters*, **2** [3] 245-247 (1984)

[5]K. Ishizaki, T. Egashira, K. Tanaka, and P. B. Celis, "Direct production of ultra-fine nitrides (Si_3N_4 and AlN) and carbides (SiC, WC and TiC) powders by the arc plasma method," *J. Mater. Sci.*, **24** [9] 3553-3559 (1989)

[6]A. E. Berkowitz and J. L. Walter, "Spark erosion: A method for producing rapidly quenched fine powders," *J. Mater. Res.*, **2** [2] 277-288 (1987)

[7]A. Kumar and R. Roy, "RESA-A wholly new process for fine oxide powder preparation," *J. Mater. Res.*, **3** [6] 1373-77 (1988).

[8]A. Kumar and R. Roy, "Reactive-Electrode Submerged-Arc process for producing fine non-oxide powders," *J. Am. Ceram. Soc.*, **72** [2] 354-56 (1989)

[9]N. Kuramoto, "Aluminum nitride powder and its situation," *Seramikkusu*, **22** [1] 29-34 (1987)

[10]R. Kieffer, W. Wruss, and B. Willer, "Physical and mechanical properties of AlN-Al_2O_3 ceramic bodies prepared by hot-pressing," *Rev. Int. Hautes Temp. et Refract.*, **13** [2] 97-107 (1976)

APPENDIX 14

SOLUTION - SOL - GEL PROCESSING OF SUPERCONDUCTORS

S. Komarneni
P. Ravindranathan
A. S. Bhalla
R. Roy

Solution - sol - gel processing of superconductors

S Komarneni, P Ravindranathan, A S Bhalla and R Roy
Materials Research Laboratory, The Pennsylvania State University, University Park, PA 16802, USA

Abstract. Bulk materials and thin films of pure and homogeneous $YBa_2Cu_3O_{7-x}$ and $Bi_2Sr_2CaCu_2O_{8+x}$ compounds were prepared by a nanocomposite solution - sol - gel (SSG) method. The superconducting oxides of $YBa_2Cu_3O_{7-x}$ and $Bi_2Sr_2CaCu_2O_{8+x}$ were made at very low temperatures i.e., 750°C and 850°C, respectively by the SSG method. Pellets sintered from these nanophasic sol powders showed sharp resistivity drops at Tc ~ 90°K for $YBa_2Cu_3O_{7-x}$ and Tc ~ 67°K for $Bi_2Sr_2CaCu_2O_{8+x}$. Thin films were prepared using triphasic sol of Y, Ba, Cu and tetraphasic sol of Bi, Sr, Ca and Cu on MgO and $SrTiO_3$ substrates. The triphasic sol coated on $SrTiO_3$ substrates and calcined at 800°C for 12 h showed the formation of superconducting phase, $YBa_2Cu_3O_{7-x}$ with preferred orientation along the C- axis . X-ray diffraction patterns of the $Bi_2Sr_2CaCu_2O_{8+x}$ films on MgO substrate showed the formation of the superconducting phase with preferential orientation along the C - axis and the microwave absorption data as a function of temperature of this film revealed the onset temperature to be 90°K.

Keywords. High temperature superconductors; sol - gel; thin film; $YBa_2Cu_3O_{7-x}$; $Bi_2Sr_2CaCu_2O_{8+x}$

1. Introduction

Innovative materials processing is the key for the technological utilization of the new high temperature superconductors such as $YBa_2Cu_3O_{7-x}$ and $Bi_2Sr_2CaCu_2O_{8+x}$. The vast majority of syntheses of these superconductors to date involved conventional solid state reactions of the starting materials, Y_2O_3, CuO, Bi_2O_3, $BaCO_3$, $CaCO_3$, and $SrCO_3$ which need high temperatures and long reaction times. The key factor for the preparation of these materials at low temperatures is the synthesis of precursors through simple solution chemistry. Generating new precursors of these high Tc oxide materials through low temperature molecular chemistry is particularly important from the standpoints of powder homogeneity, purity, and reproducibility. Solution routes, especially the SSG route is also ideal for low temperature processing of bulk materials, fibers, composites, and coatings or thin films (Yoldas and O'keefe 1979; Dislich and Hussman 1981; Hoffman et al 1984). A recent innovation of the SSG method is the utilization of heterogeneity on a nanometer scale and has been found to have profound effects on lowering the processing temperatures (Roy 1987). We have reported earlier the preparation of $YBa_2Cu_3O_{7-x}$ through this process at a very low temperature (Ravindranathan et al 1988). This paper reviews the SSG process developed in our laboratory for the preparation of both $YBa_2Cu_3O_{7-x}$ and $Bi_2Sr_2CaCu_2O_{8+x}$ in bulk as well as in thin film forms.

2. Experimental

2.1 Synthesis of bulk materials of $YBa_2Cu_3O_{7-x}$

A non aqueous sol of copper oxide was prepared by dissolving anhydrous copper acetate, $Cu(CH_3COO)_2$ in methoxyethanol at 70°C, and refluxing the solution at 135°C for 15-20 h . A brown solid separated out from the solution that was found to be fine-particle CuO, as confirmed by powder X-ray diffraction (XRD). Yttrium acetate was dissolved by heating in methoxyethanol at 70°C, and refluxing at 135°C for 12 h, which resulted in a brown colored solution, probably the ethoxide derivative of yttrium. To this solution, stoichiometric amount of barium isopropoxide was added and the mixture was heated at 70°C for a few hours. The copper sol was then added to this mixture at room temperature and stirred well. All these reactions were carried out in argon atmosphere. A slight excess of deionized water mixed with methoxyethanol in 1:4 ratio was added for hydrolysis and the mixture was refluxed for 6-10 h. The metal oxides were precipitated quantitatively from the reaction mixture by simultaneous hydrolytic decomposition of the alkoxides. The intimately mixed triphasic sol was dried at 175°C for a few hours. The resulting gel was finely ground and calcined at various temperatures.

2.2 Preparation of thin films of $YBa_2Cu_3O_{7-x}$

Thin films of $YBa_2Cu_3O_{7-x}$ were made by dropping the above triphasic sol on the cleaned $SrTiO_3$ (hot pressed) substrate and spin casting with a speed of 2000 rpm for 30 seconds. After coating the first layer of the sol, the film was dried at 175°C using an infrared lamp for one minute. The drying process was repeated after each coating of the sol and substrates with 10 layers were prepared to achive sufficient film thickness. The films on the substrates were then calcined at 800°C for 12 h and annealed in O_2 atmosphere at 500°C for 5 h.

2.3 Synthesis of bulk materials of $Bi_2Sr_2CaCu_2O_{8+x}$

A tetraphasic sol containing Bi, Sr, Ca, Cu was prepared using bismuth nitrate, $Bi(NO_3)_3 .5H_2O$, (0.03mole), strontium metal (0.03mole), calcium metal (0.015mole) and copper acetate (0.03mole) and the detailed procedure is outlined in Fig.1. The resulting homogeneous mixed sol can be gelled and processed into bulk materials or thin films (fig.1) of $Bi_2Sr_2CaCu_2O_{8+x}$. The gel powders calcined at 800°C for 12 h were made into pellets and sintered at 870°C for 12 h.

2.4 Preparation of thin films of $Bi_2Sr_2CaCu_2O_{8+x}$

The intimately mixed sols (tetraphasic) were used to make films both on $SrTiO_3$ (hot pressed) and single crystal MgO substrates. A small amount of cladan binder was added to adjust the viscosity of these sols and the films were coated using a spin coater. The sol was spin casted on the substrate at a speed of 2000 rpm for 45 seconds. After each coating, the film was dried at 100°C. About ten layers were coated to achieve sufficient thickness and calcined at 800°C for 6 h followed by another calcination at 870°C for 10 minutes in air.

3. Characterization.

Formation of the superconducting oxide phases was confirmed by XRD. The superconducting nature of the bulk materials was confirmed by measuring the resistance of the samples as a function of temperature by the standard four probe technique. Inductance measurements were also done on bulk samples to verify the superconducting behavior. The surface morphology of the films was characterized by scanning electron microscopy (SEM). The superconducting nature of $Bi_2Sr_2CaCu_2O_{8+x}$ film on MgO substrate was confirmed by measuring the microwave absorption as a function of temperature (Jackson et al 1988).

4. Results and Discussion

The as prepared triphasic gel containing yttrium, barium and copper was amorphous and the gel calcined at 800°C showed the formation of single phase $YBa_2Cu_3O_{7-x}$. When the calcination temperature was raised to 900°C for 12 h , the phase could be indexed on an orthorhombic unit cell as has been reported by Wang-Ng et al (1987). The advantages of this method are (a) it does not require repeated calcination and (b) a single phase can be obtained within 12 h. Others, however, reported a much longer time for calcination to achieve a single phase. The powders calcined at 800°C were made into pellets and sintered in air at 930°C for 12 h. Then the pellets were annealed at 450°C for 5 h in O_2 atmosphere. XRD of the above annealed pellet showed the formation of orthorhombic $YBa_2Cu_3O_{7-x}$ phase. The resistance curve (Fig.2) showed sharp superconducting transitions (~90°K) with widths less than 3°K from the onset to zero resistance. The inductance measurement also showed a sharp fall at the same temperature.

The $YBa_2Cu_3O_{7-x}$ film coated on $SrTiO_3$ substrate was calcined at 800°C for 12 h and annealed at 500°C for 5 hr in O_2 atmosphere. XRD of this thin film showed the formation of the superconducting phase. The sample surface was smooth and black in colour. The thickness of the film was about 2 μm . The XRD also showed that the film was preferentially orientated along the C- axis.

The tetraphasic gel powder containing Bi, Sr, Ca, Cu showed the formation of $Bi_2Sr_2CaCu_2O_{8+x}$ upon calcination at 850°C for 12 h. The XRD pattern of a pellet that was sintered at 870°C for 12 h is shown in fig.3. It can be seen from fig.3 that the diffraction pattern is characteristic of the $Bi_2Sr_2CaCu_2O_{8+x}$ phase. The electrical resistance measured as a function of temperature showed that the onset of Tc occurred at ~ 85°K but zero resistance was achieved at ~ 67°K. Scanning elctron micrograph of the fracture surface of the pellet showed plate like morphology which is typical of this superconducting phase.

The films coated on MgO and $SrTiO_3$ substrates using the tetraphasic sol were calcined at 800°C for 6 h and then annealed at 850°C and 870°C for 10 minutes. XRD analysis of the film annealed at 850°C indicated the presence of superconducting phase, $Bi_2Sr_2CaCu_2O_{8+x}$, semiconducting phase and some other unidentified phase where as the film calcined at 870°C

showed only the formation of superconducting phase and semiconducting phase. XRD pattern of the film annealed at 870°C for 10 minutes on MgO substrate is shown in fig.4. A strong preferred orientation along the C- axis of the superconducting phase was observed in the XRD pattern with the C- axis oriented normal to the plane of the film. All the (00l) reflections of the film showed high intensity (fig.4). It appears that the films prepared by this method are similar to those prepared by coevaporation or sputtering. The C-axis spacing observed in this film was 3.04 nm, which is slightly smaller than the 3.078 nm spacing that was determined for bulk materials (Hazen et al 1988). The small peaks marked with an asterisk (fig.4) may be assigned to the semiconducting phase with C = 2.44 nm as reported by Sunshine et al (1988). The microstructure of the film showed plate like grains which was also observed by Shah et al (1988). It also revealed a rough surface with a grain size in the 5-8 μm range. The microwave absorption of the film was measured as a function of temperature and the plot of the power ,P, reflected by the sample vs temperature is shown in fig. 5. It is clearly seen that the onset of superconductivity occurred at 90°K and the corresponding sharp change in the reflected power. The film coated on $SrTiO_3$ substrate also showed clear evidence for C- axis orientation normal to the plane of the film (figure not shown). The resistivity versus temperature measurement revealed that the onset Tc occurred at 80°K for this sample. The microstructure of this film also showed plate like grains, as expected.

5. Summary

A nanocomposite sol - gel method has been developed for making both bulk and thin film materials of the high temperature superconductors, $YBa_2Cu_3O_{7-x}$ and $Bi_2Sr_2CaCu_2O_{8+x}$. Superconducting oxides were prepared at temperatures as low as 750°C and 850°C for $YBa_2Cu_3O_{7-x}$ and $Bi_2Sr_2CaCu_2O_{8+x}$, respectively. The superconducting transition temperatures occurred at ~ 90°K for $YBa_2Cu_3O_{7-x}$ and ~ 67°K for $Bi_2Sr_2CaCu_2O_{8+x}$. Highly oriented films of $YBa_2Cu_3O_{7-x}$ and $Bi_2Sr_2CaCu_2O_{8+x}$ were prepared on MgO and $SrTiO_3$ substrates by using this SSG route. The microwave absorbtion of the $Bi_2Sr_2CaCu_2O_{8+x}$ film on MgO substrate showed the onset Tc to be 90°K.

Acknowledgements

This work was supported by the ONR-DARPA Grant under Contract No.N00014-86-K-0767 and Army.

References

Dislich H and Hussmann E 1984 Thin Solid Films 77 129

Hazen R M, Prewitt C T, and Angel R J 1988 Phys. Rev. Lett. 60 1174

Hoffman D, Roy R and Komarneni S 1984 Mater. Lett. 2 245

Jackson E M, Liao S B, Silvis J, Swihart A H, Bhagat S M, Crittenden R, Glover III R E and Manheimer M A 1988 Pysica C152 125

Ravindranathan P, Komarneni S, Bhalla A S, Roy R, and Cross L E 1988 J. Mater. Res. 3 810

Roy R 1987 Science 238 1664

Shah S I, Jones G A and Subramanian M A 1988 Appl. Phys. Lett. 53 429

Sunshine S A, Siegrist T, Schneemeyer L F, Murphy D W, Cava R J, Batlogg B, van Dover R B, Fleming R M, Glarum S H, Nakahara S, Farrow R, Krajewski J J, Zahurak S M, Waszczak S M, Marshall J H, Marsh P, Rupp Jr. L W and Peck W F 1988 Phys. Rev. B38 893

Wong-Ng W, Roth R S, Swartzendruber L J, Bennett L H, Chiang C K, Beech F and Hubbard C R 1987 Adv. Ceram. Mater. 2 365

Yoldas B E and O'keefe T W 1979 Appl. Optics 18 3133

Figure captions

Fig. 1 Flow chart for the preparation of bulk materias and thin films of $Bi_2Sr_2CaCu_2O_{8+x}$.

Fig. 2 Temperature dependence of electrical resistance for the sol- gel derived bulk $YBa_2Cu_3O_{7-x}$

Fig. 3 X- ray powder diffraction pattern of $Bi_2Sr_2CaCu_2O_{8+x}$ pellet (made from powders calcined at 800°C for 12 h) sintered at 870°Cfor 12 h.

Fig. 4 X- ray powder diffraction pattern of highly oriented thin film of $Bi_2Sr_2CaCu_2O_{8+x}$ on MgO substrate.

Fig. 5 Temperature dependence of the power, P reflected by $Bi_2Sr_2CaCu_2O_{8+x}$ film on MgO substrate.

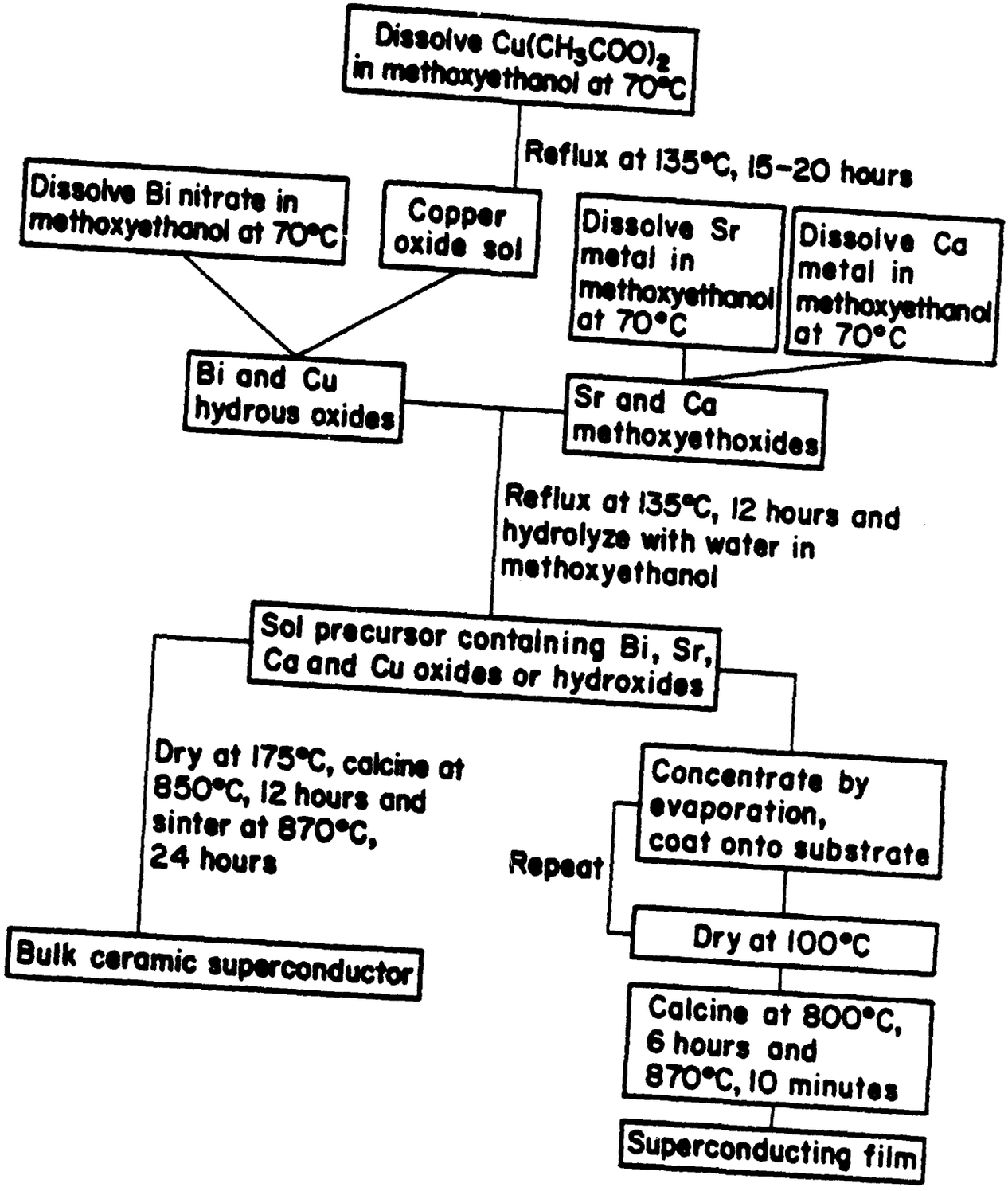
Dissolve $Cu(CH_3COO)_2$ in methoxyethanol at 70°C
Reflux at 135°C, 15–20 hours
Dissolve Bi nitrate in methoxyethanol at 70°C
Copper oxide sol
Dissolve Sr metal in methoxyethanol at 70°C
Dissolve Ca metal in methoxyethanol at 70°C
Bi and Cu hydrous oxides
Sr and Ca methoxyethoxides
Reflux at 135°C, 12 hours and hydrolyze with water in methoxyethanol
Sol precursor containing Bi, Sr, Ca and Cu oxides or hydroxides
Dry at 175°C, calcine at 850°C, 12 hours and sinter at 870°C, 24 hours
Bulk ceramic superconductor
Concentrate by evaporation, coat onto substrate
Repeat
Dry at 100°C
Calcine at 800°C, 6 hours and 870°C, 10 minutes
Superconducting film

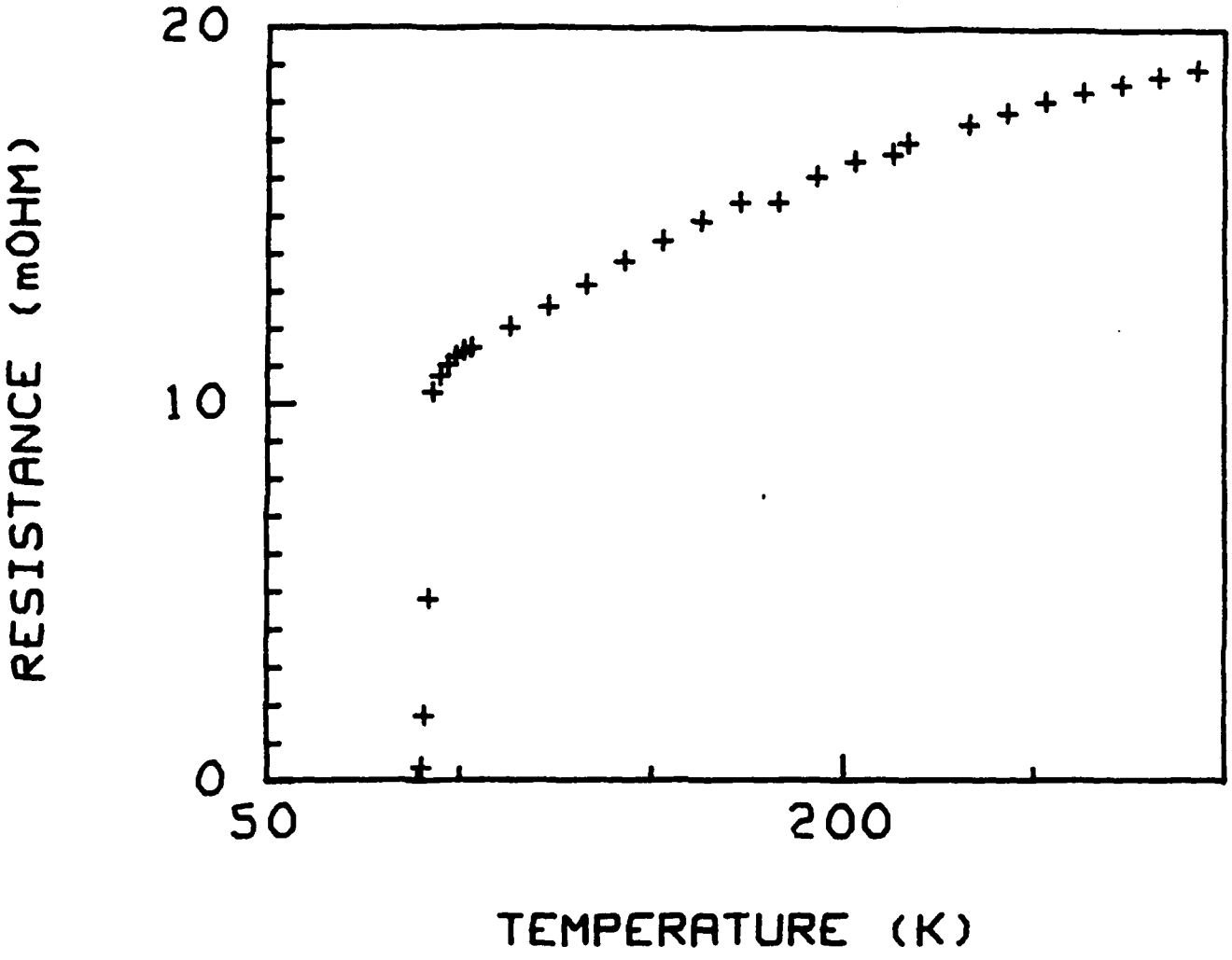
20
10
0
50
200
RESISTANCE (mOHM)
TEMPERATURE (K)

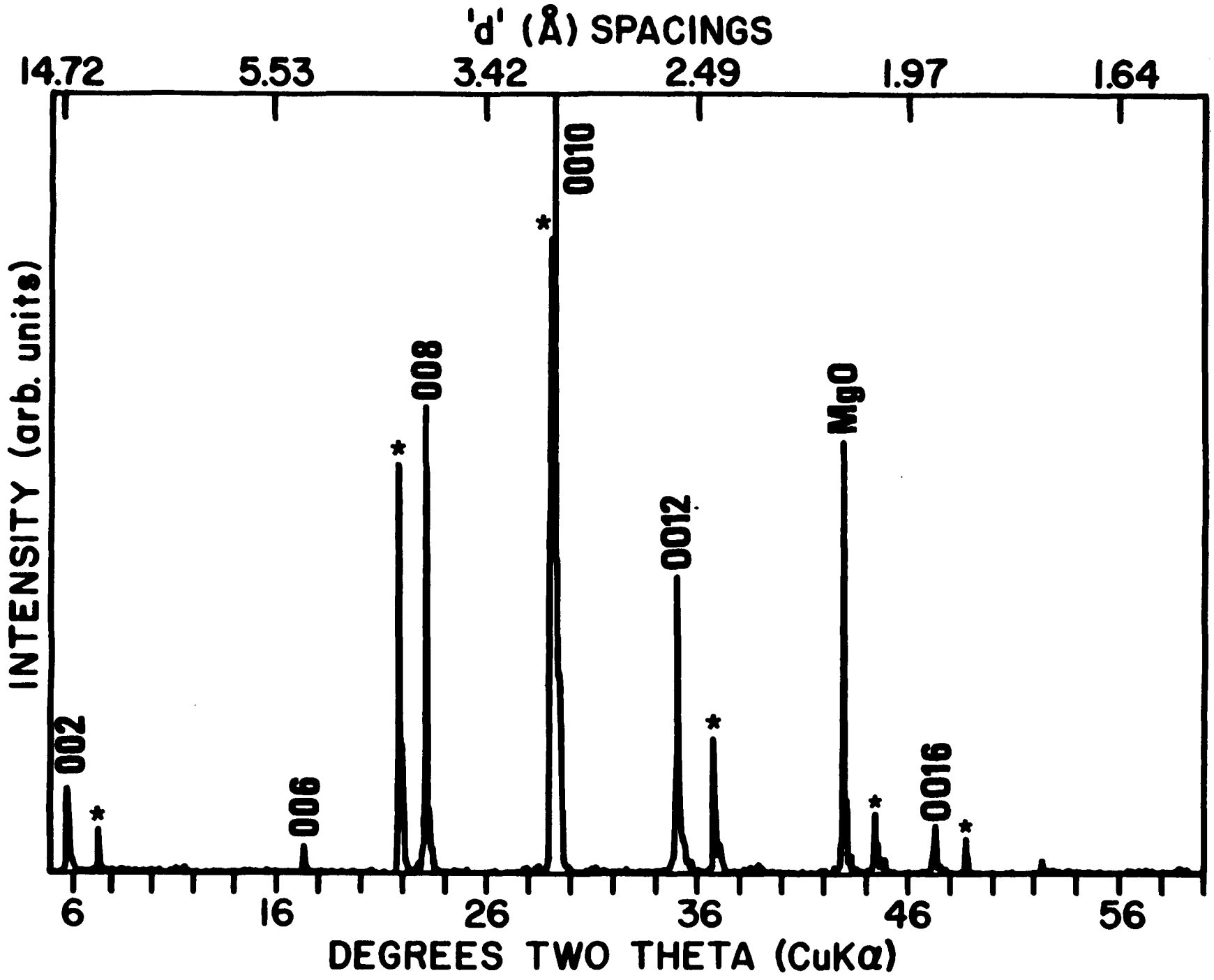
'd' (Å) SPACINGS
14.72
5.53
3.42
2.49
1.97
1.64
INTENSITY (arb. units)
002
006
008
0010
0012
MgO
0016
*
6
16
26
36
46
56
DEGREES TWO THETA (CuKα)

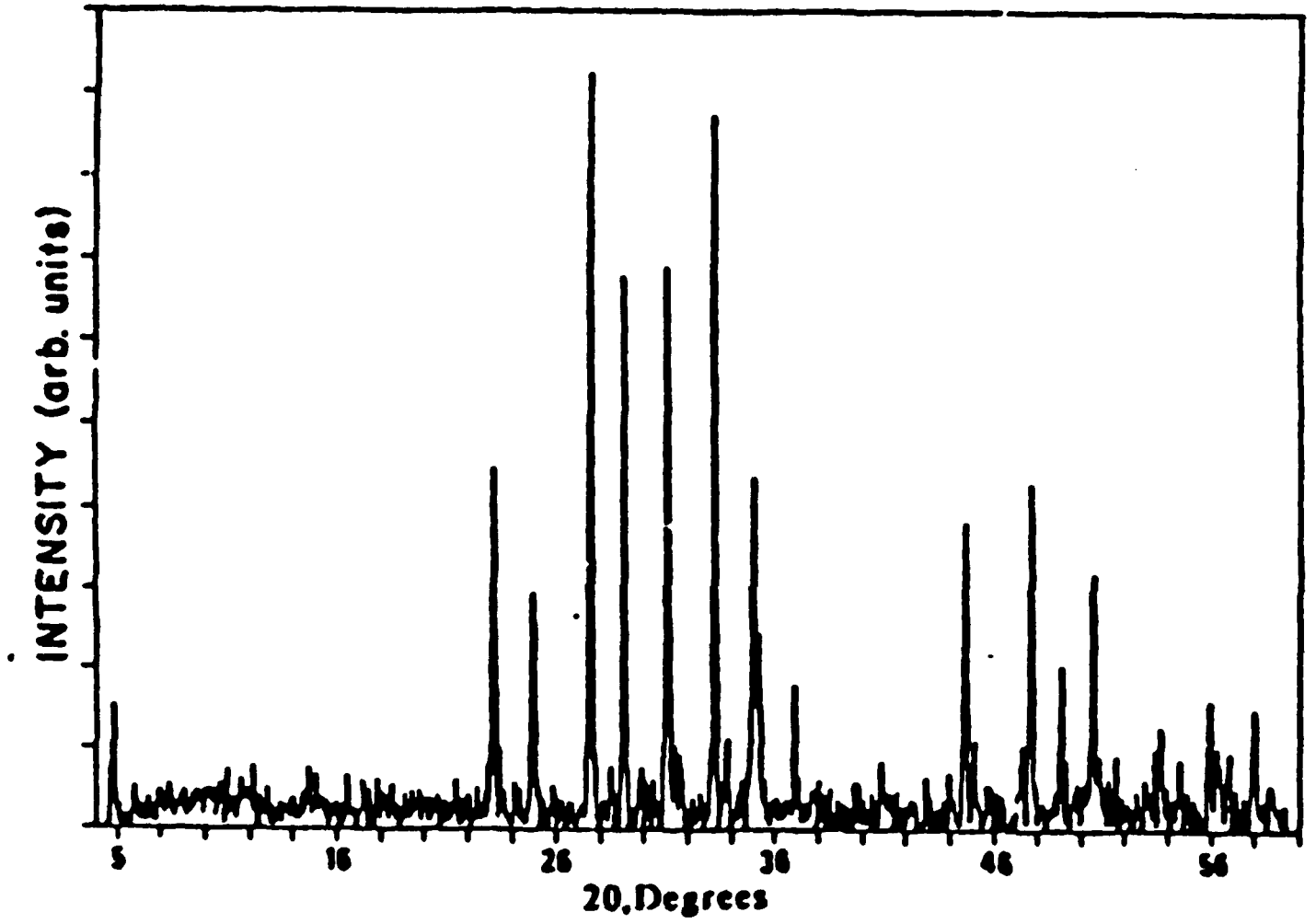
INTENSITY (arb. units)
5
16
26
36
46
56
2θ, Degrees

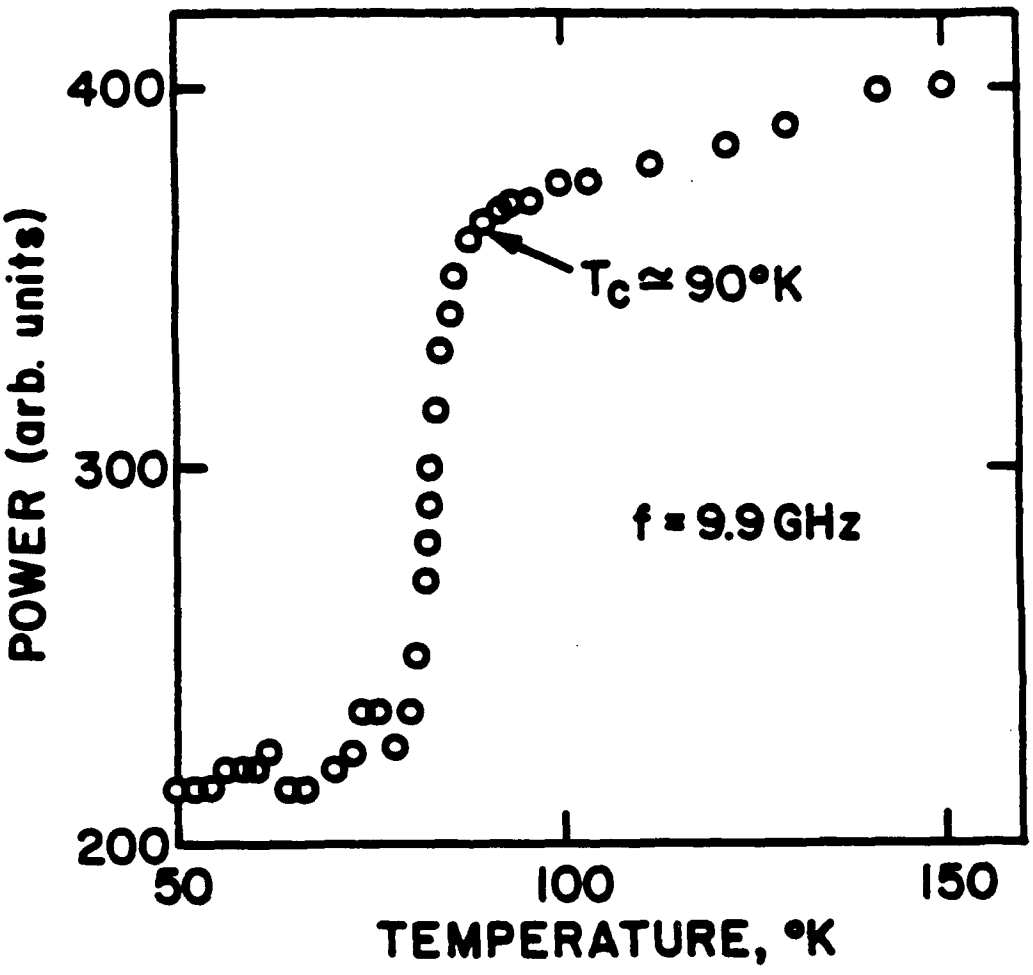
400
300
200
50
100
150
POWER (arb. units)
TEMPERATURE, °K
$T_c \simeq 90°K$
f = 9.9 GHz

APPENDIX 15

CERAMIC/POLYMER NANOCOMPOSITE PROPERTIES FOR MICROELECTRONIC PACKAGES

A. Das
T. T. Srinivasan
R. E. Newnham

CERAMIC/POLYMER NANOCOMPOSITE PROPERTIES FOR MICROELECTRONIC PACKAGES

AMITTABH DAS, THALLAM T. SRINIVASAN * AND ROBERT E. NEWNHAM
Materials Research Laboratory, The Pennsylvania State University, University Park, PA16802.

ABSTRACT

This paper reviews some of the research efforts in microelectronic packaging to develop composites with dimensions of the fillers ranging down to nanometer dimensions. Some initial experiments have been conducted with nanocomposites, where the thermal and dielectric properties of polymer/fumed silica composites have been studied. The bulk samples were prepared in different ratios of polymer to silica using polydimethyl siloxane and Cab-O-Sil . Differential thermal analyses carried out on these samples show no shift in their transition temperatures (330°C). The dielectric constant of the 70:30 (Cab-O-Sil-Polymer by Wt.%) composite is 3.8, similar to that of the pure silica. For the same composite the value of the thermal expansion coefficient is 350 ppm, closer to the value of pure polymer (439 ppm). It is suggested that the key to model these nanocomposites with ceramic and polymer phases is to understand the interfaces and their chemical bonding.

INTRODUCTION

The rapid evolution of microelectronic packaging in recent years is causing a number of concerns in the microelectronics industry. Many of the concerns are materials science related. Packaging has been defined as the effective housing, cooling and *interconnecting* of IC chips in a reliable fashion[1]. With the advent of VLSI (very large scale integration) devices, the limits of packaging are being stretched. What was once treated as an engineering problem has now become a major problem in materials science. To elucidate this point, there are problems of dielectric permittivity limiting signal propagation and crosstalk, and the heat dissipation problem with chips generating as much as 40 watts[2]. Thermal expansion mismatch is another materials related area which is of great concern in multilayer packages. Other problems such as impedance matching, rise-time degradation, simultaneous switching noise, thermal and mechanical fatigue, all require an imaginative use of materials science and engineering[3,4].

Certain material properties will have a greater weight over others, depending on the application. In this regard, it has been suggested that specific figures of merit (FOM) be developed. A weighted figure of merit is as follows[5]:

$$FOM_{substrate} = \{W_1K.W_2\sigma\}/\{W_3\rho.W_4T_{proc}.W_5\varepsilon_r.W_6\tan\delta.W_7[\alpha_{Subs}-\alpha_{Si}].W_8\emptyset\}$$

where,

- K = thermal conductivity
- σ = mechanical strength
- ρ = surface roughness
- ε_r = dielectric constant
- $\tan\delta$ = dielectric loss
- α = thermal expansion coefficient
- $T_{proc.}$ = processing temperature
- $\emptyset$ = radiation sensitivity

W_1-W_n=weights

The weighted averages can be determined from the other area of major concern, that being reliability and testing. From various failure mode analyses, weights can be developed for different applications. Thus for a comprehensive approach [5], packaging has to be considered from three different major areas: 1. Application, 2. Materials Science, and 3. Testing and Reliability. However, in this study the focus has been given to materials science.

With increased trends towards miniaturization and reliability in microelectronic packaging, homogeneity in materials processing is playing an important role. In addition, increased demands on materials properties are driving substrates toward composite materials. To increase the homogeneity in composites, they should be processed with phases reaching dimensions in the nanometer scale. In the present work an attempt has been made to improve the substrate properties for microelectronic packaging application. We have chosen Cab-O-Sil (fumed silica) and polydimethyl siloxane as a starting materials to make nanocomposites with various weight proportions: 30-70, 50-50, and 70-30. The nanocomposites are characterized by differential thermal analysis, thermal expansion coefficient and measurements of dielectric constant and dielectric loss at frequencies from 100Hz to 10MHz.

EXPERIMENTAL

Cab-O-Sil and polydimethyl siloxane (Eccosil from Emerson Comming and Cab-O-Sil from Cabot Corporation) are mixed in required proportions in a beaker. The mixture is stirred well and the trapped airpores are removed through vacuum dessicator. Then the composites are cured in a 150°C oven for 20 minutes. Transparent samples were obtained and used for characterization. The flow chart can be seen in Figure 1. X-ray analyses carried out on all these specimens showed the amorphous nature of the samples.

Small pieces (0.1x0.1x0.2 cms) were cut and used for differential thermal analyses. The analyses were carried out in air between 25 and 400°C using a Perkin Elmer DTA 1700 Differential Thermal Analyzer.

For dielectric measurements rectangular samples (2x1x0.3 cms) were cut and electroded using evaporated aluminum. Capacitance and loss measurements were done using HP4274A and 4275A from 100Hz to 10MHz. From the dimensions of the electroded area and the thickness of the samples, the dielectric constant and loss were calculated for all samples and are shown in Figures 2, 3, and 4. To determine the effect of electrodes on the dielectric properties, we have also used other electrodes such as sputtered gold, air dry silver paste and thin brass foil. Sputtered gold did not adhere well to the sample, therefore, evaporated aluminum was used followed by sputtered gold. The dielectric constant and loss did not change very much (less than 3% variation) for various electrodes.

Thermal expansion measurements were carried out using Perkin Elmer TMS-2 Thermomechanical Analyzer from 25 to 150°C. The typical thermal expansion graph for one of the samples (Cab-O-Sil 70 - Polymer 30 by Wt.%) is shown in Fig.5. Repeated thermal cycling (three times) of the samples did not show any hysteresis. The measurements were also carried out at the rate of 10°/min, and 2°/min. The rate of heating had no effect on the values of thermal expansion coefficient (TCE)within this range.

RESULTS

The differential thermal analysis of the composites did not show any change in the glass transition temperature, which was found to be around 330°C (same as that of pure

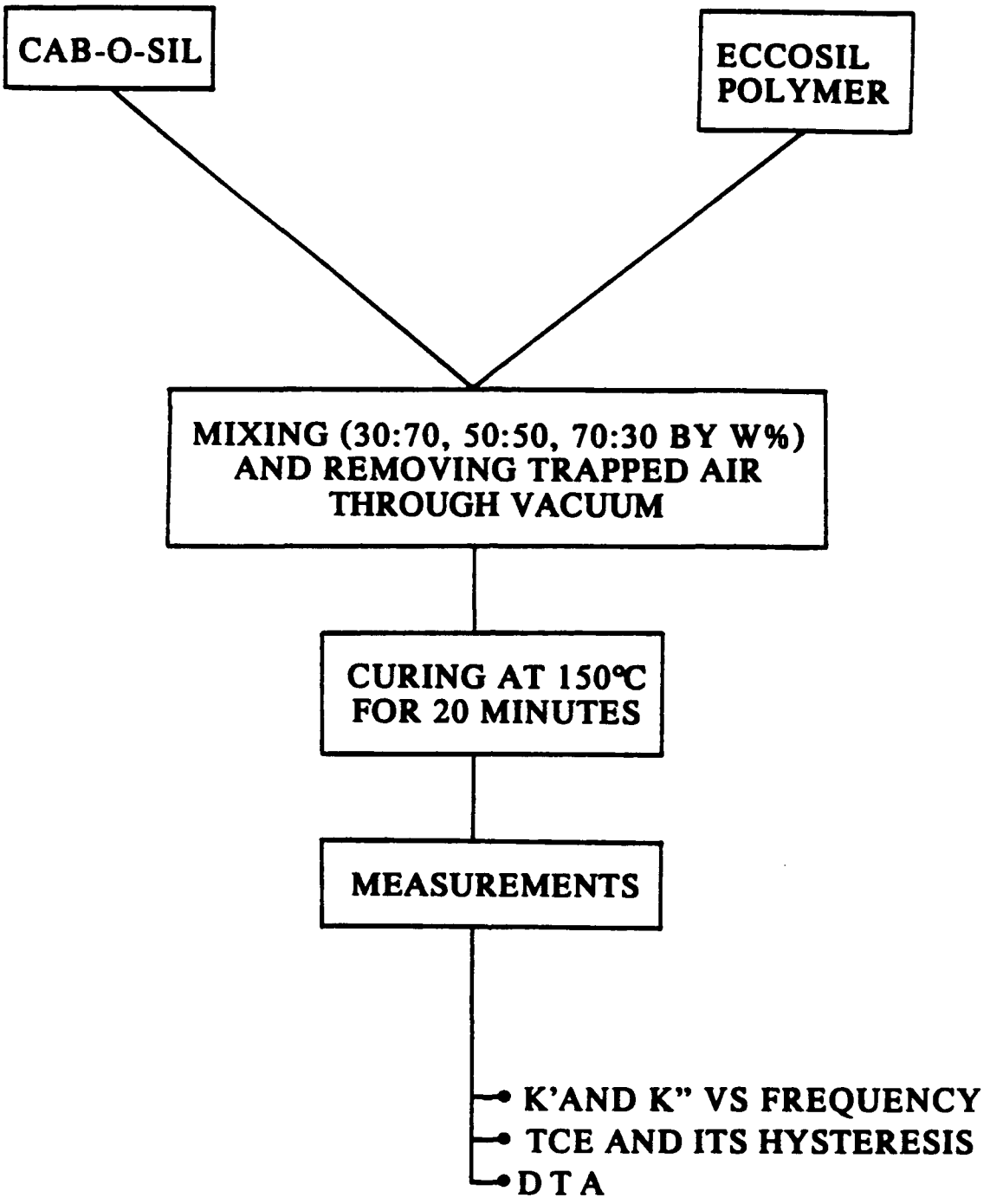

Fig.1. Flow chart for the preparation of nanocomposite

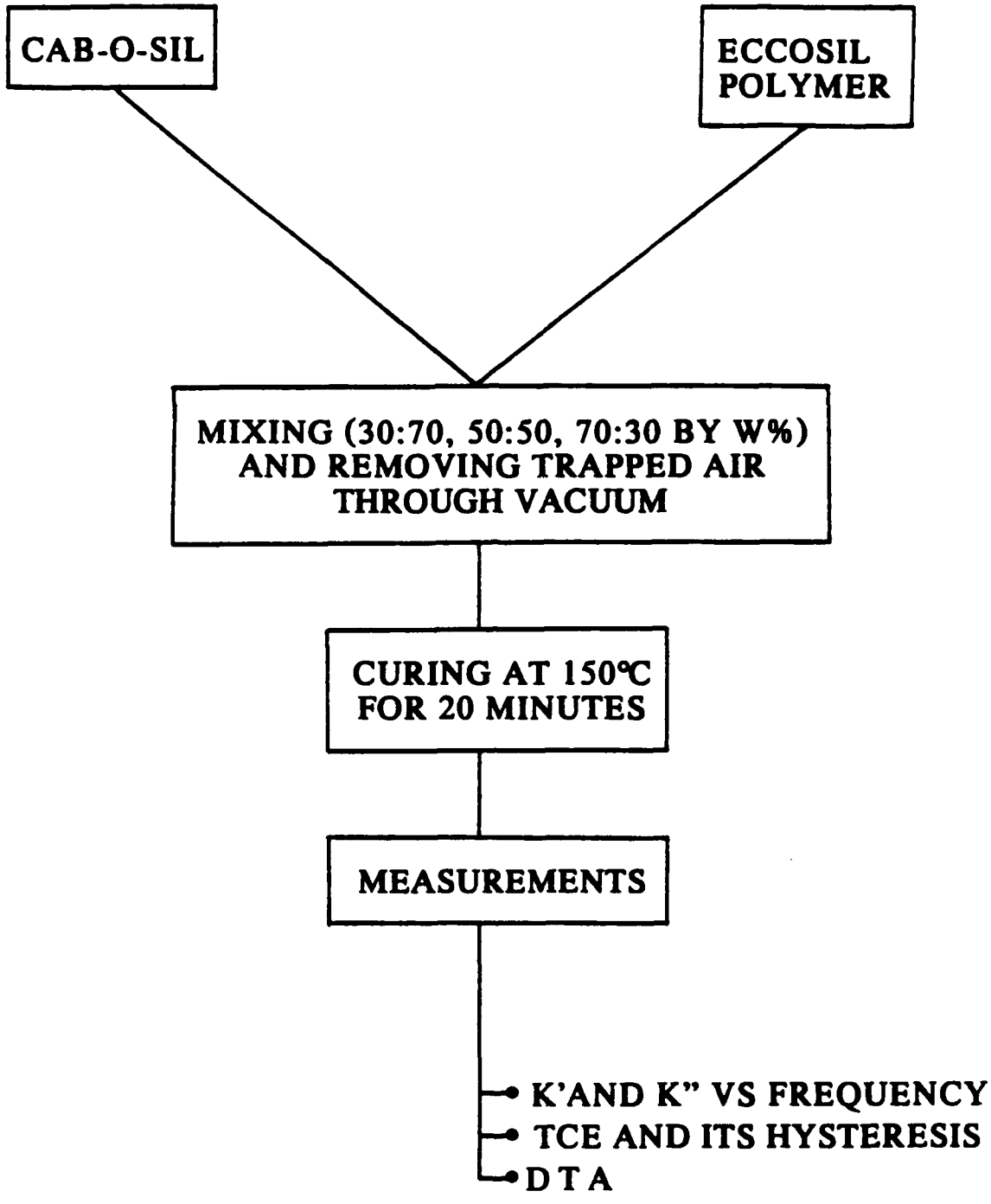

Fig.1. Flow chart for the preparation of nanocomposite

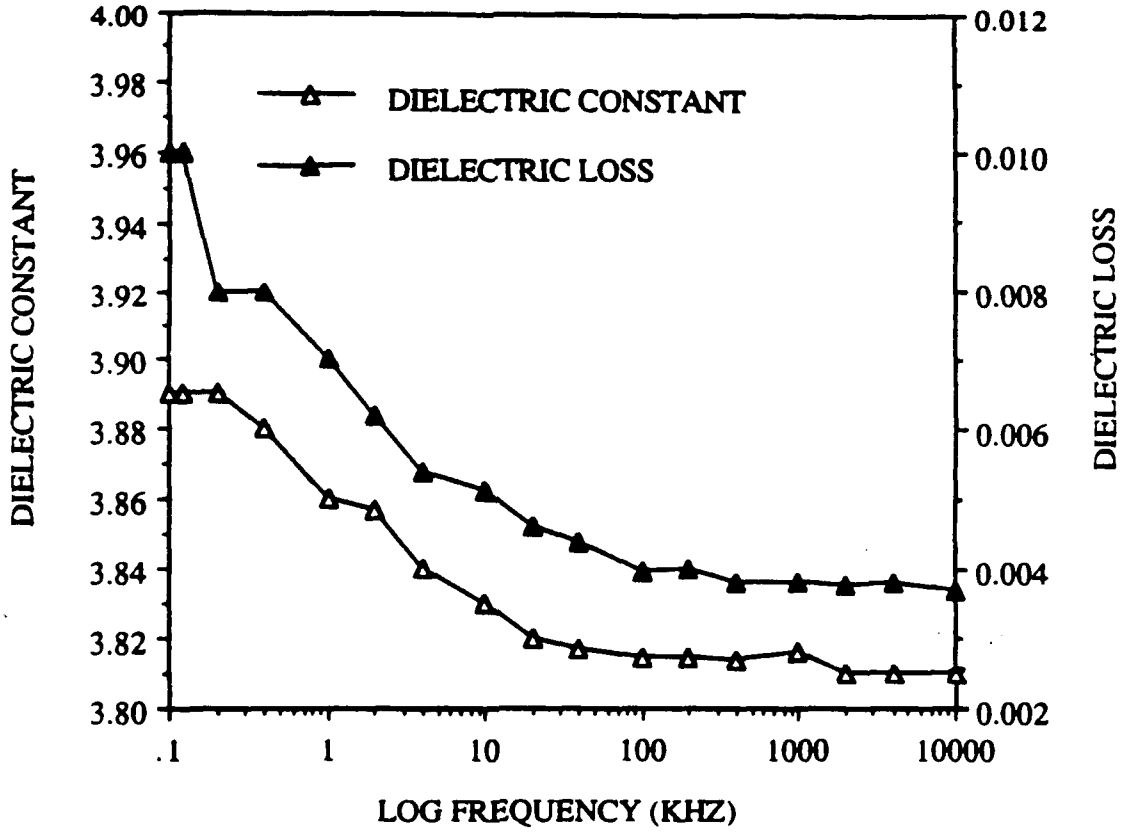

Fig.4. Variation of dielectric constant and loss vs log frequency for Cab-O-Sil 70-Polymer 30 composite

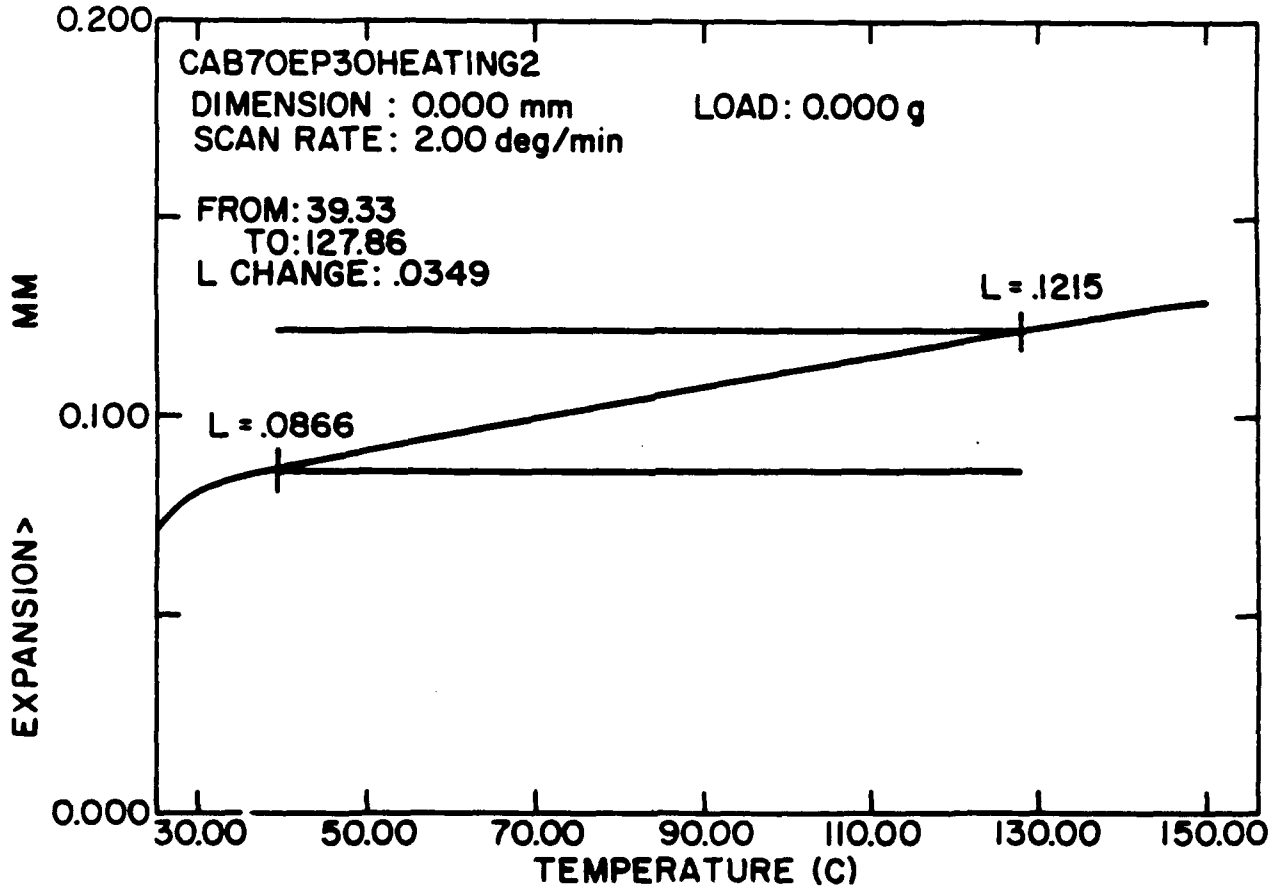

Fig.5. Thermal expansion graph for Cab-O-Sil 70-Polymer 30 composite

polymer) . The composite samples were found to be transparent, indicating homogeneous mixing of polymer and the Cab-O-Sil at nanometer scale. As seen from Figures 2, 3, and 4 that the dielectric constant and loss for all the composite compositions, decreased with frequency. The dielectric loss for all the samples was resistive in nature and decreased from 0.01(at 100 Hz) to 0.004 (at 10MHz). The dielectric loss decreased with increased silica content (above 10KHz) in the polymer matrix (see Figures 2,3, and 4), implying the presence of impurities in the polymer. The variation of dielectric constant (at 1KHz) vs. percent polymer is shown in Figure 6 along with the theoretical values predicted by various models. The value of k for pure polymer was found to be 7.8, and that of Cab-O-Sil was assumed to be 3.8 (that of pure silica). The selection of the polymer was based on Eccosils having a high glass transition temperature. The dielectric constant was found to decrease with increase in silica content probably because of the increase in the number of interfaces containing porosity and defects. Since a sudden change in the dielectric constant was observed between 50 and 70 weight % silica, it is possible that at lower silica loadings, the polymer wets well with the fewer silica particles. The dielectric constant of the composites for the lower loadings of silica (30 and 50 wt.%) was closer to that of the polymer and was 6.8 and 6.4 respectively. However, for 70 wt. % silica loading, the dielectric constant was found to be similar to that of pure silica (3.8). Our model of the dielectric properties was based on two phases, a ceramic and a polymer, but since in nanocomposites, the interface has a significant volume fraction [24], it should be incorporated as another phase. This would lead to a more accurate model for the dielectric behavior.

The variation of TCE with different weight percent polymer is shown in Figure 7. The TCE values for 0, 30, 50, and 70 weight % Cab-O-Sil were 439, 428, 424, and 350 ppm respectively. The TCE of pure silica is known to be 0.6 ppm , which was used to extrapolate the TCE results. The value of TCE did not change very much from that of the polymer, even up to 70 weight percent loading of silica. This shows at low temperature (up to 150°C) the thermal expansion coefficient is controlled by the polymer rather than polymer-silica composite. The deviations of the experimental data from the models of Turner, Fahmy and the simple mixing rule indicates again that the properties of the interface have been neglected.

DISCUSSIONS

Composite properties can be categorized according to (a) Sum property, (b) Combination property and (c) Product property [6,7]. For a sum property, the property coefficient depends on the corresponding coefficients of its constituent phases. Dielectric constant can be termed as a sum property, because the k of the composite depends directly on the k of the constituent phases. For a combination property, the property coefficient depends on two or more different coefficients of the constituent phases. Thermal expansion coefficient can be termed as a combination property, because the thermal expansion of a composite depends not only on the thermal expansion of the constituent phases but also on their elastic stiffnesses. In a product property, completely different properties of the constituent phases are involved. The two properties chosen for this study of nanocomposites are dielectric constant (sum property) and thermal expansion (combination property), because these types of composites have been extensively investigated and modeled using effective medium theories, percolation theory and others, and are shown in Figures 6 and 7 respectively.

Substrates for microelectronic packaging have to incorporate many materials related properties depending on the level of integration required and the application for which they are to be used. Therefore, a composite material has to be developed.

A composite route has been developed from the early times of printed circuit boards, which used a glass (ceramic) and polymer composite. These were macro scale composites where the dimensions of the glass phase were comparable to that of the

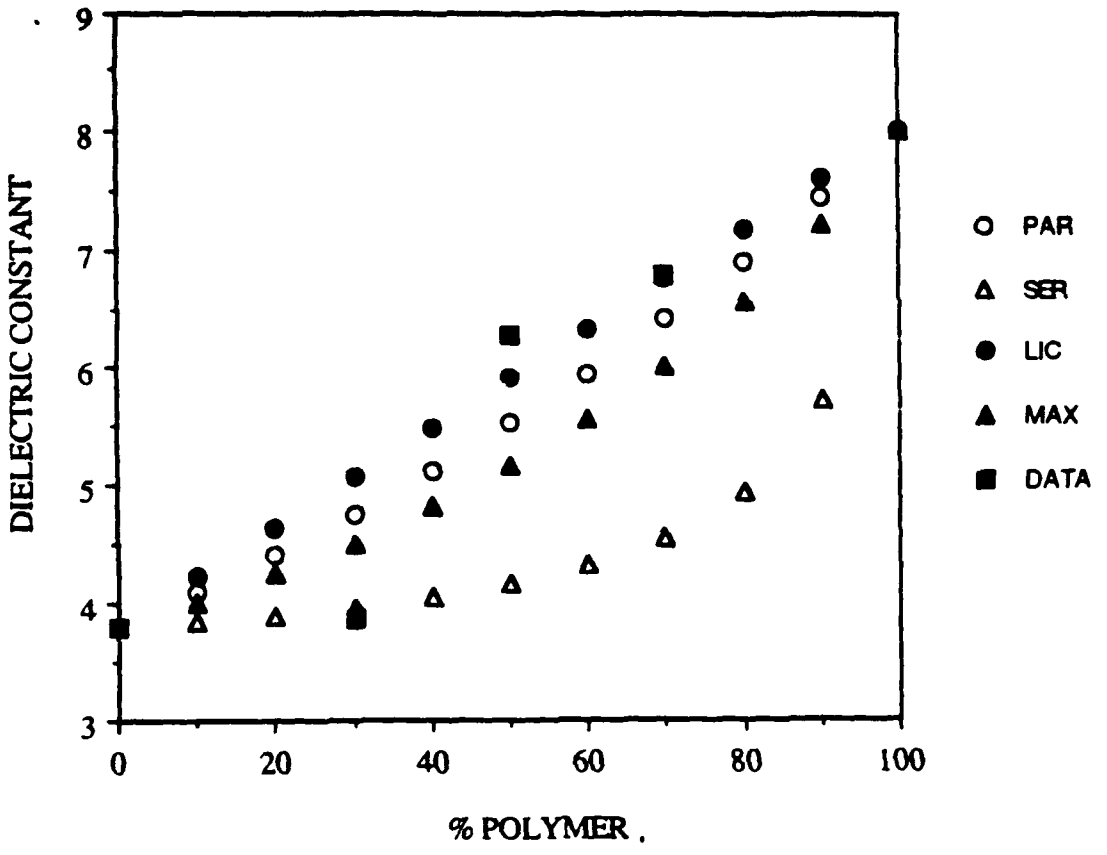

Fig.6. The variation of dielectric constant vs percent polymer along with the theoretical fitting for different models

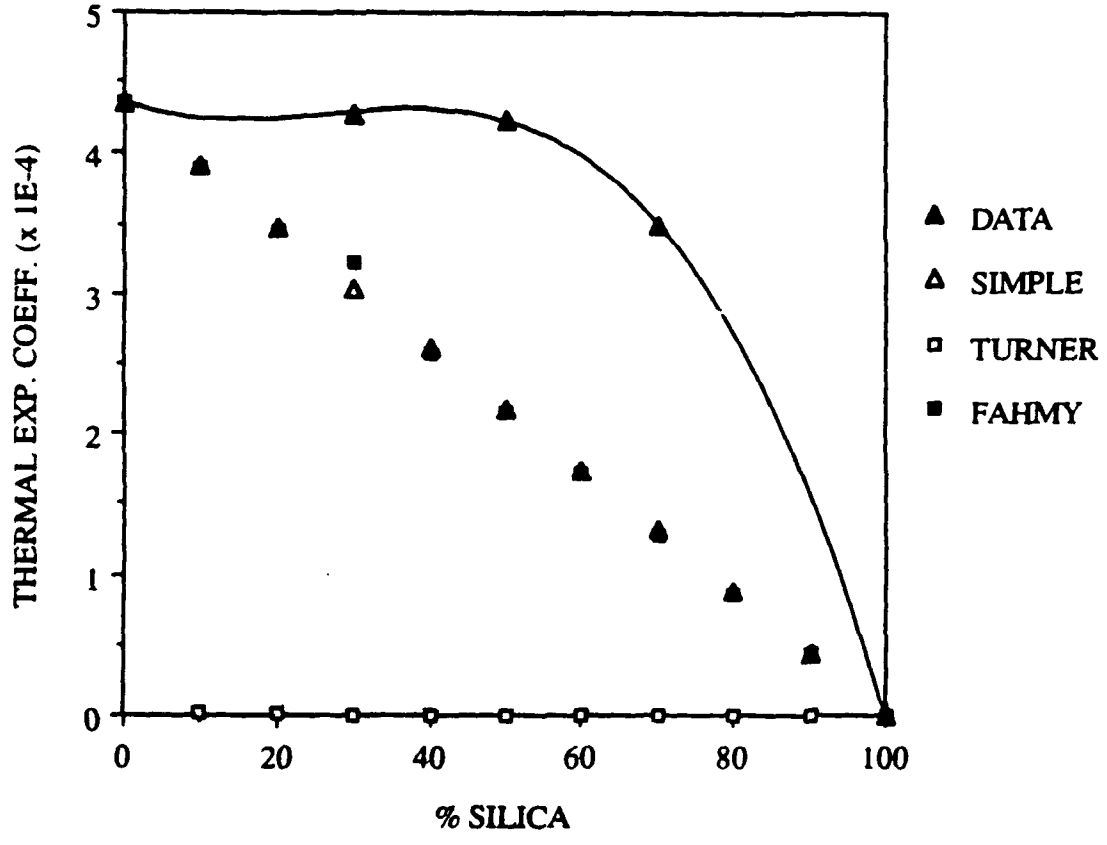

Fig.7. The variation of TCE vs percent silica along with the theoretical fitting for different models

polymer matrix. Various polymers have been used like polyimides, FR-4, polycynate etc. [8,9] along with a matted glass filler to incorporate strength and dimensional stability to these printed circuit boards.

In the case of calculating the thermal expansion of a composite, consisting of a ceramic and a polymer, with very different expansion coefficients, a change of temperature (well below T_g) gives rise to elastic strains[10]. This changes the overall TCE from a simple volume average of the constituents (as is often the case with sum properties). The thermal expansion of two-phase solids has been studied extensively for macro and micro composites. Turner [11] studied the TCE of various filled plastics and modeled them assuming a uniform hydrostatic stress that exists between the phases because of different elastic properties. The classical approach by Turner has been since modified. Fahmy and Ragai [12] modified the TCE of composites by incorporating a geometrical factor to include the shape of the inclusions in a matrix. The orientation of the inclusions in a composite is also known to cause anamolous behavior in ceramic polymer composites. Glass matte/epoxy reinforced composites have been studied[13,14] and these composites are used to separate copper conductors that form a helical field coil in the Advanced Toroidal Facility[13]. An anomalous behavior was observed in the TCE(measured perpendicular to the plane of the glass fiber inclusion) in these composites showing a discontinuity in slope of the expansion curve, well below the Tg of the polymer. They concluded that the orientation of the glass fibres was key to uniform or anamolous behavior.

Since one of the major thrusts in packaging today is to develop low dielectric constant (k) and low dielectric loss substrates, a lot of research effort has gone into the development of porous silica composites with k less than 3.0. Much of this research deals with micro-scale composites, where the porosity has micrometer dimensions. The leaching of Vycor glasses with various acids has been studied to introduce porosity and thereby decrease the dielectric constant to below 3.0. These composites had interconnected porosity (3-3) and could be well modeled using the Licktenecker's (Logarithmic) mixing rule [15]. In another study, sol gel processing, using colloidal silica with low T_g polymers have been used. The polymer phase was removed by thermal treatment to yield porous silica with ultra low dielectric properties ($k < 2.0$) [16,17]. The resulting microstructure in these systems had both (0-3) and (3-3) connectivity at the micrometer scale. These structures could be modeled using a combination of Maxwell's and Licktenecker's mixing rules. Composite substrate materials also have been developed by tape casting low melting lead based glass with hollow glass (silica) microspheres, whose diameter ranged between 20 and 80 micrometers. These composites had dispersed porosity (3-0 composite) varying between 40 to 88 volume percent with dielectric constants ranging between 2.5 and 4.0 [18]. In another similar study, hollow silica microspheres were cast with calcium aluminate cements with dielectric constants varying between 5 and 8 [19]. These composites followed the Maxwell's mixing rule, as predicted from theory.

Sputter deposited silica films were also studied with low dielectric constant ($k=3.2$) and loss ($\tan \delta<0.002$) [20], but they could not be modeled because of their complex fractal morphology and the trade off between morphology and stoichiometry according to deposition conditions. However, the porosity in these films was believed to be in the nanometer scale, but it was too complex to determine with any level of accuracy, what kind of distribution was in a complex columnar matrix [21].

Another unique technique, using a composite approach to form a ceramic /polymer composite for microelectronic application was a modification of the replamine process [22]. In this study, organic templates (Nylon 66) were vacuum impregnated with colloidal silica (Cab-O-Sil and TEOS). The organic component was removed by heating the composite to 500°C, leaving a fragile silica network. This silica network structure had a 3-3 interconnected porosity. The last step was dip-coating the inorganic structure in a silicone polymer. The final composite was modeled for dielectric properties with a combination of the Licktenecker's and parallel mixing rules [23].

The interest in studying nanocomposites, comes from the fact that they have been known to exhibit unique properties, not predictable by the mixing rules for composite materials. This uniqueness is attributed to the large volume fraction of surfaces or grain boundaries that make up the composite [24]. These interfaces have little or no short range order, causing a large variation in properties from micro or macro composites. The TCE of nanocrystalline Cu has been found to be 80 % greater than polycrystalline or glassy Cu, and the specific heat of nanocrystalline Fe is also 50 % higher than polycrystalline or glassy Fe [24]. The melting point of Au is known to drop significantly as the particles approach submicrometer dimensions[25]. The transition temperature of ferroelectric materials like $BaTiO_3$ and $PbTiO_3$ have been found to drop suddenly as a result of grain size approaching nanometer dimensions [26,27]. It has been found that as the surface free energy of zirconia increased as a result of nanocrystallite size (300 Å), the transition temperature dropped to 27°C from 827°C for the tetragonal to monoclinic phase [28]. Thus, in all the above mentioned references, the key issue was the increase in surface area or interfacial region, that caused drastic property variations.

Another concept about nanocomposites that has evolved out of Schmidt's work [29,30,31] has to do with organically modified ceramics (ORMOCERS). These nanocomposites have a chemical bond between a ceramic network and various polymer /monomer chains. Depending on the polymer/monomer loading, a 3-0 or 3-3 type composite could be formed. In the former case, short polymer chains would be bonded to the ceramic network. In the latter case, the polymeric chains and the ceramic network form a three dimensionally interconnected structure. These nanocomposites would exhibit unique properties because in addition to the increase in interfaces, the chemical bond would play a role in the final property of the composite. Thus, nanocomposites of ceramic and polymers could be classified as (1) pure nanocomposites and/or (2) ORMOCERs. At this point no attempt has been made to model these types of nano structures, because further investigation is needed into the evaluation of interfaces and bond strength or number of bonds per unit area of ceramic/polymer nanocomposites.

CONCLUSION AND FUTURE WORK

There is evidence in the literature that when the size of the phases in a composite approaches the nanometer scale, the properties vary drastically, and cannot be predicted by simple mixing rules used for composites at a micro or macro scale. The key to understanding nanoscale composites is to try to categorize them as (1) ORMOSERS and (2) pure nanocomposites. In the first case chemical bond exists between the two phases which plays an important role in why properties vary. In the second case, no chemical bond exists as in (1) but the volume fraction of the interface region between the phases can be as high as 50 % [24]. Thus, the interface region, which would contain defects, voids, etc has to be incorporated as a separate phase into the modelling problem.

At this stage we are trying to understand the nature of the sudden variations in dielectric and thermal phenomena that is exhibited by these nanocomposites. This will not only aid in understanding nanocomposites but also the processing of homogeneous substrates with tailored properties for packaging VLSI and VHSIC devices.In this type of composites there are various parameters which can be controlled and hence, we may be able to make a good nanocomposite substrate materials for microelectronic packaging applications with the required substrate properties. In the future, attempts will be made in characterizing the interfaces between the ceramic and organic phase, not only to determine its density but also whether a chemical bond exists.

ACKNOWLEDGEMENTS

Thanks to Ms. Yan chen for dielectric measurements of all the samples.

REFERENCES

1. Rao R. Tummala and Eugene J. Rymaszewski, Microelectronic Packaging Handbook, (Van Nostrand Reinhold, New York, 1989), p. 3.

2. Personal communications with T. Gupta, ALCOA.

3. A.J. Blodgett. Jr., Sci. Amer. 249 (1), 86 (1983).

4. B. Schwartz, Ceram. Bull., 63 (4), 577 (1984).

5. A. Das, and L.E. Cross, Proceedings of the Ninth Annual International Electronics Packaging Conference, San Diego, California, September 11-13, 2, p.1223, (1989).

6. R.E. Newnham, Ann. Rev. Mater. Sci., 16, 47 (1986).

7. R.E. Newnham, Ferroelectrics, 68, 1 (1986).

8. D.W. Wang, Mat. Res. Soc. Symp. 108, p. 125 (1987).

9. R.W. Seibold, R.T. Lamoureux and S.H. Goodman, Mat. Res. Soc. Symp. 108, p. 141 (1987).

10. P.G. Klemens, International J. of Thermophysics, 9 (2), 171 (1988).

11. P.S. Turner, J. Res. Bur. Std., 37, 239 (1946).

12. A.A. Fahmy, and A.N. Ragai, J. Appl. Phys., 41 (13), 5108 (1970).

13. D.L. McElroy, F.J. Weaver and C. Bridgeman, International J. of Thermophysics, 9 (2), 233 (1988).

14. J.A. Dudek, and J.A. Kargol, International J. of Thermophysics, 9 (2), 245 (1988).

15. J.K. Yamamoto, Dielectric Properties Of Porous Glass In The Microwave Region, M.S Thesis, The Pennsylvania State University, December (1986).

16. W.A. Yarbrough, T.R. Gururaja, L.E. Cross, Am. Ceram. Soc. Bull., 66 (4), 692 (1987).

17. U. Mohideen, Ultra-low Permittivity Porous Silica Thick Films For GaAs IC Packaging, M.S. Thesis, The Pennsylvania State University, December (1987).

18. M.J. Leap, The Processing and Electrical Properties Of Hollow Microsphere Composites, M.S. Thesis, The Pennsylvania State University, May (1989).

19. P. Sliva, The Development and Processing Of Calcium Aluminate Cement As a Low Relative Dielectric Permittivity Material, Ph.D Thesis, The Pennsylvania State University, December (1988).

20. A. Das, Sputter Deposited Silica Films As Substrates For Microelectronic Packaging Applications, Ph.D Thesis, The Pennsylvania State University, August (1988).

21. A. Das, R. Messier, T.R. Gururaja, L.E. Cross, Proc. Spring MRS meeting, Palo Alto, Ca, April (1986).

22. K. Rittenmyer, T. Shrout, W.A. Schulze and R.E. Newnham, Ferroelectrics, 41, 189 (1982).

23. C.A. Sullivan, The Use Of Synthetic Organic Templates In The Preparation Of Tailored Ceramic Microstructure, M.S. Thesis, The Pennsylvania State University, December (1989).

24. G.A. Niklasson, and H.G. Craighead, App. Optics. 22, 1237 (1983).

25. J.P. Borel, Sur. Sci. 106, 1 (1981).

26. K. Uchino, E. Sadanaga, T. Hirose, J. Amer. Ceram. Soc. (to be published in 1989).

27. K. Ishikawa, Phys. Rev. B 37, 5852 (1988).

28. R.C. Garvie, J. of Phy. Chem. 69 (4), 1238 (1965).

29. H. Schmidt, Proceedings of The Nanocomposite Conference, Tokyo, (1989).

30. D. Ravaine, A. Seminel, Y. Charbouillot, and M. Vincens, J. of Non-Crystalline Solids. 82, 210 (1986).

31. H. Schmidt, J. of Non-Crystalline Solids. 73, 681 (1985).

APPENDIX 16

MULTIFUNCTIONAL FERROIC NANOCOMPOSITES

R. E. Newnham
S. E. McKinstry
H. Ikawa

MULTIFUNCTIONAL FERROIC NANOCOMPOSITES

R.E. NEWNHAM, S. E. McKINSTRY, and H. IKAWA
Materials Research Laboratory, the Pennsylvania State University, University Park, PA 16802

ABSTRACT

As trends towards miniaturized components and systems continue in many fields, there has been a rapid development in similarly scaled-down composites. In the electronics industry, these nanocomposites (and especially active nanocomposites based on ferroic elements) form a basis for many of the recent advances in both information and charge storage. While the overall properties of some of these composites can be explained as straightforward extrapolations from the bulk properties, in other instances the small size of the ferroic phase has important consequences on the macroscopic behavior of the composite. This paper reviews some of the recent developments in small-scale ferroic nanocomposites and details the relation between component size and the resultant properties.

INTRODUCTION

The study of composite electroceramics has resulted in several new families of devices with properties superior to those obtainable from single phase materials [1]. Typically, the success of such composites can be traced to well-designed phase connectivity patterns, which can, for example, force desirable field concentrations in a single phase, enhance the anisotropy of property coefficients, and control the transport of heat or charge. Engineering of this type accounts for the rapid growth in composite biomedical transducers, thermistors, hydrophones, and chemical sensors.

However, the drive towards small-scale components has resulted in a new generation of composites in which not only the connectivity, but the scale of the components also plays a remarkable role in the overall properties. This is especially important in the case of ferroic materials, where both the presence of domain walls and indeed, the ferroic transition itself, is controlled by the crystallite size. In order to predict what properties to expect from ferroic nanocomposites, then, it is necessary to understand how size affects the behavior of single phase ferroics. This is easiest to illustrate with the family of ferromagnetic materials, as they are by far the best studied of the ferroics, but new experimental evidence is accumulating that small ferroelectric, ferroelastic, and secondary ferroic particles will show similar behavior.

Beginning from the larger end of the size spectrum, it is well known that large grained ferroic ceramics exhibit complex domain structures which are often bounded by several different types of domain walls. As the size of the system decreases, however, the volume free energy necessarily decreases as well, and it becomes increasingly difficult to support the energy term associated with domain walls [2]. Consequently, the number of domains is projected to decrease as first one and then the other types of walls are eliminated.

At still smaller sizes (~20nm for many magnets), ferroic particles undergo a phase change to the high temperature symmetry group. In the case of ferromagnetic particles (and more recently relaxor ferroelectrics as well) this has been correlated with the size at which the decrease in volume free energy accompanying magnetization is on the order of the thermal energy[3,4]. As a result, the spin direction is randomized with time, leading to an unmagnetized but highly orientable single domain crystal. Thus a magnet in this size regime is characterized by a zero net magnetization, the disappearance of a magnetic hysteresis loop, and extremely high magnetic susceptibilities. Materials displaying this type of enhanced responsiveness are termed superparamagnetic, superparaelectric, or superparaelastic solids.

Because ferroic properties are caused by cooperative phenomena, it is intuitively appealing to suppose that the system will be forced to revert to the para-state at some size where there are simply too few atoms to sustain the cooperative interactions. Thus, at sizes approaching atomic dimensions, superparamagnetic materials should revert to ordinary paramagnetism in which the magnetic susceptibility follows a Curie law with temperature.

In summary, then, we expect four regions in the size dependence of ferroic properties (Fig. 1). In large crystallites, multidomain effects accompanied by hysteresis take place. Reductions in size lead to single domain particles, and at yet smaller sizes to destabilized ferroics with large property coefficients, and finally to normal behavior as the particle size approaches the atomic scale. Similar transitions with size are expected in secondary ferroics. Typical sizes at which ferromagnetic, ferroelectric, and ferroelastic materials undergo these transitions and the effect of size on the transformations temperatures have been reviewed previously [5].

MAGNETIC NANOCOMPOSITES

Magnetic nanocomposites based on either small particles or thin films are by far the most extensively studied of the ferroic nanocomposites. Fundamental research on the properties of fine magnets has, in recent years, been spurred by the burgeoning market in technological applications of nanoscale devices. One of the obvious benefits to be reaped from the use of smaller magnetic particles (especially in the magnetic recording industry) is that smaller storage units lead to the possibility of storing information at a higher density. There are also some applications, however, where the small size of the ferroic component results in properties considerably different from those of a bulk magnet. Composites designed to exploit this effect include some thin film ferromagnetic/paramagnetic sandwiches and the magnetic fluids used in clean seals.

The magnetic recording industry has played a substantial role in the development of fine ferroic powders. Magnetic disks and tapes for recording and computer memories are prepared by coating a substrate, typically a smooth nylon film, with a layer of ferromagnetic powder dispersed in a binder. Powders are chosen for their retentivity, coercivity, low noise, and the density of information they can store [6]. As the last two characteristics are strongly correlated to the particle size, preparation of high quality fine particles is of considerable importance to the industry. For most applications acicular γ-Fe_2O_3 particles about .2 μm long and 0.02 μm in diameter are aligned parallel to both the film plane and the tape play direction. These materials qualify as composites through the use of a polymeric backing layers and a permanent binder to fix the magnetic particles to the backing.

In a number of instances, however, even higher storage densities are desired, and finer particles for both parallel and perpendicular recording are being investigated. In pioneering studies with the perpendicular recording technique, Iwasaki and coworkers developed an rf sputtered Co-Cr composition (thickness ~ 1 μm) which can store up to 15,000 bits/in [6]. This demonstration of feasibility, coupled with projected upper limits on the linear recording density topping 100,000 bits/inch (by contrast, current technology for parallel recording is limited to 15,000 bits of information/in, although 25,000 may eventually be possible [7]) has generated tremendous interest in this field. As of 1983, disks for perpendicular recording with densities on the order of 40,000 bits/in had been reported by several different firms [8] Principal among the materials systems being investigated for perpendicular recording are Co-doped iron oxide powders, Co films, and hexagonal barium ferrite platelets < 500 nm in diameter [9]. Because of the comparative fragility of the metallic films used in perpendicular recording, they are most typically utilized in hard disk drives or other "flying head" applications where there is no contact between the recording head and the magnetic medium. The development of more durable, corrosion resistant oxide films may lessen these restrictions somewhat, opening perpendicular recording to more and more applications.

One promising example of what is possible with ingenious processing is the 1-3 composite developed by Tsuya et al for uniform, high density magnetic components [10]. In their experiments, an aluminum alloy substrate is oxidized under conditions which result in the generation of a regular network of honeycomb cells on the surface. The columnar pores formed during oxidation can subsequently be etched to increase the diameter to >400Å and backfilled with iron to create a high density of magnetic elements with practical values for the coercive force (See Fig. 2) .

Fig. 1: Changes in the domain configurations of ferroics as a function of size

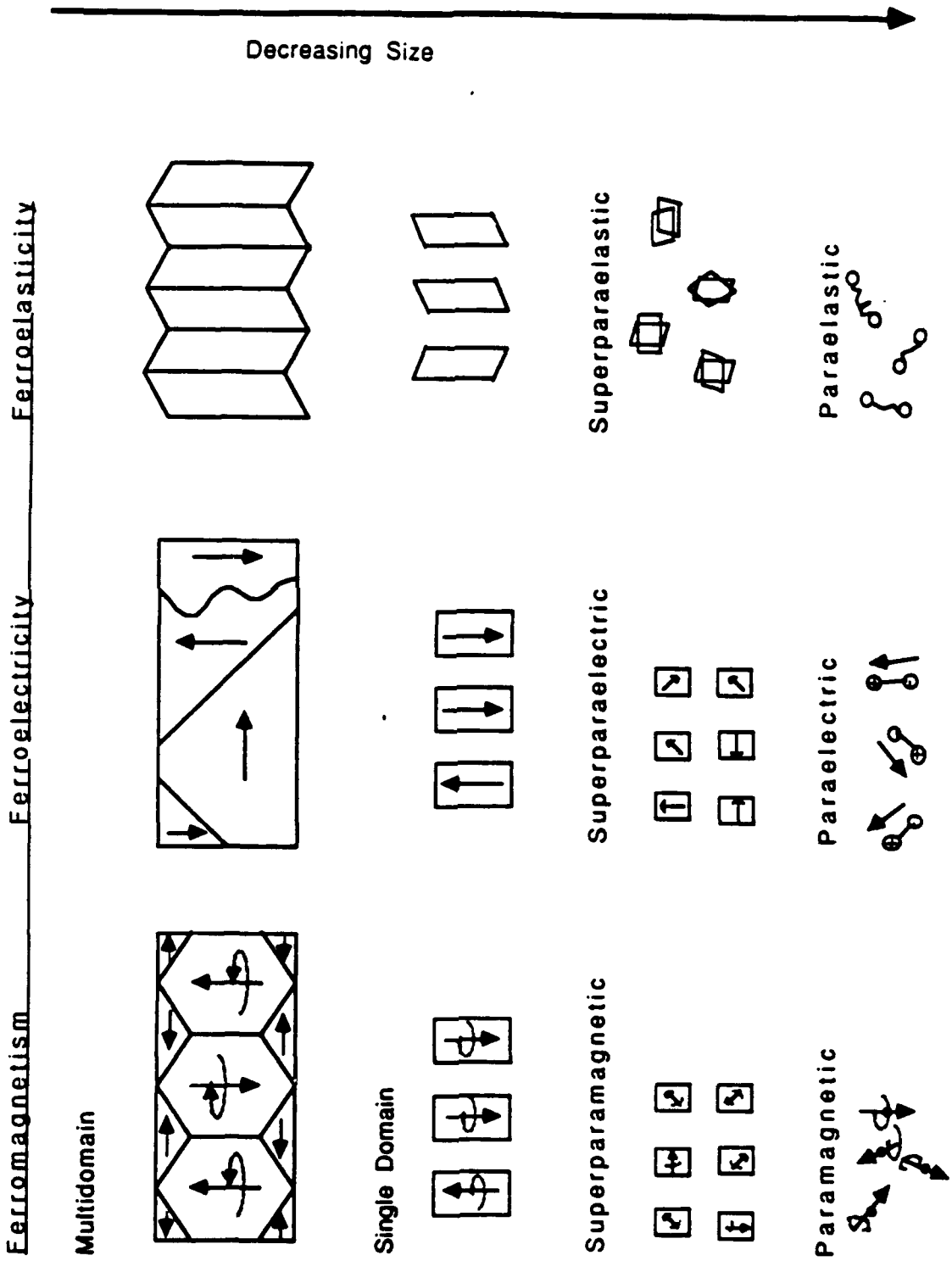

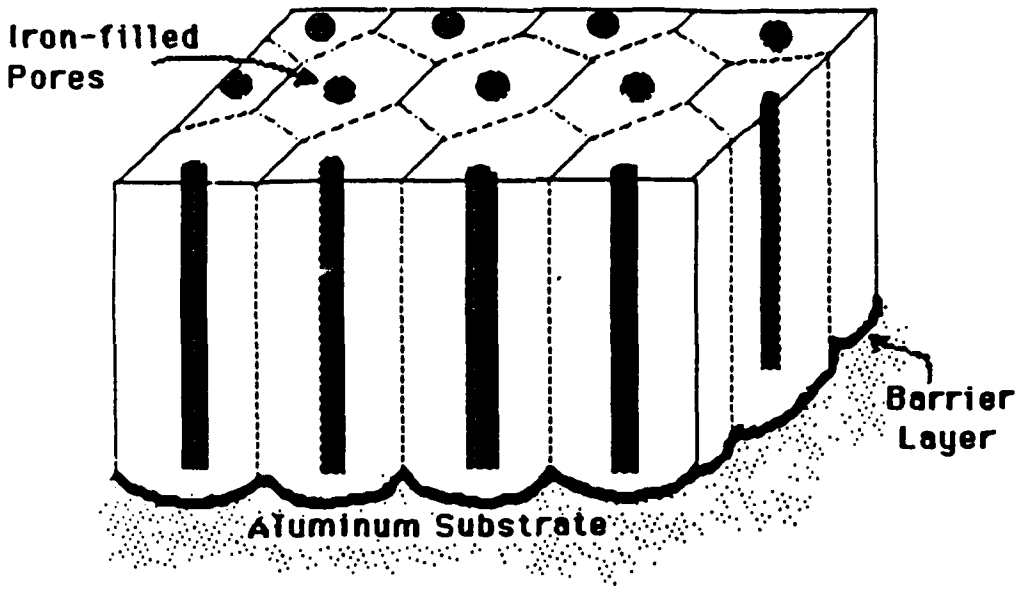

Fig. 2: 1-3 nanocomposite used for perpendicular recording. To produce this structure a honeycomb network of cells is created by oxidizing an aluminum alloy. The pores are then etched and backfilled with iron [10].

Another 2-2 composite which has been favored by the progress in vertical recording is the thin film lamellae structure used in magnetooptical recording. In this type of device, polarized light is either reflected from or transmitted through a thin magnetic layer. The ellipticity of the resulting light is affected by the magnetization state, leading to the possibility of storing and reading digital information. In order to eliminate noise which could otherwise interfere with the comparatively weak signal, a multilayer structure similar to that shown in Fig. 3 and designed to effectively magnify the desired signal through interference effects is sometimes incorporated [10].

Another growing field in magnetic recording is the use of ultrathin sandwiches of ferroic and non-magnetic layers. Using sophisticated deposition techniques, magnetic layers on the order of 5 - 20 Å can be separated by buffering films thin enough to permit magnetic coupling through the intermediate layer. This type of film will constitute a new type of magnetic recording media with exceptional storage properties. Currently under study are a variety of transition metal or rare earth multilayers which, when deposited under appropriate conditions, display an innate perpendicular magnetic anisotropy over limited thickness ranges [11-15]. Expecially exciting are some of the Co-based composites which couple the preferential alignment with an enhanced Kerr rotation angle, an excellent combination for magnetooptical recording applications [12]. Moreoever, the Co/Pd and Co/Pt composites under scrutiny are more corrosion resistant than the rare earth-containing alloys currently in use.

Work on this type of structure has also been extended to oxide superlattice systems. Bando has prepared CoO/NiO superlattices on sapphire and CoO/Fe_3O_4 on rocksalt, obtaining highly crystalline products in which the in-plane lattice spacings of each layer differed from the bulk values to provide a better match to other layers. In order to minimize concurrent changes in the unit cell volume, this was accompanied by variations in the out-of-plane spacings. Neutron diffraction results for the CoO/NiO modulated structures show a strong magnetic correlation between the layers and a well-defined Neel temperature for each composition. The transition temperature for the films all lie on the line joining the Neel temperatures of NiO and CoO [16, 17].

In contrast to the case of magnetic memory elements where a permanent magnet is essential for long-term storage, ferrofluids rely on the enhancement of magnetic properties that can be achieved through the use of superparamagnetic particles with no lasting moments.

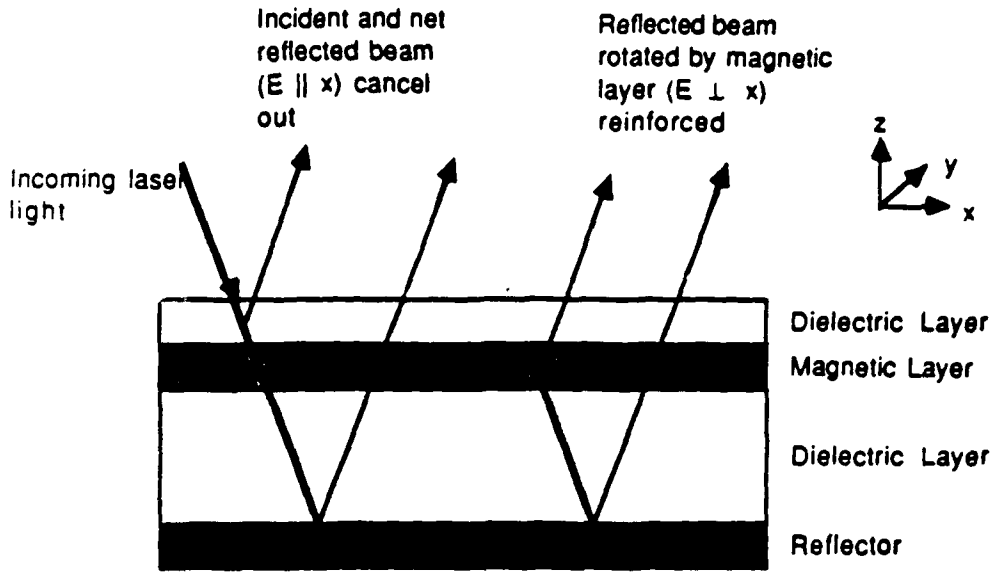

Fig. 3: 2-2 composite utilized in magnetooptic memories. This arrangement cancels out components of the light wave which are not rotated by the magnetic layer while amplifying the rotated signal [8]

Typically, a ferrofluid consists of a suspension of magnetic particles small enough (~10nm) so that Brownian motion is sufficient to prevent settling. As superparamagnets, each particle behaves as a paramagnet, but one in which the magnetic moment is hundreds or thousands of times higher than that of a single unit cell. Consequently, the use of exceptionally fine particles, mandated by the need for colloid stability, leads to the added benefit of magnetic properties superior to those which could be achieved with larger ferromagnetic particles.

Long term stability of such suspensions, however, also requires that individual particles be shielded from each other by a buffer layer thick enough to prevent agglomeration due to van der Waals forces. This has been approached primarily by two different routes, a) coating the particles with a polymer to insure mechanical separation and b) endowing all of the particles with a like surface charge so that Coulombic repulsion maintains the necessary distance [18,19].

The first approach most often utilizes organic solvents and surfactants to realize a well-dispersed colloid. As discussed below, dispersions of this type have found widespread use as non-contaminating seals. In the second means of suspending the powders, however, the particles are charged in the same way so that each behaves as a macro-ion. One of the distinct advantages of this system is the ease with which the ferrofluid can be dispersed in water-based solutions. This could prove extremely beneficial in medical technology as a ferrofluid with a pH and salinity comparable to blood could be introduced into the circulatory system and manipulated throughout the body by external magnetic fields. Once located in position, it could then serve as an aid in diagnostic imaging, a temporary means of blocking blood flow, a drug dispenser, or as a means of selectively concentrating high doses of X-rays in diseased tissue while minimizing damage to neighboring areas [19,20].

Several of the more conventional uses of ferrofluids also entail controlling the position of the fluid with an external magnetic field. A magnetic fluid separating two gaseous phases, for example, can be pinned in place by an encircling magnetic field, even if there is a pressure differential across the seal. Seals and bearings of this type, being non-abrasive, have received wide acceptance in industries where the dust created through ordinary wear on solid-solid seals can be catastrophic. Consequently, this type of seal is regularly used in computer hard disks to prevent dust from entering and "crashing" a head. Similarly, ferrofluid seals have been incorporated into cleanroom design, crystal growth units, gas lasers, motors, blowers,

cryogenic units, and cleanroom robotics [10,21].

Other applications in which the liquid position is controlled by a magnetic field include loudspeakers and inkjet printers. Loudspeaker designs of this type incorporate magnetic fluids to fill the gap between the voice coil and the permanent magnet. The fluid is retained in the gap by the existing magnetic field; its presence dissipates heat which would otherwise limit the power handling, and flattens the frequency response. Ferromagnetic inks for inkjet printers have also been studied at the Matsushita Electric company in Japan. The use of magnetic ink aids in the formation and resorption of the jet, leading to output with quality comparable to the lower end of available laser printers [19,21].

Other prototype ferrofluid-based devices are aimed at the detection of magnetically induced anisotropy in composite properties (i.e. birefringence in the refractive index). Thus, for example, a viscometer suitable for small samples has been constructed on the principle that as a magnetic field is removed from a liquid to which a small amount of ferrofluid has been mixed, the observed birefringence will decay exponentially at a rate proportional to the host fluid viscosity. In principle, the induced birefringence could also be utilized in magneto-optic devices for manipulating polarized light [22].

Ferrofluids have also found application in a number of different fields, including levitation systems for separating materials of differing density, vibration dampers, engines for converting low grade heat to useable energy, and devices to measure very small inclination angles [19,21].

Self Assembling Nanocomposites

The definition of nanocomposite can also be extended to encompass macroscopically "single phase" materials displaying inhomogeneities in structure or properties on a fine scale. Examples of this behavior found among ferromagnetic composites include solid solutions of magnetic and nonmagnetic materials (i.e. Fe in Cu) in which the interactions between isolated magnetic dipoles (iron atoms) can be either ferromagnetic or antiferromagnetic [23]. As a consequence of the complicated magnetic interactions that occur, the lowest energy state in such spin glasses consists of islands of aligned spins. Recent studies suggest that a few magnetic perovskites also behave like spin glasses (See Fig. 4). In this latter case, the formation of nanodomains in an essentially disordered matrix has been coupled to a charge disproportionation:

$$2\ Fe^{4+} \leftrightarrow Fe^{(4-\lambda)+} + Fe^{(4+\lambda)+}$$

and the appearance of a combination of ferromagnetic and antiferromagnetic ordering [24,25]. The resultant picture bears many qualitative similarities to a relaxor ferroelectric. Although few, if any, practical applications for spin glasses are under development, the attempts to mathematically model such complicated, "dirty" systems has had interesting implications on problems as diverse as finding optimized solutions for large sets of variables and constraints and determining if polymer sequencing could have affected the process of evolution [23].

FERROELECTRIC NANOCOMPOSITES

In contrast to the case of ferromagnetic nanocomposites, ferroelectric nanocomposites are largely unstudied. This is due, in part, to the concentration on the larger scale composites currently utilized as pressure sensors, vibration dampers, and transducers. However, there are an increasing number of applications in which a small component size is mandated by the need for optical transparency or low driving voltages, prompting a growing interest in the field of fine ferroelectrics. While much of this work is in its preliminary stages, current results promise properties which cannot currently be achieved with bulk ferroelectrics.

One interesting example of this is the family of relaxor ferroelectrics, which although prepared as bulk materials, display inhomogeneities in both composition and ordering on a nanometer scale [4,26-29]. In TEM studies on compositions including many of the

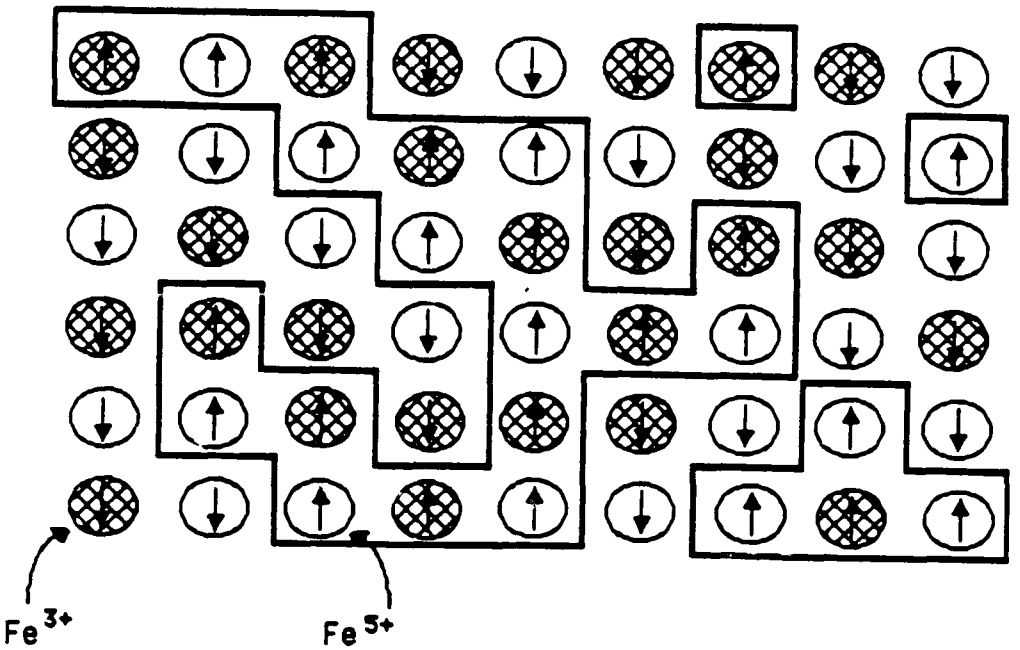

Fig. 4: Schematic of a spin glass showing the regions of aligned domains [24,25] caused by antiferromagnetic coupling between like ions and ferromagnetic coupling between unlike ions.

$A(B'_{1/2},B''_{1/2})O_3$ and $A(B'_{2/3},B''_{1/3})O_3$ perovskites, it has been found that such materials exhibit microdomains (typically 20 - 300 Å in size) of 1:1 ordering on the B sublattice dispersed in a disordered matrix [27-29]. It has been suggested that as a result of this local nonstoichiometry the spontaneous polarization in these materials is also disordered on a very fine scale [4,28]. Thus a lead magnesium niobate ceramic can be regarded as a collection of disordered, but highly orientable, dipoles. Moreover, these incongruities in the lattice lead to different regions of a crystallite having different Curie temperatures. The result, much like the case of superparamagnetism, is a high dielectric permittivity over a broad temperature range even though the net spontaneous polarization is zero. The low temperature coefficient of capacitance (TCC) of these materials coupled with the high dielectric constant (a marked contrast to homogeneous ferroelectrics where the well-defined Curie temperature results in a large TCC in those regions where the dielectric constant is also high) makes relaxors attractive as capacitors. The comparatively low firing temperatures of these materials is also eliciting interest from the electronic component packaging industry as it should permit co-firing of capacitors with high conductivity, low-cost electrodes.

In many of the relaxor compositions, the small-scale heterogeneities present on quenching can be controlled by annealing at high temperatures to produce larger ordered regions. Once the ordered microdomains in a relaxor grow beyond a certain size, however, the material reverts to ordinary ferroelectric (or antiferroelectric) behavior with a well defined transition temperature and a non-dispersive dielectric response. This, in turn, raises the TCC, minimizing its potential use as a capacitor composition. For lead indium niobate the critical domain size at which antiferroelectric ordering appears is 80 nm [28].

Another example of the effect of nano-scale heterogeneities on macroscopic properties is the recent discovery of exceptional optical properties in the incommensurate phase of $[N(CH_3)_4]_2ZnCl_4$ [30]. Here, the deviation from the crystal periodicity is accompanied by a peak in the electrooptic coefficient to a value 10^5 times higher than has been reported for any other material. When the temperature is raised to the point that this material returns to a commensurate lattice, effectively regaining its small scale periodicity, the electro-optic coefficient returns to more common value.

In addition to such nanocomposites where the pertinent inhomogeneity is caused by a small-scale restructuring of the lattice, there are ferroelectric nanocomposites produced by

mixing two or more different phases together. Among these more conventional two-phase ferroelectric nanocomposites is the electronic analog to the ferromagnetic fluid. Using fine $BaTiO_3$ particles suspended in an organic carrier liquid, Miller et al have shown that the resulting liquid displays a maximum in the dielectric constant at the tetragonal- cubic phase transition of the perovskite [31]. Similarly, Bachmann and Barner have determined that milled particles (average diameter = 10nm) dispersed in a mixture of heptane and oleic acid have permanent polar moments [32]. Hopefully as work in this area proceeds, these liquids will find applications in areas as diverse as those employing ferromagnetic fluids. In particular, ferroelectric fluids could be used as an alternative to liquid crystals in display panels.

These goals do not seem unreasonable in light of the some of the recent successes in preparing solid 0-3 ferroelectric nanocomposites with ferroic properties. Indicative of the advances in this area is the work of Lee at al with coprecipitated $PbTiO_3$ powders dispersed in a polymeric matrix. In a series of poling studies they demonstrated that the polarization vectors of powders <~20 nm in diameter could be aligned under strong electric fields, leading to a net polar moment and piezoelectricity in the composite [33]. 0-3 composites of this type have traditionally been used as vibration sensors and dampers. It is hoped that by miniaturizing the ferroic component such materials can be integrated into optical applications (see below).

Another area where small particulate ferroelectrics may be useful is in the preparation of materials for frequency doubling high intensity IR lasers down to a wavelength at which SiO_2 optical fibers transmit light well. In order to accomplish this, it is necessary to use a material which is both an efficient second harmonic generator and for which the refractive index can be matched at the primary and secondary frequencies. While ferroelectrics fulfill the first requirement, the refractive indices of ferroelectrics undergo ordinary dispersion, so index matching is not possible in an unpoled ceramic. However, it should be possible to compensate for the dispersion by using a crystal's birefringence to slow the frequency doubled wave [34]. Unfortunately, no single material couples the necessary magnitude for the optical anisotropy and efficient conversion of the primary to the secondary frequency with resistance to optical damage. One of the schemes proposed to overcome this difficulty entails preparing a composite of non-spherical ferroelectric particles embedded in a transparent matrix. If all of the particles could be aligned, the resulting material should display form birefringence (due to the particle shape anisotropy) of a magnitude large enough for index matching. To insure transparency of such a composite, though, the dispersed phase must be considerably smaller than the wavelength of light (~500nm) to avoid scattering losses.

FERROELASTIC NANOCOMPOSITES

Although ferroelastic materials were first described by Aizu in 1969, there are still very few devices utilizing the ferroic nature of these materials. Instead, the gadolinium molybdate crystals proposed for use in optical shutters, read only memories, and electronically variable SAW/bulk delay lines [35] most often possess few domain walls. Part of the reason that comparatively little is known about ferroelastics with artificially generated fine domain structures is that there are a limited number of materials for which the coercive stress is low enough to move the domain walls without affecting either the crystal's structural state or its mechanical integrity. Indeed, the amount of energy it would take to induce controlled, closely spaced twins is often too large to be sustained.

This may be the reason that the ferroic properties of zirconia, an additive widely used for toughening ceramics, are largely unstudied. Although one would expect domain wall movement to permit stress relaxation and so increase the fracture toughness of zirconia ceramics, available experimental data are contradictory and do not completely support this hypothesis. Studies by Virkar and Matsumoto, for example, indicate that the toughness of tetragonal zirconia is related to ferroelastic contributions [36]. Although these results have been called into question [37], similar conclusions can be inferred from the careful studies of Michel et al [38]. In contrast, Ingel et al [39] concluded on the basis of mechanical property measurements on pure zirconia as a function of temperature that the major contribution to the

toughness in zirconia is the tetragonal to monoclinic phase transition. The exceptionally large fracture toughnesses of partially stabilized zirconia ceramics are also explained as stemming from the same stress- induced phase transformation [40,41]. At temperatures above 900° C, Ingel's data does contain a slight upward trend in fracture strength which may be related to ferroelasticity. However, if this indicates the magnitude of energy (temperature) necessary to free the domain walls, it clearly precludes using ferroelasticity as the sole toughening mechanism at room temperature for zirconia ceramics. Consequently, it can be concluded that the coercive stress of many ferroelastics is too high for practical manipulation at low temperatures.

One notable exception to this is neodymium pentaphosphate (NPP), a pure ferroelastic crystal first discovered in 1972 by Danielmeyer and Weber. The high temperature, prototype form of NPP is orthorhombic while the ferroelastic low temperature form is monoclinic (point group 2/m). There are two types of domain structures in NPP; those separated by a (001) twin plane (a-type domain wall) and others bounded by (100) twin planes (b-type domain wall). Interesting from a practical point of view is the fact that in NPP the domain walls can be moved by a shear stress of only 0.014 N/mm^2.

Meeks and Auld have made outstanding progress in controlling the domain structure in NPP by using a mechanical stress in conjunction with a laser beam [42]. Several types of domain structures can be generated in this fashion, including tunable arrays with domain wall periods between 100 and 3 μm. This lower value agrees with an estimate based on theoretical considerations of the minimum achievable domain size. However, it was also shown that periods down to 0.5 μm could be obtained with arrays trapped between two types of domain walls (See Fig. 5). Periodic structures like this interact with both optical and acoustic waves, leading to potential applications as a new functional material for tunable active gratings for lasers, tunable diffraction gratings, tunable Bragg reflection gratings, tunable acoustic filters, optical modulators, and optical domain wall memories. As their lowest periodicity is just at the border where a structure can be considered nanoscale, this work offers the possibility that true nanocomposites based on pure ferroelastics *may eventually* be possible.

One approach designed to overcome the difficulties associated with producing nanoscale domains is to utilize ferroics in which the ferroelasticity arises only as a consequence of the primary order parameter. In the perovskite ferroelectrics, for example, the 90° domains are both ferroelectric and ferroelastic due to the spontaneous strain. Thus, in relaxor ferroelectrics, where the regions of coherent polarization can be on the order of 100 nm, ferroelastic domains with similar scales should also be present. Lead lanthanum zirconate titanate (PLZT) ceramics fulfilling these requirements have been shown to demonstrate shape memory effects [43], a property closely tied with ferroelasticity. This is a particularly exciting result as ferroelastics with very small domains might become superparaelastic. The high mechanical compliance that should accompany such a transition would be extremely useful in preparing ceramics with high fracture toughnesses.

CONCLUSIONS

The study of composite electroceramics has been a fruitful source of new properties and new functional materials. As these components are miniaturized, however, the focus of composite design has broadened from engineering of advantageous connectivity patterns to include the utilization of size effects to control the macroscopic behavior of nanocomposites. This has proved to be especially important for ferroic nanocomposites, where a reduction in size profoundly affects the number and type of domain walls present in the material. The role of this type of behavior on several functional ferromagnetic, ferroelectric, and ferroelastic nanocomposites has been discussed.

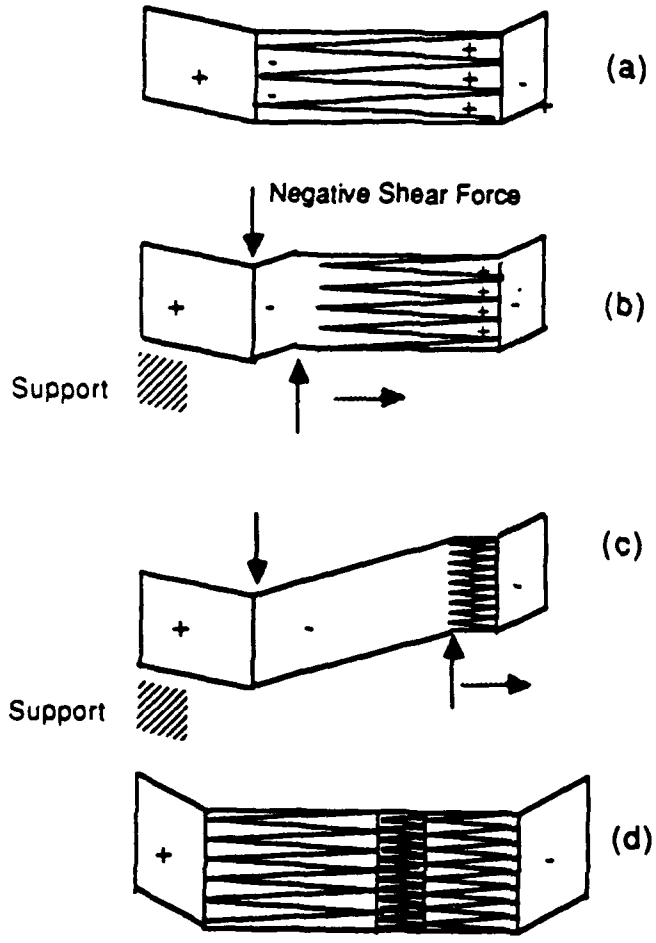

Fig. 5: One method of obtaining tunable twins. The initial state shown in (a) is stressed in (b). As the bottom stress point is moved to the right, the domains become much smaller (c). (d) shows the configuration with which the 500nm periodic domains were created [42].

ACKNOWLEDGEMENTS

The authors would like to thank DARPA, Alcoa, and Corning Glass for their financial support of this project.

REFERENCES

1. R. E. Newnham, Ann. Rev. Mater. Sci. 1986. 16 47 (1986).
2. C. Kittel, Phys. Rev 70(11,12) 965 (1946).
3. C.P. Bean and I.S. Jacobs, J. Appl. Phys. 27(12) 1448 (1956).
4. L.E. Cross Ferroelectrics 76(3-4) 241 (1987).
5. R. E. Newnham and S.E. McKinstry, Indianapolis Meeting of the American Ceramic Society 1989.
6. Marvin Camras, Magentic Recording Handbook, (Van Nostrand Reinhold Company, New York, 1988)
7. Robert M. White, Sci. Amer. 243 138 (1980).
8. Robert M. White, IEEE Spectrum 20 32 (1983).
9. O. Kubo, T. Ido, H. Yokoyama, and Y. Koike, J. Appl. Phys. 57(1) 4280 (1985).

10. N. Tsuya, Y. Saito, H. Nakamura, S. Hayano, A. Furugohri, K. Ohta, Y. Wakui, and T. Tokushima, J. Mag. Mag. Mat. 54-57 1681-1682 (1986).
11. Noboru Sato, J. Appl. Phys. 59(7) 2514 (1986).
12. Y. Ochiai, S. Hashimoto, and K. Aso, IEEE Trans. Mag. 25(5) 3755 (1989).
13. W.B. Zeper, F.J.A.M. Greidanusm and P.F. Carcia, IEEE Trans. Mag. 25(5) 3764 (1989).
14. S. Honda, S. Nishimura, and T. Kusuda, IEEE Trans. Mag. 25(5) 4027 (1989).
15. P.J. Grundy, S.S. Babkair, and M. Ohkoshi, IEEE Trans. Mag. 25(5) 3626 (1989).
16. Y. Bando, Proc. Seventh Seminar on Frontier Technology - Nano-Hybridization and Creation of New Functions Feb. 7-10, 1989 Oiso, Japan.
17. M. Takano, T. Terashima, Y. Bando, and H. Ikeda, "Neutron diffraction study of artificial CoO-NiO superlattices," Appl. Phys. Lett 51(3) 205 (1987).
18. B. Berkovsky, ed., Thermomechnaics of Magnetic Fluids, (Hemisphere Publishing Corporation, Washington, 1978)
19. Jean-Claude Bacri, Regine Perzynski, and Dominique Salin, Endeavor, New Series 12(2) 76 (1988).
20. M.P. Perry, in Thermomechanics of Magnetic Fluids, edited by B. Berkovsky (Hemisphere Publishing Corporation, Washington 1978)
21. Ronald E. Rosenweig, Scientific American Oct. 1982, 136.
22. R.V. Mehta, in Thermomechanics of Magnetic Fluids, edited by B. Berkovsky (Hemisphere Publishing Corporation, Washington 1978).
23. Daniel L. Stein, Scientific American July 1989, 52.
24. P.D. Battle, T.C. Gibb, P. Lightfoot, and M. Matsui, submitted to J. Solid State Chem. (1989).
25. T.C Gibb and M. Matsuo, J. Solid State Chem. 81 82 (1989).
26. G.A. Smolensky, J. Phys. Soc. Jpn 28 suppl. 26-37 (1970).
27. J. Chen, H. M. Chan, and M.P. Harmer, J. Am. Ceram. Soc. 72(4) 593 (1989).
28. C.A. Randall, D.J. Barber, P. Groves, and R.W. Whatmore, J. Mat. Sci.23(10) 3678 (1988).
29. C.A. Randall and A.S. Bhalla, submitted to Jap. J. Appl. Phys. (1989).
30. K. Saito, T. Watanabe, and J. Kobayashi, Ferroelectrics 75 153 (1987).
31. D. Miller, unpublished work
32. R. Bachmann and K. Barner, Sol. State Comm. 68(9) 865 (1988).
33. M. Lee, A. Halliyal, and R. E. Newnham, Ferroelectrics 87 71 (1988).
34. Frits Zernicke and John E. Midwinter, Applied Nonlinear Optics (John Wiley and Sons, New York 1973).
35. L.A. Coldren, R.A. Lemons, A.M. Glass, and W.A. Bonner, Appl. Phys. Lett 30(10) 506 (1977).
36. A.V. Virkar and R.L.K. Matsumoto J. Am. Ceram. Soc. 69(10) C224 (1986).
37. M.V. Swain in Science and Technology of Zirconia III edited by S. Somiya, N. Yamamoto, and H. Yanagida (The American Ceramic Soc. Inc., Columbus, Ohio 1988) p. 439.
38. D. Michel, L. Mazerolles, and M.P. Jorba in Science and Technology of Zirconia II, edited by N. Clausen, M. Ruhle, and A. Heuer (The American Ceramic Society Inc., Columbus, Ohio1983) p. 131.
39. R.P. Ingel, P.A. Wilging, and B.A. Bender in Science and Technology of Zirconia III edited by S. Somiya, N. Yamamoto, and H. Yanagida (The American Ceramic Soc. Inc., Columbus, Ohio 1988) p. 459.
40. A.G. Evans and R.M. Cannon Acta Metall. 34(5) 761 (1986).
41. K. Urabe, A. Nakajima, H. Ikawa, and S. Udagawa in Science and Technology of Zirconia III edited by S. Somiya, N. Yamamoto, and H. Yanagida (The American Ceramic Soc. Inc., Columbus, Ohio 1988) p. 345.
42. S.W. Meeks and B.A. Auld, Adv. Electron. Electron. Phys. 71 251 (1988).
43. T. Kimura, R.E. Newnham, and L.E. Cross, Phase Trans. 2 113 (1981).

APPENDIX 17

INCOMMENSURATE PHASE IN $Ba_2TiSi_2O_3$

S. A. Markgraf
C. A. Randall
A. S. Bhalla
R. J. Reeder

INCOMMENSURATE PHASE IN $Ba_2TiSi_2O_8$

S. A. Markgraf, C. A. Randall, A. S. Bhalla

Materials Research Laboratory, The Pennsylvania State University
University Park, PA 16802

and

R. J. Reeder

Department of Earth and Space Science, S.U.N.Y. at Stony Brook
Stony Brook, NY 11794

Transmission electron microscope examination of $Ba_2TiSi_2O_8$ has revealed a new incommensurate phase. The incommensurate reflections occur along <100>, and in the *hk*l/2 level. At elevated temperatures the incommensurate reflections disappear; it is suggested that the property anomalies previously reported in this material at 160°C are due to the onset of the incommensuration. Differences and similarities with other related compounds are discussed.

INTRODUCTION

Fresnoite, $Ba_2TiSi_2O_8$ (BTS), is a relatively rare mineral found in sanbornite-bearing metamorphic rocks[1]. It has been studied primarily for its polar properties, where much of the work has centered on the possibility of using BTS in surface acoustic wave devices[2]. Fresnoite-based materials can be fabricated through the polar glass-ceramic process[3]. A comparative study between single crystals of BTS and the related polar glass-ceramics revealed an unusual anomaly at 160°C[4]. The most striking signature of this anomaly was found in the pyroelectric behavior. With increasing temperature the pyroelectric coefficient increases steadily until 160°C, whereupon it decreases rapidly, passing through zero at 190°C. A broad peak in the dielectric constant and the piezoelectric coupling coefficient were also indications of the anomaly. Although these anomalies suggested a phase transition at 160°C in BTS, single-crystal structure refinements at 25 and 300°C resulted in satisfactory residuals within the same space group[5]. This result seemed to rule out the possibility of a phase transition, and although several possible explanations were presented (cancellation of primary and secondary effects[4]; anomalies in the elastic constants[5], which have since been observed by Chang and Bhalla[6]), the cause of the anomaly remained unclear.

The germanium analog of BTS, $Ba_2TiGe_2O_8$ (BTG), has two phase transitions: a ferroelastic phase transition at 850°C, and an unusual low-temperature transition at -50°C on cooling, 0°C on heating. An incommensurate modulation of the structure exists throughout the temperature range 850°C to -50°C[7].

Transmission electron microscope (TEM) examination of single crystals of BTS has revealed a previously unreported set of superlattice reflections. We show that these reflections are incommensurate. This communication reports on the incommensurate phase in BTS, its relationship with the 160°C anomaly, and its correspondence to similar compounds.

EXPERIMENTAL

Several different samples were used in this study. Single crystals of BTS were grown by the Czochralski technique, and with a miniature float zone technique from ceramic feed stock and Czochralski-grown BTS seeds. Ceramic samples were prepared through a conventional mixed-oxide technique.

The samples were ion-beam thinned and examined initially at room-temperature with a Philips 420 TEM. All samples showed identical diffraction patterns; therefore we will only discuss the Czochralski-grown sample. This crystal was also examined on a J.E.O.L. 200 CX Electron Microscope equipped with a Gatan model 628 hot stage.

The crystal used in the previous structure refinements of Markgraf et al.[5] was reexamined with an x-ray precession camera operating with filtered Mo radiation.

RESULTS

Previous studies on single crystals of BTS showed a tetragonal cell in space group P4bm (C_{4v}^2), a = 8.52 Å, c = 5.21 Å. Figure 1 presents a zone axis <001> electron diffraction pattern from a BTS single crystal. The arrows mark the weak reflections we consider as incommensurate. These reflections occur at $(1+\delta)a^*/3$, where δ=0.20, although the accuracy of this measurement is not high. Electron diffraction patterns on tilted [001] samples show incommensurate reflections in the *hk*l/2 level (Fig. 2). These reflections effectively double the *c* lattice parameter. Figure 3 shows the room-temperature three-dimensional reciprocal lattice of BTS.

The single crystal used in the structure analysis of Markgraf et al.[5] was examined with a x-ray precession camera for reflections in the *hk*l/2 level. An extremely long exposure (six weeks) confirmed the presence of the incommensurate reflections in this sample.

Heating the sample *in-situ* within the electron microscope revealed that the incommensurate reflections become progressively weaker, until they are no longer observable (Figs. 1 and 2). The incommensurate reflections reappear with no noticeable difference in position or intensity upon cooling to room-temperature. The specimen/furnace assembly utilized in this hot-stage can lead to

large thermal differences between the temperature at the observation area and the thermocouple readout from the microscope furnace. We are therefore reluctant to compare the transition temperature obtained from the microscope hot-stage with the transition temperature obtained from property anomalies; they are however within the same range (Fig. 1b was obtained with a furnace temperature of 345°C, Fig. 2b was obtained with a furnace temperature of 210°C on a subsequent run).

Dark-field imaging using several incommensurate reflections showed the presence of domains (Figure 4). These domains are very fine, on the order of 100 nm. in size, and show very weak contrast. On the lower energy microscope (Philips: 120 kV) we observed only a mottled background; with the higher energy microscope (J.E.O.L: 200 kV) the contrast was much better. Unfortunately we could not isolate reflections along just the <100> direction or the <010> direction for dark-field work. We had hoped to determine if different domains were excited by using reflections either along <100> or <010>.

DISCUSSION

Previous work has shown that BTS has the same structure at room-temperature and at 300°C[5]. Because of the structural similarity above and below 160°C, no structural explanation was available for the unusual anomaly observed in BTS. However, the temperature behavior of the incommensurate reflections leads us to the conclusion that the anomaly in BTS is the result of a prototypic to incommensurate type of phase transition. Prototype-to-incommensurate phase transitions are commonly subtle in their signature.

There are several unexplained features of our TEM analysis. The incommensurate reflections are strongest in the center of the *hk*0 diffraction pattern. From a kinematical treatment this indicates that the cause of the incommensuration may be compositional in nature[8]. Incommensurates with displacive origins may show the incommensurate reflections becoming stronger with increasing distance from the center of the diffraction pattern. However it seems unlikely that the cause of the incommensuration is due to a modulation of the composition. Rather it is more likely that the Debye-Waller parameters, ignored in the above analysis, play a major role in the intensity of the

incommensurate reflections. It should be noted that not all incommensurate crystals, wherein the modulation is well understood, follow a simple compositional *versus* displacive guideline (e.g. Rb_2ZnCl_4[9], $Ba_2NaNb_5O_{15}$[10]) in their diffraction behavior.

We are uncertain of the cause of the domains formed by dark field imaging the incommensurate reflections. Analysis is difficult due to their high density and weak contrast. One possibility is that they represent discommensurations. Discommensurations are the crystallographic equivalent of antiphase boundaries, in that they are imaged with satellite reflections, or in this case incommensurate reflections. Microscopically discommensurations represent walls separating commensurate regions. The dark areas on Fig. 4 would then be regions with a different modulation vector, areas not excited by the incommensurate reflections chosen. Unfortunately, because of the resolution of the micrographs, we are not able to correlate the density of the domains with δ, or analyze their interactions for some understanding of the symmetry of the modulation vector(s).

As mentioned previously the germanium analog of BTS has an incommensurate phase, and this incommensurate phase is coupled with a ferroelastic phase transition occurring at 850°C. This behavior is attributed to the buckling of the pyrogermanate group. Adding silicon to the germanium endmember suppresses the ferroelastic phase transition, until at approximately 40 atomic percent silicon the phase is no longer ferroelastic at room-temperature[11]. It is therefore surprising to find an incommensurate phase in BTS, especially without the appearance of ferroelasticity.

Aspects of the incommensurate phase in BTS are similar to those observed in BTG. The most obvious similarity is the occurrence of the reflections at *hk*l/2 in both compounds. Only superlattice reflections are present in this level, and these reflections are quite strong relative to superlattice reflections in the *hk*0 level. An important difference in the two incommensurate phases is that in BTG the modulation is along the prototypic <110> direction, whereas in BTS it is found along <100>.

Although the strain present in BTS is evidently not great enough to induce ferroelastic behavior, it is apparently enough to cause slight structural distortions and the concomitant incommensurate phase. The cause for these structural distortions is a matter of speculation. One

possibility is that barium in the ten-fold site causes a strain in the basal plane containing the Si_2O_7 and TiO_5 linkage. Certainly it is the basal plane that contains much of the strain in BTS. Chang and Bhalla[6] have shown that only the c_{11}, c_{12}, and c_{66} elastic constants are affected by the phase transition. Other indications of this strain can be found in an optical conoscopic examination of BTS. The interference figure expected for a uniaxial crystal is slightly distorted, showing the effects of strain, and giving a hint of biaxial character. One test of this argument would be through examination of $(Ba,Sr)_2TiSi_2O_8$. Strontium, with a smaller ionic radius, should not cause as much strain in the structure. Similar arguments have been advanced to explain the incommensurate phase in several melilite compounds[12,13], which have a closely related structure.

CONCLUSION

An incommensurate phase is described in $Ba_2TiSi_2O_8$ for the first time. The incommensuration has also been confirmed to occur in samples previously examined with x-rays. It is postulated that the incommensurate phase is responsible for the property anomalies observed at 160°C through a prototype-to-incommensurate type of phase transition. The modulation in BTS occurs in a different direction than that found in the germanium analog, although both show superlattice reflections in the *hkl*/2 level. The modulation is suggested to be associated with the large barium cation causing distortions in the basal Si_2O_7 and TiO_5 linkage.

Acknowledgement: We would like to thank Z.P. Chang for the donation of the Czochralski-grown crystal.

REFERENCES

1. J. T. Alfors, M.C. Stinson & R.A. Matthews, Am. Mineral. **50**, 314 (1965).

2. J. Melngailis, J.F. Vetelino, A. Jhunjhunwala, T.B. Reed, R.E. Fahey & E. Stern, Appl. Phys. Lett. **32**, 203 (1978), and references therein.

3. A. Halliyal, A.S. Bhalla, R.E. Newnham & L.E. Cross, J. Mat. Sci. **16**, 1023 (1981).

4. A. Halliyal, A.S. Bhalla, S.A. Markgraf, L.E. Cross & R.E. Newnham, Ferroelec. 62, 27 (1985).

5. S. A. Markgraf, A. Halliyal, A.S. Bhalla, R.E. Newnham & C.T. Prewitt, Ferroelec. 62, 17 (1985).

6. Z. P. Chang & A.S. Bhalla, Materials Letters **8**, 418 (1989).

7. S. A. Markgraf & A.S. Bhalla, Phase Trans. **18**, 55 (1989).

8. J. W. Steeds, D. M. Bird, D. J. Eaglesham, S. McKernan, R. Vincent & R.L. Withers, Ultramicroscopy **18**, 97 (1985).

9. H. Bestgen, Sol. State Comm. **58**, 197 (1986).

10. G. Van Tendeloo, S. Amelinckx, C. Manolinkas & W. Shulin, Phys. Stat. Sol. (a) 91, 483 (1985).

11. H. Schmid, P. Genequand, H. Tippmann, G. Pouilly & H. Guédu, J. Mat. Sci. 13, 2257 (1978).

12. B. S. Hemingway, H. T. Evans, G. L. Nord, Jr., H. T. Haselton, R. A. Robie & J. J. McGee, Can. Mineral. 24, 425 (1986).

13. F. Seifert, M. Czank, B. Simons and W. Schmahl, Phys. Chem. Minerals. 14, 26 (1987).

FIGURE CAPTIONS

Figure 1. BTS single crystal zone axis <001> electron diffraction pattern : (a) room temperature; (b) elevated temperature.

Figure 2. BTS single crystal *tilted* zone axis <001> electron diffraction pattern: (a) room temperature; (b) elevated temperature.

Figure 3. Three-dimensional view of the observed reciprocal lattice found in BTS at room temperature with electron diffraction. The thick lines outline the prototypic tetragonal unit cell, the thin lines serve as a guide for the eye.

Figure 4. Dark-field image using several *hk*l/2 incommensurate reflections at room temperatu (a) observed contrast; (b) enlargement of region of (a); (c) incommensurate reflections utilized are arrowed.

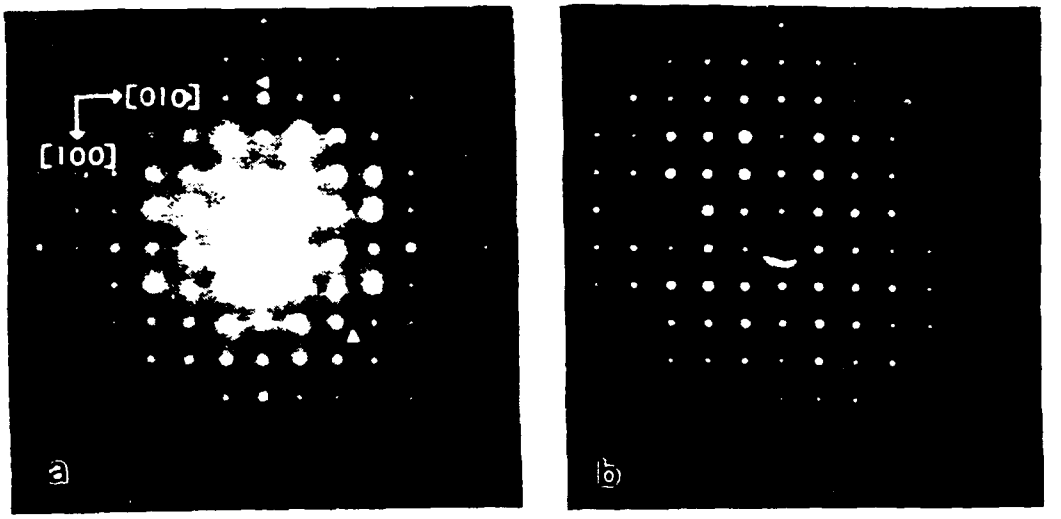
[010]
[100]
a
b

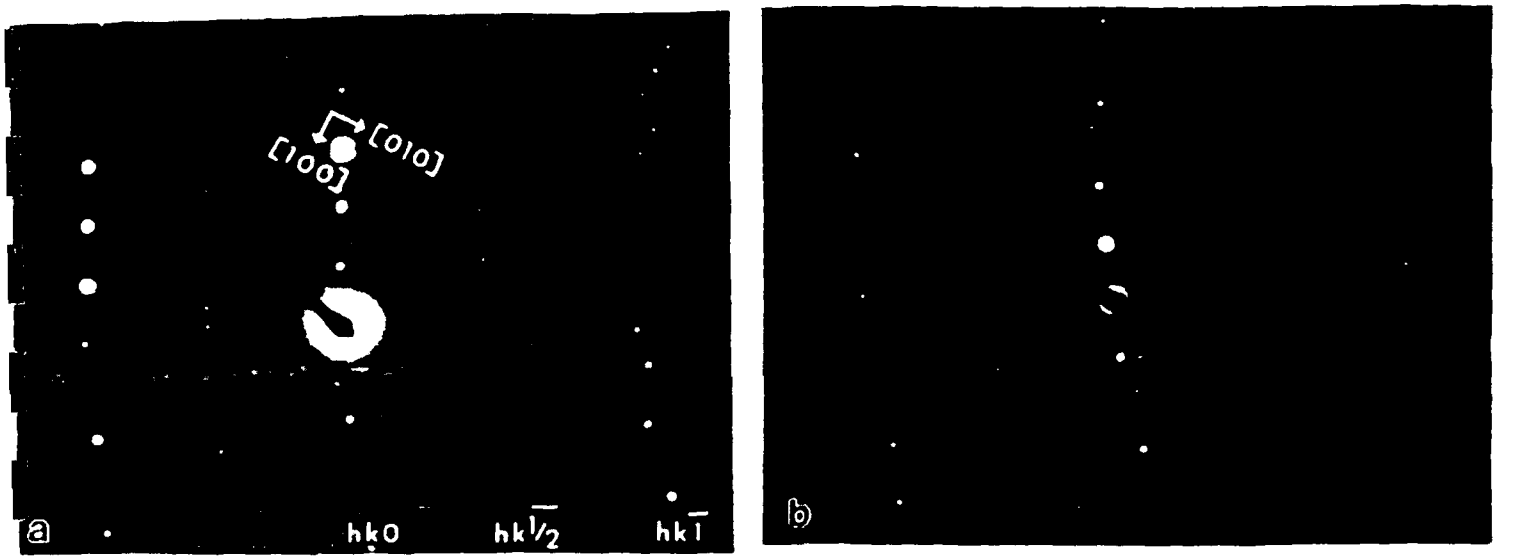
[010]
[100]
a
hk0
hk1/2
hk1
b

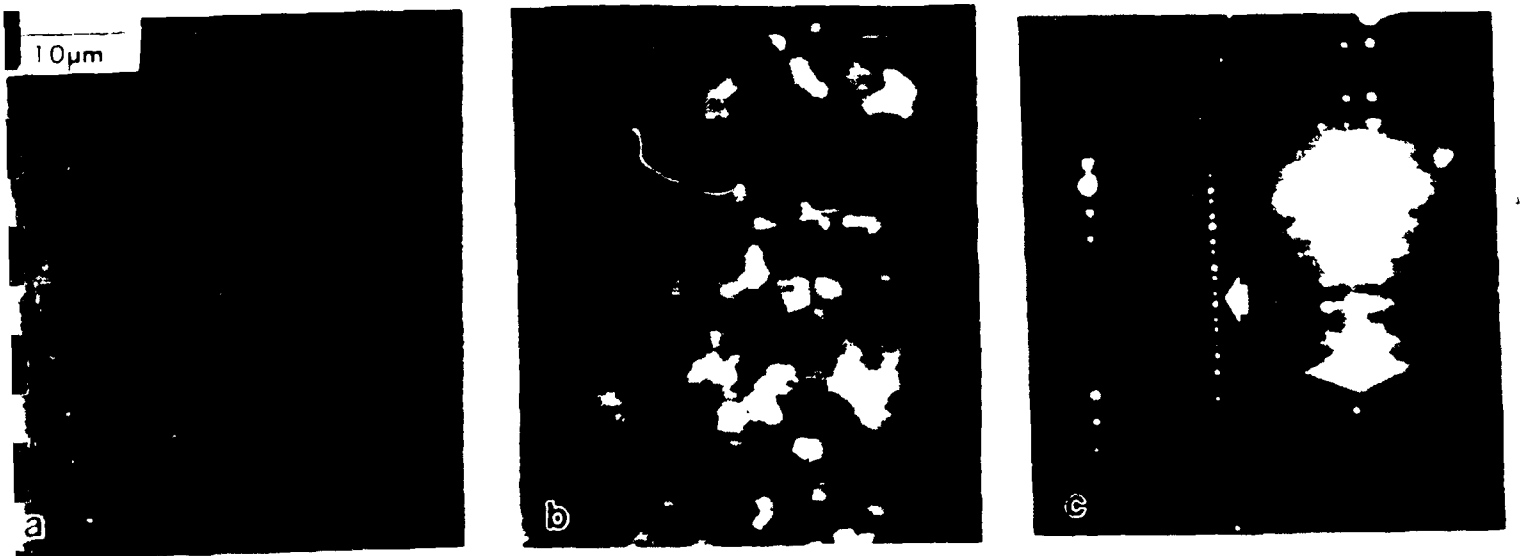
10μm
a
b
c

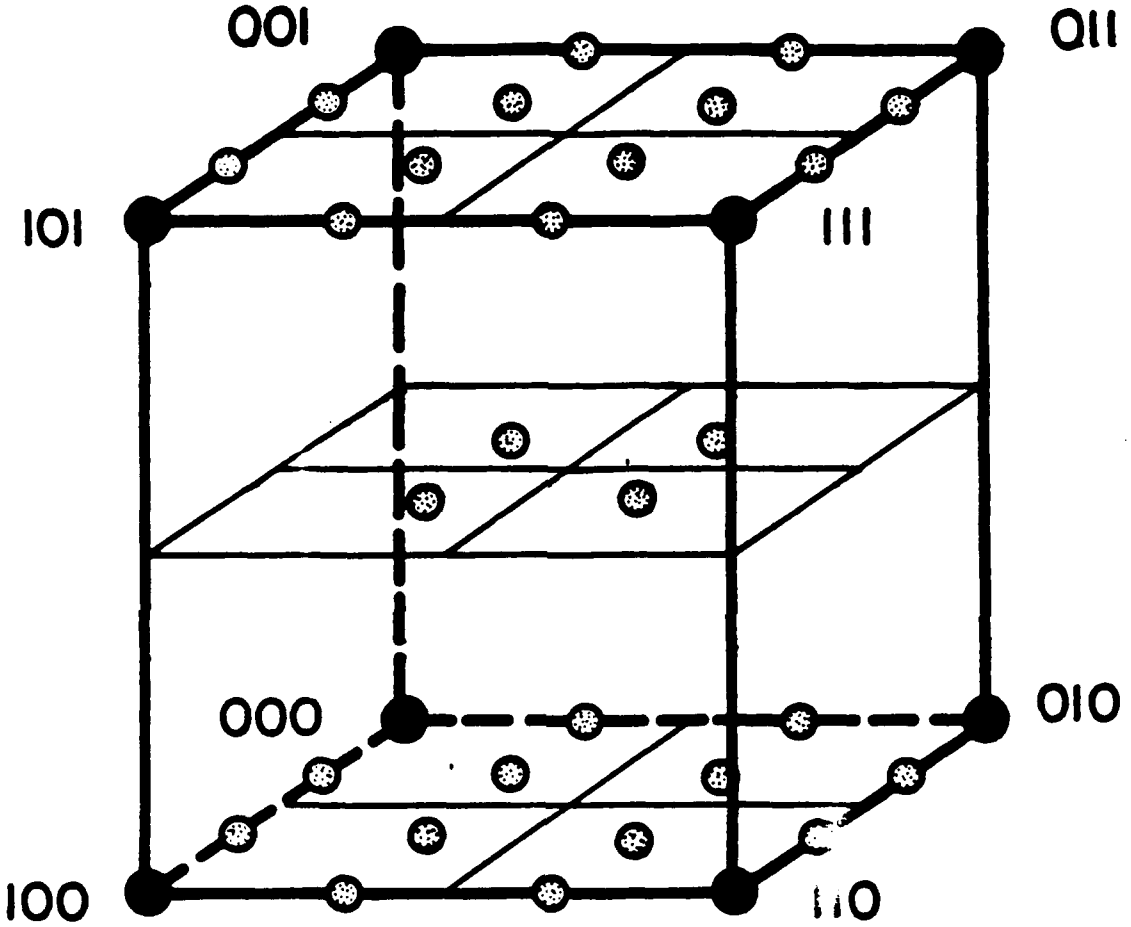

● Observed P4bm reflections
◎ Incommensurate reflections

FIGURE 4

APPENDIX 18

PYROELECTRIC, PIEZOELECTRIC, AND DIELECTRIC PROPERTIES OF β-BaB_2O_4 SINGLE CRYSTAL

R. Guo
A. S. Bhalla

Pyroelectric, piezoelectric, and dielectric properties of β-BaB_2O_4 single crystal

R. Guo and A. S. Bhalla
Materials Research Laboratory, The Pennsylvania State University, University Park, Pennsylvania 16802

(Received 13 July 1989; accepted for publication 5 September 1989)

Dielectric and pyroelectric properties of single-crystal β-barium metaborate (β-BaB_2O_4) are measured in the temperature range from 50 °C down to − 190 °C. Thermal expansion and piezoelectric properties are measured at room temperature. Piezoelectric and electromechanical coupling coefficients in β-BaB_2O_4 are low where as pyroelectric figure of merit p/K is quite attractive for some device applications.

β-barium metaborate (β-BaB_2O_4) is one of the most important second harmonic generation materials.[1,2] It has a high nonlinear optical coefficient, $d_{11} \sim 4 \times d_{36}$ (KDP) and phase matching over a wavelength range from 2000 Å to 1.5 μm. Its transmission range (from 1900 Å to 3.5 μm) and damage threshold > 10 GW/cm² at 100 ps make this material a most desirable candidate for frequency conversion in the ultraviolet range.

β-BaB_2O_4 belongs to the crystal point group symmetry $3m$. Although it is difficult to grow the crystals of β-BaB_2O_4, high optical homogeneity and quality crystals have been grown successfully by the flux technique.[2] Since this crystal belongs to the polar crystal point group, it may have interesting pyroelectric and piezoelectric properties. In this communication we describe the measurements of dielectric and pyroelectric properties over a temperature range − 180–+ 50 °C and piezoelectric properties at room temperature.

The rectangular plates with a c or a axes perpendicular to the major faces were cut, polished, and Au electroded for the measurements of dielectric and pyroelectric properties. Dielectric measurements were carried out over a temperature range of − 180 °C to about 50 °C and a frequency range of 100 Hz-100 kHz by using a computerized automatic measuring system. The pyroelectric coefficients were measured by the Byer and Roundy technique (1972). The remanent polarization P_r was obtained by the integration of the pyroelectric coefficient versus temperature data.

The electromechanical responses of the samples were measured by the piezoelectric resonance method.[3] Since the resonant frequencies are determined by the dimensions of the samples care was taken that all surfaces of the samples were flat and the opposite surfaces parallel to each other. The b-cut plate shaped crystal was used for determining the d_{21} and $d_{15} = d_{24}$, and the c-cut plate shaped crystal was used for determining the d_{33} and $d_{31} = d_{32}$. Poisson ratio σ was determined from the c-cut plate by using the expression

$$\frac{v_3}{v_1} = \frac{1-\sigma}{\sqrt{(c_{11}^E/c_{33}^E)/(1-2\sigma)}},$$

where v_1 and v_3 are the wave velocities of the LE and TE mode, respectively.

Figure 1 shows the temperature dependencies of the pyroelectric coefficient and the ΔP over a temperature range 50

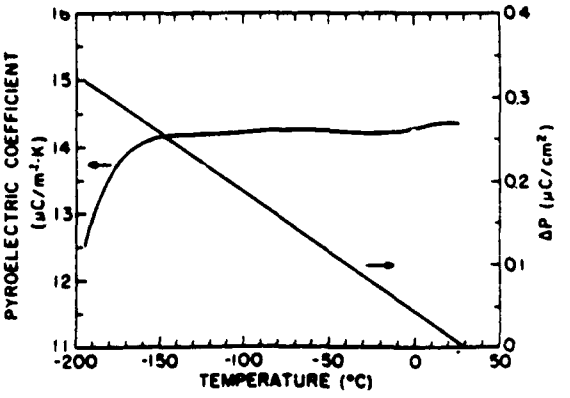

FIG. 1. Temperature dependence of polarization and pyroelectric coefficient of β-BaB_2O_4 single crystal.

 0021-8979/89/246186-03$02.40 © 1989 American Institute of Physics

to -180 °C. The pyroelectric coefficients of β-BaB_2O_4 are practically constant over the entire temperature range, except those close to the liquid nitrogen temperature, indicating the minimal contribution from the secondary pyroelectricity in this range. In the case of point group $3m$ the secondary pyroelectricity can be calculated from the expression,

$$p_{sec} = 2d_{31}(c_{11}\alpha_1 + c_{12}\alpha_1 + c_{13}\alpha_3) + d_{33}(2c_{31}\alpha_1 + c_{33}\alpha_3).$$

The elastic coefficients, c_{ij}, for the β-BaB_2O_4 as reported[4,5] are listed in Table I (all in N/m^2). The room-temperature values of piezoelectric constants $d_{33} \sim 4\times10^{-12}$ C/N and $d_{31} = -0.85\times10^{-12}$ C/N were determined from the piezoelectric resonance measurement, and the thermal expansion, $\alpha_3 = 0.36\times10^{-6}$/°C and $\alpha_1 = -2.54\times10^{-6}$/°C were determined from the strain-versus-temperature measurements.

TABLE I. Thermal, mechanical, electrical, and electromechanical properties of β-BaB_2O_4 single crystal.[a]

Crystal point group	3m
Thermal expansion	$\alpha_1 = -2.54\times10^{-6}$/°C $\quad \alpha_3 = 0.36\times10^{-6}$/°C
Mechanical properties	
Density $\rho = 3.83$ g/cm^3	
Compliances ($\times10^{-12}$ m^2/N)	Stiffnesses ($\times10^9$ N/m^2)[b]
$s_{11}^E = 11.24$	$c_{11}^E = 123.78$
$s_{33}^E = 18.51$	$c_{12}^E = 60.34$
$s_{44}^E = 332.0$	$c_{13}^E = 49.34$
$s_{12}^E = -3.765$	$c_{33}^E = 53.33$
$s_{66}^E = 30.01$	$c_{44}^E = 7.75$
	$c_{66}^E = 32.60$
Young's modulus: $Y^E = 8.898\times10^{10}$ N/m^2	
Poisson's ratio: $\sigma = 0.335$	
Mechanical quality factor: planar mode $Q_m^E = 328$	
thickness mode $Q_m^E = 2095$	
Electrical properties	
Dielectric constant	
$K_{33}^T = 8.2$ (1 kHz)	
$K_{11}^T = 6.5$ (1 kHz)	
$K_{33}^E = 6.6$ (1 MHz)	
$K_{11}^E = 5.78$ (1 MHz)	
$\tan\delta < 10^{-3}$ $(10^2$–10^5 Hz)	
Resistivity	
$\rho_{33} = 16.31\times10^6\ \Omega$ m	
$\rho_{11} = 10.15\times10^6\ \Omega$ m	
Piezoelectric	
Charge constants ($\times10^{-12}$ C/N)	
$d_{33} = 4.0$	
$d_{31} = -0.85$	
$d_{15} = 1.26$	
$d_{16} = 0.3$	
Hydrostatic	
$d_h = 2.2$	
Voltage constants ($\times10^{-3}$ V m/N)	
$g_{33} = 55.12$	
$g_{31} = -11.73$	
$g_{15} = 23.3$	
$g_{16} = 5.2$	
Hydrostatic	
$g_h = 30.6$	
Electromechanic coupling constants ($\times10^{-2}$)	
$k_{33} = 7.8$	
$k_{31} = 3.0$	
$k_{15} = 0.9$	
$k_{16} = 0.7$	
$k_t = 2.4$	
Pyroelectric coefficient	
$p_3 = 14.5\ \mu$C/m^2 K	

[a] All values at room temperature.
[b] Reference 4.

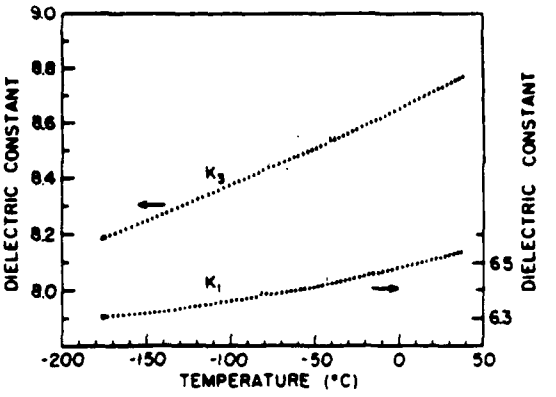

FIG. 2. Temperature dependence of dielectric constants K_3(∥[100]) and K_1(∥[001]) of β-BaB_2O_4 single crystal (frequency range 10^2–10^5 Hz).

Using the values of c_{ij}, d_{ij}, and α_i in the above expression, the secondary pyroelectric contribution was estimated to be $-0.16\ \mu$C/m^2 + K. The observed total pyroelectric coefficient ($p_T = p_{pnm} + p_{sec}$) at room temperature was $14.5\ \mu$C/m^2 K. In general in the nonferroelectric pyroelectric crystals the major temperature dependence of the pyroelectric coefficient is due to the secondary contribution. Since in the case of β-BaB_2O_4 the secondary contribution is negligible, the room-temperature coefficients are representative of the primary pyroelectricity. Also the temperature dependence of the pyroelectric coefficient with decrease in temperature is very small (Fig. 1).

The dielectric constant K and loss $\tan\delta$, on c and a plates were measured over a temperature range 50–-180 °C and frequency range 100 Hz–100 kHz. Figure 2 shows the room temperature $K_3 \simeq 8.2$ and $K_1 \simeq 6.5$, and these values along with $\tan\delta_3 \simeq \tan\delta_1 < 10^{-3}$ (not shown in the figure) are almost constant down to the liquid nitrogen temperature. The calculated figure of merit $p/K \sim 2\times10^{-6}$ μC/m^2 K is about half of that of $LiTaO_3$ at room temperature. At lower temperature, (p/K) in β-BaB_2O_4 stays almost constant as compared to the p/K in many of the ferroelectric materials, in which case it decreases with the decrease in temperature. Also, it is interesting to note that the $\tan\delta$ values are $<10^{-3}$ and stay practically the same throughout the measurement temperature range. Although the pyroelectric coefficients are not very high, the reasonable p/K, low $\tan\delta < 10^{-3}$, and the temperature-independent p, K, and $\tan\delta$ coefficients are still attractive for a number of applications.

As listed in Table I, the piezoelectric and electromechanical coupling coefficients in β-BaB_2O_4 are rather low and thus this material may not be very interesting for the piezoelectric transducer applications.

The authors wish to acknowledge Professor Q. C. Xu for his help in hydrostatic measurement.

[1]S. Lu, M. Ho, and J. Huang, Acta Phys. Sinica 33, 948 (1982).
[2]A. Jiang, F. Cheng, Q. Lin, Z. Cheng, and Y. Zheng, J. Cryst. Growth 79, 963 (1986).
[3]IEEE Standard on Piezoelectricity, ANSI/IEEE, Std. (IEEE, New York, 1978), p. 176.
[4]E. K. Graham, E. G. Hilbert, and A. S. Bhalla, "β-BaB_2O_4: Elastic and Dielectric Properties" (private communication, 1986).
[5]A. S. Bhalla, in *Landolt-Bornstein, New Series* (Springer, Berlin, 1984), Vol. 18, p. 325.